The Flow of Amorphous Solids: Elastoplastic Models and Mode-Coupling Approach

Alexandre Nicolas

UNIVERSITÉ DE GRENOBLE

THÈSE

Pour obtenir le grade de

DOCTEUR DE L'UNIVERSITÉ DE GRENOBLE

Spécialité : **Physique des matériaux**

Arrêté ministériel : 7 août 2006

Présentée par

Alexandre NICOLAS

Thèse dirigée par **Jean-Louis BARRAT**

préparée au sein **Laboratoire Interdisciplinaire de Physique**
et de **École Doctorale de Physique**

Écoulements de solides amorphes : modélisation élastoplastique et théorie de couplage de modes

Thèse soutenue publiquement le **8 octobre 2014**,
devant le jury composé de :

M. Jean-Louis BARRAT
Professeur, Université Grenoble I, Directeur de thèse

M. Matthias FUCHS
Professeur, Université de Constance, Examinateur

M. Olivier POULIQUEN
Directeur de recherche, Polytech Marseille (IUSTI), Examinateur

M. Stéphane ROUX
Directeur de recherche, École Normale Supérieure de Cachan (LMT), Rapporteur

M. Peter SOLLICH
Professeur, King's College London, Rapporteur

M. Gioacchino VIGGIANI
Professeur, Université Grenoble I, Examinateur

Alexandre NICOLAS : *The Flow of Amorphous Solids: Elastoplastic Models and Mode-Coupling Approach,* July 2014

Université de Grenoble

Laboratoire Interdisciplinaire de Physique

Alexandre Nicolas

The Flow of Amorphous Solids : Elastoplastic Models and Mode-Coupling Approach

This thesis is submitted for the degree of
Docteur de l'Université de Grenoble

September 2014

À la différence des liquides simples, les solides amorphes, une vaste catégorie de matériaux allant des verres métalliques aux émulsions concentrées, ne se mettent à s'écouler qu'au-delà d'une contrainte finie. Notre thèse a pour objet la modélisation de cet écoulement, dans un cadre général et avec un accent mis sur les hétérogénéités.

En premier lieu, notre travail a porté sur l'inclusion d'inhomogénéités dans le cadre de la théorie de couplage de modes appliquée à la rhéologie et nous avons notamment obtenu une équation générale d'évolution des inhomogénéités de densité.

À basse température, l'écoulement est en effet fortement hétérogène : des phases de déformation élastique sont entrecoupées de réarrangements de particules, brusques et localisés, qui interagissent par le biais des déformations élastiques qu'ils génèrent. En second lieu, nous avons donc considéré un modèle calqué sur ce scénario et affiné ses éléments constitutifs pour rendre compte de la compétition entre cisaillement appliqué et réarrangements locaux, à l'origine de la courbe d'écoulement des matériaux athermiques. Cette dernière a été reproduite de manière satisfaisante.

Pour ce qui est des corrélations spatiales dans l'écoulement, nous avons montré qu'il n'existe pas de loi d'échelle universelle dans les modèles élasto-plastiques, malgré la présence d'une classe de longueurs de corrélation décroissant comme $\dot{\gamma}^{-1/d}$ en d dimensions, dans le régime dominé par le cisaillement.

Par ailleurs, dans diverses variantes du modèle, le cisaillement se trouve localisé dans une région du matériau. Ce phénomène apparaît dès lors que les blocs élasto-plastiques sont durablement fragilisés à la suite d'un événement plastique.

Enfin, les prédictions du modèle ont été directement mises en regard avec des expériences sur l'écoulement en microcanal d'émulsions concentrées et des simulations de dynamique moléculaire à température nulle. Les écarts observés nous ont poussé à développer et implémenter un code plus flexible, qui s'appuie sur une routine simplifiée d'Éléments Finis et rend mieux compte du désordre structurel et des effets inertiels.

Contrary to the case of simple fluids, a finite stress is required to initiate the flow of amorphous solids, a broad class of materials ranging from bulk metallic glasses to dense emulsions. The objective of this thesis is to model the flow of these materials in a general framework, with an emphasis on heterogeneities.

In a first approach, using the liquid regime as a starting point, I have investigated to what extent inhomogeneities can be accommodated in the framework of the mode-coupling theory of rheology. A generic equation for the evolution of density inhomogeneities has been derived.

At low temperatures, the flow is indeed quite heterogeneous: it consists of periods of elastic deformation interspersed with swift localised rearrangements of particles, that induce long-range elastic deformations and can thereby spark off new rearrangements. In a second approach, a model rooted in this scenario has been refined so as to reflect the interplay between the external drive and the localised rearrangements, which is at the origin of the flow curve of athermal solids. The latter has been reproduced satisfactorily.

Turning to spatial correlations in the flow, we have shown that there exists no universal scaling for these correlations in elastoplastic models, although a broad class of correlation lengths scale with $\dot{\gamma}^{-1/d}$ in the shear-dominated regime in d dimensions.

Besides, shear localisation has been observed in diverse variants of the model, whenever blocks are durably weakened following a plastic event.

Finally, we have directly compared model predictions to experimental results on the flow of dense emulsions through microchannels and to athermal molecular dynamics simulations. Spurred on by the observation of some discrepancies, we have developed and implemented a more flexible code, based on a simplified Finite Element routine, which notably provides a better account of structural disorder and inertial effects.

ACKNOWLEDGEMENTS

I am indebted to a number of colleagues in the academic world.

My first words of thanks are naturally directed to my supervisor, Jean-Louis Barrat, who has granted me all the latitude that I could hope for in my research, but, at the same time, has been tirelessly responsive to my questions, which were always addressed with sharp scientific insight. I am grateful for his trust and his patience with my remarks and objections, whether grounded or not. I am also grateful to Kirsten Martens, whose scientific advice, availability and soft skills I greatly appreciated. Many thanks, too, to my fellow group members, with whom it has been a pleasure to interact, Natalia Bedoya, who bravely put up with me in our shared office for two years, Ezequiel Ferrero, for the lively scientific discussions that we had, but also the many other colleagues with whom I have collaborated (Francesco Puosi, Hideyuki Mizuno, Luca Marradi) or discussed, in the healthy and friendly atmosphere of the group and the lab in general.

I would also like to thank Matthias Fuchs, who most kindly welcomed me in his research group in Constance for quite a few months and introduced me to the spirit of the mode-coupling theory, and with whom I enjoyed discussing. I thank Marianne Griesser for taking care of all practicalities during these stays and the members of the research unit, Fabian Frahsa, for answering my countless questions, Sebastian Fritschi, Simon Papenkort, etc.

I am also grateful to Joerg Rottler for the active scientific collaboration and the very pleasant visit to his research group in Vancouver.

In addition, during the course of my thesis, I have benefitted from enlightening scientific discussions with Thibaut Divoux, Sébastien Manneville, David Rodney, Pinaki Chaudhuri, Suvendu Mandal, Fathollah Varnik, Nima Siboni, Marc-Antoine Fardin, Lydéric Bocquet, Alexander Morozov, Mike Cates, Anton Smessaert, among others.

I should also sincerely thank the members of my PhD Committee who have accepted the task of assessing my thesis, which has turned out to be somewhat longer than originally expected.

Qu'on me permette de conclure cette section [1] avec des remerciements plus personnels, que j'adresse à mes parents, à mon frère et à mes proches, qui m'accompagnent depuis bien des années déjà.

1. This document was typeset with a template that I have modified from the typographical look-and-feel `classicthesis` developed by André Miede. The style was inspired by Robert Bringhurst's seminal book on typography *"The Elements of Typographic Style"*.

CONTENTS

1 A bird's eye view 1
- 1.1 Phenomenology 1
- 1.2 An intractable set of equations 4
- 1.3 Dynamical theories 4
- 1.4 A Potential Energy Landscape (PEL) approach to quiescent systems 5
- 1.5 The PEL approach to systems under shear 8
- 1.6 From the global PEL to mesoscopic PELs 9
- 1.7 Structure of the thesis 11

I Density and stress heterogeneities in the mode-coupling description of flow 13

2 From microscopic equations to a constitutive equation 17
- 2.1 Microscopic equations 17
- 2.2 The mode-coupling view of the glass transition 19
- 2.3 Inclusion of shear 23
- 2.4 Some remarks regarding the flow 24
- 2.5 A generalised Green-Kubo formula 25
- 2.6 Inhomogeneous case: Recovery of the advection term 29
- 2.7 Inhomogeneity relaxation and creation 31
- 2.8 Appendices 36

3 A perturbative approach to slightly heterogeneous flows 43
- 3.1 Coupling to linear density modes 43
- 3.2 Symmetries of the flow 44
- 3.3 (Absence of) density fluctuations for slight deviations from homogeneity 46
- 3.4 Corrective terms due to flow inhomogeneities 47
- 3.5 Perspectives 48
- 3.6 Appendix 49

4 Elastic instability in a schematic model 51
- 4.1 The elastic instability 52
- 4.2 Schematic model 53
- 4.3 Linear stability analysis of the base flow 56

II The elastoplastic description of the flow of amorphous solids 61

5 A similar flow scenario for extremely diverse disordered solids 65
- 5.1 The elastic-rebound theory of earthquakes 65
- 5.2 Localised shear transformations 66
- 5.3 Non-local effects 67
- 5.4 Flow curve 68

6 Mesoscopic models: state of the art 71
6.1 Generic viscoelastic models 71
6.2 Extremal models 72
6.3 Models based on a periodic potential landscape 73
6.4 The Soft Glassy Rheology (SGR) Model 74
6.5 The Shear-Transformation Zone (STZ) theory 76
6.6 Hébraud-Lequeux's model and related models based on a latency time 76

7 Identification of the relevant processes in the rheology of athermal solids 81
7.1 Relevant timescales for the bulk rheology 81
7.2 Athermal regime 83
7.3 Thermal regime and ageing 84
7.4 Description of the stress relaxation during a plastic event 84
7.5 Appendices 89

8 Methods 93
8.1 General algorithm 93
8.2 Derivation of the elastic propagator in a two-dimensional uniform elastic medium 94
8.3 How to account for convection 97
8.4 Appendix 101

III Numerical investigation of the flow properties using an elasto-plastic model 105

9 General flow properties 109
9.1 Flow curve within Picard's model: assessment of the importance of stress tensoriality and convection 109
9.2 Yield angles 111
9.3 Realistic dynamical rules in the athermal regime 112
9.4 Extension to thermal materials; ageing 115
9.5 Appendix 121

10 Of effective temperatures 123
10.1 Various definitions of effective temperatures 123
10.2 Effective temperatures based on the fluctuation-dissipation theorem 126
10.3 An effective activation temperature due to mechanical noise? 128
10.4 Appendices 135

11 Shear localisation 139
11.1 Analytical approach to shear localisation in Picard's model 139
11.2 Numerical investigation of shear-banding in Picard's model 141
11.3 Shear-localisation in the refined model 143
11.4 Speculative general criterion for shear localisation 144

12 Correlation lengths 147
12.1 Scalings of the correlation lengths in Picard's model 147

12.2 Scalings of the correlation lengths in the refined athermal model 153
12.3 Appendix 158

13 Flow in a microchannel 161
13.1 Simulation of a genuine 2D microchannel 161
13.2 Simulation of the flow 164
13.3 Cooperativity in the bulk flow: a manifestation of the coupling between heterogeneous regions 167
13.4 A specific rheology near the walls? 172
13.5 Appendices 178

14 Spatiotemporal correlations between plastic events 183
14.1 Comparative study of general flow properties obtained in Molecular Dynamics (MD) and with the elastoplastic model 183
14.2 Conceivable protocols for the detection of plastic event avalanches 188
14.3 Correlations between plastic events 190

IV Elastoplastic modelling based on a simplified Finite Element routine 199

15 Finite Elements (FE): Methods 203
15.1 The Finite Element method in a glance 203
15.2 Spatial discretisation 206
15.3 Discretisation of the dynamics 210
15.4 Boundary conditions 211
15.5 Simple tests and appraisal of the algorithm 213

16 Response to a single plastic rearrangement 217
16.1 MD simulations with Dissipative Particle Dynamics 217
16.2 Fitting of the model parameters 218
16.3 Artificially triggered shear transformations 223
16.4 Disorder-averaged propagation 223
16.5 Effect of structural disorder 228
16.6 Time-dependent response to a particular plastic event 228
16.7 Shear rearrangement dynamics 229
16.8 Appendix 233

17 Correlations between plastic events: a preliminary revisitation using the FE-based approach 239
17.1 MD simulations with Dissipative Particle Dynamics 239
17.2 Presentation of the elastoplastic model 240
17.3 Flow simulations with the elastoplastic model 242

18 Force chains in granular media 247
18.1 Basics about sheared granular media 247
18.2 How to model force chains in the elastoplastic framework? 249
18.3 Preliminary results 251
18.4 Some open questions 254

RECURRENT SYMBOLS AND ABBREVIATIONS

SYMBOLS

Symbol	Meaning
γ	shear strain
$\boldsymbol{\epsilon}$	linearised deformation tensor
η	dynamic viscosity
μ	shear modulus
n	(often) plastic activity of an elastoplastic block (1 if plastic, 0 otherwise)
ρ_k	k-Fourier mode of the local density
$\boldsymbol{\sigma}$	(generally) local stress tensor
Σ	macroscopic shear stress

ABBREVIATIONS

Acronym	Meaning
BC	boundary condition(s)
DPD	dissipative particle dynamics
FE	finite element(s)
lhs	left-hand side
MD	molecular dynamics
MCT	mode-coupling theory
PEL	potential energy landscape
rhs	right-hand side
SGR	soft glassy rheology (model)
2D	two dimensions

PRÉAMBULE

Hac in re scilicet una
Multum dissimiles, ad cætera pæne gemelli
(Horace, *Épître X*)

La magie propre au soufflage du verre provient, en partie, du fait qu'un verre de silicates, le matériau cassant par excellence à température ambiante, est transformé en une substance visqueuse, malléable, par simple chauffage. Pour peu que l'on s'enquière de l'origine physique de cette transformation frappante, le mystère ne fait que s'épaissir. En effet, les interactions entre les constituants atomiques du verre n'ont guère changé au cours du chauffage. De manière encore plus intrigante, l'observation microscopique du verre dur et de son pendant visqueux, qui sera désormais appelé liquide surfondu, ne révèle aucune différence remarquable au niveau de l'arrangement des atomes et molécules de ces matériaux, c'est-à-dire de leur structure moléculaire.

Cette similitude en termes de structure constraste vivement avec les changements qui se produisent à la fonte d'un glaçon. Pour ce dernier, quand la température approche 0°C, les molécules d'eau, alors régulièrement empilées, se mettent à vibrer à tel point que la structure ordonnée, quoique énergétiquement favorable, laisse place au tohu-bohu du liquide. Ce changement d'état se produit à une température précise, la température de fusion, soit 0°C en l'occurrence.

En revanche, entre le verre et le liquide surfondu, il n'existe pas de transition aussi nette. Certes, on peut définir, par commodité, une température de transition vitreuse T_g, comme la température en deça de laquelle le matériau devient «vraiment trop visqueux», autrement dit, par convention, lorsque sa viscosité franchit le seuil des $10^{12}\text{Pa} \cdot \text{s}$ [Binder and Kob, 2011]. Mais la température ainsi définie dépendra de la vitesse de chauffage ou de refroidissement, si celle-ci n'est pas prescrite.

Phénoménologie de la transition vitreuse à l'échelle microscopique

L'augmentation spectaculaire de la viscosité autour de la transition vitreuse s'accompagne d'une augmentation tout aussi spectaculaire du temps de relaxation structurel du matériau. Il faut en effet quelques minutes ($\sim 10^2\,\text{s}$) à ce dernier pour perdre la mémoire de sa configuration instantanée à la température de transition vitreuse, soit un temps supérieur de 15 ordres de grandeur au temps de vibration moléculaire, et l'écart s'amplifie encore plus drastiquement si la température diminue davantage. Il s'ensuit qu'au repos, les verres silicatés ne peuvent pas atteindre leur état d'équilibre en quelque durée expérimentalement réaliste que ce soit. Ils ne peuvent pas non plus relâcher la contrainte accumulée suite à une petite déformation, ce qui, à la grande satisfaction des souffleurs de verre et de l'industrie verrière, leur assure une solidité effective.

Si l'on descend à l'échelle microscopique, l'extrême lenteur de la relaxation structurelle s'explique par le fait que les particules [2] sont piégées dans la "cage" formée par les nombreux voisins qui les entourent; en dessous de T_g, les fluctuations thermiques, par exemple les vibrations cinétiques, deviennent trop faibles pour permettre aux particules de quitter cette cage [Goldstein, 1969, Götze and Voigtmann, 2001] et la *plupart* d'entre elles se contentent d'évoluer en son sein (c'est le processus de relaxation β). Ce n'est qu'au bout d'un temps extrêmement long qu'elles parviennent enfin à s'échapper, et que la mémoire de la configuration initiale est finalement effacée (c'est le processus de relaxation α). Mais, après cette évasion, les particules tombent dans une cage encore plus solide en moyenne (la physique est sans merci pour les particules en cavale !), et le verre devient de plus en plus stable. Cette évolution structurelle est connue sous le nom de *vieillissement* [Binder and Kob, 2011].

La transition de blocage

On observe également une transition donnant lieu à de la rigidité sans mise en ordre dans un tout autre type de matériaux, dans lesquels les fluctuations thermiques n'ont, au mieux, qu'un rôle négligeable. Aussi l'émergence de la rigidité (la *transition de blocage*) n'y est-elle pas contrôlée par la température, mais par l'accroissement de la fraction volumique ϕ: les particules sont entassées de manière tellement dense que leurs contacts empêchent tout mouvement, pour la majorité d'entre elles.

La transition vitreuse et la transition de blocage sont des phénomènes a priori distincts [Mari et al., 2009, Ikeda et al., 2012]. Pour illustrer ce point, il suffit de considérer une dispersion légèrement polydisperse de sphères dures, c'est-à-dire de boules de billard. Lorsque augmente la fraction volumique à température finie, si la cristallisation est évitée, la matériau voit sa dynamique quasiment gelée à l'entrée dans l'état vitreux, autour de $\phi = 58\%$ en trois dimensions, état caractérisé par des forces entropiques (finies) et donc des constantes élastiques finies. Si l'on comprime davantage le système, il atteint le point d'empilement aléatoire compact autour de $\phi = 64\%$; à ce point de blocage, quelle que soit la température, la pression résulte des forces de contacts et diverge donc [Mari, 2011], ainsi que le font alors les modules élastiques.

Des matériaux d'une diversité étonnante

Mais laissons cette distinction de côté et tentons d'englober du regard l'étonnante diversité de la classe des matériaux solides, mais désordonnés. Ils couvrent de nombreux ordres de grandeur en termes de taille de particule, comme l'illustre la Fig. 1.1 : les atomes métalliques composant les verres métalliques, de même que les atomes de silicium et d'oxygène dans les verres de silices, ont une taille

2. Tout au long de cette thèse, nous emploierons le mot "particle" pour faire référence à l'entité élementaire du matériau, c'est-à-dire l'atome dans le cas du verre de silicates ou du verre métallique, la gouttelette pour une émulsion, la bulle pour une mousse, ou encore le grain pour un matériau granulaire.

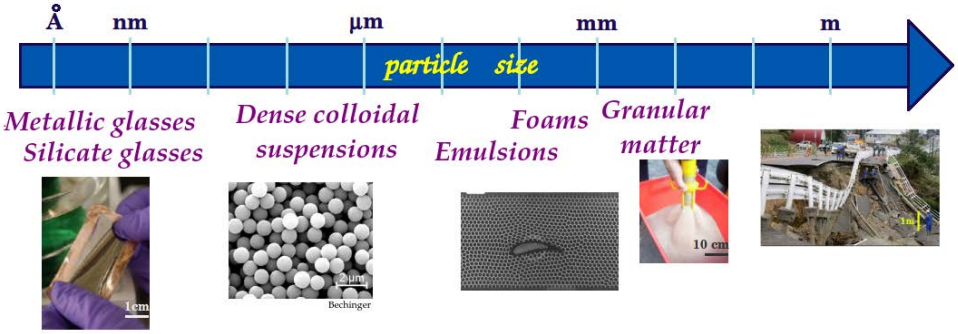

Figure 0.1: Exemples de solides amorphes, rangés en fonction de la taille de leurs constituents élémentaires.

de l'ordre de l'Angström; les colloïdes sont des agrégats compacts, en général de nature polymérique, qui mesurent moins d'un micron; les mousses et émulsions sont faites de gouttelettes ou de bulles de quelques dizaines de microns à quelques dizaines de millimètres; enfin, les matériaux granulaires comprennent les grains de riz, macroscopiques, le sable, les billes de verre, etc. Pour ce qui est de la rigidité, le module d'Young d'un verre métallique est de l'ordre de 100 GPa, quand celui d'une mousse molle tourne autour de 100 Pa.

L'ambitieuse idée qui nous a guidés, nous comme bien d'autres, est que, nonobstant leur extrême diversité, ces matériaux (compte tenu de leur solidité, ainsi que de l'absence de structure ordonnée, et donc de défauts facilement identifiables) manifestent des propriétés communes. Nous aspirons donc à appréhender dans un cadre général la déformation et l'écoulement de ces matériaux, en réponse à un cisaillement.

Un cadre commun pour modéliser l'écoulement des solides amorphes?

Du fait de leur solidité, les matériaux amorphes se déforment de manière élastique lorsque de faibles contraintes de cisaillement leur sont appliquées. Pour des contraintes légèrement plus élevées, on peut observer un certain niveau de déformation plastique mais la déformation n'est pas auto-entretenue et ne s'exerce que pour une durée finie, à moins que la contrainte dépasse une valeur critique, appelée contrainte seuil en rhéologie. Pour des contraintes plus importantes, le matériau cède: s'il est cassant, comme le verre silicaté, cela aboutit à une fracture macroscopique. En revanche, pour la plupart des verres mous, il s'ensuit un écoulement permanent. Ces deux catégories de matériaux sont habituellement étudiées par des communautés scientifiques différentes : d'un côté, on trouve les ingénieurs des matériaux, qui distinguent matériaux cassants et matériaux ductiles; de l'autre, les rhéologues, qui mettent en exergue le contraste entre localisation du cisaillement et écoulement homogène. Dans une vision globale, ces différences peuvent-elles se ramener à la variation d'un paramètre physique général ?

De manière non moins importante, les effets collectifs et les hétérogénéités dans l'écoulement persistent, même quand les solides amorphes sont macro-

scopiquement fluidifiés par le cisaillement. Ces effets non locaux sont une manifestation de la solidité du matériau au repos. En effet, si nous nous rappelons l'exemple du soufflage de verre, il ne fait pas de doute que le matériau répondra à, mettons, un coup d'aiguillon de manière essentiellement locale à haute température, alors que la réponse sera globale dans l'état solide. Quel rôle ces effets collectifs jouent-ils dans l'écoulement ? Dans quelle mesure retrouve-t-on la limite du liquide simple à vitesse de forçage élevée, c'est-à-dire à fort taux de cisaillement ?

D'autres différences au sein de l'hétéroclite catégorie des solides amorphes appellent d'autres questions : les mécanismes à l'œuvre dans l'écoulement des matériaux thermiques, d'un côté, et athermiques, de l'autre, sont-ils différents ? Les systèmes de grains durs, frottants, peuvent-ils être traités comme les émulsions à l'échelle mésoscopique ?

Plan d'ensemble de la thèse

La première partie de ce manuscrit est dédiée à l'approche de la rhéologie des liquides surfondus et des verres par la théorie de couplage de modes, avec en ligne de mire l'inclusion d'inhomogénéités (de contrainte ou de densité) dans la théorie, dans l'optique, par exemple, d'obtenir une description plus réaliste des écoulements fortement hétérogènes observés à basse température.

Dans les parties suivantes, nous adoptons d'entrée de jeu une approche mieux adaptée au régime de basse température, à savoir, la modélisation élasto-plastique. Les parties 2 et 3 visent à davantage rapprocher les ingrédients de ces modèles des processus physiques à l'œuvre dans les solides amorphes en situation d'écoulement, et, à l'aide de simulations numériques, d'atteindre à une meilleure compréhension de phénomènes tels que la localisation du cisaillement, les corrélations spatiales dans l'écoulement et les phénomènes collectifs dans les écoulements dans des microcanaux. Enfin, dans la dernière partie, nous travaillons à une implémentation bien plus flexible des modèles élastoplastiques, fondée sur une routine d'Éléments Finis simplifiée, laquelle rend notamment mieux compte du désordre structurel et, éventuellement, de l'anisotropie locale du matériau.

1 A BIRD'S EYE VIEW

Hac in re scilicet una
Multum dissimiles, ad cætera pæne gemelli
(Horace, *Epistle X*)

Part of the magic of glassblowing comes from the fact that silicate glass, the paradigmatic example of a brittle material at room temperature, is turned into a viscous, malleable substance through plain heating. Should one inquire into the physical origin of this dramatic transformation, the mystery will get even deeper. Indeed, the interactions between the atomic constituents of the glass do not change significantly in the heating process. Even more intriguingly, observing the brittle glass and its viscous counterpart, hereafter called supercooled liquid, at the microscale does not reveal any consipicuous difference in the arrangements of their atoms and molecules, *i.e.*, in their molecular structure.

This structural similarity is in marked contrast with the changes occurring when an ice cube is melted. In the latter case, as the temperature approaches 0°C, the regularly stacked water molecules in the ice cube start vibrating so much that the ordered structure, albeit energetically favourable, finally turns into a jumble. The change of state occurs exactly at a specific *melting temperature*, 0°C here.

On the other hand, no such clearcut transition temperature separates the glass from the supercooled liquid. For sure, a glass transition temperature T_g can still be defined out of convenience, as the temperature below which the material becomes "really too viscous", that is, conventionally, when its viscosity η exceeds $10^{12}\text{Pa} \cdot \text{s}$ [Binder and Kob, 2011]. But the temperature thus defined will depend on the heating or cooling rate, if it is not prescribed.

1.1 PHENOMENOLOGY

1.1.1 *Microscopic picture of the glass transition*

The dramatic increase of viscosity around the glass transition is associated with a dramatic increase of the structural relaxation time: at the glass transition temperature, the material needs a couple of minutes ($\sim 10^2\,\text{s}$) to forget about its instantaneous configuration, *i.e.*, about 15 orders of magnitude longer than the molecular vibration time, and drastically more when the material is further cooled down. It follows that silicate glasses cannot equilibriate over any experimental time scale, at rest. Nor can they relax in response to a small deformation, which, to the great relief of glassblowers and glass manufacturers, implies that they are effectively solid.

Microscopically, the sluggish structural relaxation is rationalised by the fact that particles [1] are trapped in the "cage" formed by the many neighbours that surround them; below T_g, thermal fluctuations, *e.g.*, kinetic vibrations, become too small to allow particles to escape from this cage [Goldstein, 1969, Götze and Voigtmann, 2001], and *most* of them can only move within the precincts of their cages (this is the so called *β-relaxation process*). An extremely long time elapses before they finally break out of their cages, *i.e.*, before the memory of the initial configuration has been fully erased (this is the *α-relaxation process*). But, after their escapes, particles end up in yet stronger cages on average (physics is adamant to cage breakers!), and the glass becomes more and more stable. This structural evolution is known as *ageing* [Binder and Kob, 2011].

1.1.2 *The jamming transition*

Interestingly, a transition to rigidity without ordering is also observed in a very different class of materials, in which thermal fluctuations play a negligible role. The onset of rigidity in these systems, known as the *jamming transition*, is not controlled by a decline of temperature, but by an increase of the volume fraction ϕ: particles are packed so densely that their contacts prevent (the majority of) them from moving.

The glass transition and the jamming transition are distinct phenomena *a priori* [Mari et al., 2009, Ikeda et al., 2012]. To illustrate this, let us consider a slightly polydisperse dispersion of hard spheres, *i.e.*, bowling-ball-like particles. If the volume fraction is increased at finite temperature and crystallisation is avoided, the material is arrested into a glassy state, characterised by (finite) entropic forces and therefore finite elastic constants, around $\phi = 58\%$ in three dimensions. If the density is further increased, the system reaches the random close packing point around $\phi = 64\%$; at this (jamming) point, regardless of the temperature, the pressure is set by contact forces and thus diverges [Mari, 2011]; so do the elastic moduli.

1.1.3 *Extremely diverse materials*

If one leaves aside this distinction, the breadth and diversity of the class of solid, but disordered, materials are arresting. These materials span many orders of magnitude in terms of particle size, as illustrated in Fig. 1.1: the metal atoms composing metallic glasses, as well as the silicon and oxygen atoms in silica glass, lie in the Angström range; colloids are compact (generally polymeric) aggregates of less than one micron in radius; foams and emulsions are made of droplets or bubbles from tens of micrometers up to a couple of millimeters; finally, granular matter encompasses macroscopic rice grains, sand, glass beads, etc. In terms of

1. Throughout this manuscript, the word 'particle' shall refer to the elementary entity of the material: the atom in a silicate or a metallic glass, the droplet in an emulsion, the bubble in a foam, the grain in granular matter.

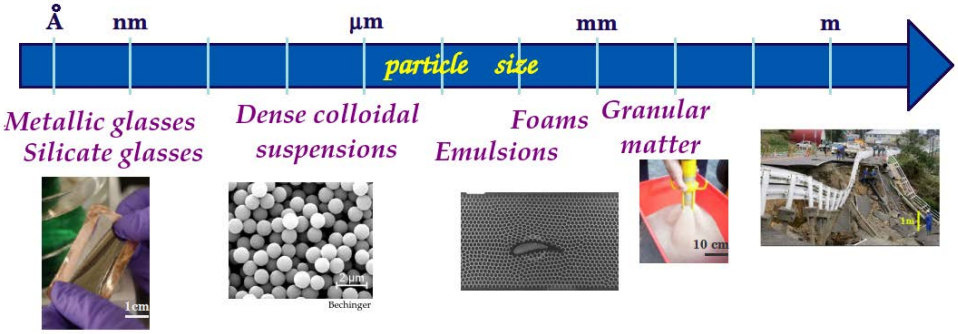

Figure 1.1: Amorphous solids, sorted by the size of their elementary constituents.

stiffness, the Young modulus of a metallic glass is of order 100 GPa, whereas that of a soft foam lies around 100 Pa.

The ambitious hope that has guided us and many others is that, no matter how diverse these materials are, their solidity, combined with the absence of ordered structure, and, therefore, of easily identifiable defects, entails some common properties. Our goal is then to capture the deformation and the flow of these materials, in response to shear, in a general framework.

1.1.4 *A common framework for the flow of amorphous solids?*

On account of their solidity, amorphous solids deform elastically upon application of very small shear stresses. For slightly larger stresses, some extent of plastic strain may be observed, but the deformation is not self-sustained and finally dies out, as long as the applied stress does not exceed a critical value, known as yield stress in rheology. If larger stresses are applied, the material yields: for brittle materials, such as silicate glasses, this culminates in macroscopic fracture; on the other hand, for the majority of soft glassy materials, a steady-state flow ensues. These two categories of materials are generally studied by distinct scientific communities: on the one hand, materials' scientists, who make a distinction between brittle and ductile materials; on the other hand, rheologists, who put to the forefront the contrast between shear localisation and homogeneous flow. In a global perspective, can these differences be subsumed under a generic physical parameter?

Another important aspect is that, even when disordered solids are fluidised, collective effects and flow heterogeneities subsist. The presence of non-local effects bears the signature of the material's solidity at rest: calling back to mind the example of glassblowing, it is clear that the response of the material to, say, a prod with a sharp pencil is mostly local at high temperatures, but global in the solid state. What role do these collective effects play in the flow? To what extent is the simple fluid limit recovered when the driving velocity, *i.e.*, the shear rate, is increased?

Other discrepancies in the heteroclite category of amorphous solids lead to other questions: Are different mechanisms responsible for the flow of thermal

and athermal materials? Are hard frictional grains amenable to the same treatment as emulsion droplets, on the mesoscale?

Several approaches compete to find answers to these broad questions.

1.2 AN INTRACTABLE SET OF EQUATIONS

A priori, the problem of the flow of an amorphous solid, made of N interacting particles labelled $i \in \{1, \dots, N\}$, requires to solve pN coupled equations of motion, where $p > 1$ is the number of relevant degrees of freedom of each particle. For concreteness, one may consider the simple case in which the motion of each particle, of mass m, is governed by an overdamped Langevin equation,

$$\mathbf{0} = \boldsymbol{F_i}\left(\Gamma_t\right) - m\zeta \dot{\boldsymbol{r}}_{\boldsymbol{i}}(t) + \boldsymbol{f}_{\boldsymbol{i}}^{\mathbf{th}}(t), \tag{1.1}$$

where $\dot{\boldsymbol{r}}_{\boldsymbol{i}}$ is the velocity of particle i, ζ is a friction coefficient, the $\boldsymbol{f}_{\boldsymbol{i}}^{\mathbf{th}}$'s are yet unspecified thermal fluctuations (see Chapter 2), and the $\boldsymbol{F_i}$'s are conservative forces that originate in interparticle interactions. Deformation is imposed, for instance, by controlling the position of a slab of particles in the sample.

Unsurprisingly, the problem, as it stands now, is intractable, even in this highly simplified case.

1.3 DYNAMICAL THEORIES

To circumvent the difficulty, a first approach consists in making use of the traditional tools of statistical physics, namely, ensemble averages and the recourse to mean-field approximations. However, one of the first obstacles is that, as a prerequisite to the study of flow, the theory should describe the emergence of rigidity in the quiescent state; otherwise, no yield stress would be observed. In this respect, one of the most successful approaches rooted in first principles is undoubtedly the mode-coupling theory [Bengtzelius et al., 1984, Reichman and Charbonneau, 2005].

1.3.1 *The mode-coupling approach to rheology*

The microscopic equations of motion can be recast into equations involving the probability distribution function of the system, *i.e.*, the function giving the probability to find the system in a given configuration. In order to capture the slow reponse of the system, the mode-coupling theory, which will be presented in greater detail in Chapter 2, relates the evolution of the system to that of a carefully chosen set of slow variables. At the end of the day, the theory predicts that the dynamics of the quiescent system freeze below some critical temperature and the system becomes non-ergodic. The only nontrivial input parameter in the final equation is the equilibrium structure factor of the material.

Flow is brought into the picture by writing the microscopic equations, not in the lab frame, but rather in a frame that moves at a prescribed, space-dependent velocity [Fuchs and Cates, 2002], which can be thought of as the solvent velocity, in the case of a colloidal suspension. It is then shown that flow restores ergodicity and the study culminates in the derivation of a constitutive equation for the stress, based on a generalised Green-Kubo relation. This equation, or schematic variants thereof, gives (almost) quantitative agreement with experimental measurements on concentrated colloidal suspensions close to the glass transition [Siebenbürger et al., 2012, Amann et al., 2013, Fritschi et al., 2014] (also see Ref. [Fritschi et al., 2014] for a comparison with atomistic simulations).

On the downside, the technical calculations involve some uncontrolled approximations, all potential flow heterogeneities have been left behind, and the solvent velocity is an input parameter of the theory, instead of being self-consistently adjusted.

1.4 A POTENTIAL ENERGY LANDSCAPE (PEL) APPROACH TO QUIESCENT SYSTEMS

1.4.1 *The Potential Energy Landscape perspective*

Owing to the technical difficulty associated with the mode-coupling calculations, one may wish to turn to a simplified approach, offering a more intuitive understanding. To this end, let us temporarily forget about the kinetic details in the microscopic equations and focus only on the potential energy landscape (PEL) $V(\Gamma)$ in which the system evolves. Here, $\Gamma \equiv (\boldsymbol{r_1}, \ldots, \boldsymbol{r_N}) \in \mathcal{U}^N$ denotes a possible configuration of the system, $\mathcal{U}$ is the (potentially periodic) space in which the particles move[2], *e.g.*, $\mathcal{U} = \mathbb{R}^d$, for some spatial dimension d, and V is the global potential energy of the system. By definition, the interparticle force exerted on particle i in configuration Γ reads $\boldsymbol{F_i}(\Gamma) = -\frac{\partial V}{\partial \boldsymbol{r}_i}\Big|_{\Gamma}$.

The PEL is therefore oblivious to inertial effects and dissipative forces. This selective perception is prompted by the idea that the dynamics of the dense system, whether at rest or in flow, are dominated by excluded volume effects and, when applicable, short-range attractions, both of which are exclusively contained in $\boldsymbol{F_i}(\Gamma)$.

In the overdamped regime, the evolution of the system is entirely described by the trajectory of the state point, $\Gamma_t \equiv \Gamma(t)$, in phase space, where $t \in \mathbb{R}^+$ denotes the time coordinate. But, then, where do the discrepancies between the glassy state and the liquid state emerge in this perspective? The question is all the more pertinent as the PEL is blind to temperature and, given that the structure of a glass does not differ much from that of a liquid, one may think that both explore similar configurations Γ.

2. Formally, the PEL is then a hypersurface of the high-dimensional space $\mathcal{U}^N \times \mathbb{R}$.

Goldstein [1969] addressed this question in an insighful paper published in 1969. In the liquid state, at high temperatures, the thermal energy is of the order of, or larger than, the typical energy barriers encountered in the PEL, so that the system virtually "hovers" over the PEL without being significantly delayed by any barrier. When the temperature declines and the liquid draws closer the glass transition [3], the presence of energy barriers large compared to the thermal energy starts to dominate the dynamics. Most of the time, the system is then trapped near a local energy minimum, in the vicinity of which it vibrates (if inertia is present), until it finally jumps into another valley, and so on. The trapping of the system in a potential valley reflects the increasing difficulty for particles to escape from the cage formed by their neighbours, in real space.

These seminal ideas have since been refined, notably to take into account the multiple scales of valleys [Stillinger, 1995]: at the smallest scale, valleys are defined as the basins of attraction of a minimum, *i.e.*, the portion of space from which strict downhill motion leads to the considered minimum. Zooming out, larger-scale funnel-shaped valleys ("metabasins") with jagged slopes due to the smaller-scale valleys, become apparent. In other words, valleys of different scales are nested. A faithful representation of this hierarchical structure is presented by Doliwa and Heuer in Ref. [Doliwa and Heuer, 2003] and reproduced here in Fig. 1.2a. These authors conducted a detailed investigation of the PEL of a numerical model for a supercooled liquid comprising 50 particles (for larger systems, the PEL becomes too complex for any useful information to be extracted from it). For further details, the reader is referred to the comprehensive works presented in Refs. [Doliwa and Heuer, 2003, Heuer, 2008] and to the references therein.

1.4.2 *Bouchaud's trap model*

Bouchaud [1992]'s trap model provides a quantitative description of Goldstein's ideas about the glass transition. The author envisioned the evolution of the state point in a Gedanken-PEL composed of basins ("traps") of exponentially distributed depths E. This means that the number of traps of depths E in the PEL is proportional to $\rho(E) \propto \exp(-E/E_g)$, E_g being a material parameter. The thermally activated escape from a trap of depth E takes a time $\tau(E) \sim \omega_0^{-1}\exp(E/k_BT)$, where ω_0 is some attempt frequency and k_BT is the thermal energy. Immediately after its escape, the state point lands in a new trap, whose depth is picked at random from the distribution ρ.

For all its simplicity, this model predicts a glass transition at $k_BT = E_g$. Indeed, for $k_BT > E_g$, the average life time in a trap is finite, because $\int dE\rho(E)\tau(E) < \infty$, and an ergodic steady state is reached. On the contrary, for $k_BT < E_g$, the average life time diverges, *i.e.*, $\int dE\,\rho(E)\tau(E) = \infty$. As time elapses, the system falls into deeper and deeper traps on average: this is the ageing process characteristic of the glassy state.

3. Goldstein assessed that the change of regime should occur when the viscosity gets larger than $1\,\mathrm{Pa}\cdot\mathrm{s}$.

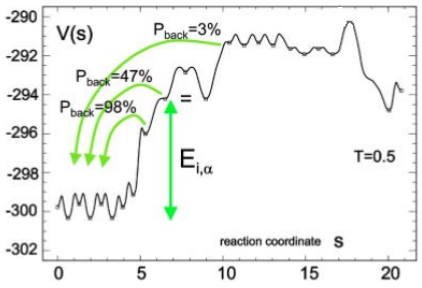

(a) Potential energy along a reaction path. p_{back} denotes the probability to return to the bottom of the initial metabasin, as calculated by Molecular Dynamics. Taken from Ref. [Doliwa and Heuer, 2003].

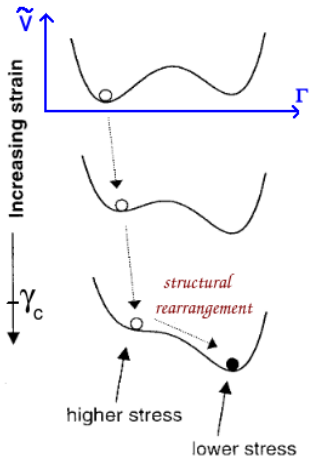

(b) Tilting of the effective PEL by the application of strain and the ensuing destabilisation of the first energy minimum. Adapted from Ref. [Gagnon et al., 2001].

Figure 1.2: The Potential Energy Landscape perspective

1.4.3 *Energy barriers and entropic barriers*

At this stage, I would like to append a word of caution regarding the possible misconceptions about energy barriers due to schematic representations of the PEL.

The trapping of the state point in a PEL valley can naturally occur because the energy barriers in all possible escape directions are *too high*. Alternatively, there may exist *too few* exit paths with low enough barriers. Consequently, "energy" barriers also encompass entropic barriers (where entropy should measure the number of trajectories, here). This remark is particularly relevant in the context of hard spheres, for which

$$V(\Gamma) \quad = \quad \begin{cases} 0 & \text{if no particles overlap,} \\ \infty & \text{otherwise.} \end{cases}$$

In such systems, the dynamics get frozen when the volume fraction ϕ is increased above a critical volume fraction $\phi_c \approx 58\%$ in three dimensions. Clearly, the dynamical arrest is not associated with higher energy barriers here, but with fewer available directions of motion of the state point.

1.5 THE PEL APPROACH TO SYSTEMS UNDER SHEAR

1.5.1 *Shear-induced tilting of the PEL*

In general, not all configurations $\Gamma \in \mathcal{U}^N$ are accessible, because boundary conditions (BC) constrain the evolution of the system. External drive usually modifies these BC continuously. In particular, shear is experimentally applied by moving one wall of a shear cell, thereby dragging the particles in contact with it (unless there is wall slip). In this section, we show how this effectively affects the PEL.

To enforce the BC, the equations of motion, for instance, the overdamped Langevin equation (Eq. 1.1) should be supplemented with a prescription of the form

$$\mathcal{P}_t(\Gamma) = 0,$$

for some time-dependent function[4] $\mathcal{P}_t$. This prescription restricts the motion of the state point to the submanifold $\mathcal{P}_t^{-1}(0)$. A convenient way to enforce this restriction is to add a penalty term to the potential $V(\Gamma)$ in the Langevin equation (Eq. 1.1) through a Lagrange multiplier λ, *viz.*,

$$V(\Gamma) \to \tilde{V}_t(\Gamma) \equiv V(\Gamma) + \lambda \mathcal{P}_t(\Gamma).$$

Assuming that $\mathcal{P}_{t=0}(\Gamma) = 0$, λ is chosen so as to fulfil

$$\begin{aligned}
0 &= \frac{D}{Dt}\left[\mathcal{P}_t(\Gamma_t)\right] \\
\textit{viz.},\ 0 &= \partial_t \mathcal{P}_t\Big|_{\Gamma_t} + \sum_{j=1}^{N} \partial_j \mathcal{P}_t \cdot \dot{\boldsymbol{r}}_j \\
0 &= \partial_t \mathcal{P}_t\Big|_{\Gamma_t} + \sum_{j=1}^{N} \partial_j \mathcal{P}_t \cdot \frac{-\partial_j \tilde{V}_t(\Gamma_t) + \boldsymbol{f}_i^{\mathbf{th}}}{m\zeta} \\
\lambda &= \frac{m\zeta \partial_t \mathcal{P}_t + \sum_{j=1}^{N} \partial_j \mathcal{P}_t \cdot \boldsymbol{F}_j^{(\mathrm{tot})}}{\sum_{j=1}^{N} \left(\partial_j \mathcal{P}_t\right)^2},
\end{aligned} \tag{1.2}$$

where $\boldsymbol{F}_j^{(\mathrm{tot})} \equiv -\partial_j V + \boldsymbol{f}_j^{\mathbf{th}}$, and we have used the shorthands: $\partial_j V \equiv \partial V / \partial \boldsymbol{r}_j$ and $\partial_t \mathcal{P}_t \equiv \partial \mathcal{P}_t / \partial t$.

For example, assume that we want to fix the x-coordinate of particle 1, $x_1(t)$, to a time-dependent value $x_1^{(t)}$. The associated prescription function reads $\mathcal{P}_t\left(\Gamma_p\right) = x_1 - x_1^{(t)}$. Then, from Eq. 1.2, the Lagrange multiplier is $\lambda = -m\zeta \dot{x}_1^{(t)} + F_1^{x\,(\mathrm{tot})}$, *i.e.*, the conjugate quantity to x_1. The manipulation thus boils down to applying a fictitious force on particle 1 such that it moves with the prescribed velocity.

4. We have assumed that the constraint acts only on the positional (and not kinetic, *i.e.*, $\dot{\boldsymbol{r}}_1, \ldots, \dot{\boldsymbol{r}}_N$) degrees of freedom. This is clearly the case for a strain-controlled system. But even in a stress-controlled setup, this restriction is reasonable so long as the stress is dominated by the interparticles (e.g., elastic) interactions.

Now, in order to apply a shear strain $\gamma(t)$ to the system, some particles are treated as "wall particles" ($\mathcal{W}$). Their y-coordinates are frozen at $y = \theta L_y$, where

$$\theta = \begin{cases} 0 & \text{if the particle belongs to the bottom wall,} \\ 1 & \text{if the particle belongs to the top wall,} \end{cases}$$

and their x-displacements are set to $x(t) = x^{(0)} + \theta\gamma(t)L_y$. With these constraints, for slow shear ($\|m\zeta\dot{\boldsymbol{r}}_i\| \ll \|\boldsymbol{F}_i\|$), the effective potential reads

$$\begin{aligned} \tilde{V}_t(\Gamma) &\equiv V(\Gamma) + \sum_{i\in\mathcal{W}} \left(y_i - \theta L_y\right) F_i^{y\,(\mathrm{tot})} + \sum_{i\in\mathcal{W}} \left(x_i - x_i^{(0)} - \theta\gamma(t)L_y\right) F_i^{x\,(\mathrm{tot})} \\ &= V(\Gamma) + \sum_{i\in\mathcal{W}} \left(\boldsymbol{r}_i - \boldsymbol{r}_i^{(0)}\right) \cdot \boldsymbol{F}_i^{(\mathrm{tot})} - \mathcal{U}_0\Sigma_{xy}\gamma(t), \end{aligned}$$

where $\mathcal{U}_0$ is the volume of the system and we have introduced the macroscopic shear stress, $\Sigma_{xy} \equiv \mathcal{U}_0^{-1}\sum_{i\in\mathcal{W}} \theta L_y F_i^{x\,(\mathrm{tot})}$. The terms involving, *e.g.*, $F_i^{y\,(\mathrm{tot})}$ impede the dilation of the system in the presence of walls, a tendency known as Reynolds' dilatancy in granular matter; but the most interesting term for the bulk flow is clearly the tilting of the potential with the shear stress, namely, $-\mathcal{U}_0\Sigma_{xy}\gamma(t)$.

1.5.2 *Topological changes in the PEL and structural rearrangements*

Figure 1.2b shows the increasing tilt of the effective PEL $\tilde{V}$ as $\gamma(t)$ increases. As a result of the tilt, the position $\Gamma_{\min}(t)$ of the minimum in $\tilde{V}$ is gradually shifted (Fig. 1.2b, middle). At low temperature, the state point vibrates around that minimum. Therefore, the response to $\gamma(t)$ is elastic: if $\gamma(t)$ is inverted, $\Gamma_{\min}(t)$ reverts to its previous location, and so does the state point.

However, this only holds over a finite strain window: past a critical strain γ_c, a (fold) catastrophe is bound to occur (Fig. 1.2b, bottom): $\Gamma_{\min}(t)$ collides with the inflection point and is abruptly shifted to another location, as the first minimum vanishes. Following this change in the PEL topology, the state point is attracted to a new minimum, associated with a lower stress, and a structural rearrangement occurs. This corresponds to an irreversible, plastic deformation. Note that, in the presence of thermal fluctuations, the system may anticipate the topological change by hopping to the more favourable minimum as soon as the effective barrier (saddle point) is low enough.

1.6 FROM THE GLOBAL PEL TO MESOSCOPIC PELS

1.6.1 *Collective destabilisation* vs. *avalanche of local rearrangements*

So far we have dealt with the PEL of the global system. However, the PEL of a macroscopic system suffers from the double disadvantage of being uneasy to

characterise through atomistic simulations [Doliwa and Heuer, 2003] and inconvenient to use in spatially resolved models. To counter these problems, could the global system be partitioned into weakly coupled mesoscopic regions? Here, weak coupling means that the dynamics within a mesoscopic region are not sensitive to the detailed changes of positions of particles in other regions, in other words, that the rest of the medium can be idealised from the viewpoint of that region.

In the elastic regime, such idealisation poses no serious problem: Tsamados and Barrat showed that Hooke's law holds for regions as small as 5 particle diameters, in a Lennard-Jones glass [Tsamados et al., 2009]. To a good approximation, the internal dynamics of a mesoscopic region (*e.g.*, in response to shear) can then be described by

(i) its internal potential, and

(ii) the boundary conditions imposed by an *idealised* medium made of a patchwork of Hookean blocks.

On the other hand, close to a critical point in the global PEL, one stands on shaky ground: the upcoming structural rearrangement could potentially originate in a *strictly collective* destabilisation of the whole sample, instead of being initiated by a particularly weak region (and then potentially triggering other rearrangements). This counterargument may in particular apply to packings of repulsive particles close to jamming, which exhibit delocalised soft modes and extended structural rearrangements [Reichhardt and Reichhardt, 2014].

1.6.2 *Elastoplastic models*

In subtle constrast with the idea of a strictly collective destabilisation, elastoplastic models are based on the premise that mesoscopic regions are destabilised individually. Collective effects are then interpreted as avalanches of localised rearrangements, interacting *via* elastic interactions. This assumption is strongly supported by the observation of small cooperatively rearranging regions in materials deep within the solid phase, *i.e.*, far below the glass transition temperature or significantly above the jamming point (see Refs. [Argon and Kuo, 1979, Schall et al., 2007, Amon et al., 2012b, Schuh et al., 2007] and Chapter 5). The existence of *localised* rearrangements can tentatively be interpreted as the consequence of the fact that *most* mesoscopic regions are stable, *i.e.*, not on the brink of failure, deep in the solid phase.

Accordingly, this line of modelling focuses on an assembly of elastic blocks subject to *local* yield criteria. Once the yield criterion is met in a block, a plastic rearrangement is triggered locally and the local elastic stress is redistributed to the other blocks in the system, thus potentially inducing new yield events.

1.7 STRUCTURE OF THE THESIS

The first part of this manuscript is dedicated to the mode-coupling approach to the rheology of supercooled liquids and glassy materials. It is guided by the endeavour to include (stress or density) inhomogeneities in this theory, with the perspective, for instance, to obtain a more direct reflection of the strongly heterogeneous flow observed at low temperatures.

In the following parts, we adopt an approach better suited to the low temperature regime, namely, elastoplastic models. Parts 2 and 3 aim to tighten the connection between the ingredients of these models and the physical processes at play in flowing amorphous solids and, with the help of numerical simulations, to gain a better understanding of phenomena such as shear localisation, spatial correlations in the flow, and collective effects in microchannel flows. Finally, in the last part, we report on the development of a more flexible implementation of elastoplastic models, based on a simplified Finite Element routine, which notably offers a better account of structural disorder and anisotropy.

Part I

DENSITY AND STRESS HETEROGENEITIES IN THE MODE-COUPLING DESCRIPTION OF FLOW

Chapter 1 has provided a glimpse of the phenomenology associated with the glass transition: as the supercooled liquid is cooled down, structural relaxation becomes so sluggish that it starts to occur on (at least) macroscopic time scales, and the material behaves like a solid on any finite timescale.

The liquid-glass transition has been the cradle of many a theory in the past decades, ranging from the Adam-Gibbs scenario [Adam and Gibbs, 1965] to the mode-coupling theory (MCT) of the glass transition [Bengtzelius et al., 1984] and the Random First Order Theory [Kirkpatrick et al., 1989]. More recently, the focus has been shifted, in part, to the response of these materials to external drive, in particular shear stress. This marks the advent of the rheology of disordered solids, the oxymoronically named study of the flow of disordered solids.

In this field, too, different approaches are in competition, ranging from elastoplastic models at low temperatures to the rheological extension of the mode coupling theory, dubbed ITT-MCT, closer to T_g. In spite of intense research efforts, between these lines of thought, a chasm subsists, which mirrors the distinction associated with scale change pointed out by Anderson [1972]:

> *The chemists will tell you that ammonia "is" a triangular pyramid with the nitrogen negatively charged and the hydrogens positively charged, so that it has an electric dipole moment (μ), negative toward the apex of the pyramid. Now this seemed very strange to me, because I was just being taught that nothing has an electric dipole moment. The professor was really proving that no nucleus has a dipole moment, because he was teaching nuclear physics, but as his arguments were based on the symmetry of space and time they should have been correct in general.*
>
> P.W. Anderson, "More is different", *Science*, **177**, 4047, 393-396 (1972)

In the same way as it is of considerable importance to the chemist to know that the ammonia molecule possesses an electric dipole moment at any given time, although over long times quantum tunneling restores isotropy, the physicist will take an interest in the ferromagnetic behaviour of a (finite) block of iron even though, in the long run, thermal fluctuations destroy the spontaneously created asymmetry. The lower the magnitude of thermal fluctations, the more relevant the asymmetric description.

These contentions are echoed in the dilemma between the mean-field-like MCT and elastoplastic models. The ensemble averages performed in the former, along with its approximations, may wash out heterogeneities and mask their importance, say, at low temperature. Just imagine that the most probable configurations in the ensemble all exhibited shear localisation, *i.e.*, a strongly sheared region embedded in a solid medium.[5] After averaging over all configurations, this heterogeneity would be washed out and global translational invariance, restored.

It is therefore of major interest to dig below the homogeneous situation in ITT-MCT and study whether heterogeneities can be brought to light and han-

5. Technically, however, this situation appears unlikely in the present ITT-MCT formalism, notably because of the use of a mean-field solvent drag.

dled within this framework. The following chapters are a very first step in this direction.

In Chapter 2, after a concise presentation of the principle of ITT-MCT, the presence in the equations of terms associated with heterogeneities, such as advection and relaxation, is established by exploring, in particular, the evolution of arbitrary colloidal density fluctuations in an incompressible solvent *flow*. In Chapter 3, we investigate to what extent the constitutive equations derived for a homogeneous flow are altered by the addition of small heterogeneities in the prescribed solvent flow. The last chapter of this part, Chapter 4, presents a study of the occurrence of elastic instabilities in model colloidal suspensions with the help of a schematic equation derived from ITT-MCT, duly complemented with the advection term identified in Chapter 2.

2

FROM MICROSCOPIC EQUATIONS TO A CONSTITUTIVE EQUATION

2.1 MICROSCOPIC EQUATIONS

2.1.1 *The Langevin equation*

One of the major assets of the mode-coupling approach to rheology is that it is rooted in the microscopic equations governing the motion of individual particles.

Of course, given the immense diversity of glass-forming materials (and kins), the specific equations should vary considerably, depending on whether the particles are metal atoms, colloids, liquid droplets in an emulsion, or bubbles. Therefore, to be specific, Fuchs and Cates, the developers of ITT-MCT, explicitly wrote that they focus mainly on dense colloidal suspensions [Fuchs and Cates, 2002].

The adequate starting point is then the microscopic Langevin equation [Langevin, 1908]. Consider an assembly of N colloids, with labels $i \in \{1, \ldots, N\}$, positions $\boldsymbol{r}_i$, and equal masses m. The Langevin equation for colloid i reads

$$m\ddot{\boldsymbol{r}}_i(t) = \boldsymbol{F}_i\left(\Gamma_t\right) - m\zeta\dot{\boldsymbol{r}}_i(t) + \boldsymbol{f}_i^{\mathrm{th}}(t). \tag{2.1}$$

Here, ζ is a friction coefficient and the $\boldsymbol{f}_i^{\mathrm{th}}$'s are random forces due to collisions with small solvent molecules. They can be thought of as thermal fluctuations and are usually assumed Gaussian, *i.e.*, characterised by $\left\langle \boldsymbol{f}_i^{\mathrm{th}}(t)\right\rangle = \boldsymbol{0}$ and $\left\langle \boldsymbol{f}_i^{\mathrm{th}}(t) \otimes \boldsymbol{f}_j^{\mathrm{th}}(t')\right\rangle = 2m\zeta k_B T\delta_{ij}\delta(t-t')\mathbb{I}$, where k_B is the Boltzmann constant and $\mathbb{I}$ is the identity matrix in d dimensions, the latter equality resulting from the equipartition theorem. The drag forces $-m\zeta\boldsymbol{v}_i(t)$ and the thermal fluctuations $\boldsymbol{f}_i^{\mathrm{th}}(t)$ build up the dissipative contribution to Eq. 2.1. The conservative forces $\boldsymbol{F}_i\left(\Gamma_t\right)$ originate in interactions between particles and derive from the global potential energy $V\left(\Gamma_t\right)$ of the system, *viz.*, $\boldsymbol{F}_i\left(\Gamma_t\right) = -\frac{\partial V(\Gamma)}{\partial \boldsymbol{r}_i}\Big|_{\Gamma=\Gamma_t}$, where $\Gamma_t \equiv (\boldsymbol{r}_1(t), \ldots, \boldsymbol{r}_N(t))$ denotes the configuration of the system (in terms of positions) at time t. The inertial term $m\dot{\boldsymbol{v}}_i(t)$ on the left hand side (lhs) of Eq. 2.1 is generally negligible in dense colloidal suspensions, and accordingly neglected. This leads to the *overdamped* Langevin equation,

$$\dot{\boldsymbol{r}}_i(t) = \boldsymbol{F}_i\left(\Gamma_t\right) + \boldsymbol{f}_i^{\mathrm{th}}(t), \tag{2.2}$$

where we have set $m = 1$ and $\zeta = 1$, for the rest of the discussion.

2.1.2 *Some remarks on the neglect of hydrodynamic interactions*

Some remarks pertaining to the assumptions made in Eqs. 2.1 and 2.2 are now in order. First, we note the absence of gravity forces: sedimentation is thereby excluded from this approach. This is no serious issue for the investigation of colloidal dispersions; colloids can anyway be made buoyant by density-matching the solvent. A more serious concern resides in the neglect of the hydrodynamic interactions between particles. In practice, this omission is required to preserve any hope to get a tractable theory, but it is also hoped that they play a "subordinate role" in slowly sheared, dense colloidal suspensions [Fuchs and Cates, 2002]. Indeed, the consensus view is that, qualitatively, excluded volume effects and direct (non-solvent-mediated) interparticle interactions suffice to explain the divergence of the viscosity (η) at the jamming transition in these systems, $\eta \sim (\phi_c - \phi)^{-\alpha}$, where ϕ_c is the volume fraction at the jamming point. Even quantitatively, there may be no need to account for hydrodynamic interactions in order to recover the correct exponents associated with this divergence [Andreotti et al., 2012]. Thence, it may be reasonable to expect that hydrodynamic interactions remain subdominant when the system is slowly sheared. We must however admit that the issue is still debated and gets particularly prickly if the system is more vigorously sheared. For instance, the shear-thickening phenomenon, characterised by a dramatic hike of the viscosity as the shear rate $\dot{\gamma}$ is increased, has recently been associated either to the formation of hydrodynamic clusters and the ensuing large lubrication in interparticle layers [Cheng et al., 2011], or to the upsurge of frictional contacts between particles [Seto et al., 2013, Wyart and Cates, 2014].

Nevertheless, the observation of similar features in systems either with or without solvent and the ability of the present approach to capture them support the assumptions made in Eqs. 2.1 and 2.2. Indeed, besides the natural tests of the ITT-MCT predictions on colloidal suspensions [Siebenbürger et al., 2012], the theory has been shown to reproduce interesting facets of the rheology of supercooled melts (the Bauschinger effect) [Frahsa et al., 2013], molecular glasses below T_g (residual stresses after shear cessation) [Ballauff et al., 2013], and bulk metallic glasses (stress overshoot) [Amann et al., 2013]. These successes bolster the idea that colloids can be viewed as model systems for these diverse materials. To draw a historical parallel, we may recollect that, in the late 40s of the past century, Bragg and Nye [1947] had initiated the study of crystalline bubble rafts in order to better understand dislocations and other defects in metallic crystals, the former being considered as upscaled models for the latter.

The basic ingredients of the theory have now been introduced, in the form of the overdamped Langevin equation, Eq. 2.2. Lying ahead of us at present is the formidable challenge of deriving rigorous macroscopic equations on this microscopic basis.

2.2 THE MODE-COUPLING VIEW OF THE GLASS TRANSITION

A comprehensive survey of the mode-coupling theory of the glass transition is obviously out of the scope of this thesis. We just aim to give a bird's eye view of the key steps involved in the reasoning.

2.2.1 *The Smoluchowski operator*

The random forces $\boldsymbol{f}_i^{\mathbf{th}}(t)$ appearing in the overdamped Langevin equation (Eq. 2.2) are inconvenient to handle. But their statistical properties, *e.g.*, $\left\langle \boldsymbol{f}_i^{\mathbf{th}}(t) \right\rangle = \mathbf{0}$ and $\left\langle \boldsymbol{f}_i^{\mathbf{th}}(t) \otimes \boldsymbol{f}_j^{\mathbf{th}}(t') \right\rangle = 2m\zeta k_B T \delta_{ij} \delta(t-t') \mathbb{I}$, are advantageously used to derive deterministic equations operating on the probability density $\psi(\Gamma, t)$, where $\psi(\Gamma, t) d\Gamma$ is the probability to find the system $d\Gamma$-close to configuration Γ at time t. The derivation involves for instance a Kramers-Moyal expansion and is well known [Risken, 1989]. It yields the continuity equation,

$$\begin{aligned} \partial_t \psi(\Gamma, t) &= -\sum_{i=1}^{N} \partial_i \cdot \boldsymbol{j}_i, \\ \text{where } \boldsymbol{j}_i &\equiv \left[\underbrace{\boldsymbol{F}_i(\Gamma)}_{\text{drift force}} - \underbrace{D_0 \partial_i}_{\text{"osmotic pressure"}} \right] \psi(\Gamma, t), \end{aligned} \tag{2.3}$$

where $\partial_i \equiv \frac{\partial}{\partial \boldsymbol{r}_i}$ and $D_0 = k_B T / m\zeta$ will be set to unity. Equation 2.3 can be reformulated as a Fokker-Planck equation, or, equivalently, a Smoluchowski equation, *viz.*,

$$\partial_t \psi(\Gamma, t) = \Omega_{\text{eq}}(\Gamma) \psi(\Gamma, t), \tag{2.4}$$

where we have introduced the equilibrium Smoluchowski operator

$$\Omega_{\text{eq}}(\Gamma) \equiv \sum_{i=1}^{N} \partial_i \cdot \left[\partial_i - \boldsymbol{F}_i(\Gamma) \right],$$

with operators acting on everything to their right, including ψ. The differential equation, Eq. 2.4, is formally solved by

$$\psi(\Gamma, t) = e^{\Omega_{\text{eq}}(\Gamma) t} \psi(\Gamma, t = 0).$$

Its stationary solution is the equilibrium probability density function ψ_{eq}, which obeys $\Omega_{\text{eq}}(\Gamma) \psi_{\text{eq}}(\Gamma) = 0$ for all Γ.

Now, consider an observable g, *i.e.*, a generalised function defined over configuration space $\{\Gamma\}$. Its average value $\langle g \rangle_{(t)}$ at time t is, by definition,

$$\langle g \rangle_{(t)} = \int g(\Gamma) \psi(\Gamma, t) \, d\Gamma. \tag{2.5}$$

2.2.2 *A dual approach*

So far, the probability distributions evolve in time, while the observables are fixed. In a *dual* approach, one can choose to evolve the observables while keeping $\psi(\Gamma)$ fixed, $\psi(\Gamma) = \psi_{\text{eq}}(\Gamma)$. This is done by means of a partial integration of Eq. 2.5, *viz.*,

$$\begin{aligned}
\langle g \rangle_{(t)} &= \int g(\Gamma)\psi\left(\Gamma, t\right) d\Gamma \\
&= \int g(\Gamma) \left[e^{\Omega_{\text{eq}}(\Gamma)t} \psi(\Gamma, t=0) \right] d\Gamma \\
&= \int \left[\left(e^{\Omega_{\text{eq}}(\Gamma)t} \right)^{\dagger} g(\Gamma) \right] \psi(\Gamma, t=0) d\Gamma \\
&= \int \left[e^{\Omega^{\dagger}_{\text{eq}}(\Gamma)t} g(\Gamma) \right] \psi(\Gamma, t=0) d\Gamma,
\end{aligned} \tag{2.6}$$

where we have introduced the adjoint Smoluchowski operator

$$\Omega^{\dagger}_{\text{eq}}\left(\Gamma\right) = \sum_{i=1}^{N} \left(\partial_i + \boldsymbol{F_i}\left(\Gamma\right) \right) \cdot \partial_i .$$

It follows that, in the dual approach, $\psi = \text{cst}$ and $g(t) = e^{\Omega^{\dagger}_{\text{eq}}(\Gamma)t} g(0)$. This change is analogous to the switch from the Schrödinger formalism to the Heisenberg formalism in Quantum Mechanics [Brader et al., 2012], or from the Eulerian approach to the Lagrangian approach in, *e.g.*, Fluid Mechanics.

The distinction in mathematical nature between the *mathematical distribution* ("generalised function") g and its test function ψ is obscured by their apparent symmetry in Eq. 2.6. Albeit technical, this remark shall have its importance for the validation of the formal manipulations carried out below. In Appendix 2.8.1, we show that some concerns with regard to these manipulations are alleviated by considering g as a distribution acting on regular enough probability density functions $\psi(\Gamma)$. Furthermore, if g itself has a dependence on space, *i.e.*, $g = g(\boldsymbol{r})$, it should also act on *regular enough* test functions $\phi : \mathcal{U} \longrightarrow \mathbb{R}$ (with, *e.g.*, $\mathcal{U} = \mathbb{R}^3$), more precisely, functions that are the sum of their (multi-dimensional) Taylor series.

2.2.3 *Projections onto slow variables*

Without further manipulation, the reformulation into a Smoluchowski equation sheds no light on the slow dynamics arising at the liquid-glass transition. The basic idea of MCT, fleshed out in the works of Sjögren [1980], Bengtzelius et al. [1984], is "that a fluctuation (or 'excitation') of a given dynamical variable decays predominantly into pairs of hydrodynamic modes associated with conserved single-particle or collective dynamical variables", as Hansen and McDonald [1990] phrased it . Because quickly relaxing properties obviously cannot capture slow relaxations by themselves, intrinsically slow variables are used as a

starting point, the usual suspects being conserved quantities, *ergo*, here, density modes.

Accordingly, the so called Zwanzig Mori projection formalism involves projections onto Fourier modes ρ_q of the density $\rho(\boldsymbol{r}) \equiv \sum_i \delta(\boldsymbol{r} - \boldsymbol{r_i})$. The projector is defined by

$$\mathcal{P} \equiv \sum_q \rho_q \rangle \frac{1}{NS_q} \langle \rho_q^\star, \tag{2.7}$$

where $S_q \equiv \langle \rho_q^\star \rho_q \rangle / N$ is the (equilibrium) static structure factor and angular brackets denote a $\psi_{\rm eq}$-weighted average over configurations Γ. Thus, for a function g, using the full explicit notations,

$$\mathcal{P}g = \sum_q \frac{\int \rho_q^\star(\Gamma) g(\Gamma) \psi_{\rm eq}(\Gamma) d\Gamma}{NS_q} \rho_q.$$

Let us specialise to $g = \rho_q$ and project its time derivative, *viz.*,

$$\begin{aligned} \dot{\rho}_q(t) &= e^{\Omega_{\rm eq}^\dagger(\Gamma)t} \Omega_{\rm eq}^\dagger \rho_q(0) \\ &= e^{\Omega_{\rm eq}^\dagger(\Gamma)t} \mathcal{P}\Omega_{\rm eq}^\dagger \rho_q(0) + e^{\Omega_{\rm eq}^\dagger(\Gamma)t} \left(\mathbb{I} - \mathcal{P}\right) \Omega_{\rm eq}^\dagger \rho_q(0). \end{aligned} \tag{2.8}$$

At time $t = 0$, part of ρ_q evolves along $\mathcal{P}$, yielding the first term on the right-hand side (rhs) of Eq. 2.8, and the remaining part grows orthogonally to it, *i.e.*, along $\mathbb{I} - \mathcal{P}$ (second term). The first part is evolved with the full propagator $e^{\Omega_{eq}^\dagger(\Gamma)t}$. Regarding the second term, as sketched in Fig. 3.1, it has one part, $f(t)$, that keeps growing *orthogonally* to $\mathcal{P}$ throughout its evolution, while the remainder grows along $\mathcal{P}$ at some point and therefore couples back to the evolution of $\rho_q(t)$ *via* the so called memory function $M(\tau) \equiv \mathcal{P}\dot{f}(\tau)$. Collecting these three parts, while leaving aside any attempt for a rigorous derivation (which can be found for instance in Ref. [Binder and Kob, 2011]), and projecting Eq. 2.8 onto $\langle \rho_q^\star$ leads to

$$\langle \rho_q^\star \dot{\rho}_q(t) \rangle = \langle \rho_q^\star \rho_q(t) \rangle \underbrace{\langle \rho_q^\star \dot{\rho}_q(0) \rangle}_{\equiv \Gamma_q} + \int_0^t M_q(\tau) \langle \rho_q^\star \rho_q(t-\tau) \rangle d\tau + \underbrace{\langle \rho_q^\star f(t) \rangle}_{0}. \tag{2.9}$$

Let us introduce the transient density correlator

$$\Phi_q(t) \equiv \frac{\langle \rho_q^\star \rho_q(t) \rangle}{NS_q}$$

and divide Eq. 2.9 by NS_q to obtain

$$\dot{\Phi}_q(t) = \Gamma_q \Phi_q(t) + \int_0^t M_q(\tau) \Phi_q(t-\tau) d\tau.$$

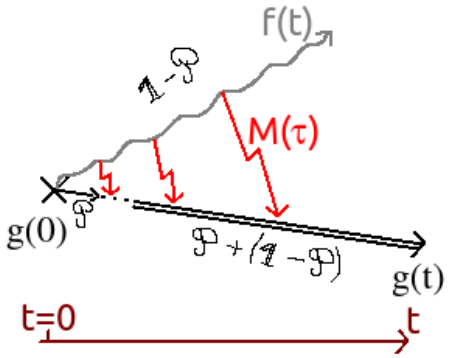

Figure 2.1: Diagrammatic sketch of the Zwanzig-Mori projection formalism (see text).

2.2.4 *The memory kernel*

The memory function $M_q(\tau)$ still needs to be expressed. To this purpose, we have to go through the derivation steps from Eq. 2.8 to Eq. 2.9 again, but using the orthogonal part f instead of ρ_q, *i.e.*, M_q instead of Φ_q, and the projector onto density *pairs* $\rho_q\rho_k$ instead of $\mathcal{P}$ (because f is orthogonal to $\mathcal{P}$ by definition!). Finally, the diffusion kernel $M_q(\tau)$ is transformed into a frictional kernel $m_q(\tau)$ and, at the expense of some uncontrolled approximations, one arrives at the main MCT equations,

$$\dot{\Phi}_q(t) = \Gamma_q\Phi_q(t) + \int_0^t m_q(\tau)\dot{\Phi}_q(t-\tau)d\tau. \tag{2.10}$$

$$m_q(\tau) = \sum_k V_{q,k}\Phi_q(\tau)\Phi_{q-k}(\tau), \tag{2.11}$$

where the vertices $V_{q,k}$ can be expressed as functions of the equilibrium structure factor S_q (see Ref. [Binder and Kob, 2011], for instance). Note that, if inertia were present, Eq. 2.10 would be complemented with a term in $\ddot{\Phi}_q$, but this is mainly a cosmetic change.

2.2.5 *Feedback mechanism and ideal glass transition*

If the convolution $\int_0^t m_q(\tau)\dot{\Phi}_q(t-\tau)d\tau$ were removed from Eq. 2.10, one would only get the fast initial relaxation at rate Γ_q that is expected in a liquid at high temperature. But, not too far from the glass transition temperature, density fluctuations induce perturbations in the orthogonal space that later couple back to the density fluctuations in a feedback mechanism. The memory function m_q involved in this feedback loop, instead of being a function obtained independently with a known decay in time, is here a function of the transient density correlators Φ_k. This fact can lead to the survival of correlations over very long times,

so much so that, below a critical temperature T_c, a bifurcation occurs: a solution exists, in which density fluctuations can never fully relax, *viz.*,

$$\Phi_q(t) \xrightarrow{t\to\infty} f_q \neq 0.$$

Because the relaxation time τ_{rel} tends to infinity at T_c, the viscosity $\eta \sim \tau_{\text{rel}}^{-1}$ also diverges: this is the ideal glass transition predicted by MCT.

In the very well written Ref. [Götze and Voigtmann, 2001], Götze and Voigtmann propose a more visual interpretation of Eqs. 2.10. Any density 'excitation' $\delta\rho_q$ distorts the (interconnected) cages around particles, in real space; this distortion is scattered throughout the medium. In reciprocal space, the fluctuation waves thereby emitted will live in a space essentially orthogonal to the initial density 'excitation'. However, they may be backscattered at some time and come to interact with the initial 'excitation'; this coupling is described by the memory kernel m_q. Finally, because the particles building the cage are subject to the same cageing effects as the 'excited' ones, the memory kernel should be a function of the density correlator $\Phi_q(t)$.

2.3 INCLUSION OF SHEAR

The way shear was included in Section 1.5.1, by moving a slab of particles identified as "wall particles", is quite inconvenient for an analytical theory, insofar as it violates translational invariance and assigns a specific role to some particles. As a more tractable alternative, shear is implemented by prescribing the solvent velocity field, $\boldsymbol{v}^{\text{solv}}(\boldsymbol{r},t)$, in the Langevin equation *a priori*, regardless of the motion of the colloids:

$$\left[\dot{\boldsymbol{r}}_i(t) - \boldsymbol{v}^{\text{solv}}\left(\boldsymbol{r}_i(t),t\right)\right] = \boldsymbol{F}_i(\Gamma_t) + \boldsymbol{f}_i^{\text{th}}(t), \tag{2.12}$$

where the lhs is the solvent drag force. Colloids then perform a random walk in the moving solvent frame. The associated Smoluchowski equation reads

$$\begin{aligned} \partial_t\psi(\Gamma,t) &= \Omega(\Gamma,t)\psi(\Gamma,t), \\ \text{where } \Omega(\Gamma,t) &\equiv \sum_{i=1}^{N}\partial_i\cdot\left[\partial_i - \boldsymbol{F}_i(\Gamma) - \boldsymbol{v}^{\text{solv}}(\boldsymbol{r}_i,t)\right], \end{aligned} \tag{2.13}$$

or, in the dual approach,

$$\begin{aligned} \partial_t g(\Gamma,t) &= \Omega^\dagger(\Gamma,t)g(\Gamma,t), \\ \text{where } \Omega^\dagger(\Gamma,t) &\equiv \sum_{i=1}^{N}\left[\partial_i + \boldsymbol{F}_i(\Gamma) + \boldsymbol{v}^{\text{solv}}(\boldsymbol{r}_i,t)\right]\cdot\partial_i. \end{aligned} \tag{2.14}$$

2.4 SOME REMARKS REGARDING THE FLOW

In this section, I would like to put a personal emphasis on some features that are already apparent in Eq. 2.12 or its probabilistic version, Eq. 2.13.

2.4.1 *Rigidity length*

First, let us compare the relative motion of two particles, i and j, *viz.*,

$$\begin{aligned} \zeta\left[\dot{\boldsymbol{r}}_i(t)-\dot{\boldsymbol{r}}_j(t)\right] &= \zeta\left[\boldsymbol{v}^{\mathrm{solv}}\left(\boldsymbol{r}_i\left(t\right)\right)-\boldsymbol{v}^{\mathrm{solv}}\left(\boldsymbol{r}_j\left(t\right)\right)\right]+\left[\boldsymbol{F}_i\left(\Gamma_t\right)-\boldsymbol{F}_j\left(\Gamma_t\right)\right]+\boldsymbol{f}_i^{\mathrm{th}}(t)-\boldsymbol{f}_j^{\mathrm{th}}(t), \\ \zeta\left\|\dot{\boldsymbol{r}}_i(t)-\dot{\boldsymbol{r}}_j(t)\right\| &\lesssim \zeta\left\|\boldsymbol{\kappa}\left(\boldsymbol{r}_i\left(t\right)\right)\right\|\left\|\boldsymbol{r}_i\left(t\right)-\boldsymbol{r}_j\left(t\right)\right\|+\left\|\boldsymbol{F}_i\left(\Gamma_t\right)\right\|+\text{a few }\sqrt{k_BT} \end{aligned} \tag{2.15}$$

Here I have temporarily restored the friction parameter ζ, $\boldsymbol{\kappa}\equiv\nabla\boldsymbol{v}^{solv}$ is the velocity gradient, and I have assumed that the forces exerted on particles decorrelate fast in space on the length scales that will be considered, so that $\left\|\boldsymbol{F}_i-\boldsymbol{F}_j\right\|\sim\left\|\boldsymbol{F}_i\right\|$. Thanks to Eq. 2.15, a rigidity length scale $\xi\equiv\left\|\boldsymbol{F}_i\right\|/\zeta\left\|\boldsymbol{\kappa}\right\|$ comes to light, at low enough temperature:

- on distances $\left\|\boldsymbol{r}_i-\boldsymbol{r}_j\right\|$ larger than ξ, the rhs of Eq. 2.15 is dominated by the first term, that is to say, the shear forces applied by the solvent control the relative motion of the particles. Considered on these large length scales, the material is thus fluid,

- on the contrary, the relative motion of particles within a region of size smaller than ξ is dominated by interparticle forces: the region behaves like a solid.

We should however insist that the force scale $\left\|\boldsymbol{F}_i\right\|$ entering the definition of ξ need be assessed in the flowing system, and not in the quiescent one, which somewhat hampers the practical use one can draw from this analysis.

2.4.2 *Condition for flow homogeneity*

In Eq. 2.13, the solvent velocity $\boldsymbol{v}^{\mathrm{solv}}(\boldsymbol{r})$ formally plays exactly the same role as an external force. Intuitively, one may expect the creation of spatial heterogeneities (*e.g.*, in the density or the stress) in a non-uniform force field. On the other hand, still according to the intuition, the distribution function should remain homogeneous in a non-uniform velocity field, provided that the *velocity gradient* is uniform. Hence the question: Under what conditions can the steady-state colloidal flow remain homogeneous when the velocity (or force) field is not uniform? The answer, given in the following theorem, is that detailed balance must be violated, which is indeed the case in a shear flow.

> THEOREM - Only if specific detailed balance is broken in the steady state can the stationary probability function ψ_{stat} be *more* symmetric than the prescribed velocity (or force) field $\boldsymbol{v}^{\mathrm{solv}}\left(r\right)$ (with respect to isometric transformations).

Proof
Detailed balance means that

$$\forall i,\ \boldsymbol{j_i} \equiv \partial_i \psi_{\text{stat}}(\Gamma) + \psi_{\text{stat}}(\Gamma)\partial_i V(\Gamma) - \boldsymbol{v}^{\text{solv}}(\boldsymbol{r_i})\psi(\Gamma) = 0.$$

Let $\mathcal{A}$ be an isometric transformation; the associated change of coordinates: $\boldsymbol{r} \to \boldsymbol{r'} = \mathcal{A}(\boldsymbol{r})$.

Let us express the density current $\boldsymbol{j_i}$ in the transformed frame:

$$0 = \boldsymbol{j_i'} = \partial_{i'} \psi_{\text{stat}}\left(\Gamma'\right) + \psi_{\text{stat}}\left(\Gamma'\right) \partial_{i'} V\left(\Gamma'\right) - \boldsymbol{v}^{\text{solv}}(\boldsymbol{r_i}')\psi_{\text{stat}}\left(\Gamma'\right). \tag{2.16}$$

Suppose now that ψ_{stat} is invariant under this transformation, i.e., $\psi_{\text{stat}}\left(\Gamma'\right) = \psi_{\text{stat}}\left(\Gamma\right) \forall \Gamma$. It follows that $\partial_{i'} \psi_{\text{stat}}\left(\Gamma'\right) = \frac{\partial \boldsymbol{r}}{\partial \boldsymbol{r'}}\left(\boldsymbol{r_i}\right) \cdot \partial_i \psi_{\text{stat}}\left(\Gamma\right)$.

Moreover, since $\mathcal{A}$ is an isometric transformation, and the potential depends only on the relative distances between particles,

$$\partial_{i'} V\left(\Gamma'\right) \quad = \quad \frac{\partial \boldsymbol{r}}{\partial \boldsymbol{r'}}\left(\boldsymbol{r_i}\right) \cdot \partial_i V\left(\Gamma\right).$$

Equation 2.16 turns into

$$\begin{aligned} \mathbf{0} &= \frac{\partial \boldsymbol{r}}{\partial \boldsymbol{r'}}\left(\boldsymbol{r_i}\right) \cdot \left[\partial_i \psi_{\text{stat}}(\Gamma) + \psi_{\text{stat}}\left(\Gamma\right) \partial_i V\left(\Gamma\right) - \boldsymbol{v}^{\text{solv}}(\boldsymbol{r_i}')\psi_{\text{stat}}\left(\Gamma\right)\right] \\ \mathbf{0} &= \boldsymbol{j_i} + \left[\boldsymbol{v}^{\text{solv}}(\boldsymbol{r_i}') - \boldsymbol{v}^{\text{solv}}(\boldsymbol{r_i})\right] \psi\left(\Gamma\right), \end{aligned}$$

because $\partial \boldsymbol{r} / \partial \boldsymbol{r'}$ is invertible. Therefore, $\boldsymbol{v}^{\text{solv}}(\boldsymbol{r_i}') = \boldsymbol{v}^{\text{solv}}(\boldsymbol{r_i})$, *i.e.*, $\boldsymbol{v}^{\text{solv}}$ is invariant under $\mathcal{A}$. QED.

2.5 A GENERALISED GREEN-KUBO FORMULA

About one decade ago, Fuchs and Cates [2002, 2003, 2009], then joined by Brader et al. [2009, 2012], and independently Miyazaki et al. [2004], were able to extend the mode-coupling theory of the glass transition to flow situations, through the so called Integrated-Through-Transient Mode-Coupling Theory (ITT-MCT). Expressions were obtained for a time-dependent, tensorial, but *necessarily homogeneous*, velocity gradient tensor $\boldsymbol{\kappa}$ in two dimensions (2D) [Brader et al., 2012], *i.e.*, $\boldsymbol{v}^{\text{solv}}\left(\boldsymbol{r}, t\right) = \boldsymbol{\kappa}(t) \cdot \boldsymbol{r}$. An extension to three dimensions has very recently been proposed by Amann and Fuchs [2014].

The starting point is the non-stationary Smoluchowski equation, Eq. 2.14, along with its formal solutions,

$$\begin{aligned} \psi(\Gamma, t) &= e_{+}^{\int_0^t \Omega(\Gamma, s) ds} \psi(\Gamma, 0) \text{ in the Schrödinger viewpoint,} \\ g(\Gamma, t) &= e_{-}^{\int_0^t \Omega^{\dagger}(\Gamma, s) ds} g(\Gamma, 0) \text{ in the Heisenberg viewpoint.} \end{aligned}$$

2.5.1 *Time-ordered exponentials*

Because the operators $\Omega(\Gamma, s)$ at distinct times s need not commute, some care has to be taken during the integration, hence the use of time-ordered exponentials [Brader et al., 2012], *viz.*,

$$\begin{aligned} e_{+}^{\int_{t_1}^{t_2} A(s)ds} &\equiv 1 + \int_{t_1}^{t_2} ds_1 A(s_1) + \int_{t_1}^{t_2} ds_1 \int_{t_1}^{s_1} ds_1 A(s_1)A(s_2) + \ldots, \\ \text{hence, } \frac{\partial}{\partial t_2}\left[e_{+}^{\int_{t_1}^{t_2} A(s)ds}\right] &= A(t_2)\left[e_{+}^{\int_{t_1}^{t_2} A(s)ds}\right], \end{aligned}$$

or negatively ordered exponentials, *viz.*,

$$\begin{aligned} e_{-}^{\int_{t_1}^{t_2} A(s)ds} &\equiv 1 + \int_{t_1}^{t_2} ds_1 A(s_1) + \int_{t_1}^{t_2} ds_1 \int_{t_1}^{s_1} ds_1 A(s_2)A(s_1) + \ldots, \\ \text{hence, } \frac{\partial}{\partial t_2}\left[e_{-}^{\int_{t_1}^{t_2} A(s)ds}\right] &= \left[e_{-}^{\int_{t_1}^{t_2} A(s)ds}\right] A(t_2). \end{aligned}$$

2.5.2 *Generalised Green-Kubo formula*

If the system is initially at equilibrium, it is helpful to separate the flow-induced perturbations from the equilibrium parts, *viz.*, in the Schrödinger approach,

$$\psi(\Gamma, t) = \psi_{\text{eq}}(\Gamma) + \delta\psi(\Gamma, t).$$

The incompressibility condition, $\partial_i \boldsymbol{v}^{\text{solv}}(\boldsymbol{r_i}, t) = 0$, and detailed balance at equilibrium, *i.e*, $\boldsymbol{j_i} = \boldsymbol{0}$, *ergo* $\partial_i \psi_{\text{eq}}(\Gamma) = \psi_{\text{eq}}(\Gamma)\boldsymbol{F_i}(\Gamma)$, allow us to compute the flow-induced deviations from ψ_{eq} at time t,

$$\begin{aligned} \Omega(t)\psi_{eq}(\Gamma) &= \Omega_{\text{eq}}(\Gamma)\psi_{\text{eq}}(\Gamma) - \sum_{i=1}^{N} \partial_i \cdot \left[\boldsymbol{v}^{\text{solv}}(\boldsymbol{r_i}, t)\psi_{\text{eq}}(\Gamma)\right] \\ &= -\sum_{i=1}^{N} \boldsymbol{v}^{\text{solv}}(\boldsymbol{r_i}, t) \cdot \partial_i \psi_{\text{eq}}(\Gamma) \\ &= -\sum_{i=1}^{N} \underbrace{\boldsymbol{F_i}(\Gamma) \cdot \boldsymbol{v}^{\text{solv}}(\boldsymbol{r_i}, t)}_{\boldsymbol{\kappa}(t):\boldsymbol{\sigma}(\Gamma)} \psi_{\text{eq}}(\Gamma). \end{aligned}$$

From $\partial_t \psi(\Gamma, t) = \Omega(\Gamma, t)\left[\psi_{\text{eq}}(\Gamma) + \delta\psi(\Gamma, t)\right]$, it follows that

$$\psi(\Gamma, t) = \psi_{\text{eq}}(\Gamma) + \int d\Gamma \int_0^t d\tau e_{+}^{\int_{\tau}^{t} \Omega(\Gamma, s)ds} \boldsymbol{\kappa}(\tau) : \boldsymbol{\sigma}(\Gamma)\psi_{\text{eq}}(\Gamma).$$

Applying this to an arbitrary observable g, *e.g.*, $g = \sigma$, and partially integrating the time ordered exponential yields the generalised Green-Kubo relation à la Heisenberg, that is to say, with ψ_{eq}-weighted ensemble average,

$$\langle g(t) \rangle = \langle g \rangle + \int_0^t d\tau \boldsymbol{\kappa}(\tau) : \left\langle \sigma e_-^{\int_\tau^t \Omega^\dagger(s) ds} g \right\rangle . \tag{2.17}$$

2.5.3 *Translational invariance of the system and advected wave vectors*

The derivation then heavily relies on the demonstration of translation invariance in the system for a uniform velocity gradient $\boldsymbol{\kappa}$, which we bypass here. Note that such invariance does not conflict with the theorem presented in Section 2.4, because detailed balance is violated in shear flow. It directly follows from translational invariance that, for a space-dependent observable g,

$$\left\langle g_{\boldsymbol{q}}(t) \right\rangle = \delta_{\boldsymbol{q},\boldsymbol{0}} \left\langle g(t) \right\rangle ;$$

in simpler words, ensemble averages cannot be biased towards any particular wave vector. The same holds for two-time correlations between observables f and g,

$$\left\langle f_{\boldsymbol{q}}^\star(t_1) g_{\boldsymbol{k}}(t_2) \right\rangle = \left\langle f_{\boldsymbol{q}}^\star(t_1) e_-^{\int_{t_1}^{t_2} \Omega^\dagger(s) ds} g_{\boldsymbol{k}}(t_1) \right\rangle .$$

(Note that $f_{-\boldsymbol{q}} = f_{\boldsymbol{q}}^\star$ because f is real-valued.) Once again, homogeneity (here, at time t_1) requires that the modes $f_{\boldsymbol{q}}(t_1)$ and $e_-^{\int_{t_1}^{t_2} \Omega^\dagger(s) ds} g_{\boldsymbol{k}}(t_1)$ be uncorrelated if they are associated with distinct wave vectors. Therefore, correlations can only exist if the propagator $e_-^{\int_{t_1}^{t_2} \Omega^\dagger(s) ds}$ advects wavevector $\boldsymbol{q}$ (at time t_1) onto $\boldsymbol{k}$ (at time t_2). This advection criterion reads [Brader et al., 2012]

$$\boldsymbol{q} = \boldsymbol{k} \cdot \boldsymbol{E}(t_2, t_1), \tag{2.18}$$

where $\boldsymbol{E}(t_2, t_1) \equiv e_+^{\int_{t_1}^{t_2} \boldsymbol{\kappa}(s) ds} = \partial \boldsymbol{r}(t_2) / \partial \boldsymbol{r}(t_1)$ is the deformation gradient tensor.

In particular, the only non-zero transient density correlator is

$$\Phi_{\boldsymbol{q}}(t_2, t_1) = \frac{\left\langle \rho^\star_{\boldsymbol{q} \cdot \boldsymbol{E}(t_2,t_1)} e_-^{\int_{t_1}^{t_2} \Omega^\dagger(s) ds} \rho_{\boldsymbol{q}} \right\rangle}{N S_{\boldsymbol{q}}}.$$

Because $\boldsymbol{E}(t_2, t_1) \neq \mathbb{I}$ under shear, flow couples distinct Fourier modes. More precisely, shear flow advects slowly relaxing modes (including the mode associated with the wavenumber $\boldsymbol{q}$ where the structure factor peaks) into higher wavenumbers $\|\boldsymbol{q} \cdot \boldsymbol{E}(t_1, t_2)\|$, thereby opening faster channels for thermally-induced structural relaxation [Fuchs and Cates, 2002]:

$$
\begin{array}{rcl}
t_1 & \rightsquigarrow & t_2 \\
\text{Quiescent system: } \boldsymbol{q} & \rightsquigarrow & \boldsymbol{q} \\
\text{Homogeneous flow: } \boldsymbol{q} & \rightsquigarrow & \boldsymbol{q}\cdot\boldsymbol{E}(t_1,t_2)
\end{array}
$$

2.5.4 *Final constitutive equations*

With this in hand, the generalised Green-Kubo relation (Eq. 2.17) is applied to the stress observable. Because the latter does not couple to linear density modes (once again, because of homogeneity), a projector onto density pairs, $\mathcal{P}_2$, is introduced, and, after a significant number of further projection steps and approximations, one arrives at the final ITT-MCT equations for the macroscopic stress $\boldsymbol{\sigma}$ [Brader et al., 2009]:

$$
\begin{aligned}
\boldsymbol{\sigma}(t) &= -\int_0^t dt' \int \frac{d\boldsymbol{k}}{32\pi^3}\left[\frac{\partial}{\partial t'}\left(\boldsymbol{k}\cdot\boldsymbol{B}(t,t')\cdot\boldsymbol{k}\right)\right]\frac{\boldsymbol{k}\boldsymbol{k}}{\|\boldsymbol{k}\|\,\|\boldsymbol{k}\cdot\boldsymbol{E}(t,t')\|}\frac{S'_k S'_{\boldsymbol{k}\cdot\boldsymbol{E}(t,t')}}{S_k^2}\Phi^2_{\boldsymbol{k}\cdot\boldsymbol{E}(t,t')}(t,t') \\
0 &= \dot{\Phi}_{\boldsymbol{q}}(t_2,t_1)+\Gamma_{\boldsymbol{q}}(t_2,t_1)\left[\Phi_{\boldsymbol{q}}(t_2,t_1)+\int_{t_1}^{t_2} d\tau m_{\boldsymbol{q}}(t_2,\tau,t_1)\dot{\Phi}_{\boldsymbol{q}}(\tau,t_1)\right] \qquad (2.19)
\end{aligned}
$$

$$
\begin{aligned}
\text{where } \Gamma_{\boldsymbol{q}}(t_2,t_1) &= \frac{D_0\,\|\boldsymbol{q}\cdot\boldsymbol{E}(t_1,t_2)\|^2}{S_{\boldsymbol{q}\cdot\boldsymbol{E}(t_1,t_2)}} \\
m_{\boldsymbol{q}}(t_2,\tau,t_1) &= \frac{\rho}{16\pi^3}\int d\boldsymbol{k}\frac{S_{\boldsymbol{q}\cdot\boldsymbol{E}(t_1,t_2)}S_{\boldsymbol{k}\cdot\boldsymbol{E}(t_1,\tau)}S_{\boldsymbol{p}\cdot\boldsymbol{E}(t_1,\tau)}}{\|\boldsymbol{q}\cdot\boldsymbol{E}(t_1,\tau)\|^2\,\|\boldsymbol{q}\cdot\boldsymbol{E}(t_1,t_2)\|^2} \\
&\quad\times V_{\boldsymbol{q}\boldsymbol{k}\boldsymbol{p}}(\tau,t_1)V_{\boldsymbol{q}\boldsymbol{k}\boldsymbol{p}}(t_2,t_1)\Phi_{\boldsymbol{k}\cdot\boldsymbol{E}(t_1,\tau)}(t_2,\tau)\Phi_{\boldsymbol{p}\cdot\boldsymbol{E}(t_1,\tau)}(t_2,\tau) \\
\text{with } V_{\boldsymbol{q}\boldsymbol{k}\boldsymbol{p}}(t_2,t_1) &= \boldsymbol{q}\cdot\boldsymbol{E}(t_1,t_2)\cdot\left(\boldsymbol{k}\cdot\boldsymbol{E}(t_1,t_2)c_{\boldsymbol{k}\cdot\boldsymbol{E}(t_1,t_2)}+\boldsymbol{p}\cdot\boldsymbol{E}(t_1,t_2)c_{\boldsymbol{p}\cdot\boldsymbol{E}(t_1,t_2)}\right),
\end{aligned}
$$

where $\boldsymbol{p}\equiv\boldsymbol{q}-\boldsymbol{k}$, ρ is the number density, and $c_k\equiv 1-1/S_k$.

2.5.5 *Schematic models*

A schematic theory is obtained by dropping all wave vector information in these equations while preserving material objectivity [Brader et al., 2009]. It is very interesting to observe that, if the density correlator is crudely assumed to decay exponentially, *viz.*, $\Phi(t_2,t_1)=\exp\left[-\Gamma(t_2-t_1)\right]$, then the schematic version of Eq. 2.19 turns into the well-known Upper Convected Maxwell equation,

$$
\begin{aligned}
\frac{1}{2\Gamma}\overset{\triangledown}{\boldsymbol{\sigma}}+\boldsymbol{\sigma} &= \mathbb{I} \\
\text{where } \overset{\triangledown}{\boldsymbol{\sigma}} &\equiv \dot{\boldsymbol{\sigma}}(t)-\boldsymbol{\kappa}(t)\cdot\boldsymbol{\sigma}(t)-\boldsymbol{\sigma}(t)\cdot\boldsymbol{\kappa}^{\top}(t). \qquad (2.20)
\end{aligned}
$$

2.6 INHOMOGENEOUS CASE: RECOVERY OF THE ADVECTION TERM

In the Maxwell equation (Eq. 2.20) that has just been derived, one may notice that the usual stress advection term $v \cdot \nabla\sigma$ is missing in the upper convected derivative! This is annoying, because the presence of stress advection is very well grounded physically: the local stress is encoded in the local arrangement of particles, and the latter are advected by the flow. However, the lack of this term is not much of a surprise here, because the calculations are premised on a homogeneous flow, so $\nabla\sigma = \mathbf{0}$.

Nevertheless, we would like to know how an advection term can be recovered in the equations, in particular, in the generalised Green-Kubo relation (Eq. 2.17). More generally, our goal is to investigate to what extent heterogeneities can be accommodated within ITT-MCT, with the prospect to turn the global constitutive equation it yields into local equations.

2.6.1 *Entanglement of density advection and creation processes*

First, we should understand that the advection term might be entangled with other terms arising in the presence of heterogeneities. As an example to illustrate this point, consider the density observable ρ. We aim to obtain the (ensemble-average of the) mass conservation equation,

$$\begin{aligned} \partial_t \langle \rho(\boldsymbol{r},t)\rangle + \nabla\cdot[\langle \boldsymbol{j}(\boldsymbol{r},t)\rangle] &= 0, \\ \partial_t \langle \rho(\boldsymbol{r},t)\rangle + \boldsymbol{V}(\boldsymbol{r},t)\cdot\nabla\langle \rho(\boldsymbol{r},t)\rangle &= -\langle \rho(\boldsymbol{r},t)\rangle \nabla\cdot\boldsymbol{V}(\boldsymbol{r},t). \end{aligned} \tag{2.21}$$

Here, while $\boldsymbol{j}(\boldsymbol{r},t) = \sum_i \dot{\boldsymbol{r}}_i \delta(\boldsymbol{r}-\boldsymbol{r}_i)$ is the configuration-dependent momentum flux of the *colloids*, $\boldsymbol{V}(\boldsymbol{r},t) \equiv \langle \boldsymbol{j}(\boldsymbol{r},t)\rangle / \langle \rho(\boldsymbol{r},t)\rangle$ is a density-weighted, "mesoscopic" velocity. The term on the rhs of Eq. 2.21 is a source term creating density inhomogeneities. In Fourier space, Eq. 2.21 reads

$$\partial_t \langle \rho_{\boldsymbol{q}}(t)\rangle + \sum_{\boldsymbol{k}} \boldsymbol{V}_{\boldsymbol{q}-\boldsymbol{k}}(t)\cdot\boldsymbol{k}\langle \rho_{\boldsymbol{k}}(t)\rangle = -\sum_{\boldsymbol{k}} \langle \rho_{\boldsymbol{k}}(t)\rangle (\boldsymbol{q}-\boldsymbol{k})\cdot\boldsymbol{V}_{\boldsymbol{q}-\boldsymbol{k}}(t). \tag{2.22}$$

Suppose that the initial configuration is homogeneous, *i.e.*, $\langle \rho_{\boldsymbol{k}}(t=0)\rangle = \langle \rho_{\boldsymbol{0}}(0)\rangle \delta_{\boldsymbol{k},\boldsymbol{0}}$, and that the velocity field does not change too fast. Then the $\boldsymbol{q}\neq\boldsymbol{0}$-density mode will initially grow as $\langle \rho_{\boldsymbol{q}}(t)\rangle \sim \langle \rho_{\boldsymbol{0}}(0)\rangle \boldsymbol{q}\cdot\boldsymbol{V}_{\boldsymbol{q}}t$, thanks to the source term. Insertion into Eq. 2.22 proves that the advection term will be dominated by the source term as long as

$$\left\| \boldsymbol{V}_{\boldsymbol{0}}\cdot\boldsymbol{q}\left(\langle \rho_{\boldsymbol{0}}(0)\rangle \boldsymbol{q}\cdot\boldsymbol{V}_{\boldsymbol{q}}t\right)\right\| \lesssim \left\|\langle \rho_{\boldsymbol{0}}(0)\rangle \boldsymbol{q}\cdot\boldsymbol{V}_{\boldsymbol{q}}\right\|,$$

that is, for a duration $t \sim \left(\|\boldsymbol{V}_{\boldsymbol{0}}\|\,\|\boldsymbol{q}\|\right)^{-1}$ (which diverges in the hydrodynamic limit $\boldsymbol{q}\to\boldsymbol{0}$).

2.6.2 *Arbitrary initial configuration*

Therefore, in order to concentrate on the recovery of the advection term only, without the complications associated with the creation of inhomogeneities, we consider an initially inhomogeneous situation at $t = 0$, with an initial probability density $\psi_0(\Gamma)$ that differs from $\psi_{\text{eq}}(\Gamma)$. At times $t \geqslant 0$, an arbitrary *incompressible* flow $\boldsymbol{v}^{\text{solv}}(\boldsymbol{r}, t)$ is applied and the adjoint Smoluchowski operator keeps its previous expression (Eq. 2.14):

$$\Omega^\dagger(\Gamma, t \geqslant 0) = \sum_{i=1}^{N} \left[\partial_i + \boldsymbol{F_i}(\Gamma) + \boldsymbol{v}^{\text{solv}}(\boldsymbol{r_i}, t)\right] \cdot \partial_i.$$

The equivalent of the Green-Kubo relation (Eq. 2.17), giving the average value of g at time t and (fixed) position $\boldsymbol{r}_M$, is readily derived:

$$\begin{aligned} \langle g(\boldsymbol{r}_M)\rangle_{(t)} &= \langle g(\boldsymbol{r}_M)\rangle_0 + \int d\Gamma \int_0^t dt_1 \Omega(\Gamma, t_1)\psi_0(\Gamma) e_-^{\int_{t_1}^t \Omega^\dagger(\Gamma,s)ds} g(\Gamma, \boldsymbol{r}_M) \\ &= \langle g(\boldsymbol{r}_M)\rangle_0 + \int_0^t dt_1 \left\langle \Omega^\dagger(t_1) e_-^{\int_{t_1}^t \Omega^\dagger(s)ds} g(\boldsymbol{r}_M) \right\rangle_0, \end{aligned} \tag{2.23}$$

where $\langle\cdot\rangle_0$ denotes a ψ_0-weighted average and $\Omega(\Gamma, t_1)\psi_0(\Gamma)$ is the deviation from $\psi_0(\Gamma)$ created at time t_1 (per unit time).

Let us now consider an *auxiliary* system, with subscripts M, identical to the previous one except that the solvent velocity field at $\boldsymbol{r}_M$ is always zero:

$$\begin{aligned} \boldsymbol{v}_M^{\text{solv}}(\boldsymbol{r}, t) &= \boldsymbol{v}^{\text{solv}}(\boldsymbol{r}, t) - \boldsymbol{v}^{\text{solv}}(\boldsymbol{r}_M, t) \\ \Omega_M^\dagger(\Gamma, t \geqslant 0) &= \sum_{i=1}^{N} \left[\partial_i + \boldsymbol{F_i}(\Gamma) + \boldsymbol{v}_M^{\text{solv}}(\boldsymbol{r_i}, t)\right] \cdot \partial_i \\ &= \Omega^\dagger(\Gamma, t \geqslant 0) - \underbrace{\boldsymbol{v}^{\text{solv}}(\boldsymbol{r}_M, t) \cdot \sum_{i=1}^{N} \partial_i}_{A^\dagger(t)} \end{aligned}$$

The contribution $A^\dagger(t)$ to the operator associated with the advection of the material point at $\boldsymbol{r}_M$ corresponds to a global shift of particle positions along $\boldsymbol{v}^{\text{solv}}(\boldsymbol{r}_M, t)$. Realising that $A^\dagger$ commutes with $\Omega_M^\dagger$, *ergo*, $e_-^{\int_{t_1}^t \Omega^\dagger(\Gamma,s)ds} = e_-^{\int_{t_1}^t \Omega_M^\dagger(\Gamma,s)ds} e_-^{\int_{t_1}^t A^\dagger(\Gamma,s)ds}$, and that $A^\dagger(t) g(\Gamma, \boldsymbol{r}) = -\boldsymbol{v}^{\text{solv}}(\boldsymbol{r}_M, t) \cdot \partial_{\boldsymbol{r}} g(\Gamma, \boldsymbol{r})$, one arrives at:

$$\langle g(\boldsymbol{r}_M)\rangle_{(t)} = e_-^{-\int_{t_1}^t ds\, \boldsymbol{v}^{\text{solv}}(\boldsymbol{r}_M,s)\cdot\partial_{\boldsymbol{r}}} \langle g(\Gamma, \boldsymbol{r})\rangle_{(t)}^M.$$

Deriving this equation with respect to time leads to

$$\partial_t \left[\langle g(\boldsymbol{r}_M)\rangle_{(t)}\right] + \boldsymbol{v}^{\text{solv}}(\boldsymbol{r}_M, t) \cdot \partial_{\boldsymbol{r}} \left[\langle g(\boldsymbol{r}_M)\rangle_{(t)}\right] = e_-^{-\int_{t_1}^t ds\, \boldsymbol{v}^{\text{solv}}(\boldsymbol{r}_M,s)\cdot\partial_{\boldsymbol{r}}} \partial_t \left[\langle g(\boldsymbol{r}_M)\rangle_{(t)}^M\right], \tag{2.24}$$

where $\langle\cdot\rangle^M_{(t)}$ obviously denotes an average in the *auxiliary* system at time t. Details of the derivation are provided in Appendix 2.8.2.

The second term on the lhs of Eq. 2.24 is the desired advection term, while the rhs term is the intrinsic relaxation term that subsists when the material point at $\boldsymbol{r}_M$ is not displaced by the solvent flow. The exponential prefactor simply advects this intrinsic relaxation term to the appropriate position in space.

2.6.3 *Aspects of non-locality in the constitutive equation*

As a short aside, let us note that the foregoing endeavour to recover non-local terms in the constitutive equations actually echoes a much wider debate in Continuum Mechanics. Truesdell and Noll [1965], who pioneered the formalisation of generalised Continuum Mechanics, made a distinction between *simple materials*, in which the response to a deformation is strictly local, that is to say, is unaffected by deformation *gradients*, and higher-order materials, in which transformation gradients up to a given order $n \geqslant 2$ matter.[1] Such a dependence on deformation gradients naturally arises when the material features a *microstructure* which is advected during the transformation. To name but one (famous) example, the local microstructure of Cosserat media is represented by a rigid body rotation (*e.g.*, of a 'reference' microstructure) [Forest, 2006].

The ITT-MCT equations describe materials whose "microstructure" strongly depends on the deformation history, *via* the memory kernel m_q in Eq. 2.19. The recovery of an advection term in the equations (see Eq. 2.24) shows that this strong non-locality in time naturally entails an advection of the "microstructure" with the flow, hence, a non-locality in space. However, it should be clear that the spatial non-locality need not be *restricted* to this term: in the presence of flow heterogeneities (see Chapter 3), other non-local terms may emerge, either also resulting from the dependence on the local-deformation history, or directly caused by spatial interactions between distinct regions of the sample.

2.7 INHOMOGENEITY RELAXATION AND CREATION

(The whole chapter results from collaborative work with Prof. Fuchs *[Nicolas and Fuchs, 2014].)*

Equation 2.24 shows that the physically evident process of advection of heterogeneities is indeed accounted for in the Green-Kubo equations. However, the existence of heterogeneities requires a creation process and entails a specific structural relaxation associated with their presence. So far, both of these processes are, rather unsatisfactorily, hidden in the term $\langle g(\boldsymbol{r}_M)\rangle^M_{(t)}$. Can the projection formalism help us unwrap this term? To address the question, we consider the simplest observable, the density ρ.

1. Bear in mind that the deformation tensor is already the gradient of the transformation, hence, $n = 1$ for simple materials.

2.7.1 *Relaxation process*

Taking the generalised Green-Kubo relation (Eq. 2.23) in Fourier space, *i.e.*,

$$\left\langle \rho_q \right\rangle_{(t)} = \left\langle \rho_q \right\rangle_0 + \int_0^t dt_1 \left\langle \Omega^\dagger(t_1) e_-^{\int_{t_1}^t \Omega^\dagger(s)ds} \rho_q \right\rangle_0 , \tag{2.25}$$

and deriving it with respect to time yields

$$\left\langle \partial_t \rho_q \right\rangle_{(t)} = \left\langle \Omega^\dagger(t)\rho_q \right\rangle_0 + \int_0^t dt_1 \left\langle \Omega^\dagger(t_1) U^\dagger(t,t_1)\, \Omega^\dagger(t)\rho_q \right\rangle_0 , \tag{2.26}$$

where $U^\dagger(t,t_1)$ is a shorthand for $e^{\int_{t'}^t \Omega^\dagger(\Gamma,s)ds}$. Consistently with the mode-coupling spirit, we use the projector $\mathcal{P}$ onto *equilibrium* linear density modes to separate the evolution of the propagator $U^\dagger$ into a part along $\mathcal{P}$ and an orthogonal part along $\mathcal{Q} \equiv \mathbb{I} - \mathcal{P}$, *viz.*,

$$\partial_t U^\dagger(t,t_1) = U^\dagger(t,t_1)\left(\mathcal{P}+\mathcal{Q}\right)\Omega^\dagger(t) . \tag{2.27}$$

Here, because of the possible confusion between ψ_0 and ψ_{eq}, let us clarify the definition of $\mathcal{P}$, for an observable g_q:

$$\mathcal{P} g_q(\Gamma) = \sum_k \frac{\rho_k(\Gamma)}{S_k} \left[\int \rho_k^\star(\Gamma')\, g_q(\Gamma')\, \psi_{\text{eq}}(\Gamma')\, d\Gamma' \right] .$$

Coming back to Eq. 2.27 and formally considering $U^\dagger(t,t_1)\,\mathcal{P}\Omega^\dagger(t)$ as a perturbation to the "irreducible" propagator $U^{\dagger\prime}(t,t_1)$, defined by $\partial_t U^{\dagger\prime}(t,t_1) = U^{\dagger\prime}(t,t_1)\,\mathcal{Q}U^{\dagger\prime}(t)$, one gets

$$U^\dagger(t,t_1) = U^{\dagger\prime}(t,t_1) + \int_{t_1}^t ds U^\dagger(s,t_1)\,\mathcal{P}\Omega^\dagger(s)\,U^{\dagger\prime}(t,s) ,$$

and, upon derivation with respect to t,

$$\begin{aligned} U^\dagger(t,t_1)\,\Omega^\dagger(t) = {} & U^{\dagger\prime}(t,t_1)\,\mathcal{Q}\Omega^\dagger(t) + U^\dagger(t,t_1)\,\mathcal{P}\Omega^\dagger(t) \\ & + \int_{t_1}^t ds U^\dagger(s,t_1)\,\mathcal{P}\Omega^\dagger(s)\,U^{\dagger\prime}(t,s)\,\mathcal{Q}\Omega^\dagger(t). \end{aligned}$$

Inserting this identity into Eq. 2.26 yields the following, rather cumbersome equation,

$$
\begin{aligned}
\left\langle \partial_t \rho_{\boldsymbol{q}} \right\rangle_{(t)} &= \left\langle (\mathcal{P}+\mathcal{Q})\,\Omega^\dagger(t)\rho_{\boldsymbol{q}} \right\rangle_0 \\
&\quad + \int_0^t dt_1 \left\langle (\mathcal{P}+\mathcal{Q})\,\Omega^\dagger(t_1) U^{\dagger\prime}(t,t_1)\,\mathcal{Q}\Omega^\dagger(t)\rho_{\boldsymbol{q}} \right\rangle_0 \\
&\quad + \int_0^t dt_1 \left\langle \Omega^\dagger(t_1) U^\dagger(t,t_1)\,\mathcal{P}\Omega^\dagger(t)\rho_{\boldsymbol{q}} \right\rangle_0 \\
&\quad + \int_0^t dt_1 \left\langle \Omega^\dagger(t_1) \int_{t_1}^t ds U^\dagger(s,t_1)\,\mathcal{P}\Omega^\dagger(s)\,U^{\dagger\prime}(t,s)\,\mathcal{Q}\Omega^\dagger(t)\rho_{\boldsymbol{q}} \right\rangle_0 \\
&= \underbrace{\left\langle \mathcal{Q}\Omega^\dagger(t)\rho_{\boldsymbol{q}} \right\rangle_0 + \int_0^t dt_1 \left\langle \mathcal{Q}\Omega^\dagger(t_1) U^{\dagger\prime}(t,t_1)\,\mathcal{Q}\Omega^\dagger(t)\,\rho_{\boldsymbol{q}} \right\rangle_0}_{(1)} \qquad (2.28) \\
&\quad + \underbrace{\left\langle \mathcal{P}\Omega^\dagger(t)\rho_{\boldsymbol{q}} \right\rangle_0 + \int_0^t dt_1 \left\langle \Omega^\dagger(t_1) U^\dagger(t,t_1)\,\mathcal{P}\Omega^\dagger(t)\,\rho_{\boldsymbol{q}} \right\rangle_0}_{(2)} \\
&\quad + \underbrace{\int_0^t dt_1 \Big\langle \Big[\mathcal{P}\Omega^\dagger(t_1) U^{\dagger\prime}(t,t_1)}_{(3)} \\
&\quad \overbrace{+\Omega^\dagger(t_1) \int_{t_1}^t ds U^\dagger(s,t_1)\,\mathcal{P}\Omega^\dagger(s)\,U^{\dagger\prime}(t,s) \Big]\,\mathcal{Q}\Omega^\dagger(t)\,\rho_{\boldsymbol{q}} \rangle_0}^{} . \qquad (2.29)
\end{aligned}
$$

The term denoted by (1) is fully irreducible, in the sense that it evolves only *orthogonally* to the density modes considered in $\mathcal{P}$.

In Appendix 2.8.3, we show that term (2) can be recast as:

$$
(2) \;=\; \frac{-q^2}{S_{\boldsymbol{q}}} \left\langle \rho_{\boldsymbol{q}} \right\rangle_{(t)} - \sum_{\boldsymbol{k}} v^{\mathrm{solv}}_{\boldsymbol{q}-\boldsymbol{k}}(t) \cdot i\boldsymbol{k} \left\langle \rho_{\boldsymbol{k}} \right\rangle_{(t)} ,
$$

while term (3) takes the following form,

$$
(3) \;=\; -\sum_{\boldsymbol{k}} \int_0^t ds\, M_{\boldsymbol{k}\boldsymbol{q}}(t,s) \left\langle \rho_{\boldsymbol{k}} \right\rangle_{(s)} ,
$$

where the memory kernel $M_{\boldsymbol{k}\boldsymbol{q}}(t,s) \equiv \frac{-1}{NS_k} \left\langle \rho^\star_{\boldsymbol{k}} \Omega^\dagger(s)\, U^{\dagger\prime}(t,s)\, \mathcal{Q}\Omega^\dagger(t)\,\rho_{\boldsymbol{q}} \right\rangle$ is an ensemble average over the *equilibrium* distribution and therefore does not depend on the initial heterogeneity in the system. Incidentally, note that $M_{\boldsymbol{k}\boldsymbol{0}}(t,s) = 0$, because the particle number is conserved.

Collecting these contributions into Eq. 2.28, one arrives at the main result of this section:

$$\left\langle \partial_t \rho_{\boldsymbol{q}} \right\rangle_{(t)} + \sum_{\boldsymbol{k}} \boldsymbol{v}^{\mathrm{solv}}_{\boldsymbol{q}-\boldsymbol{k}}(t) \cdot i\boldsymbol{k} \left\langle \rho_{\boldsymbol{k}} \right\rangle_{(t)} = (1) - \frac{\boldsymbol{q}^2}{S_{\boldsymbol{q}}} \left\langle \rho_{\boldsymbol{q}} \right\rangle_{(t)} - \sum_{\boldsymbol{k}} \int_0^t ds\, M_{\boldsymbol{k}\boldsymbol{q}}(t,s) \left\langle \rho_{\boldsymbol{k}} \right\rangle_{(s)} . \tag{2.30}$$

2.7.2 *Physical interpretation*

Equation 2.30 is exact and describes the evolution of density fluctuations $\left\langle \rho_{\boldsymbol{q}} \right\rangle_{(t)}$ at time t in a sheared system, starting from an arbitrary (potentially *heterogeneous*) situation at $t = 0$. It features recognisable terms that all deserve a comment.

First, the fully **irreducible** term (1) is the only term that can potentially ***create*** density inhomogeneities starting from a homogeneous situation, presumably *via* collective mechanisms. It is worth noting that this "source" term vanishes in the situation considered by Brader et al. [2012], namely, the application of a uniform velocity gradient to an initially homogeneous system. Unfortunately, owing to its irreducible nature, this term has remained intractable to me. However, some mechanisms giving rise to density fluctuations, that should therefore be captured by (1), possibly amongst other processes, will be mentioned in Section 2.7.3.

Secondly, the term $\sum_{\boldsymbol{k}} \boldsymbol{v}^{\mathrm{solv}}_{\boldsymbol{q}-\boldsymbol{k}}(t) \cdot i\boldsymbol{k} \left\langle \rho_{\boldsymbol{k}} \right\rangle_{(t)}$ on the lhs is the reciprocal space version of the **advection term** $\boldsymbol{v}^{\mathrm{solv}}(\boldsymbol{r},t) \cdot \nabla \left\langle \rho(\boldsymbol{r}) \right\rangle_{(t)}$ identified in the previous section, in real space.

Thirdly, $\frac{\boldsymbol{q}^2}{S_{\boldsymbol{q}}} \left\langle \rho_{\boldsymbol{q}} \right\rangle_{(t)}$ represents a **diffusive** process for structural **relaxation** of inhomogeneities. The structure factor $S_{\boldsymbol{q}}$ in the denominator is expected, because the relaxation of a $\boldsymbol{q}$-density fluctuation does not require single-particle diffusion over distances $\|\boldsymbol{q}\|^{-1}$. Instead, a collective homogenisation of the system *via* local sprawl/squeeze is sufficient.

Finally, term (3) describes the **memory effect** through which inhomogeneities $\left\langle \rho_{\boldsymbol{k}} \right\rangle_{(s)}$ existing at times s in the past couple to the present. Crucially, the memory kernel $M_{\boldsymbol{k}\boldsymbol{q}}(t,s)$ is evaluated in the *equilibrium* distribution, *i.e.*, independently of the initial heterogeneities, and its definition bears close resemblance to that of the diffusion kernel for the transient density correlation used by Brader et al. [2012] (Eq. 91 of this reference), when the velocity gradient is uniform. It is therefore tempting to replace it with the final expression derived by these authors in that situation. In any case, we expect this term to be responsible for the long structural relaxation of inhomogeneities in dense systems.

Incidentally, let us note that, although Eq. 2.30 describes density fluctuations, it is not expected to account *per se* for flow-concentration coupling instabilities [Furukawa and Tanaka, 2006, Besseling et al., 2010], whereby a small density decrease increases the local shear, leading to a further decrease in density. Indeed,

here, the velocity field is prescribed, instead of being self-consistently adjusted. To go beyond this prescription, an equation should be added to describe the feedback loop of density fluctuations on the solvent velocity field.

2.7.3 *Creation of density inhomogeneities*

In the previous section, we have highlighted the co-emergence of fluctuation advection and relaxation processes in the equations. However, the term that may potentially account for the creation of such fluctuations by the flow has remained intractable.

The ensuing question is: How can density heterogeneities be created?

Conceptually, the simplest way to create heterogeneities is to apply a space-dependent potential $U(\boldsymbol{r})$ at times $t < 0$. Experimentally, the potential could for instance be generated by optical tweezers or holographic optical set-ups [Hanes et al., 2012]. This potential generates an additional force $-\nabla U$ and therefore induces deviations from the equilibrium distribution at negative times. In particular, one expects a higher concentration of particles near the minima of U. It should be noted that the compressional or dilational part of a *compressible* solvent flow, with $\nabla \cdot \boldsymbol{v}^{\mathrm{solv}} = \mathrm{Tr}\,(\boldsymbol{\kappa}) \neq 0$, can be thought of as deriving from an external potential U such that $-\Delta U(\boldsymbol{r}) = \nabla \cdot \boldsymbol{v}^{\mathrm{solv}}(\boldsymbol{r}) = \mathrm{Tr}\,[\boldsymbol{\kappa}(\boldsymbol{r})]$.

With an incompressible solvent flow, density inhomogeneities are not so readily created. If the flow is homogeneous, *i.e.*, $\boldsymbol{\kappa} = \mathrm{cst}$, Brader et al. [2012] demonstrated that within ITT-MCT the density remains uniform. In the next Chapter, we show that, for an incompressible inhomogeneous flow that only slightly deviates from homogeneity, *viz.*, $\boldsymbol{\kappa}(\boldsymbol{r}) = \boldsymbol{\kappa}^{\mathrm{hom}} + \boldsymbol{\delta\kappa}(\boldsymbol{r})$, the density also remains constant to (the very) leading order, because on average particles simply follow stream lines. Nevertheless, beyond the leading order, a collective phenomenon known as shear-induced migration does exist, whereby particles tend to migrate towards regions of lower shear, for instance, the centre of the channel in a Poiseuille flow. Intuitively, in strongly sheared regions, particles often collide; this enhances the local pressure and drives particles away from the high-shear-rate regions [Nott and Brady, 1994]. However, keeping the example of a channel flow, one may easily see that the migration would not be altered if the pressure gradient were inverted (and, accordingly, $\boldsymbol{\delta\kappa}(\boldsymbol{r}) \to -\boldsymbol{\delta\kappa}(\boldsymbol{r})$). Consequently, the migration current is not linear in $\boldsymbol{\delta\kappa}(\boldsymbol{r})$.

A

2.8 APPENDICES

2.8.1 *Clarification of the mathematical basis of some formal manipulations performed in ITT-MCT*

In deriving the ITT-MCT equations, we encounter equations of the form

$$\partial_t g(r;t) = A^\dagger g(r;t), \tag{2.31}$$

where g is a given observable (for instance, the density), and $A^\dagger = -V\partial_r$. Here, for convenience, the discussion is restricted to a one-dimensional system. Formally, Eq. 2.31 is solved by,

$$\begin{aligned} g(r;t) &= e^{\int A^\dagger ds} g(r;t=0) && (2.32)\\ &= e^{-tV\partial_r} g(r;t=0). && (2.33) \end{aligned}$$

One should be arrested by the fact that the evaluation of this expression (Eq. 2.32) only involves *local* terms, namely, the values of $g(r;t=0)$ and its derivatives at position r. This conspicuously leads to a problem if one takes, for instance $g(r;t=0) = \delta(r-r_0)$. Indeed, the solution of Eq. 2.31 is then $g(r;t) = \delta(r - r_0 - Vt)$ and involves *non-local* terms at $t=0$!

To circumvent the problem, $g(\cdot;t)$ should not be thought of as a normal function [2], but as a *mathematical distribution* (a "generalised function") that is to be evaluated against a test function $\phi(r) \in \mathcal{T}$, where $\mathcal{T}$ is the set of *real analytic functions;*

$$\begin{aligned} g : \mathcal{T} &\to \mathbb{R} \\ \phi &\mapsto \langle g|\phi\rangle = \int g(r)\phi(r)dr \end{aligned}$$

Then, using a test function ϕ, we get the desired result,

$$\begin{aligned} \langle g(r,t)|\phi\rangle &= \left\langle e^{-tV\partial_r} g(t=0)\,|\phi \right\rangle \\ &= \left\langle \delta(r-r_0)\,|e^{Vt\partial_r}\phi \right\rangle \\ &= \sum_{n=0}^{\infty} \frac{(Vt)^n}{n!}\phi^{(n)}(r_0) \\ &= \phi(r_0+Vt). \\ \text{hence, } g(r,t) &= \delta(r-r_0-Vt). \end{aligned}$$

To conclude, it should be noted that the observable g will in practice also depend on the positions of the particles $\Gamma \equiv \{r_1,\ldots,r_N\}$, so that one should

2. For the sake of simplicity, the functions are defined in periodic space $\mathbb{R}/\mathbb{Z}$.

write $g(r, \Gamma; t)$ A problem analogous to that studied above for r arises for Γ. The solution is similar: instead of evaluating g for a specific configuration Γ, one should test g against a probability density function $\psi(\Gamma)$ which is the sum of its (multidimensional) Taylor series. For instance, $\langle g \rangle$ is the value obtained by testing g against ψ_{eq}.

2.8.2 *Recovery of the advection term*

Recall that we have introduced an *auxiliary* system (M) identical to the original one, except that the solvent velocity field at $\boldsymbol{r}_M$ is always zero:

$$\begin{aligned} \boldsymbol{v}_M^{\text{solv}}(\boldsymbol{r}, t) &= \boldsymbol{v}^{\text{solv}}(\boldsymbol{r}, t) - \boldsymbol{v}^{\text{solv}}(\boldsymbol{r}_M, t) \\ \Omega_M^\dagger(\Gamma, t \geqslant 0) &= \sum_{i=1}^{N} \left[\partial_i + \boldsymbol{F_i}(\Gamma) + \boldsymbol{v}_M^{\text{solv}}(\boldsymbol{r_i}, t) \right] \cdot \partial_i \\ &= \Omega^\dagger(\Gamma, t \geqslant 0) - \underbrace{\boldsymbol{v}^{\text{solv}}(\boldsymbol{r}_M, t) \cdot \sum_{i=1}^{N} \partial_i}_{A^\dagger(t)} \end{aligned}$$

The crucial point is to realise that $A^\dagger$ commutes with $\Omega_M^\dagger$. Indeed, because the flow is incompressible, *i.e.*, $\partial_i \boldsymbol{v}_M^{\text{solv}}(\boldsymbol{r_i}, t) = 0$, and forces are invariant under a global shift of particles, *i.e.*, $\sum_j \partial_j \boldsymbol{F_i} = \boldsymbol{0}$, one can easily calculate

$$\begin{aligned} \Omega_M^\dagger(\Gamma, t) A^\dagger(t) g &= \sum_{i=1}^{N} \left[\partial_i + \boldsymbol{F_i}(\Gamma) + \boldsymbol{v}_M^{\text{solv}}(\boldsymbol{r_i}, t) \right] \cdot \partial_i \left[\boldsymbol{v}^{\text{solv}}(\boldsymbol{r}_M, t) \cdot \sum_{j=1}^{N} \partial_j \right] g \\ &= A^\dagger(t) \Omega_M^\dagger(\Gamma, t) g. \end{aligned}$$

In addition, commonly used observables, such as the stress and the density, do not depend intrinsically on space, *i.e.*, $g(\Gamma, \boldsymbol{r}) = g(\boldsymbol{r_1}, \ldots, \boldsymbol{r_N}, \boldsymbol{r}) = \tilde{g}(\boldsymbol{r_1} - \boldsymbol{r}, \ldots, \boldsymbol{r_N} - \boldsymbol{r})$. Consequently,

$$\begin{aligned} \sum_i \partial_i g(\Gamma, \boldsymbol{r}) &= \sum_i \partial_i \tilde{g}(\boldsymbol{r_1} - \boldsymbol{r}, \ldots, \boldsymbol{r_N} - \boldsymbol{r}) \\ &= -\partial_{\boldsymbol{r}} \tilde{g}(\boldsymbol{r_1} - \boldsymbol{r}, \ldots, \boldsymbol{r_N} - \boldsymbol{r}) \\ &= -\partial_{\boldsymbol{r}} g(\Gamma, \boldsymbol{r}), \end{aligned}$$

and $A^\dagger(t) g(\Gamma, \boldsymbol{r}) = -\boldsymbol{v}^{\text{solv}}(\boldsymbol{r}_M, t) \cdot \partial_{\boldsymbol{r}} g(\Gamma, \boldsymbol{r})$.

It follows that

$$\begin{aligned} e_-^{\int_{t_1}^t \Omega^\dagger(\Gamma, s) ds} g(\Gamma, \boldsymbol{r}) &= e_-^{\int_{t_1}^t \left(\Omega_M^\dagger + A^\dagger\right)(\Gamma, s) ds} g(\Gamma, \boldsymbol{r}) \\ &= e_-^{\int_{t_1}^t \Omega_M^\dagger(\Gamma, s) ds} e_-^{\int_{t_1}^t A^\dagger(\Gamma, s) ds} g(\Gamma, \boldsymbol{r}) \\ &= e_-^{\int_{t_1}^t \Omega_M^\dagger(\Gamma, s) ds} e_-^{-\int_{t_1}^t ds\, \boldsymbol{v}^{\text{solv}}(\boldsymbol{r}_M, s) \cdot \partial_{\boldsymbol{r}}} g(\Gamma, \boldsymbol{r}). \end{aligned}$$

One can finally highlight the emergence of the advection term by inserting this equality into a simpler form of Eq. 2.23, namely,

$$\begin{aligned}
\langle g(\boldsymbol{r}_M)\rangle_{(t)} - \langle g(\boldsymbol{r}_M)\rangle_0 &= \int_0^t dt_1 \left\langle \left[\left(\Omega_M^\dagger + A^\dagger\right)(t_1)\right] e_-^{\int_{t_1}^t \left(\Omega_M^\dagger + A^\dagger\right)(s)ds} g(\boldsymbol{r}_M) \right\rangle_0 \\
&= -\left\langle \int_0^t dt_1 \partial_{t_1} \left[e_-^{\int_{t_1}^t \left(\Omega_M^\dagger + A^\dagger\right)(s)ds} g(\boldsymbol{r}_M)\right] \right\rangle_0 \\
&= \left\langle \left(e_-^{\int_0^t \left(\Omega_M^\dagger + A^\dagger\right)(\Gamma,s)ds} - 1 \right) g(\boldsymbol{r}_M) \right\rangle_0 \\
\text{hence, } \langle g(\boldsymbol{r}_M)\rangle_{(t)} &= \left\langle e_-^{\int_0^t \left(\Omega_M^\dagger + A^\dagger\right)(\Gamma,s)ds} g(\boldsymbol{r}_M) \right\rangle_0 \\
&= e_-^{-\int_{t_1}^t ds\, \boldsymbol{v}^{solv}(\boldsymbol{r}_M,s)\cdot\partial_{\boldsymbol{r}}} \left\langle e_-^{\int_{t_1}^t \Omega_M^\dagger(\Gamma,s)ds} g(\Gamma,\boldsymbol{r}) \right\rangle_0 \\
&= e_-^{-\int_{t_1}^t ds\, \boldsymbol{v}^{solv}(\boldsymbol{r}_M,s)\cdot\partial_{\boldsymbol{r}}} \langle g(\Gamma,\boldsymbol{r})\rangle_{(t)}^M ,
\end{aligned} \tag{2.34}$$

where $\langle\cdot\rangle_{(t)}^M$ denotes an average in the fictional auxiliary system at time t. Deriving Eq. 2.34 with respect to time yields our final result,

$$\partial_t \left[\langle g(\boldsymbol{r}_M)\rangle_{(t)}\right] + \boldsymbol{v}^{\text{solv}}(\boldsymbol{r}_M,t)\cdot\partial_{\boldsymbol{r}}\left[\langle g(\boldsymbol{r}_M)\rangle_{(t)}\right] = e_-^{-\int_{t_1}^t ds\, \boldsymbol{v}^{\text{solv}}(\boldsymbol{r}_M,s)\cdot\partial_{\boldsymbol{r}}} \partial_t \left[\langle g(\boldsymbol{r}_M)\rangle_{(t)}^M\right]. \tag{2.35}$$

2.8.3 *Expression of terms in the full equation*

Let us recall Eq. 2.28:

$$\begin{aligned}
\langle \partial_t \rho_q \rangle_{(t)} = &\underbrace{\left\langle \mathcal{Q}\Omega^\dagger(t)\rho_q \right\rangle_0 + \int_0^t dt_1 \left\langle \mathcal{Q}\Omega^\dagger(t_1) U^{\dagger\prime}(t,t_1)\, \mathcal{Q}\Omega^\dagger(t)\, \rho_q \right\rangle_0}_{(1)} \\
&+\underbrace{\left\langle \mathcal{P}\Omega^\dagger(t)\rho_q \right\rangle_0 + \int_0^t dt_1 \left\langle \Omega^\dagger(t_1) U^\dagger(t,t_1)\, \mathcal{P}\Omega^\dagger(t)\, \rho_q \right\rangle_0}_{(2)} \\
&+\underbrace{\int_0^t dt_1 \Big\langle \Big[\mathcal{P}\Omega^\dagger(t_1) U^{\dagger\prime}(t,t_1)}_{(3)} . \\
&\overbrace{+\Omega^\dagger(t_1) \int_{t_1}^t ds U^\dagger(s,t_1)\, \mathcal{P}\Omega^\dagger(s)\, U^{\dagger\prime}(t,s)\Big]\, \mathcal{Q}\Omega^\dagger(t)\, \rho_q \rangle_0}^{} .
\end{aligned}$$

The reader will probably not be much surprised to learn that our goal is to express terms (2) and (3), term (1) being the "irreducible" term.

Let us first consider term (2). Recalling the definition of our projector $\mathcal{P}$,

$$\begin{aligned}\mathcal{P}g_q(\Gamma) &\equiv \sum_k \frac{\rho_k(\Gamma)}{NS_k}\left[\int \rho_k^\star(\Gamma)\, g_q(\Gamma)\, \psi_{eq}(\Gamma)\, d\Gamma\right] \\ &= \sum_k \frac{\rho_k(\Gamma)}{NS_k}\left\langle \rho_k^\star g_q\right\rangle,\end{aligned}$$

we get:

$$\begin{aligned}\left\langle \mathcal{P}\Omega^\dagger(t)\rho_q\right\rangle_0 &= \sum_k \int d\Gamma \rho_k(\Gamma)\psi_0(\Gamma)d\Gamma \frac{\left\langle \rho_k^\star \Omega^\dagger(t)\rho_q\right\rangle}{NS_k} \\ &= \langle\rho_k\rangle_0 \Gamma_{kq}(t),\end{aligned}$$

where we have introduced the shorthand $\Gamma_{kq}(t)$ for $\frac{\left\langle \rho_k^\star \Omega^\dagger(t)\rho_q\right\rangle}{NS_k}$.

The integral part of (2) is

$$\begin{aligned}&\int_0^t dt_1 \left\langle \Omega^\dagger(t_1)U^\dagger(t,t_1)\,\mathcal{P}\Omega^\dagger(t)\,\rho_q\right\rangle_0 \\ =\ &\int_0^t dt_1 \sum_k \left\langle \Omega^\dagger(t_1)U^\dagger(t,t_1)\,\rho_k(t,t_1)\right\rangle_0 \frac{\left\langle \rho_k^\star \Omega^\dagger(t)\,\rho_q\right\rangle}{NS_k} \\ =\ &\sum_k \underbrace{\int_0^t dt_1 \left\langle \Omega^\dagger(t_1)U^\dagger(t,t_1)\,\rho_k(t,t_1)\right\rangle_0}_{\langle\rho_k\rangle_{(t)}-\langle\rho_k\rangle_0} \Gamma_{kq}(t),\end{aligned}$$

where we have used the generalised Green-Kubo relation (Eq. 2.25) to replace the brace.

Adding up these contributions, we obtain:

$$(2) = \sum_k \Gamma_{kq}(t)\langle\rho_k\rangle_{(t)},$$

and we are left with the evaluation of $\Gamma_{kq}(t) = \left\langle \rho_k^\star \Omega^\dagger(t)\rho_q\right\rangle / NS_k$. Noting that

$$\left\langle \rho_k^\star \Omega^\dagger(t)\rho_q\right\rangle = \left\langle \rho_k^\star \Omega_{\text{eq}}^\dagger \rho_q\right\rangle + \left\langle \rho_k^\star \sum_j v^{\text{solv}}(r_j,t)\cdot\partial_j\rho_q\right\rangle,$$

we simplify the first term by means of partial integration

$$\begin{aligned}
\left\langle \rho_{\boldsymbol{k}}^{\star}\Omega_{\mathrm{eq}}^{\dagger}\rho_{\boldsymbol{q}}\right\rangle &= \left\langle \rho_{\boldsymbol{k}}^{\star}\sum_{j}\left(\partial_{j}+\boldsymbol{F}_{j}\right)\cdot\partial_{j}\rho_{\boldsymbol{q}}\right\rangle \\
&= \int d\Gamma\psi_{\mathrm{eq}}(\Gamma)\rho_{\boldsymbol{k}}^{\star}\sum_{j}\left(\partial_{j}+\boldsymbol{F}_{j}\right)\cdot\partial_{j}\rho_{\boldsymbol{q}} \\
&= -\int d\Gamma\sum_{j}\left\{\partial_{j}\left[\psi_{\mathrm{eq}}(\Gamma)\rho_{\boldsymbol{k}}^{\star}\right]-\rho_{\boldsymbol{k}}^{\star}\sum_{j}\boldsymbol{F}_{j}\psi_{\mathrm{eq}}(\Gamma)\right\}\cdot\partial_{j}\rho_{\boldsymbol{q}} \\
&= -\boldsymbol{q}^{2}\left\langle \sum_{j}e^{i(\boldsymbol{k}-\boldsymbol{q})\cdot\boldsymbol{r}_{j}}\right\rangle \\
&= -\boldsymbol{q}^{2}\delta_{\boldsymbol{k}\boldsymbol{q}}N.
\end{aligned}$$

where we have used detailed balance, $\partial_j\psi_{\mathrm{eq}} = \boldsymbol{F}_j\psi_{\mathrm{eq}}$ to get the penult line.

The second term, $\left\langle \rho_{\boldsymbol{k}}^{\star}\sum_j \boldsymbol{v}^{\mathrm{solv}}\left(\boldsymbol{r}_j,t\right)\cdot\partial_j\rho_{\boldsymbol{q}}\right\rangle \equiv F_{\boldsymbol{k}\boldsymbol{q}}$, calls for more subtlety, because the solvent velocity field is not uniform. The "trick" is to backward-Fourier transform $F_{\boldsymbol{k}\boldsymbol{q}}$ *with respect to* $\boldsymbol{q}$ *only, viz.*,

$$\begin{aligned}
F_{\boldsymbol{k}}\left(\boldsymbol{r}_0\right) &= \left\langle \rho_{\boldsymbol{k}}^{\star}\sum_{j}\boldsymbol{v}^{\mathrm{solv}}\left(\boldsymbol{r}_j,t\right)\partial_{j}\rho\left(\boldsymbol{r}_0-\boldsymbol{r}_j\right)\right\rangle, \\
&= -\left\langle \rho_{\boldsymbol{k}}^{\star}\sum_{j}\boldsymbol{v}^{\mathrm{solv}}\left(\boldsymbol{r}_j,t\right)\partial_{\boldsymbol{r}_0}\delta\left(\boldsymbol{r}_0-\boldsymbol{r}_j\right)\right\rangle
\end{aligned}$$

and to notice [3] that this term shall not be altered in any way if the true solvent velocity $\boldsymbol{v}^{\mathrm{solv}}\left(\boldsymbol{r},t\right)$ is substituted by a *uniform* velocity field $\boldsymbol{v}_{\boldsymbol{r}_0}(t) \equiv \boldsymbol{v}^{\mathrm{solv}}\left(\boldsymbol{r}_0,t\right)$, with fixed $\boldsymbol{r}_0$ (independently of the position, *e.g.*, $\boldsymbol{r}_j$, where it is evaluated):

$$F_{\boldsymbol{k}}\left(\boldsymbol{r}_0\right) = -N\left\langle \rho_{\boldsymbol{k}}^{\star}\boldsymbol{v}_{\boldsymbol{r}_0}(t)\partial_{\boldsymbol{r}_0}\delta\left(\boldsymbol{r}_0-\boldsymbol{r}_j\right)\right\rangle.$$

Now, we can transform $F_{\boldsymbol{k}}\left(\boldsymbol{r}_0\right)$ back into reciprocal space (with respect to $\boldsymbol{r}_0$), to obtain:

$$\begin{aligned}
F_{\boldsymbol{k}\boldsymbol{q}} &= -N\sum_{\boldsymbol{p}}\left\langle \rho_{\boldsymbol{k}}^{\star}\boldsymbol{v}_{\boldsymbol{p}}(t)\cdot i\left(\boldsymbol{q}-\boldsymbol{p}\right)e^{-i(\boldsymbol{q}-\boldsymbol{p})\cdot\boldsymbol{r}_j}\right\rangle \\
&= -N\boldsymbol{v}_{\boldsymbol{p}}(t)\cdot i\left(\boldsymbol{q}-\boldsymbol{p}\right)\sum_{\boldsymbol{p}}\left\langle \rho_{\boldsymbol{k}}^{\star}e^{-i(\boldsymbol{q}-\boldsymbol{p})\cdot\boldsymbol{r}_j}\right\rangle \\
&= -iN\boldsymbol{v}_{\boldsymbol{q}-\boldsymbol{k}}^{\mathrm{solv}}\left(t\right)\cdot\boldsymbol{k}S_{\boldsymbol{k}}.
\end{aligned}$$

Finally, let us collect the different contributions to term (2):

$$(2) = \frac{-\boldsymbol{q}^{2}}{S_{\boldsymbol{q}}}\left\langle \rho_{\boldsymbol{q}}\right\rangle_{(t)} - \sum_{\boldsymbol{k}}\boldsymbol{v}_{\boldsymbol{q}-\boldsymbol{k}}^{\mathrm{solv}}\left(t\right)\cdot i\boldsymbol{k}\left\langle \rho_{\boldsymbol{k}}\right\rangle_{(t)}.$$

3. Actually, this point is less trivial than it seems, because we have to bear in mind that we are dealing with mathematical distributions. However, the proof straightforwardly follows from the evaluation of $F_{\boldsymbol{k}}\left(\boldsymbol{r}_0\right)$ against a suitable test function $\phi(\boldsymbol{r}_0)$.

With this in hand, we can move on to term (3),

$$
\begin{aligned}
(3) \quad = \quad & \int_0^t dt_1 \left\langle \mathcal{P}\Omega^\dagger(t_1) U^{\dagger\prime}(t,t_1)\, \mathcal{Q}\Omega^\dagger(t)\, \rho_q \right\rangle_0 \\
& + \int_0^t dt_1 \left\langle \Omega^\dagger(t_1) \int_{t_1}^t ds U^\dagger(s,t_1)\, \mathcal{P}\Omega^\dagger(s)\, U^{\dagger\prime}(t,s)\, \mathcal{Q}\Omega^\dagger(t)\, \rho_q \right\rangle_0 .
\end{aligned}
$$

The first part obeys,

$$
\begin{aligned}
\int_0^t dt_1 \left\langle \mathcal{P}\Omega^\dagger(t_1) U^{\dagger\prime}(t,t_1)\, \mathcal{Q}\Omega^\dagger(t)\, \rho_q \right\rangle_0 \quad = \quad & \int_0^t dt_1 \sum_{\boldsymbol{k}} \left[\int d\Gamma \psi_0(\Gamma) \rho_{\boldsymbol{k}}(\Gamma) \right] \\
& \times \underbrace{\frac{1}{NS_{\boldsymbol{k}}} \left\langle \rho_{\boldsymbol{k}}^\star \Omega^\dagger(t_1) U^{\dagger\prime}(t,t_1)\, \mathcal{Q}\Omega^\dagger(t)\, \rho_q \right\rangle}_{\equiv -M_{\boldsymbol{kq}}(t,t_1)} \\
= \quad & -\int_0^t dt_1 \sum_{\boldsymbol{k}} \langle \rho_{\boldsymbol{k}} \rangle_0 M_{\boldsymbol{kq}}(t,t_1) ,
\end{aligned}
$$

while the second part is

$$
\begin{aligned}
& \int_0^t dt_1 \left\langle \Omega^\dagger(t_1) \int_{t_1}^t ds U^\dagger(s,t_1)\, \mathcal{P}\Omega^\dagger(s)\, U^{\dagger\prime}(t,s)\, \mathcal{Q}\Omega^\dagger(t)\, \rho_q \right\rangle_0 \\
= \quad & \sum_{\boldsymbol{k}} \int_0^t dt_1 \left\langle \Omega^\dagger(t_1) \int_{t_1}^t ds U^\dagger(s,t_1)\, \rho_{\boldsymbol{k}} \right\rangle_0 \frac{1}{NS_{\boldsymbol{k}}} \left\langle \rho_{\boldsymbol{k}}^\star \Omega^\dagger(s)\, U^{\dagger\prime}(t,s)\, \mathcal{Q}\Omega^\dagger(t)\, \rho_q \right\rangle \\
= \quad & -\sum_{\boldsymbol{k}} \int_0^t ds \underbrace{\int_0^s dt_1 \left\langle \Omega^\dagger(t_1) U^\dagger(s,t_1)\, \rho_{\boldsymbol{k}} \right\rangle_0}_{\langle \rho_{\boldsymbol{k}} \rangle_{(s)} - \langle \rho_{\boldsymbol{k}} \rangle_0} M_{\boldsymbol{kq}}(t,s) ,
\end{aligned}
$$

where we have exchanged the time integrals in the last lines and, once more, used the generalised Green-Kubo relation (Eq. 2.25) to replace the brace.

Collecting the contributions to term (3) finally yields

$$
(3) = -\sum_{\boldsymbol{k}} \int_0^t ds\, M_{\boldsymbol{kq}}(t,s) \langle \rho_{\boldsymbol{k}} \rangle_{(s)} ,
$$

where we recall that $M_{\boldsymbol{kq}}(t,t_1) \equiv \frac{-1}{NS_{\boldsymbol{k}}} \left\langle \rho_{\boldsymbol{k}}^\star \Omega^\dagger(t_1) U^{\dagger\prime}(t,t_1)\, \mathcal{Q}\Omega^\dagger(t)\, \rho_q \right\rangle$.

3

A PERTURBATIVE APPROACH TO SLIGHTLY HETEROGENEOUS FLOWS

The previous chapter has shown that specific terms emerge in the generalised Green-Kubo equations that lie at the heart of ITT-MCT in the presence of heterogeneities. These terms notably reflect processes of heterogeneity advection or relaxation. However, the process of *ex nihilo* creation of heterogeneities has remained analyticially out of our reach. Moreover, the memory kernel involved in Eq. 2.30 has so far been approximated only for a strictly homogeneous flow, *i.e.*, with $\boldsymbol{\kappa} = \text{cst}$. On top of that, Eq. 2.30 has been derived for the density observable; its extension to the stress $\boldsymbol{\sigma}$ is somewhat complicated by the fact that not only particles exactly at $\boldsymbol{r}$, but also particles in the vicinity of $\boldsymbol{r}$, matter for the computation of $\boldsymbol{\sigma}(\boldsymbol{r})$, contrary to the density.

To overcome these deficiencies, one can hope to extend the original framework, for $\boldsymbol{\kappa} = \text{cst}$, to heterogeneous solvent flows, encountered, for instance, in typical extensional flows or (non purely azimuthal) Taylor-Couette flows. However, the complexity inherent in this type of approach has been a hard blow to my original ambitions in this regard. Even a perturbative study of heterogeneities has proved technically challenging. Nevertheless, I have deemed that the skeleton of the derivation is still worth some interest, for two reasons:

(i) it sheds vivid light on the techical difficulties associated with the inclusion of any heterogeneity within MCT,

(ii) it clarifies the additional terms that the homogeneous equations must be supplemented with in that case, thereby blazing the trail for *schematic* ITT-MCT equations for heterogeneous flows, for want of exact ones.

3.1 COUPLING TO LINEAR DENSITY MODES

Let us recall the generalised Green-Kubo relation,

$$\langle g(t)\rangle = \langle g\rangle + \int_0^t d\tau \left\langle \boldsymbol{\kappa}(\tau) : \boldsymbol{\sigma} e_-^{\int_\tau^t \Omega^\dagger(s)ds} g \right\rangle .$$

As we have seen in the previous chapter, to simplify this expression, ITT-MCT heavily relies on translational invariance of the probability density ψ, *i.e.*, the equiprobability of configurations Γ and $\Gamma + \boldsymbol{a} \equiv \{\boldsymbol{r_1} + \boldsymbol{a}, \dots, \boldsymbol{r}_N + \boldsymbol{a}\}$ for any vector $\boldsymbol{a}$, and the ensuing absence of linear couplings to density fluctuations [Brader et al., 2012]. Indeed, because the equilibrium distribution is isotropic, all equilibrium ensemble averages of the form $\left\langle \boldsymbol{\kappa}(\tau) : \boldsymbol{\sigma} e_-^{\int_\tau^t \Omega^\dagger(s)ds} g_{\boldsymbol{q}} \right\rangle$, which are related to

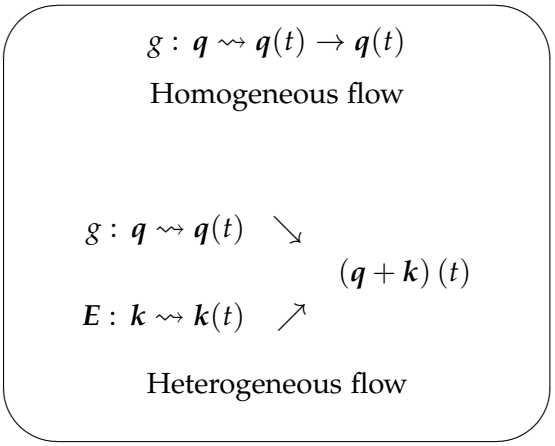

Figure 3.1: Diagrammatic sketch of the interaction between the drive (here, the flow of deformation gradient tensor $\boldsymbol{E}$) and an arbitrary observable (g).

a specific wave vector $\boldsymbol{q} \neq \boldsymbol{0}$, must vanish. Similarly, ensemble averages of the form $\left\langle \boldsymbol{\kappa}(\tau) : \sigma e^{\int_{\tau}^{t} \Omega^{+}(s)ds} g_{\boldsymbol{q}} g_{\boldsymbol{k}} \right\rangle$ are finite only if $\boldsymbol{q} + \boldsymbol{k} = \boldsymbol{0}$.

However, if the flow is no longer homogeneous, the prescribed velocity gradient $\boldsymbol{\kappa}$ will display (finite) $\boldsymbol{q} \neq \boldsymbol{0}$-Fourier modes $\boldsymbol{\kappa}_{\boldsymbol{q}}$. As sketched in Fig. 3.1 and justified in Section 3.3, finite $\boldsymbol{q}$-modes of an observable may then produce $\boldsymbol{0}$-Fourier mode in the equilibrium average *via* an interaction with $\boldsymbol{\kappa}_{-\boldsymbol{q}}$. This leads to the emergence of couplings to linear density modes.

It follows that the complex scaffolding of homogeneous ITT-MCT would need substantial alteration in the presence of solvent flow heterogeneities. Given the intricacy of the task, it is sensible to restrict one's attention to a perturbative approach, *i.e.*, to slight deviations from a homogeneous flow, starting from equilibrium.

3.2 SYMMETRIES OF THE FLOW

To fill the gap left by the absence of translational invariance, we seek other (probably weaker) flow symmetries that may be satisfied in the slightly heterogeneous case. We hypothesise that, in a limit to be specified later, particles are on average advected along the solvent flow field, so that, if two configurations are equiprobable at some time t, their "$\boldsymbol{v}^{\text{solv}}$-advected" images remain equiprobable at a later time.

Translational invariance holds in the initial (equilibrium) state, so, for any real-space vector $\boldsymbol{a}$, initial configurations $\Gamma \equiv \{\boldsymbol{r_1}, \ldots, \boldsymbol{r_N}\}$ and Γ', obeying

$$\forall i,\ \boldsymbol{r}_i'(t=0) = \boldsymbol{r_i}(t=0) + \boldsymbol{a},$$

are equivalent. Our hypothesis then elicits us to define, for any configuration $\Gamma^{(t)} \equiv \left\{\boldsymbol{r_1}^{(t)}, \ldots, \boldsymbol{r_N}^{(t)}\right\}$ at a given time t, the *twin configuration* $\Gamma'(t)$ such that

$$\begin{aligned}\forall i,\, \boldsymbol{r_i'}(\mathrm{t}) &= \phi^{\mathrm{solv}}_{0\to t}\left(\boldsymbol{r_i}+\boldsymbol{a}\right)\\ &\simeq \phi^{\mathrm{solv}}_{0\to t}\left(\boldsymbol{r_i}\right)+\nabla\phi^{\mathrm{solv}}_{0\to t}\cdot\boldsymbol{a},\\ &= \boldsymbol{r_i}^{(t)}+\underbrace{\boldsymbol{E}\left[t,0,\phi^{\mathrm{solv}}_{t\to 0}\left(\boldsymbol{r_i}^{(t)}\right)\right]\cdot\boldsymbol{a}}_{\equiv\boldsymbol{a_i}(\Gamma,t)},\end{aligned}$$

where $\phi^{\mathrm{solv}}_{t_0\to t}(\boldsymbol{r}_0)$ is the "$\boldsymbol{v}^{\mathrm{solv}}$-advected" position at time t of the point that was at $\boldsymbol{r}_0$ at time t_0, $\boldsymbol{r_i}\equiv\phi^{\mathrm{solv}}_{t\to 0}(\boldsymbol{r_i}^{(t)})$, and $\boldsymbol{E}(t,t_0,\boldsymbol{r}_0)\equiv\partial\phi^{\mathrm{solv}}_{t_0\to t}(\boldsymbol{r}_0)/\partial\boldsymbol{r}_0$ is the deformation gradient tensor based on initial positions. Also note that, in order to define the twin configuration, we only have access to the $\boldsymbol{r_i}^{(t)}$'s at a given time t, and not at all times!

It behoves us now to show that twin configurations are indeed equiprobable in some limit, *i.e.*,

$$\psi\left(\Gamma'(t),t\right)=\psi\left(\Gamma,t\right).$$

To this purpose, we introduce the probability spread between twin configurations,

$$\Delta\left(\Gamma,t\right)\equiv\psi\left(\Gamma'(t),t\right)-\psi\left(\Gamma,t\right).$$

Thanks to translational invariance at equilibrium, $\Delta(\Gamma,0)=0$, $\forall\Gamma$. In Appendix 3.6.1, it is shown that, for small $\|\boldsymbol{a}\|$,

$$\begin{aligned}\partial_t\Delta\left(\Gamma,t\right) &= \left[\Omega'+\sum_i\boldsymbol{\kappa_i}\cdot\boldsymbol{E_i}\cdot\boldsymbol{a}\cdot\partial_i\right]\Delta\left(\Gamma,t\right)\\ &\quad+\mathcal{O}\left(\max\|\boldsymbol{a_i}\|^2\left\|\partial_{r_0}\boldsymbol{\kappa}\right\|_\infty+\left\|\partial_{r_0}\boldsymbol{E}\right\|_\infty\|\boldsymbol{a}\|+\sum_i\left\|\boldsymbol{F_i'}+\boldsymbol{F_i}\right\|\right)\end{aligned}\tag{3.1}$$

For a homogeneous flow, only the terms involving Δ survive, so that Δ remains zero at all times: twin configurations are exactly equivalent.

On the other hand, in presence of heterogeneities, corrective terms subsist, and their origin must be identified. The corrective terms involving $\partial_{r_0}\boldsymbol{\kappa}$ and $\partial_{r_0}\boldsymbol{E}$, which scale as the magnitude of the heterogeneous deviations times their inverse wavelength, stem from the linearisations of the solvent velocity field that were performed, notably in the definition of the twin configuration, and this approximation could be refined. But the corrective term (roughly) of order $\sum_i\|\boldsymbol{F_i'}+\boldsymbol{F_i}\|$ is inherent in the mechanics of the system: the inhomogeneous flow distorts the local arrangement of particles differently around $\boldsymbol{r_i}$ and around $\boldsymbol{r_i'}$. To understand this, suppose that the solvent velocity varies fast over a small distance; because of the finite rigidity length evidenced in Section 2.4, regions that move "fast" will tend to push, or drag, their "slow" neighbours. As a consequence of this collective effect, particles will not be advected by the *local* solvent velocity only.

Following Eq. 3.1, for the probability spread between twin configurations to remain negligible, we must (tentatively) consider a stringent limit in which the cumulated heterogeneous part of the deformation is exponentially small in mag-

nitude and/or wave number, in absolute value and with respect to the rigidity length.

3.3 (Absence of) density fluctuations for slight deviations from homogeneity

Suppose that the stringent condition required to keep the spread Δ under control is met, over a given time window, for a slightly heterogeneous (Fourier-transformed [1]) deformation gradient tensor $\boldsymbol{E}_{\boldsymbol{k}}(t,0)$ obeying

$$\begin{cases} \|\boldsymbol{E}_{\boldsymbol{k}}(t,0)\| \ll \|\boldsymbol{E}_{\boldsymbol{0}}(t,0)\| & \text{for } 0 < \|\boldsymbol{k}\| < \epsilon, \\ \boldsymbol{E}_{\boldsymbol{k}}(t,0) = \boldsymbol{0} & \text{for } \|\boldsymbol{k}\| > \epsilon, \end{cases}$$

where $0 < \epsilon \ll 1$. We want to use the resulting symmetry to compute density fluctuations.

For an arbitrary configuration Γ, density modes in the twin configuration $\Gamma'(t)$ obey

$$\begin{aligned}
\rho_{\boldsymbol{q}}\left(\Gamma'(t)\right) &= \sum_{j=1}^{N} e^{-i\boldsymbol{q}\cdot\boldsymbol{r}_j} e^{-i\boldsymbol{q}\cdot\boldsymbol{a}_j}. \\
&= \sum_{j=1}^{N} e^{-i\boldsymbol{q}\cdot\boldsymbol{r}_j} e^{-i\boldsymbol{q}\cdot\int d\boldsymbol{k}\boldsymbol{E}_{\boldsymbol{k}}\cdot\boldsymbol{a}\, e^{i\boldsymbol{k}\cdot\boldsymbol{r}_j}} \\
&= \sum_{j=1}^{N} e^{-i\boldsymbol{q}\cdot\boldsymbol{r}_j} \left[\sum_{n=0}^{\infty} (-i)^n \frac{\left(\int d\boldsymbol{k}\, \boldsymbol{q}\cdot\boldsymbol{E}_{\boldsymbol{k}}\cdot\boldsymbol{a}\, e^{i\boldsymbol{k}\cdot\boldsymbol{r}_j}\right)^n}{n!}\right] \\
&= \sum_{n=0}^{\infty} \frac{(-i)^n}{n!} \left(\int \prod_{p=1}^{n} d\boldsymbol{k}_p \boldsymbol{q}\cdot\boldsymbol{E}_{\boldsymbol{k}_p}\cdot\boldsymbol{a} \sum_{j=1}^{N} e^{i\left(-\boldsymbol{q}+\sum_{p=1}^{n}\boldsymbol{k}_p\right)\cdot\boldsymbol{r}_j}\right) \\
&= \sum_{n=0}^{\infty} \frac{(-i)^n}{n!} \left(\int \prod_{p=1}^{n} d\boldsymbol{k}_p \boldsymbol{q}\cdot\boldsymbol{E}_{\boldsymbol{k}_p}\cdot\boldsymbol{a}\, \rho_{\boldsymbol{q}-\sum_{p=1}^{n}\boldsymbol{k}_p}(\Gamma)\right). \\
&\approx \sum_{n=0}^{\infty} \frac{(-i)^n}{n!} (\boldsymbol{q}\cdot\boldsymbol{E}_{\boldsymbol{0}}\cdot\boldsymbol{a})^{n-1} \left(\boldsymbol{q}\cdot\boldsymbol{E}_{\boldsymbol{0}}\cdot\boldsymbol{a}\rho_{\boldsymbol{q}} + n\boldsymbol{q}\cdot(\boldsymbol{E}\star\rho)(\boldsymbol{q})\cdot\boldsymbol{a}\right), \\
&= e^{-i\boldsymbol{q}\cdot\boldsymbol{E}_{\boldsymbol{0}}\cdot\boldsymbol{a}} \left(\rho_{\boldsymbol{q}} - i\boldsymbol{q}\cdot(\boldsymbol{E}\star\rho)(\boldsymbol{q})\cdot\boldsymbol{a}\right),
\end{aligned}$$

where $(\boldsymbol{E}\star\rho)(\boldsymbol{q})$ denotes the multi-dimensional convolution $\int \boldsymbol{E}(\boldsymbol{q}-\boldsymbol{k})\rho(\boldsymbol{k})d\boldsymbol{k}$. Let us now make use of the equiprobability of twin configurations and integrate over all configurations:

$$\int d\Gamma \rho_{\boldsymbol{q}}\left(\Gamma'(t)\right)\psi\left(\Gamma'(t),t\right) \approx \int d\Gamma e^{-i\boldsymbol{q}\cdot\boldsymbol{E}_{\boldsymbol{0}}\cdot\boldsymbol{a}} \left(\rho_{\boldsymbol{q}} - i\boldsymbol{q}\cdot(\boldsymbol{E}\star\rho)(\boldsymbol{q})\cdot\boldsymbol{a}\right)\psi\left(\Gamma,t\right),$$

1. A priori, $\boldsymbol{E}(t,0,\boldsymbol{r})$ is not Fourier-transformable because it is not integrable. However, this raises no serious issue, because it can be smoothly cut off at large $\|\boldsymbol{r}\|$ without it affecting the local rheology.

where we should note that $\det\left(\frac{d\Gamma'(t)}{d\Gamma}\right) = 1$ because of incompressibility. Finally, we arrive at

$$\left\langle \rho_{\boldsymbol{q}} \right\rangle_{(t)} \approx e^{-i\boldsymbol{q}\cdot\boldsymbol{E}_0\cdot\boldsymbol{a}} \left(\left\langle \rho_{\boldsymbol{q}} \right\rangle_{(t)} - i \int_{\boldsymbol{k}\neq\boldsymbol{0}} d\boldsymbol{k} \left\langle \rho_{\boldsymbol{q}-\boldsymbol{k}} \right\rangle_{(t)} \boldsymbol{q}\cdot\boldsymbol{E}_{\boldsymbol{k}}\cdot\boldsymbol{a} \right). \tag{3.2}$$

For a homogeneous flow, $\forall \boldsymbol{k} \neq \boldsymbol{0}$, $\boldsymbol{E}_{\boldsymbol{k}}(t,0) = \boldsymbol{0}$, so Eq. 3.2 implies that $\left\langle \rho_{\boldsymbol{q}} \right\rangle_{(t)} = 0$ for any finite wave vector, consistently with Ref. [Brader et al., 2012]. In an inhomogeneous flow, Eq. 3.2 contains the first two terms of a diagrammatic expansion of the interaction of a density mode with the solvent flow. Thus, it justifies Fig. 3.2.

However, incompressibility implies that $\boldsymbol{q}\cdot\boldsymbol{E}_{\boldsymbol{k}} = 0$, the time derivative of this quantity being zero. Therefore, in the stringent limit considered here, no density fluctuations are created. At the end of the day, this is not very surprising, because the premise on which twin configurations were devised was that particles should on average follow the (incompressible) solvent streamlines.

Finally, it is worth noting that this derivation has relied on the strict locality of the density observable and is not directly transposable to the stress observable. Indeed, stress fluctuations should be created much more easily than density fluctuations, because the former only require a distortion of the local structure of the material, whereas the latter demand a net flux of particles on a length scale $\|\boldsymbol{q}\|^{-1}$ (for the $\boldsymbol{q}$-mode).

3.4 CORRECTIVE TERMS DUE TO FLOW INHOMOGENEITIES

Can the expression of the homogeneous Green-Kubo relation for the stress be extended to the heterogeneous case? Let us first call back to mind its general expression (Eq. 2.23 of the previous chapter):

$$\left\langle \sigma(\boldsymbol{r}) \right\rangle_{(t)} = \left\langle \sigma(\boldsymbol{r}) \right\rangle + \int_0^t dt_1 \left\langle \Omega^\dagger(t_1) e_-^{\int_{t_1}^t \Omega^\dagger(s)ds} g(\boldsymbol{r}) \right\rangle.$$

Because a heterogeneous flow can induce couplings to linear density modes that do not exist with a uniform velocity gradient, projections onto *linear* density modes should be performed in addition to projections onto density *pairs*. To this end, the projector $\mathcal{P}_{1+2}$ onto the union of linear density modes and density pairs [2] can be introduced, *viz.*,

$$\left\langle \sigma_{\boldsymbol{q}} \right\rangle_{(t)} \approx \left\langle \sigma_{\boldsymbol{q}} \right\rangle + \int_0^t dt_1 \left\langle \Omega^\dagger(t_1) \mathcal{P}_{1+2} e_-^{\int_{t_1}^t \Omega^\dagger(s)ds} \mathcal{P}_{1+2} \sigma_{\boldsymbol{q}} \right\rangle.$$

2. These modes are not orthogonal, but an orthonormal basis can be extracted through, *e.g.*, a Gram-Schmidt procedure.

Formally, the first order expansion of this equation around homogeneous flow will have the following structure,

$$\left\langle \sigma_{\boldsymbol{q}} \right\rangle_{(t)} \approx \int_0^t dt_1 \sum_{\boldsymbol{p}} \left(V^{(1)} + \delta V^{(1)} \right) \left(\Phi_{\boldsymbol{p}} + \delta \Phi_{\boldsymbol{p}} \right) \left(\Phi_{\boldsymbol{q}-\boldsymbol{p}} + \delta \Phi_{\boldsymbol{q}-\boldsymbol{p}} \right) \left(V^{(2)} + \delta V^{(2)} \right).$$

Clearly, the leading order boils down to the homogeneous equation, where the vertices $V^{(1)}$ and/or $V^{(2)}$ vanish if $\boldsymbol{q} \neq \boldsymbol{0}$. Flow heterogeneities impose corrections to the vertices, indicating changes in the magnitude of the coupling, but they also alter the transient density correlator $\Phi_{\boldsymbol{p}}(t, t')$. The reason for this change is that in the time interval $[t', t]$ a small volume of the material will have travelled through regions subject to different shear rates.

3.5 PERSPECTIVES

The corrective terms $\delta V^{(1)}$, $\delta V^{(2)}$, and $\delta \Phi_{\boldsymbol{p}}$ are two-time correlators that could, in principle, be expressed with the same procedure as that employed for density fluctuations in Section 3.3, in the stringent limit exposed above.

Whether such lengthy rigorous calculations are worth the effort is however questionable, given the approximations already performed and the unrealistically stringent limit that one would need to consider. I have personally grown sceptical about the endeavour I had initiated along these lines. On the other hand, the very *existence* of these diverse corrective terms needs to be underscored, in my view, and not only because they are indicative of the technical difficulty of including heterogeneity within ITT-MCT: since these corrections pertain to the first order, they should be taken into account (*e.g.*, through the inclusion of *ad hoc* terms) in schematic constitutive equations, on top of the (also first-order) stress advection process, when heterogeneities play a role.

This remains a challenge, however. Consequently, of the corrective terms associated with flow heterogeneity, the schematic model studied in the next chapter only features stress advection.

A

3.6 APPENDIX

3.6.1 *Probability spread*

At $t = 0$, globally translated configurations are equivalent, so the spread $\Delta(\Gamma, 0) \equiv \psi(\Gamma'(0), 0) - \psi(\Gamma, 0)$ is zero for any Γ.

The variation of the spread with time is assessed with its time derivative, *viz.*, for small $\boldsymbol{a_i}$'s:

$$\begin{aligned}
\partial_t \Delta(\Gamma, t) &= \frac{\partial \boldsymbol{a_i}}{\partial t} \cdot \partial_i \psi' + \partial_t \psi' - \partial_t \psi \\
&= \frac{\partial \boldsymbol{a_i}}{\partial t} \cdot \partial_i \psi' + \Omega' \psi' - \Omega \psi \\
&= \frac{\partial \boldsymbol{a_i}}{\partial t} \cdot \partial_i \psi' + (\Omega' - \Omega)\psi + \Omega' \Delta(\Gamma, t), \qquad (3.3)
\end{aligned}$$

where $\partial_i \psi \equiv \partial \psi / \partial \boldsymbol{r_i}$, we have used the shorthands $\psi' \equiv \psi(\Gamma'(t), t)$, $\psi \equiv \psi(\Gamma, t)$ (and similarly for Ω), and Einstein summation convention have been used.

Let us evaluate the terms appearing in Eq. 3.3 one by one:

$$\begin{aligned}
\frac{\partial \boldsymbol{a_i}}{\partial t} &= \left\{ \partial_t \boldsymbol{E_i} + \partial_{r_0} \boldsymbol{E_i} \cdot \partial_t \left[\phi^{\text{solv}}_{t \to 0}(\boldsymbol{r_i}) \right] \right\} \cdot \boldsymbol{a} \\
&= \left\{ \boldsymbol{\kappa_i} \cdot \boldsymbol{E_i} - \partial_{r_0} \boldsymbol{E_i} \cdot \boldsymbol{E}(0, t, \boldsymbol{r_i}) \cdot \boldsymbol{v}^{\text{solv}}(\boldsymbol{r_i}, t) \right\} \cdot \boldsymbol{a}. \qquad (3.4)
\end{aligned}$$

Here, we have used the shorthands $\boldsymbol{E_i} \equiv \boldsymbol{E}\left[t, 0, \phi^{\text{solv}}_{t \to 0}(\boldsymbol{r_i})\right]$ and $\boldsymbol{\kappa_i} \equiv \boldsymbol{\kappa}\left[t, 0, \phi^{\text{solv}}_{t \to 0}(\boldsymbol{r_i})\right]$, as well as the equalities: $\partial_t \boldsymbol{E} = \boldsymbol{\kappa} \cdot \boldsymbol{E}$ and:

$$\begin{aligned}
\partial_t \left[\phi^{\text{solv}}_{t \to 0}(\boldsymbol{r_i}) \right] &= \lim_{dt \to 0} \frac{\phi^{\text{solv}}_{t+dt \to 0}(\boldsymbol{r_i}) - \phi^{\text{solv}}_{t \to 0}(\boldsymbol{r_i})}{dt} \\
&= \lim \frac{\phi^{\text{solv}}_{t \to 0}\left[\phi^{\text{solv}}_{t+dt \to t}(\boldsymbol{r_i})\right] - \phi^{\text{solv}}_{t \to 0}(r)}{dt} \\
&= \partial_r \phi^{\text{solv}}_{t \to 0} \cdot \left[\boldsymbol{v}^{\text{solv}}(\boldsymbol{r_i}, t) \right] \\
&= -\boldsymbol{E}(0, t, \boldsymbol{r_i}) \cdot \boldsymbol{v}^{\text{solv}}(\boldsymbol{r_i}, t).
\end{aligned}$$

Regarding the second term, if one recalls the incompressibility criterion, *i.e.*, $\partial_r \boldsymbol{v}^{\text{solv}} = 0$, one gets

$$\begin{aligned}
(\Omega' - \Omega)\psi &= \sum_i \partial_i \cdot \left\{ \left[-\boldsymbol{F_i'} + \boldsymbol{F_i} - \boldsymbol{v}^{\text{solv}}(\boldsymbol{r_i'}(t), t) + \boldsymbol{v}^{\text{solv}}(\boldsymbol{r_i}, t) \right] \psi \right\} \\
&= \sum_i \partial_i \cdot \left[\left(-\boldsymbol{F_i'} + \boldsymbol{F_i} \right) \psi \right] - \boldsymbol{\kappa}(\boldsymbol{r_i}, t) \cdot \boldsymbol{a_i} \cdot \partial_i \psi \\
&\quad + \mathcal{O}\left(\max \|\boldsymbol{a_i}\|^2 \, \|\partial_{r_0} \boldsymbol{\kappa}\|_\infty \right)
\end{aligned}$$

We can now sum up the different contributions to $\partial_t \Delta$ in Eq. 3.3, and notice that the terms in $\boldsymbol{\kappa}(\boldsymbol{r_i}, t) \cdot \boldsymbol{a_i} \cdot \partial_i \psi$ cancel out:

$$
\begin{aligned}
\partial_t \Delta(\Gamma, t) &= \Omega' \Delta(\Gamma, t) + \sum_i \boldsymbol{\kappa_i} \cdot \boldsymbol{E_i} \cdot \boldsymbol{a} \cdot \partial_i \Delta(\Gamma, t) \\
&\quad - \sum_i \left[\partial_{r_0} \boldsymbol{E} \cdot \boldsymbol{E}(0, t, \boldsymbol{r_i}) \cdot \boldsymbol{v}^{\text{solv}}(\boldsymbol{r_i}, t) \right] \cdot \boldsymbol{a} \cdot \partial_i \psi' \\
&\quad + \sum_i \partial_i \cdot \left[\left(-\boldsymbol{F_i'} + \boldsymbol{F_i} \right) \psi \right] \\
&\quad + \mathcal{O}\left(\max \|\boldsymbol{a_i}\|^2 \left\| \partial_{r_0} \boldsymbol{\kappa} \right\|_\infty \right) \\
&= \left[\Omega' + \sum_i \boldsymbol{\kappa_i} \cdot \boldsymbol{E_i} \cdot \boldsymbol{a} \cdot \partial_i \right] \Delta(\Gamma, t) \\
&\quad + \mathcal{O}\left(\max \|\boldsymbol{a_i}\|^2 \left\| \partial_{r_0} \boldsymbol{\kappa} \right\|_\infty + \left\| \partial_{r_0} \boldsymbol{E} \right\|_\infty \|\boldsymbol{a}\| + \sum_i \left\| \boldsymbol{F_i'} + \boldsymbol{F_i} \right\| \right).
\end{aligned}
$$

4

ELASTIC INSTABILITY IN A SCHEMATIC MODEL

The ITT-MCT approach exposed in the previous chapters is based on a prescribed solvent velocity field. However, it often happens that, because of an instability, the observed flow field strongly departs from the expectations, and this can cause serious concerns in the industrial context.

The issue is well examplified by the problem of polymer extrusion that polymer processing factories more or less routinely face. Often, a polymer has to be extruded, *i.e.*, pushed out of a barrel through a tube or pipe of narrow diameter (the "die") [Aarts, 1997]. No matter how smooth this tube is, the extrudate will display surface irregularities that can culminate in large distortions (known as melt fracture) from the expected cylindrical shape, unless the material is extruded very slowly. This flow instability is not inertial in nature, because the Reynolds number is usually close to zero in these problems; it is an *elastic instability* [Muller et al., 1989]. Curvature plays a major role in this type of instabilities, which have been reported for polymer melts, worm-like micellar solutions [Fardin et al., 2012a] in Taylor-Couette shear cells, *i.e.*, in the gap between two concentric rotating cylinders.

Do the ITT-MCT constitutive equations also contain this type of instability? Regardless of the answer, addressing the question will put to good use the advection term recovered in Chapter 2 (and therefore reward our endeavours...): without this term, the description of the flow would clearly be unphysical, in the presence of any perturbation to the base flow.

A convenient way to circumvent the problem of the *prescribed* velocity field in ITT-MCT, so as to address the above question, consists in deriving a tractable constitutive equation from the ITT-MCT ones (Eqs. 2.19), albeit at the expense of severe approximations, and then combining this equation with the momentum conservation equation. This gives the desired feedback loop between the stress and the velocity field.

It is now appropriate to recall, from Chapter 2, that the crudest approximation of the transient density correlator Φ in Eqs. 2.19, namely, the assumption that it decays exponentially, independently of shear, *viz.*, $\Phi(t_2, t_1) \propto \exp\left(\frac{t_2 - t_1}{\tau_M}\right)$, yields the Upper Convected Maxwell (UCM) model. Interestingly, Muller et al. [1989] demonstrated that UCM flows are susceptible to elastic instabilities (at high shear rates, large curvatures of the Taylor-Couette cells and for long relaxation times).

But the UCM model is oblivious to the interplay between structural relaxation and the shear drive that is encoded in the ITT-MCT equations. This interplay, however, strongly affects the rheology, since it is at the origin of the shear-thinning behaviour of glassy materials [Fuchs and Cates, 2002]. One may

then wonder about the effect of this shear-thinning mechanism on the elastic instability.

In this chapter, on the basis of a schematic model, we show that the shear-induced cut-off of structural relaxation suppresses the elastic instability. This may explain why, as far as we know, there have been no reports of any elastic instability in dense colloidal suspensions.

4.1 THE ELASTIC INSTABILITY

Consider a Taylor-Couette rheometer, made of a rotating inner cylinder of radius R_1 and a concentric outer cylinder of radius $R_1(1+\epsilon)$, with $\epsilon > 0$, as sketched in Fig. 4.1, and the natural polar coordinates (r, θ, z). The outer cylinder (the "stator") is kept fixed.

It has long been known that for Reynolds numbers Re (or, more precisely, Taylor numbers) larger than some critical value the purely azimuthal base flow $\boldsymbol{v}(r,\theta,z) = v_\theta(r)\boldsymbol{e_\theta}$ of a liquid is destabilised in favour of a vortex flow [Taylor, 1923]. This instability is triggered by inertial forces, while viscosity has a stabilising role. However, even when inertia is entirely negligible, *i.e.*, $Re \to 0$, it became clear some twenty years ago, both experimentally and analytically, that the base flow symmetry can be broken; the instability is then "purely elastic" [Muller et al., 1989, Larson et al., 1990, Shaqfeh et al., 1992], in that it comes from the nonlinear terms in the constitutive equation relating stress and strain derivatives, and has notably been evidenced in dilute polymer solutions [Muller et al., 1989] and semi-dilute worm-like micellar solutions [Fardin et al., 2012b]. The proper adimensional number in that case is the Weissenberg number

$$Wi \equiv \tau_M \dot{\gamma},$$

where τ_M is the relaxation time of the solution, obtained by linear rheology measurements, for instance. For low Wi, the flow only slightly distorts the microstructure.

The precise mechanism underpinning the elastic instability remains unknown to a large extent, but it clearly results from an interplay between the curvature of the (base flow) streamlines and the first normal-stress-difference (hoop stress) $N_1 \equiv \sigma_{\theta\theta} - \sigma_{rr}$ created by the stretching of the polymeric chains. For Shaqfeh [1996], a radial velocity fluctuation, on top of the base flow, stretches polymer chains in the azimuthal direction; but, in curved geometry, the radial ($\boldsymbol{e_r}$) and azimuthal ($\boldsymbol{e_\theta}$) directions are coupled in the equation, so that the hoop stress may increase because of this perturbation, which further enhances the original velocity fluctuation and leads to instability. From a dimensional analysis of general nonlinear constitutive equations, Pakdel and McKinley [Pakdel and McKinley, 1996] suggested the following criterion for the appearance of an elastic instability,

$$\frac{l_p}{\mathcal{R}} \frac{N_1}{\sigma_{r\theta}} \geqslant M_c, \tag{4.1}$$

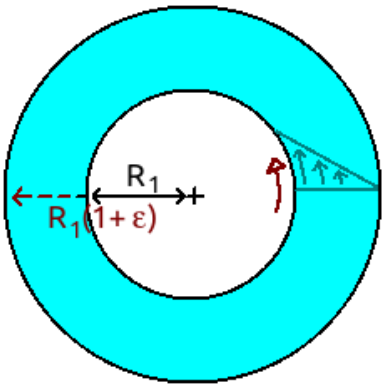

Figure 4.1: Top view of a Taylor-Couette rheometer.

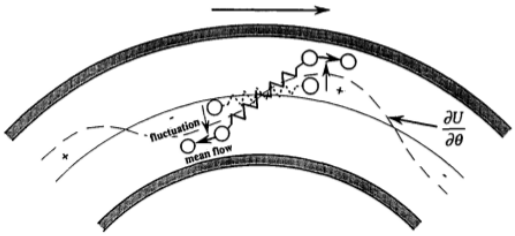

Figure 4.2: Shaqfeh's sketch explaining the driving mechanism for the (nonaxisymmetric) elastic instability. Taken from Ref. Shaqfeh [1996].

where $l_p \equiv v_\theta \tau_M$ is the typical distance travelled by a chain along the base-flow streamline while relaxing, $\mathcal{R}$ is the radius of curvature of the streamline, and M_c is a threshold value of order 1. Some efforts have been made to recover and extend this criterion on the basis of a schematic interpretation of the general equations of motion [Fardin et al., 2012a].

Although, to the best of our knowledge, elastic instabilities have not been observed in dense colloidal suspensions yet, the ITT-MCT equations predict a large first normal-stress-difference N_1 for these materials, which, according to Pakdel and McKinley's criterion (Eq. 4.1) should produce an instability. We want to test this in a schematic model.

4.2 SCHEMATIC MODEL

4.2.1 *Model*

Papenkort and Voigtmann [2013] simulated the flow of a generalised UCM fluid in a channel, derived from a schematic approximation of the ITT-MCT equations of motion. Here, we consider a similar, albeit somewhat less general,

model in a Taylor-Couette geometry. More precisely, the model constitutive equation reads

$$\begin{aligned} \frac{\boldsymbol{\sigma}}{\tau\left(\nabla \boldsymbol{v}\right)} + \overset{\triangledown}{\boldsymbol{\sigma}} &= G_\infty \left(\boldsymbol{\kappa} + \boldsymbol{\kappa}^\top\right) && (4.2) \\ \text{with } \tau\left(\nabla \boldsymbol{v}\right) &\equiv \frac{\tau_M}{1 + 2\alpha\tau_M\sqrt{J_2\left(\dot{\boldsymbol{\epsilon}}\right)}}, \\ \text{and } \overset{\triangledown}{\boldsymbol{\sigma}} &\equiv \frac{\partial \boldsymbol{\sigma}}{\partial t} + \boldsymbol{v}\cdot\nabla\boldsymbol{\sigma} - \nabla\boldsymbol{v}^\top\cdot\boldsymbol{\sigma} - \boldsymbol{\sigma}\cdot\nabla\boldsymbol{v} && (4.3) \end{aligned}$$

where τ_M is the Maxwellian relaxation time of the material at rest ($\tau_M \to \infty$ for an ideal glass), G_∞ is a shear modulus, $\alpha \geqslant 0$ is the shear-thinning parameter, $\boldsymbol{v}$ and $\nabla v_{ij} \equiv \partial v^j/\partial x^i$ (in Cartesian coordinates) are the local velocity and velocity gradient, respectively, and $J_2\left(\dot{\boldsymbol{\epsilon}}\right)$ is the second deviatoric stress invariant of the strain rate tensor $\dot{\boldsymbol{\epsilon}} \equiv \frac{\nabla\boldsymbol{v}^\top + \nabla\boldsymbol{v}}{2}$, *i.e.*,

$$J_2\left(\dot{\boldsymbol{\epsilon}}\right) \equiv \frac{1}{2}\dot{\epsilon}_{ij}\dot{\epsilon}_{ji}.$$

This model is actually known in the polymer rheology community as the White-Metzner model [White and Metzner, 1963]. For a simple shear flow as well as for a purely azimuthal flow in Taylor-Couette geometry, $J_2\left(\dot{\boldsymbol{\epsilon}}\right) = \frac{1}{4}\dot{\gamma}^2$ and, consequently,

$$\tau\left(\nabla \boldsymbol{v}\right) \equiv \frac{\tau_M}{1 + \alpha\tau_M|\dot{\gamma}|}.$$

The interpretation of this dependence is that the relaxation mechanism is cut off by the strain-induced distortion of the local structure (see Chapter 2). The shear-thinning parameter α describes how much strain is required to erase this local structure and could be thought of, crudely, as an inverse yield strain; for $\alpha = 0$, a genuine UCM model is recovered.

The constitutive equation is complemented with the inertialess momentum conservation equation,

$$0 = \nabla\cdot\boldsymbol{\sigma} - \nabla p, \tag{4.4}$$

where p is the pressure, [1] and the incompressibility postulate,

$$0 = \nabla\cdot\boldsymbol{v}. \tag{4.5}$$

4.2.2 *Non-dimensionalisation*

From now on, we set the unit of time to τ_M, the unit of length to R_1, and the unit of stress to G_∞.

1. In the UCM equation presented in Chapter 2, the pressure was included in the total stress $\boldsymbol{\sigma}$.

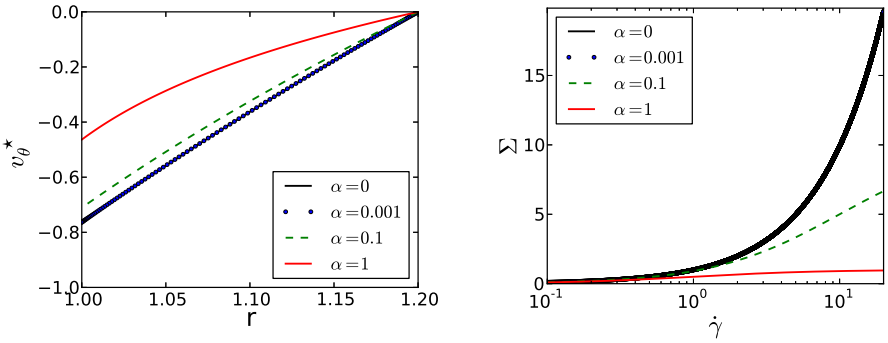

(a) Velocity profile for an applied shear rate $\dot\gamma^{(1)} = 5$ at the rotor.

(b) Flow curve $\Sigma(\dot\gamma)$.

Figure 4.3: Base flow properties of the rheological model, for a relative gap width $\epsilon = 0.2$ and using various shear-thinning parameters α, as indicated in the legend.

4.2.3 *Base flow*

First, we consider the purely azimuthal base flow, prior to any instability, $\boldsymbol{v}^\star(r,\theta,z) = v_\theta^\star(r)\boldsymbol{e_\theta}$, with the following boudary conditions,

$$\begin{cases} v_\theta'(1) - \frac{v_\theta}{1} & = \dot\gamma^{(1)} \\ v_\theta(1+\epsilon) & = 0, \end{cases}$$

where $\dot\gamma^{(1)}$ is the imposed shear rate at the rotor. One can then easily check that the following stress and velocity fields satisfy the constitutive equations, the momentum conservation equation, as well as the boundary conditions:

$$\begin{aligned} v_\theta^\star(r) &= \operatorname{sign}\left[\dot\gamma^{(1)}\right] \frac{r}{\alpha} \ln \sqrt{\frac{1 - B/r^2}{1 - B/(1+\epsilon)^2}} \\ \sigma_{rr}^\star(r) &= 0 \\ \sigma_{r\theta}^\star(r) &= \frac{\dot\gamma^\star(r)}{1+\alpha|\dot\gamma^\star(r)|} \\ \sigma_{\theta\theta}^\star(r) &= 2\left(\frac{\dot\gamma^\star(r)}{1+\alpha|\dot\gamma^\star(r)|}\right)^2, \end{aligned}$$

where $B \equiv \frac{\alpha|\dot\gamma^{(1)}|}{1+|\dot\gamma^{(1)}|}$ and $\dot\gamma^\star(r) \equiv v_\theta^{\star\prime} - \frac{v_\theta^\star}{r} = \frac{B}{\alpha(r^2-|B|)}$. The macroscopic shear stress at the rotor is: $\Sigma = \frac{\dot\gamma^{(1)}}{1+\alpha\dot\gamma^{(1)}}$.

Figure 4.3 presents the variation of the velocity profile of the base flow with the shear-thinning parameter α, at fixed gap width ϵ and applied shear rate $\dot\gamma^{(1)}$. Reasonable agreement with experimental data is obtained for large values[2] of α, $\alpha \approx 10$.

2. Matthias Fuchs, *private communication*.

4.3 LINEAR STABILITY ANALYSIS OF THE BASE FLOW

4.3.1 *Pseudo-spectral method*

Let us now study whether the previously derived base flow is stable with respect to (three-dimensional) linear perturbations

$$\delta\phi(r,\theta,z,t) \equiv \left(\begin{array}{cccccccccc} \delta\sigma_{rr} & \delta\sigma_{r\theta} & \delta\sigma_{rz} & \delta\sigma_{\theta\theta} & \delta\sigma_{\theta z} & \delta\sigma_{zz} & \delta v_r & \delta v_\theta & \delta v_z & \delta p \end{array} \right)^\top .$$

To do so, we resort to a pseudo-spectral method, similar to that used in Ref. [Nicolas and Morozov, 2012]. This method consists in linearising the equations of the problem, comprising the six constitutive equations (Eqs. 4.2), the three momentum conservation equations (Eqs. 4.4), and the incompressibility postulate (Eq. 4.5), around the base flow so as to obtain a linear equation of the form

$$\underbrace{\begin{pmatrix} \frac{\partial}{\partial t} & & & & & & \\ & \ddots & & & & & \\ & & \frac{\partial}{\partial t} & & & & \\ & & & 0 & & & \\ & & & & 0 & & \\ & & & & & 0 & \\ & & & & & & 0 \end{pmatrix}}_{\mathcal{A}} \delta\phi = \mathcal{L}^\star \delta\phi,$$

and expressing the linear operators (more precisely, the endomorphisms) $\mathcal{A}$ and $\mathcal{L}^\star$ as matrices, *viz.*, $\mathcal{A} \to \mathbf{A}$ and $\mathcal{L}^\star \to \mathbf{L}^\star$. This is done by:

- Fourier-transforming $\delta\phi$ both in the azimuthal direction (wavenumber m) and in the axial direction (wavenumber k), *viz.*,
$$\delta\phi(r,\theta,z,t) = \sum_{m=-\infty}^{\infty} \sum_{k \in 2\pi/L_z \mathbb{Z}} \delta\phi(r,m,k,t)\, e^{im\theta} e^{ikz},$$
- discretising the r-coordinate at the Chebyshev–Gauss–Lobatto points $r_n \equiv 1.0 + \frac{\epsilon}{2}\left[1 + \cos\left(\pi \frac{n}{N}\right)\right]$, $0 \leqslant n < N$, for a given $N \in \mathbb{N}^\star$, and expressing radial derivatives $\partial_r \delta\phi$ as matrix-vector products[3] "$D_r \cdot \delta\phi$",
- and, finally, Laplace-transforming $\delta\phi$ with respect to time (Laplace coordinate s), *viz.*, $\delta\phi(r,m,k,s) = \int e^{st} \delta\phi(r,m,k,t) dt$.

One then obtains a generalised eigenvalue problem

$$\mathbf{A}\delta\phi(r,m,k,s) = s\mathbf{L}^\star \delta\phi(r,m,k,s), \tag{4.6}$$

where $\mathbf{A}$ and $\mathbf{L}^\star$ are $10N \times 10N$ matrices, a few lines of which are subsequently substituted for the implementation of the boundary conditions.

3. The method is pseudo-spectral insofar as the D_r matrices are actually derived from an interpolation with Chebyshev polynomials.

Let $s^\star$ be the maximal growth rate, *i.e.*, the real part of the maximal eigenvalue [4] of Eq. 4.6 over all possible wavenumbers m and k.

The condition for the base flow to be *stable* simply reads:

The base flow is stable *iff* $s^\star < 0$.

4.3.2 *Linearised equations*

The linearised constitutive equations read

$$\begin{aligned}
\frac{\partial \delta\sigma_{rr}}{\partial t} &= \left(\frac{-1}{\tau^\star} - \frac{im}{r}v_\theta^\star\right)\delta\sigma_{rr} + \left(2\sigma_{r\theta}^\star\frac{im}{r} + 2\partial_r\right)\delta v_r \\
\frac{\partial \delta\sigma_{r\theta}}{\partial t} &= \dot\gamma^\star\delta\sigma_{rr} + \left(\frac{-1}{\tau^\star} - \frac{im}{r}v_\theta^\star\right)\delta\sigma_{r\theta} + \left[\sigma_{r\theta}^\star\frac{im}{r} + \partial_r - \frac{1}{r} - \alpha\sigma_{r\theta}^\star\left(\partial_r - \frac{1}{r}\right)\right]\delta v_\theta \\
&\quad + \left[\sigma_{r\theta}^\star\left(\partial_r + \frac{1}{r}\right) - \partial_r\sigma_{r\theta}^\star + \sigma_{\theta\theta}^\star\frac{im}{r} + \frac{im}{r} - \alpha\sigma_{r\theta}^\star\frac{im}{r}\right]\delta v_r \\
\frac{\partial \delta\sigma_{rz}}{\partial t} &= \left(\frac{-1}{\tau^\star} - \frac{im}{r}v_\theta^\star\right)\delta\sigma_{rz} + ik\delta v_r + \left(\sigma_{r\theta}^\star\frac{im}{r} + \partial_r\right)\delta v_z \\
\frac{\partial \delta\sigma_{\theta\theta}}{\partial t} &= 2\dot\gamma^\star\delta\sigma_{r\theta} + \left(\frac{-1}{\tau^\star} - \frac{im}{r}v_\theta^\star\right)\delta\sigma_{\theta\theta} + \left(\frac{2\sigma_{\theta\theta}^\star}{r} - \partial_r\sigma_{\theta\theta}^\star + \frac{2}{r} - \alpha\sigma_{\theta\theta}^\star\frac{im}{r}\right)\delta v_r \\
&\quad + \left[2\sigma_{r\theta}^\star(\partial_r - 1/r) + 2\sigma_{\theta\theta}^\star\frac{im}{r} + 2\frac{im}{r} - \alpha\sigma_{\theta\theta}^\star\left(\partial_r - \frac{1}{r}\right)\right]\delta v_\theta \\
\frac{\partial \delta\sigma_{\theta z}}{\partial t} &= \dot\gamma^\star\delta\sigma_{rz} + \left(\frac{-1}{\tau^\star} - \frac{im}{r}v_\theta^\star\right)\delta\sigma_{\theta z} + ik\delta v_\theta + \left(\frac{im}{r} + \sigma_{\theta\theta}^\star\frac{im}{r} + \sigma_{r\theta}^\star\partial_r\right)\delta v_z \\
\frac{\partial \delta\sigma_{zz}}{\partial t} &= \left(\frac{-1}{\tau^\star} - \frac{im}{r}v_\theta^\star\right)\delta\sigma_{zz} + 2ik\delta v_z,
\end{aligned}$$

where $\tau^\star \equiv \frac{1}{1+\alpha|\dot\gamma^\star|}$, while the linearised momentum conservation equations are

$$\begin{aligned}
0 &= \left(\partial_r + \frac{1}{r}\right)\delta\sigma_{rr} + \frac{im}{r}\delta\sigma_{r\theta} + ik\delta\sigma_{rz} - \frac{1}{r}\delta\sigma_{\theta\theta} - \partial_r\delta p \\
0 &= \left(\partial_r + \frac{2}{r}\right)\delta\sigma_{r\theta} + \frac{im}{r}\delta\sigma_{\theta\theta} + ik\delta\sigma_{\theta z} - \frac{im}{r}\delta p \\
0 &= \left(\partial_r + \frac{1}{r}\right)\delta\sigma_{rz} + \frac{im}{r}\delta\sigma_{\theta z} + ik\delta\sigma_{zz} - ik\delta p,
\end{aligned}$$

and incompressibility states that

$$0 = \left(\partial_r + \frac{1}{r}\right)\delta v_r + \frac{im}{r}\delta v_\theta + ik\delta v_z.$$

4. Due to the discretisation, some spurious eigenvalues may pop up in the generalised eigenvalue problem (Eq. 4.6), but they can easily be eliminated because, unlike their physical counterparts, they vary with the number of discretisation points.

4.3.3 *Numerical results*

For a shear-thinning parameter α close to zero, we expect to recover a conventional UCM model. Following Ref. [Larson et al., 1990], some axisymmetric modes should then become unstable at sufficiently large applied shear rates. We do indeed observe this destabilisation in our simulations. This trend is robust to small variations of α: in Fig. 4.4a, we show the increase of the maximal growth rate $s^\star$ with the applied shear rate for $\alpha = 4 \cdot 10^{-3}$. The relative gap width ϵ is set to 0.2, until the end of this chapter.

The influence of the shear-thinning magnitude α is studied by varying this parameter while keeping the applied shear rate fixed, here, $\dot{\gamma}^{(1)} = 40$. The results for small values of α are plotted in Fig. 4.4b, and a more detailed view of the maximal growth rates for each Fourier mode (m, k) is presented in Fig. 4.5 for two distinct values of α. Clearly, the more shear-thinning the fluid is, the more stable it is with respect to elastic instabilities. In particular, we have checked that for $\alpha \sim 10$, the base flow is quite stable with respect to all tested perturbation modes, $(k, m) \in [0, 200] \times [0, 15]$. It should however perhaps be mentioned that, for a range of shear thinning parameters, $0.1 \lesssim \alpha \lesssim 1$ here, although the modes that were elastically unstable at lower values of α are indeed stabilised, another unstable mode emerges, at $k \approx 0$ in our numerical simulations (azimuthal mode). At present, it is unsure whether this is an artifact of the model under consideration, or whether this new instability is physically grounded.

The enhanced stability of the shear-thinning fluid is the major result of this section, and it is consistent with the Pakdel-McKinley criterion introduced in Eq. 4.1. Indeed, in the model under study, the lhs of Eq. 4.1 reads $\frac{l_p}{\mathcal{R}} \frac{N_1}{\sigma_{r\theta}} \sim \frac{v_\theta}{\mathcal{R}} \frac{2\dot{\gamma}^\star(r)}{1+\alpha|\dot{\gamma}^\star|}$ and therefore decreases with increasing α. It follows that, according to the criterion, stability should be restored for large enough α.

Physically, the shear-induced acceleration of structural relaxation is therefore expected to inhibit elastic instabilities in supercooled liquids and glasses.

The success of schematic equations loosely derived from ITT-MCT to capture instabilities should not obliterate the difficulties associated with the presence of heterogeneities in the genuine ITT-MCT equations. Since heterogeneities play a central role at low temperature, we adopt another line of modelling to study the flow of materials deep within the solid phase: elastoplastic models.

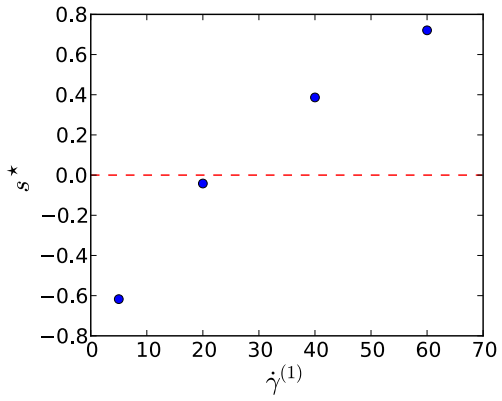

(a) At fixed shear-thinning parameter, $\alpha = 4 \cdot 10^{-3}$.

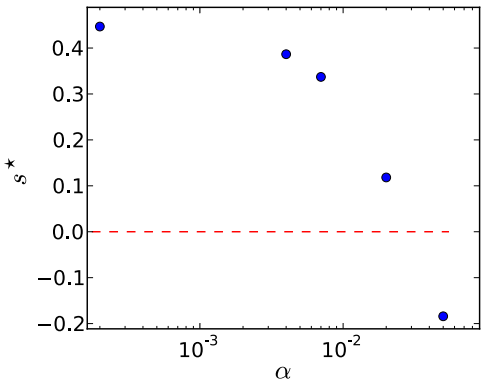

(b) At fixed applied shear rate, $\dot{\gamma}^{(1)} = 40$.

Figure 4.4: Maximal growth rate $s^\star$ (over all modes).

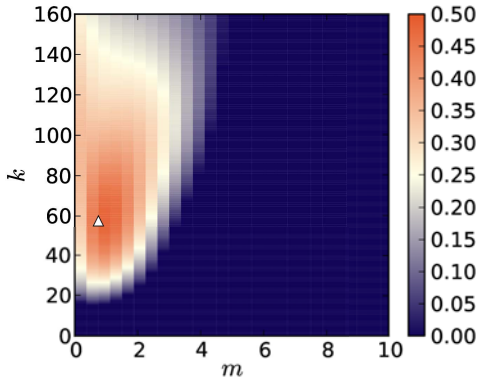

(a) $\alpha = 2 \cdot 10^{-4}$

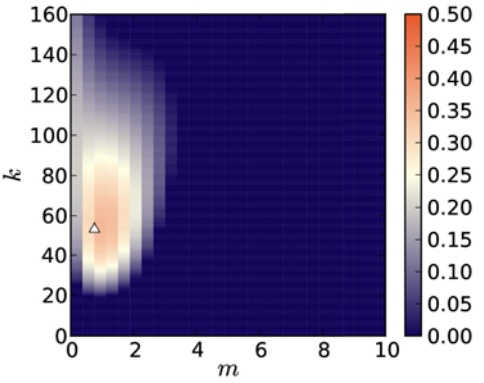

(b) $\alpha = 7 \cdot 10^{-3}$

Figure 4.5: Colour maps of the maximal growth rates associated with each pair of wavenumbers (m, k), at an applied shear rate $\dot{\gamma}^{(1)} = 40$. Stable modes appear in dark blue.

Part II

THE ELASTOPLASTIC DESCRIPTION OF THE FLOW OF AMORPHOUS SOLIDS

> *Funes remembered not only every leaf of every tree of every wood, but also every one of the times he had perceived or imagined it [...]. He was, let us not forget, almost incapable of ideas of a general, Platonic sort. Not only was it difficult for him to comprehend that the generic symbol* dog *embraces so many unlike individuals of diverse size and form; it bothered him that the dog at three fourteen (seen from the side) should have the same name as the dog at three fifteen (seen from the front) [...] He was the solitary and lucid spectator of a multiform, instantaneous and almost intolerably precise world.*
>
> Jorge Luis Borges, 'Funes The Memorious', *in Labyrinths*, translated by James E. Irby, New Directions, 1962.

Most physicists are aware that any particular dog is distinct from any other dog, as is any particular emulsion from any other emulsion, as is (and even more so) any emulsion from any metallic glass. However, the development of Physics has proved that, by turning a blind eye to petty differences and focusing on general aspects and similarities, much can be learnt about ferromagnetic systems, about phase transitions, or about the world. Here, the differences will not be petty in any way: an emulsion really does not seem to have much in common with a metallic glass (not to mention the dog...).

In comparison with the previous part, whose realm of application is mostly above or around the glass transition temperature, here the focus will be on materials much deeper in the solid phase, and often in the athermal limit, hence the centrality of the concept of elasticity. We aim to provide extensive evidence that, on account of the solidity of these materials and the absence of readily identifiable structural defects, they can be studied in a common framework. Admittedly, the emphasis will be on soft jammed materials, but I will strive to point to the major aspects which may not be generic.

This part exposes the foundations and building blocks of elastoplastic models. Chapter 5 presents the experimental and numerical observations out of which such models were devised. A review of existing models is proposed in Chapter 6. In Chapter 7, we identify the ingredients that need to be included in the elastoplastic description to account for bulk rheology and their connection to microscopic physical processes. The last chapter of this part, Chapter 8, provides details on the implementation of our elastoplastic model.

5

A SIMILAR FLOW SCENARIO FOR EXTREMELY DIVERSE DISORDERED SOLIDS

To begin with, let us summarise in a few words the *macroscopic* features that distinguish the rheology of amorphous solids from that of simple fluids:

- a finite yield stress needs to be surpassed in order to initiate and maintain a permanent flow,

- as the yield stress is approached from below, a creep regime featuring jerky, but dwindling, flow sets is,

- even (not too far) above the yield stress, the flow is jerky, and sometimes macroscopically heterogeneous.

Experimental as well as numerical evidence, detailed in this chapter, ascribe these characteristics to bursts of swift localised rearrangements of particles taking place in a solid-like medium.

5.1 THE ELASTIC-REBOUND THEORY OF EARTHQUAKES

The characteristics of the flow dynamics that have just been listed are strongly reminiscent of earthquakes.

A basic, but widely accepted, description of the mechanism of earthquakes is the elastic-rebound theory, propounded by Reid [1910] in an official report on the devastating California earthquake of 1906: potential energy is accumulated prior to the earthquake as the soil is elastically strained, due to the relative displacement of (what is now called) tectonic plates (see Fig. 5.1). As soon as the applied forces exceed the cohesion of the strained rocks and soil (represented in yellow in Fig. 5.1), the accumulated energy is suddenly released and takes the form of seismic waves, making the earth quake.

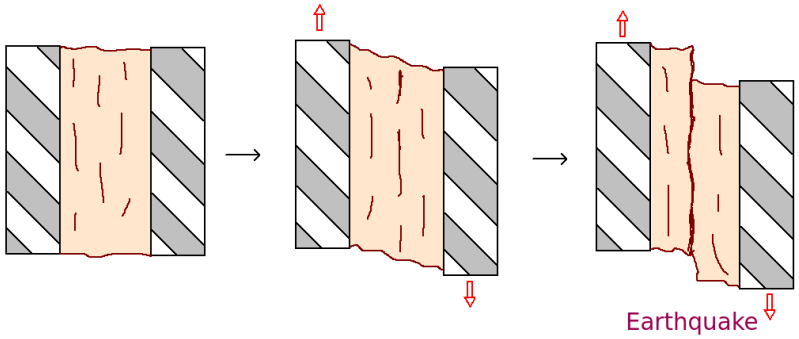

Figure 5.1: Schematic illustration of H.F. Reid's elastic-rebound theory.

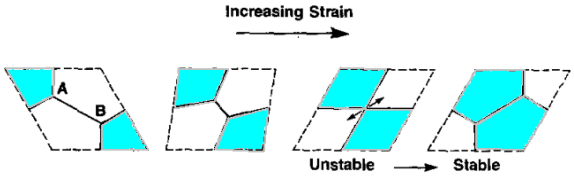

Figure 5.2: Sketch of a 'T1 event'. Adapted from Ref. [Princen and Kiss, 1989] .

This theory of *stick-slip* motion naturally also has bearing on tribology [Persson, 1999], *i.e.*, the study of the relative sliding of surfaces in contact or the propagation of cracks in matter. Since amorphous solids, too, may store elastic energy, it is tempting to apply the theory to them as well.

The analogy may suffer from a drawback, however. Structurally weak regions, where rupture is most likely to occur, can easily be identified in seismology and in tribology: these are the faults and the sliding plane, respectively. But where and how is rupture initiated in the bulk of a macroscopically homogeneous amorphous solid?

5.2 LOCALISED SHEAR TRANSFORMATIONS

Since atoms in metallic glasses can hardly be imaged, Argon and Kuo [1979] resorted to experiments on bubble rafts to gain better understanding of the deformation of amorphous metals, thereby reinvigorating an analogy pointed out by Bragg and Nye [1947]. Argon and Kuo observed that the macroscopic deformation of monolayers of bidisperse millimetric bubbles floating on an aqueous solution proceeds through very localised *shear transformations*, that is to say, internal rearrangements of regions of about 5 bubble diameters.

In his pioneering studies on dense foams and oil-in-water emulsions, Princen [1983, 1985] identified these shear transformations as *T1 events*. These events are local topological changes, more precisely first-neighbour exchanges, that occur whenever four bubbles come to share a common vertex, as a result of the macroscopic drive. This unstable situation is depicted in Fig. 5.2.

More recently, Schall et al. [2007] used confocal microscopy to visualise rearrangements in quasi-statically deformed colloidal glasses and observed rearranging regions of about 3 colloid diameters. In slowly sheared granular matter, diffusive wave spectroscopy imaging by Amon et al. [2012b] has brought to light swiftly rearranging regions of about 15 grain diameters 'randomly' bursting in an essentially still medium.

Throughout this thesis, these *elementary* rearrangements will often be referred to as plastic events,[1] regardless of their specific details. Incidentally, the geometry of these shear-induced rearrangements is very likely to differ from that of the

1. This definition may differ from that of Procaccia and co-workers [Hentschel et al., 2010] or Tanguy and co-workers [Fusco et al., 2014]

localised excitations due to thermal fluctuations in the quiescent system, which are, arguably, string-like [Keys et al., 2011].

Atomistic simulations have also greatly contributed to the understanding of the deformation of disordered solids. Because the difficulty inherent in the study of these complex systems mostly results from the large number of particles and collective effects, and not from the ignorance of elementary interparticle interactions, numerical systems are generally reliable model systems in this field. Almost two decades ago, Falk and Langer [1998] reported on the presence of localised region displaying intense non-affine deformations in molecular dynamics simulations of a low-temperature glass. This observation has since been reproduced in very diverse numerical systems, with different algorithms [Maloney and Lemaître, 2006, Tanguy et al., 2006, Chaudhuri and Horbach, 2013, Chattoraj and Lemaître, 2013].

5.3 NON-LOCAL EFFECTS

The accurate "measurements" provided by simulations have notably shed light on the existence of long-ranged displacement and strain fields induced by localised rearrangements, in glasses as well as in supercooled liquids [Maloney and Lemaître, 2006, Tanguy et al., 2006, Goldenberg et al., 2007, Lemaître and Caroli, 2007, Chattoraj and Lemaître, 2013, Mandal et al., 2013]. This long-ranged field is illustrated in Fig. 5.3a.

Theoretically, these long-ranged fields are expected when an inclusion embedded in an elastic medium gets deformed [Goldstein, 1969]. More precisely, Eshelby [1957] had worked out the exact strain field caused by an elastic inclusion bearing a spontaneous deformation (eigenstrain), in a uniform elastic medium; the displacement and strain fields have, respectively, a two-fold and a four-fold symmetry, and an r^{1-d} and an r^{-d} decay in (d-dimensional) space, in accordance with numerical simulations (see Fig. 5.3b). In 2D, if the system is incompressible, the ϵ_{xy}-strain field induced by a circular inclusion (of unit surface) located at the origin and bearing an eigenstrain $\epsilon^\star_{xy}$ is given by the elastic propagator $\mathcal{G}$ in the far field, *viz.*,

$$\epsilon_{xy}(\boldsymbol{r}) \quad = \quad \mathcal{G}(\boldsymbol{r})\epsilon^\star_{xy},$$

where $\mathcal{G}(r,\theta) \sim \cos(4\theta)/r^2$, with polar coordinates (r,θ).

Direct experimental evidence of these long-ranged fields has also been obtained, *e.g.*, *via* confocal microscopy imaging of slowly sheared colloidal glasses [Schall et al., 2007, Chikkadi et al., 2011, 2012] or *via* diffusive wave spectroscopy in granular matter [Le Bouil et al., 2014]. Besides these direct observations, non-local effects alledgedly mediated by the induced fields have also been reported. Nichol and co-workers reported on an elegant experiment in which a steel ball placed on the surface of a box filled with millimetric glass beads starts to sink if the granular material is sheared at the bottom of the box, even though, when the steel ball is removed, the surface looks unaffected by this distant shear [Nichol

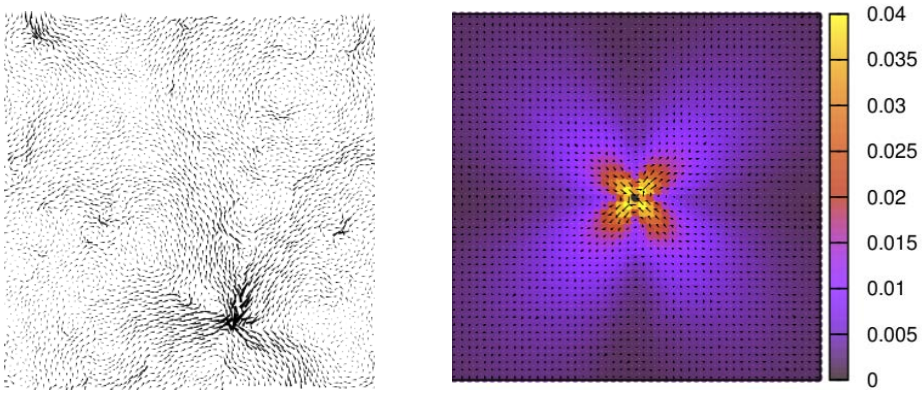

(a) (b)

Figure 5.3: (a) Non-affine displacement field observed in a quasi-static simulation, on approaching an avalanche of plastic events. Reproduced from Ref. [Maloney and Lemaître, 2006]. (b) Average displacement field induced by artificially triggered shear rearrangements in a binary Lennard-Jones glass. Taken from Ref. [Puosi et al., 2014]

et al., 2010, Nichol and van Hecke, 2012]. In microchannel flows of dense emulsions and suspensions, striking non-local effects leading to strong deviations from bulk rheology have been observed by different groups [Goyon et al., 2008, Jop et al., 2012, Geraud et al., 2013].

Such collective effects, indicative of correlations between plastic events, rationalise the observed cascades of plastic events in slow flows, and the serrated profile of *macroscopic* stress *vs.* strain curves [Baret et al., 2002, Bailey et al., 2007, Lemaître and Caroli, 2009, Chattoraj et al., 2011, Antonaglia et al., 2014].

5.4 FLOW CURVE

For materials that do not fracture, a flow curve, that is to say, a macroscopic stress *vs.* strain rate relation $\Sigma = f(\dot{\gamma})$, can be measured, in experiments as well as in atomistic simulations. Whether it be for dense emulsions [Princen and Kiss, 1989, Bécu et al., 2006, Jop et al., 2006], foams with low surface modulus (*i.e.*, fast relaxation of surface tension fluctuations) [Denkov et al., 2009], carbopol microgels [Divoux et al., 2011b], soft colloidal pastes [Cloitre et al., 2003, Nordstrom et al., 2010], hard-sphere colloidal suspensions [Ballesta et al., 2008, 2012], numerical binary Lennard-Jones glasses [Lemaître and Caroli, 2009] or numerical models of dense suspensions of deformable capsules [Gross et al., 2014], the flow curve is very often well fitted by a Herschel-Bulkley equation $\Sigma = \Sigma_0 + A\dot{\gamma}^n$, with a finite yield stress Σ_0 and an exponent n generally (but not always) around 0.5.

When the flow is macroscopically homogeneous, the flow curve reflects the relation between local stresses and strain rates. But, in a heterogeneous flow, in particular when shear localisation occurs, *i.e.*, when shear is confined in a (gener-

ally macroscopic) band in the sample, local strain rates strongly differ from the applied strain rates. In that case, the flow curve is not a local constitutive curve, and it often displays a plateau [Martens et al., 2012] or even a non-monotonic behaviour [Schall and van Hecke, 2010] at low shear rates.

6 MESOSCOPIC MODELS: STATE OF THE ART

The enticing simplicity of the generic flow scenario exposed in Chapter 5 has led to the emergence of a variety of mesoscale models. All models in this category rest on the idea of shear transformation regions, or flow defects, embedded in an essentially solid medium, and focus on the activity of these regions. Nevertheless, they differ considerably with regard to the dynamics of these regions and their coupling (or the absence thereof).

Before delving into the zoology of these models, I feel compelled to mention the following bias in favour of a physicist's, rather than a material scientist's, approach: in my view, what these models should target is *not* the perfectly faithful description of a specific system, at the expense of a large set of parameters, but, rather, a minimal framework permitting the identification of

(i) the relevant mechanisms accounting for universal rheological properties of these materials, and

(ii) the key physical parameters explaining the major differences that are observed.

It follows that the design and the appraisal of a model will depend on the properties (*i.e.*, the observable) that one wants to reproduce, from the most basic ones to the most sophisticated.

6.1 GENERIC VISCOELASTIC MODELS

6.1.1 *Kelvin-Voigt and Maxwell models*

The viscoelastic Kelvin-Voigt and Maxwell models consist of the assembly of a spring ($\sigma_s = E\gamma_s$) and a dashpot ($\sigma_d = \eta\dot{\gamma}_d$), either in parallel (Kelvin-Voigt) or in series (Maxwell), as sketched in Fig. 6.1. In the former model, both components are equally strained, but their stresses σ add up to give the total stress, *ergo*,

$$\sigma(t) = E\gamma(t) + \eta\dot{\gamma}(t),$$

whereas it works the other way round for the Maxwell model:

$$\sigma(t) + \frac{\eta}{E}\dot{\sigma}(t) = \eta\dot{\gamma}(t).$$

The Kelvin-Voigt model is therefore a generic model of dissipative deformation with respect to a fixed reference elastic configuration, whereas the Maxwell model describes the gradual loss of the memory of this reference configuration. Neither really reflects the *alternation* of processes at work in amorphous solids. Nevertheless, it may be noted that Tighe [2011] was able to derive linear rheol-

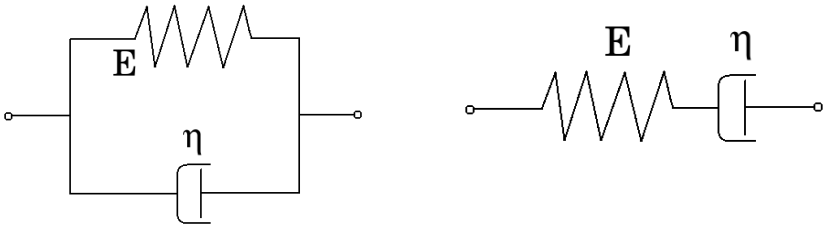

(a) Kelvin-Voigt model (b) Maxwell model

Figure 6.1: Schematic representations of the Kelvin-Voigt and the Maxwell models.

ogy properties of jammed packings by considering an assembly of Kelvin-Voigt-elements.

The elastoplastic models that follow elaborate the idea of an assembly of elastically strained mesoscopic regions that yield past a critical stress, or owing to thermal fluctuations.

6.2 EXTREMAL MODELS

Extremal models account for the elastic interactions between rearranging regions while leaving aside dynamical aspects, by investigating the quasi-static limit, $\dot{\gamma} \to 0$. Generally, the interactions are described by an (instantaneous) Eshelby-like propagator of the form $\mathcal{G}(r,\theta) \sim \cos(4\theta)/r^2$ (the reader is referred to Section 5.3 or Refs. [Eshelby, 1957, Picard et al., 2004]), in 2D, in the limits to be discussed in Chapter 8. $\mathcal{G}(r,\theta)$ gives the stress increment at position (r,θ) resulting from a unit plastic strain at the origin.

6.2.1 *Chen, Bak, and Obukhov*

This line of modelling was pioneered by Chen et al. [1991], who were interested in the statistics of earthquake magnitudes. They succeeded in recovering the characteristic Gutenberg-Richter power-law distribution by simulating a square lattice of blocks connected by springs (i,j) that break past a random stress threshold, $\sigma_y(i,j)$. Springs are gradually loaded, *via* the increment of their shear stress $\sigma(i,j)$ at each time step, *viz.*, $\sigma(i,j) \to \sigma(i,j) + \delta\sigma$. When a spring-bond (i,j) breaks, its load is entirely redistributed to the other bonds on the lattice *via* the Green function G of their elastic network, *viz.*, $\sigma(i',j') \to \sigma(i',j') + G_{i'-i;j'-j}\,\sigma(i,j)$, and a new random stress threshold is assigned to it. The earthquake magnitude is defined as the number of bonds that break in a row, *i.e.*, in an avalanche.

6.2.2 *Baret, Vandembroucq, and Roux*

Baret et al. [2002] applied a similar model to the study of plasticity in amorphous media and unveiled a diffuse localisation of the plastic strain increments over finite time windows. Their model is made explicitly extremal by controlling the macroscopic load increments so that one, and only one, site yields at each time step; thus, the macroscopic stress is not increased during an avalanche.

6.2.3 *Dahmen, Ben-Zion, and Uhl*

Dahmen et al. [2009] added strain weakening (hardening) to this picture by making use of two distinct distributions for the initial yield stresses and the ones picked thereafter. These distributions are such that the "new" yield stresses are on average smaller (larger, respectively) than the initial ones.

The authors resorted to mean-field theory and renormalisation group approaches to solve the problem, and invoked the long range of the elastic propagator to justify this recourse. [1] One of the conclusions of the study was that, while plasticity (*i.e.*, slip) is more or less uniformly distributed in strain-hardening materials, their strain-weakening counterparts are brittle, insofar as slip gets localised in a narrow band, which leads to macroscopic failure.

Similar conclusions were drawn by Vandembroucq and Roux [2011], with a different model featuring a *bona fide* Eshelby-like propagator.

6.3 Models based on a periodic potential landscape

With the particular prospect of reproducing strain localisation phenomena, Jagla [2007] proposed a 2D model of amorphous plasticity based on an *ad hoc* PEL.

The main variable of the model is the deformation tensor $\boldsymbol{\epsilon}(\boldsymbol{r})$, which is described by three scalar fields, $e_1(\boldsymbol{r})$, $e_2(\boldsymbol{r})$, and $e_3(\boldsymbol{r})$, respectively associated with local volume change ($e_1 = \frac{1}{2}\mathrm{Tr}\,\boldsymbol{\epsilon}$) and shear in two complementary directions (e_2 and e_3). The local free energy f is entirely determined by these scalars; the author's choice was

$$f(e_1, e_2, e_3) = Be_1^2 + f_0(e_2, e_3),$$

where B should be regarded as the bulk modulus of the material and the quadratic form Be_1^2 counters volumetric changes. Since plastic deformation uproots the system from a given elastic energy basin and shifts it to another *roughly similar* basin, the author chose a periodic function f_0 (more precisely, it is a linear combination

1. In Chapter 11, it will however be argued that the presence of positive and negative lobes in the propagator may undermine this argument [Budrikis and Zapperi, 2013].

of sines), in order to allow plasticity. That being set, the evolution of the system is governed by

$$\forall i \in \{1,2,3\}\,,\ \frac{\partial e_i(\boldsymbol{r})}{\partial t} = \eta \underbrace{\frac{\delta F}{\delta e_i(\boldsymbol{r})}}_{\sigma_i} + \Lambda,$$

where η sets the typical time scale of evolution, the global free energy F is the integral of f over space, and Λ is a function that accounts for the coupling between the deformation at different positions (formally, it is a Lagrange multiplier enforcing a compatibility condition on the e_i's required by continuum mechanics).

If the system is strained, *e.g.*, by controlling the value of the macroscopic shear strain $\int e_2 d^2r$, the e_i's evolve locally, and 'hops' between free energy basins are observed. However, for strain localisation to occur, an additional ingredient is needed: the system must spontaneously relax with time, that is to say, it must age. This is (successfully) achieved by guiding the evolution of the e_i's towards minima of the *global* free energy, through the introduction of additional fields.

6.4 THE SOFT GLASSY RHEOLOGY (SGR) MODEL

6.4.1 *The mean-field model*

Sollich and co-workers supplemented Bouchaud's trap model (see Section 1.4.2) with an external shear drive [Sollich et al., 1997, Sollich, 1998].

The material is divided into mesoscopic regions, each of which carries a strain l and evolves through a landscape of energy traps randomly drawn from an exponential distribution $\rho(E) \propto \exp(-E/E_g)$. Here, E is the trap depth and E_g is a material parameter that will be set to unity. Instead of being caused only by temperature-like fluctuations, the escape from a trap is now facilitated by the local strain l, insofar as the latter lowers the local energy barrier: $E \to E - \frac{1}{2}kl^2$. Here, the stiffness parameter k is such that kl is the mesoscopic stress. The escape rate then reads

$$\omega(E,l) = \omega_0 \exp\left(\frac{-E + \frac{1}{2}kl^2}{x}\right). \tag{6.1}$$

Due to the applied shear rate $\dot{\gamma}$, the local strain l increases with time, at a rate $\dot{l} = \dot{\gamma}$. After an escape event, l is set back to zero and a new trap depth E is randomly picked from the distribution ρ.

The second major difference with respect to Bouchaud's trap model is that, in Eq. 6.1, the room temperature is replaced by a "mechanical noise temperature" x, presumably of order 1, which should account for the local (*e.g.*, stress) fluctuations induced by distant rearrangements in the system, for want of an explicit computation of these interactions here.

Sollich and co-workers proposed a mean-field analysis of the model, based on a master equation for the probability distribution $P(E,l;t)$, *viz.*,

$$\frac{\partial P}{\partial t}(E,l;t) \quad = \quad -\dot{\gamma}\frac{\partial P}{\partial l}(E,l;t) - \omega(E,l)P(E,l;t) + \langle\omega(E,l)\rangle_P \rho(E)\delta(l), \quad (6.2)$$

where the average $\langle\omega(E,l)\rangle_P$ is calculated with respect to the probability distribution $P(E,l;t)$. The terms on the rhs of Eq. 6.2 describe, in their order of appearance, the strain increments due to the macroscopic drive, the depletion of highly strained regions due to escape events, and the rate of rebirth at zero strain associated with these events. From this equation, the authors were able to derive scaling laws for the linear rheology moduli and the steady-state flow curve, in the limit of vanishing shear rate, $\dot{\gamma} \to 0$, and at fixed x. Particularly encouraging aspects include the observation of a power-law equation $\Sigma \sim \dot{\gamma}^{x-1}$ above the glass transition, *i.e.*, for $x > 1$, while a yield stress Σ_0 emerges for $x < 1$, along with a Hershel-Bulkley flow curve, $\Sigma - \Sigma_y \sim \dot{\gamma}^{1-x}$.

The intuitive explanation for the increase of the stress with the shear rate in this model is that, at higher shear rates, a mesoscopic region has reached a higher local strain by the time a 'thermally' activated hop over the energy barrier occurs.

6.4.2 *Inclusion of a diffusive process for x*

In principle, the mechanical noise temperature x should not be fixed externally, but, instead, adjusted self-consistently as a function of the plastic activity in the system. As a first move in this direction, Fielding et al. [2009] described its evolution with a diffusion equation, *viz.*,

$$\dot{x} \sim (x_0 - x) + S + D\Delta x,$$

where the first term on the rhs favours relaxation to the equilibrium value x_0, S is a source term that depends on the local rearrangement rate, and the parameter D denotes a diffusion coefficient.

Depending on the expression of the source term S, the authors showed that the model displays (or not) shear localisation.

6.4.3 *Argon and Bulatov's lattice-based model*

Even before the development of the SGR theory, Bulatov and Argon [1994a,b,c] had proposed a mesoscale model also based on the lowering of (free) energy barriers $\Delta G^\star(\sigma)$ through the local stress σ. Similarly to SGR, local transition rates were evaluated as

$$\omega = \omega_0 \exp\left(\frac{-\Delta G^\star(\sigma)}{k_B T}\right).$$

On the other hand, unlike SGR, Bulatov and Argon's model is lattice-based, and a Monte-Carlo method is used to determine the mesoscopic cell that will yield at

every step of the algorithm. More importantly, the elastic interactions due to the deformation of cells on the (hexagonal) lattice were computed, using Eshelby's inclusion procedure.

A numerical investigation of the model showed that, at high temperature, the simulated flow is homogeneous, because purely thermal activation is predominant, while collective effects and heterogeneities are more and more enhanced as the temperature declines.

6.5 THE SHEAR-TRANSFORMATION ZONE (STZ) THEORY

In the wake of Spaepen [1977]'s emphasis on free volume as a rearrangement facilitator, Falk and Langer [1998] suggested to describe the deformation of (model) metallic glasses by focusing on potential defects, *i.e.*, weak regions which are most susceptible to yield. These defects are characterised by a high weakness coefficient, *e.g.*, a large free volume density. An intensive parameter χ, called effective temperature, is introduced to measure the spatial variations of this weakness coefficient, that is, the extent of structural disorder. In analogy to thermodynamics, the density of potential defects is assumed to be proportional to the Boltzmann factor $\exp\left(-1/\chi\right)$.

Within each defect, thermally activated rearrangements ("shear transformations") can take place in any direction, but, for simplicity, only two directions, forwards (+) and backwards (-), are considered. The overall concentrations of $+$ and $-$ shear transformations, written n_+ and n_-, respectively, are central in the theory, because the strain rate itself is proportional to $n_+ - n_-$. These concentrations are not known *a priori*, but, under some physical assumptions, their rates of evolution $\dot{n}_\pm$ can be expressed; the expressions notably involve the rates of creation and annihilation of forwards/backwards defects, controlled by χ, and the stress-dependent $+/-$ inversion rates.

Finally, explicit couplings between flow defects are discarded in the theory, but the effective temperature χ is allowed to vary in time,[2] according to a specified equation of motion.

If the model parameters are correctly fitted, quantitative agreement with experimental data on strained metallic glasses is obtained [Langer, 2004].

6.6 HÉBRAUD-LEQUEUX'S MODEL AND RELATED MODELS BASED ON A LATENCY TIME

6.6.1 *The mean-field model*

Unlike the previous models, Hébraud and Lequeux [1998] investigate the zero temperature limit and therefore explicitly neglect thermal activation.

2. ... and in space if the model is spatially resolved [Manning et al., 2007].

The basic ingredients of their model are elastic blocks with a unique stress threshold σ_y. The macroscopic drive contributes to increasing the (scalar) stress carried by each block, linearly with time. Past the threshold σ_y, there is a finite rate of yield τ_{liq}^{-1}; in other words, past σ_y, it takes blocks an average time τ_{liq}, presumably set by dissipative forces, to yield. When a block yields, its stress is instantaneously redistributed to the rest of the medium (see Fig. 6.2a) and reset to zero locally.

Actually, the authors wanted to proceed analytically and to obtain a tractable equation operating on the probability distribution $P(\sigma, t)$. Since this endeavour would be forlorn with an exact computation of stress redistrubtion, they described this process in a mean-field-like way. In this approach, the redistributed stress following a rearrangement is a random quantity, centred around zero. This leads to a diffusive contribution $D\frac{\partial^2 P(\sigma,t)}{\partial \sigma^2}$ to $\frac{\partial P}{\partial t}$, where the diffusivity D is proportional to the global rate of rearrangements $\Gamma(t) \equiv \tau_{\text{liq}}^{-1} \int_{|\sigma'|>\sigma_y} P(\sigma', t) d\sigma'$, with a coefficient α, *i.e.*, $D(t) = \alpha\Gamma(t)$. Overall, the equation of evolution of the probability distribution reads:

$$\frac{\partial P(\sigma,t)}{\partial t} = -\mu\dot{\gamma}\frac{\partial P(\sigma,t)}{\partial \sigma} + D\frac{\partial^2 P(\sigma,t)}{\partial \sigma^2} - \frac{\Theta\left(|\sigma| - \sigma_y\right)}{\tau_{\text{liq}}} P(\sigma,t) + \Gamma(t)\delta(\sigma) \quad (6.3)$$

Here, μ is the shear modulus, Θ is the Heaviside function, and the last two terms on the rhs account for the process of yield and rebirth at zero stress, which occurs at a rate τ_{liq}^{-1} above σ_y.

Interestingly, in the quiescent state ($\dot{\gamma} = 0$), the model predicts a glass transition at a critical value of the coupling paramater, $\alpha_c = 1/2$. For $\alpha < 1/2$, the only steady-state solution is plastically inactive, with $\Gamma = 0$, hence $D = 0$, while a solution with $D > 0$ exists for $\alpha > 1/2$. Accordingly, the model describes a liquid state for $\alpha > 1/2$; under shear, the system in this regime exhibits a Newtonian flow curve, $\Sigma \sim \dot{\gamma}$. On the other hand, for $\alpha < 1/2$, a Herschel-Bulkley behaviour with a finite yield stress and an exponent $n = 0.5$ is obtained at small shear rates [Olivier, 2011].

6.6.2 *The Kinetic Elastoplastic theory*

Bocquet et al. [2009] took due notice of the analogy between the Hébraud-Lequeux equation (Eq. 6.3) and a Boltzmann equation. In this analogy, the term $D\partial^2_{\sigma^2} P(\sigma, t)$ in Eq. 6.3 plays the role of the Boltzmann collision term.

Beyond mean field, this collision term has no reason to be uniform in space; it should actually depend on the local rates of rearrangement, through elastic couplings, *viz.*,

$$D(\boldsymbol{r}, t) = f\left[\{\Gamma(\boldsymbol{r'}, t), \text{ for all } \boldsymbol{r'}\}\right],$$

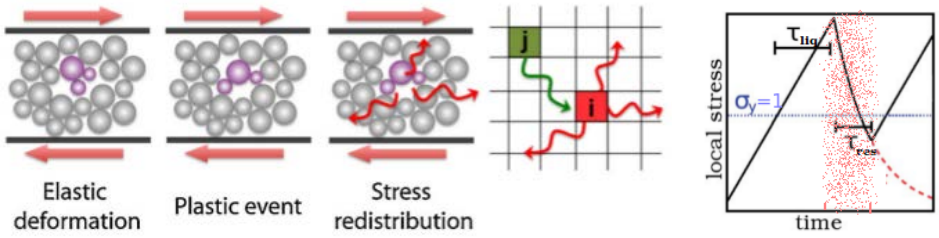

(a) Physical origin of stress redistribution.

(b) Life cycle of a block in Picard's model.

Figure 6.2: Alternation between elastic regime and plastic events. (a) Picture taken from Ref. [Bocquet et al., 2009]; (b) sketch adapted from from Ref. [Martens et al., 2012]. The plastic event is overlaid in red.

instead of depending only on the global one, $\Gamma(t)$. A low-order spatial expansion of f (*i.e.*, of the elastic interactions) yields

$$D(\boldsymbol{r},t) = \alpha\Gamma(\boldsymbol{r},t) + m\Delta\Gamma(\boldsymbol{r},t).$$

A diffusive term $m\Delta\Gamma(\boldsymbol{r},t)$ is thus added to the mean-field Hébraud-Lequeux picture, which leads to the prediction of spatial correlations in the flow. More precisely, Bocquet et al. [2009] showed that the fluidity $f \equiv \dot{\gamma}/\sigma$ then satisfies a diffusion equation,

$$f - f_b = \xi^2 \Delta f, \tag{6.4}$$

where the correlation length ξ is proportional to $\sqrt{\frac{m}{|\sigma-\Sigma_0|}}$ and f_b is the homogeneous ($m = 0$) solution given by the mean-field Hébraud-Lequeux model.

It turns out that the fluidity diffusion equation (Eq. 6.4) had already been used by Goyon et al. [2008] to describe the cooperative effects that they had observed in microchannel flows of concentrated emulsions. With well fitted parameters, this equation proved very successful in reproducing their experimental velocity measurements [Goyon et al., 2008, 2010, Geraud et al., 2013].

6.6.3 *Picard's two-time-scale model*

Picard et al. [2005] added two main refinements to this model, but jettisoned the analytical approach in favour of numerical simulations.

First, upon yielding, blocks no longer have their stresses instantaneously brought to zero, but relax exponentially, with a characteristic time scale τ (in practice, $\tau = \tau_{\text{liq}}$). The rate of recovery of the elastic regime is τ_{res}^{-1}, so that the average duration of a plastic event is the restructuring time τ_{res}, which is an additional model parameter. The use of (fixed) rates, instead fixed durations, introduces a simple element of stochasticity in the model, and is believed to indirectly account for the variability of local environements. The life cycle of an elastoplastic block is sketched in Fig. 6.2b.

Secondly, stress redistribution is now explicitly computed, with the help of an Eshelby-like propagator (see Chapter 8), which should provide a much more faithful account of spatial correlations and which renders parameters α and m superfluous .

Numerical simulations have revealed a complex spatiotemporal behaviour in slow flow, which fades into a more homogeneous picture as the shear rate is increased [Picard et al., 2005]. In Ref. [Martens et al., 2012], the model was shown to exhibit permanent shear localisation at low shear rates, when the restructuring time is long. As the Picard model will be used as both a starting point and a benchmark in the following, these flow properties will be discussed in greater detail in the next chapters.

Nevertheless, it can already be pointed out that, in Picard's model as well as in Hébraud-Lequeux's theory and its extension by Bocquet *et al.*, the origin of the stress increase with the shear rate resides in the latency time τ_{liq} prior to yield, during which blocks continue to accumulate elastic strain, *although* their yield stress has already been overcome. Annoyingly, this aspect can hardly be justified within a PEL perspective.

7

IDENTIFICATION OF THE RELEVANT PROCESSES IN THE RHEOLOGY OF ATHERMAL SOLIDS

The review of elastoplastic models conducted in the previous chapter has revealed that the apparent unity of the elastoplastic description is shattered by the diversity of the physical ingredients that are used in practice. Here, we aim to identify the physical processes that may be relevant for the bulk rheology, on a theoretical basis, with the perspective to get a clearer view on the choice of model ingredients.

7.1 RELEVANT TIMESCALES FOR THE BULK RHEOLOGY

The flow curve is central in rheology. Since it quantifies the dependence of the macroscopic stress on the driving *velocity*, we first enquire into temporal aspects.

7.1.1 *Two timescales in the limit* $\dot{\gamma} \to 0$

Consider a dense packing of particles confined between parallel walls and subject to a (macroscopically) constant shear rate $\dot{\gamma}$, imposed through successive infinitesimal displacements of one of the walls. We start the discussion with an enumeration of the timescales that subsist in the limit of vanishing shear rate. To do so, we focus on a "mesoscopic" region of the typical size of a plastic event.

First in line comes the timescale(s) for thermally-activated structural relaxation, τ_T, which diverges in the athermal limit.

Secondly, the response of the region of interest to a small displacement of the wall can take a finite time, τ_{pl}. This time essentially combines the duration of a local rearrangement, *i.e.*, the time needed to dissipate the elastic energy that was stored locally [Nicolas and Barrat, 2013b, Ikeda et al., 2012], with the delay for shear signal transmission within one avalanche [Chattoraj et al., 2011].

τ_T and τ_{pl} are the only potentially relevant timescales when $\dot{\gamma} \to 0$. Within a potential energy landscape (PEL) description, they are associated with thermally-activated hops between energy (meta)basins, and descents towards the local minimum, respectively.

7.1.2 *The quasi-static limit and beyond*

The application of a *finite* shear rate introduces a new timescale, $\dot{\gamma}^{-1}\gamma_y$, which is the duration of the elastic loading phase prior to yield. In the PEL viewpoint, this is also the "refresh rate" of the PEL topology, owing to changes in the boundary conditions.

As stated by Maloney and Lemaître [2006], quasistatic simulations, which perform an energy minimisation after each strain increment, rely on the following separation of the material and driving timescales:

$$\tau_{\text{pl}} \lll \gamma_y \dot{\gamma}^{-1} \lll \tau_T. \tag{7.1}$$

As long as Eq. 7.1 holds, *the system will follow the very same trajectory in phase space as a function of the strain* $\gamma \equiv \dot{\gamma} t$, regardless of the shear *rate*, thereby yielding a constant elastic stress σ_{el}. One should now recall that, for a solid-like material at low shear rate, the elastic stress dominates the total stress Σ to such an extent that the dissipative contribution to the stress is often discarded in computer simulations, *viz.*, $\Sigma \approx \sigma_{\text{el}}$, [Tighe et al., 2010] and can therefore be dismissed as a candidate for effecting the stress increase. This point is substantiated by the large discrepancy between the low-frequency loss and storage moduli in these materials, which differ by at least one order of magnitude in a liquid foam, for instance [Cohen-Addad et al., 1998].

Accordingly, the only way to recover a non constant flow curve $\Sigma(\dot{\gamma})$ involves the breakdown of the timescale separation (Eq. 7.1). In accordance with this deduction, Ikeda et al. [2012, 2013] recently showed that two rheological regimes can be distinguished, depending on whether $\dot{\gamma}^{-1} \gg \tau_T$ ("glassy rheology"), or not ("jammed, or athermal, rheology") .

7.1.3 *Limitations of the foregoing discussion*

Before we start exploring these two regimes, let us point out some limitations of the foregoing discussion. First, ageing effects that are not reducible to hops in the considered PEL ("coarsening") have been left aside so far. In liquid foams, *e.g.*, Gillette shaving foam, coarsening originates from gas diffusion between particles, drainage, and bubble coalescence, and it was shown to affect the linear viscoelastic properties of the material [Cohen-Addad et al., 1998]. But, a few minutes after the foam has been sprayed, the evolution occurs over timescales significantly longer than the values of $\gamma_y \dot{\gamma}^{-1}$ probed experimentally.

Secondly, the reference to a *single* timescale τ_T (or τ_{pl}) sounds of the utmost naïvety: one does indeed expect *distributions* of such timescales. But this hardly affects the arguments exposed above: Writing, e.g., $\gamma_y \dot{\gamma}^{-1} \lll \tau_T$ was just a convenient way to indicate that values $\tau_T < \gamma_y \dot{\gamma}^{-1}$ can be neglected in the distribution. The fact that that τ_{pl} may actually cover a broad spectrum of relaxation timescales (as evidenced, *e.g.*, in foams [Buzza et al., 1995, Cohen-Addad et al., 1998]) shall however prove important in Chapter 11.

7.2 ATHERMAL REGIME

7.2.1 *An interplay between the drive and (cascades of) rearrangements*

By definition, the athermal limit dictates $\tau_T \to \infty$. Consequently, to break the separation of timescales (Eq. 7.1), the driving timescale $\gamma_y \dot{\gamma}^{-1}$ must interfere with the distribution of τ_{pl}. ***In other words, the flow curve results from an interplay between the drive and the (cascades of) localised rearrangements***.

In granular media or suspensions of hard particles, the interplay is quantified by a dimensionless inertial or viscous number [da Cruz et al., 2005, Boyer et al., 2011]. More generally, the descent towards the energy minimum of the system is disrupted by the external drive. The impossibility for the system to fully relax between strain increments (see Fig.1(right) in Ref. Tsamados [2010]) is reflected, for instance, by the variations of the mean particle overlaps with the shear rate. Near the jamming transition, these variations are correlated to the flow curve [Olsson and Teitel, 2012]. Deeper in the solid phase, strain accumulation during the propagation of shear waves sets a shear-rate dependent upper bound on the spatial extent of the avalanches observed in athermal particle-based simulations [Lemaître and Caroli, 2009]. Some authors [Lemaître and Caroli, 2009, Fusco et al., 2014] claim that the macroscopic stress evolution is a direct consequence of this variation of avalanche sizes with the shear rate. [1]

However, a survey of existing elastoplastic models designed for the low-temperature regime reveals that they very generally fail to describe this disruption of plastic events through the drive. For instance, we have already noted that the origin of the stress increase in Hébraud-Lequeux's model or the related Picard model is the very questionable latency time τ_{liq}. To remedy this deficiency, we shall introduce new dynamical rules in Chapter 9, giving a more realistic reflection of the physical processes at play.

7.2.2 *Athermal materials?*

The recipe to make an athermal material *in silico* is pretty simple: thermal fluctuations are simply removed from the equation of motion. But what materials can be considered athermal in nature?

Foams and, to a lesser extent, emulsions made of large droplets are the paradigmatic examples of athermal solids, and are indeed classified as jammed, by opposition to glassy, in Ref. [Ikeda et al., 2013]. However, the possible occurrence of coarsening somewhat taints the athermal picture: these materials, too, age.

Ageing is also observed in granular matter. On top of that, although thermal fluctuations are almost systematically assumed to be negligible because of the size of the grains, in Appendix 7.5.1 we list a few arguments that might cloud this evidence for granular matter, especially under shear.

1. This claim will be questioned in Chapter 17.

7.3 THERMAL REGIME AND AGEING

Let us now turn to materials with significant thermal fluctuations, but still considerably below the glass transition temperature.

Schall et al. [2007] show that their slowly sheared colloidal suspensions fall into this category, through an assessment of the typical activation energy: plastic events are mostly of thermal origin, but the stress slightly biases the probabilities of shear transformations in one direction.

Let me mention that, in the presence of thermally activated rearrangements, the existence of a yield stress in the mathematical limit $\dot{\gamma} \to 0$ is rather unexpected (if it does indeed exist): suppose that the thermally activated escape from an energy (meta)basin takes a typical time τ_T; then, the elastic strain that is built up prior to plastic relaxation scales with $\dot{\gamma}\tau_T$, which goes to zero in the limit of vanishing shear rates.[2] The paradox is solved by calling back to mind Bouchaud's trap model or the SGR picture (see Sections 1.4.2 and 6.4): as time passes, the system ages and τ_T diverges, at vanishing shear rates. These remarks are vested with special importance for elastoplastic modelling: they imply that, to describe the rheology of *thermal* systems, even a minimal model ought to include an ageing process, at least in an *ad hoc* way..

In Chapter 9, numerical simulations of our model will allow us to investigate further aspects of the ageing regime.

Clearly, a crossover exists between the athermal limit and the thermal regime. It is noteworthy that changes in the scalings of the shear stress and the shear moduli associated with this crossover region have been reported experimentally [Basu et al., 2014, Nordstrom et al., 2010] and numerically [Ikeda et al., 2013].

7.4 DESCRIPTION OF THE STRESS RELAXATION DURING A PLASTIC EVENT

Having discussed rheologically relevant timescales on the basis of very general arguments, we are now intent on understanding the origin of the relaxation timescale during a plastic event in a more concrete situation. To do so, we develop a continuum mechanics-based framework.

2. In mode-coupling theory, the ideal glass does not age, but there are no activated processes either...

7.4.1 *A Hookean medium*

Modelling the elastic regime should pose no serious problem. In that case, the stress tensor $\underline{\underline{\Sigma}}$ is simply related to the linearised elastic deformation tensor $\underline{\underline{E}} \equiv \frac{\nabla u + \nabla u^\top}{2}$ *via* Hooke's law,

$$\underline{\underline{\Sigma}} = \underline{\underline{\underline{\underline{C}}}}\,\underline{\underline{E}}, \tag{7.2}$$

where $\underline{\underline{\underline{\underline{C}}}}$ is a fourth-rank tensor called the stiffness tensor.[3] In two dimensions,[4] it is usually convenient to extract the deviatoric part $\underline{\underline{\sigma}}$ from the total stress tensor $\underline{\underline{\Sigma}}$ through the introduction of the isotropic pressure $p \equiv -\mathrm{Tr}\,\underline{\underline{\Sigma}}/d$, where $d = 2$ is the dimension of space, *viz.*,

$$\underline{\underline{\Sigma}} = \underline{\underline{\sigma}} - p\underline{\underline{\mathbb{I}}},$$

where $\underline{\underline{\mathbb{I}}}$ is the identity matrix. Similarly, the contraction/dilation component $\epsilon^{\mathrm{vol}} \equiv \mathrm{Tr}\,\underline{\underline{E}}/d$ can be subtracted from the linear deformation tensor to obtain $\underline{\underline{\epsilon}} \equiv \underline{\underline{E}} - \epsilon^{\mathrm{vol}}\underline{\underline{\mathbb{I}}}$. It is noteworthy that, for an incompressible material, $0 = \nabla \cdot \boldsymbol{u} = \mathrm{Tr}\,\underline{\underline{E}} = \epsilon^{\mathrm{vol}} d$, therefore $\underline{\underline{E}}$ reduces to its deviatoric part $\underline{\underline{\epsilon}}$. With these notations and making the assumption that the material is isotropic, Hooke's law (Eq. 7.2) turns into

$$\underline{\underline{\sigma}} = 2\mu\underline{\underline{\epsilon}},$$

$$\text{i.e.,} \quad \begin{pmatrix} \frac{\sigma_{xx}-\sigma_{yy}}{2} & \sigma_{xy} \\ \sigma_{xy} & \frac{\sigma_{yy}-\sigma_{xx}}{2} \end{pmatrix} = 2\mu \begin{pmatrix} \frac{\epsilon_{xx}-\epsilon_{yy}}{2} & \epsilon_{xy} \\ \epsilon_{xy} & \frac{\epsilon_{yy}-\epsilon_{xx}}{2} \end{pmatrix},$$

where we have introduced the shear modulus μ. Mechanical equilibrium then states

$$\begin{aligned} \nabla \cdot \underline{\underline{\sigma}} - \nabla p &= \mathbf{0} \\ 2\mu \nabla \cdot \underline{\underline{\epsilon}} - \nabla p &= \mathbf{0}. \end{aligned} \tag{7.3}$$

To insist on the fact that Eq. 7.3 describes the elastic state of the system prior to the perturbations induced by an upcoming plastic event, let us add (0) superscripts to the variables

$$2\mu \nabla \cdot \underline{\underline{\epsilon}}^{(0)} - \nabla p^{(0)} = \mathbf{0}.$$

3. To avoid confusion regarding the tensor ranks, distinct notations for fourth-rank tensors (*e.g.*, $\underline{\underline{\underline{\underline{C}}}}$) , second-rank tensors (*e.g.*, $\underline{\underline{E}}$), and vectors (*e.g.*, $\boldsymbol{u}$) are temporarily used.

4. Although the expressions are formally simpler in two dimensions, the reasoning also holds in three dimensions, with no significant alteration.

7.4.2 *Deformation of a fluid-like plastic inclusion*

Clearly, Hooke's law will only hold to a certain extent. Indeed, when the configuration is too strained locally, say, in a region $\mathcal{S}$, particles will rearrange so that the system evolves into a new local minimum: this is a plastic event.

While this rearrangement occurs, the memory of the reference elastic configuration is lost, and, consequently, the local elastic stress vanishes. The region undergoing the rearrangement is therefore a fluid-like inclusion in an elastic medium. It follows that its stress is mainly dissipative, and elastic forces shall be neglected in the inclusion for the entire duration of the plastic event. In the overdamped regime, force balance during the plastic rearrangement reads

$$\begin{cases} \nabla \cdot \underline{\underline{\sigma}}^{\text{diss}} - \nabla p = \mathbf{0} & \text{in region } \mathcal{S}, \\ 2\mu \nabla \cdot \underline{\underline{\epsilon}} - \nabla p = \mathbf{0} & \text{outside } \mathcal{S}. \end{cases} \tag{7.4}$$

Here, the dissipative stress $\underline{\underline{\sigma}}^{\text{diss}}$ was supposed to be concentrated in the rearranging region. For simplicity, we further assume that dissipation is linear with respect to the strain rate, *viz.* $\underline{\underline{\sigma}}^{\text{diss}} = 2\eta_{\text{eff}}\, \underline{\underline{\dot{\epsilon}}}$. This linearity is naturally to be understood as a simplification, and not as a claim of the existence of some universality regarding the dissipative mechanism (see Ref. [Le Merrer et al., 2012] for a non-linear law in the case of a foam). In addition to Eqs. 7.4, mechanical equilibrium requires the continuity of the stress vector $\underline{\underline{\sigma}} \cdot \boldsymbol{n}$ across the boundary of region $\mathcal{S}$, of normal $\boldsymbol{n}$. If $\mathcal{S}$ is small enough so that the (plastic) deformation rate in this region can be considered homogeneous, *i.e.*, $\underline{\underline{\epsilon}}\,(r) \equiv \underline{\underline{\epsilon}}_{\text{in}}$ for $\boldsymbol{r} \in \mathcal{S}$, the continuity of stress[5] all along the boundary $\partial\mathcal{S}$ of $\mathcal{S}$ leads to:

$$2\eta_{\text{eff}}\, \underline{\underline{\dot{\epsilon}}}_{\text{in}} = 2\mu \underline{\underline{\epsilon}}_{\partial\mathcal{S}} \tag{7.5}$$

$$\underline{\underline{\dot{\epsilon}}}_{\text{in}} = \frac{1}{\tau} \underline{\underline{\epsilon}}_{\partial\mathcal{S}}, \tag{7.6}$$

where $\underline{\underline{\epsilon}}_{\partial\mathcal{S}}$ refers to the (elastic) strain on the boundary $\partial\mathcal{S}$ surrounding the plastic inclusion. The timescale $\tau \equiv \frac{\eta_{\text{eff}}}{\mu}$ for the viscous dissipation of the elastic energy has been made apparent. One should already note that, in this continuum description, the deformation tensor will not be continuous across the boundary $\partial\mathcal{S}$.

Comment on the neglect of dilational effects in the model

The present treatment does not describe the dilational effects that may take place during plastic events or the deformation field thereby induced. In metallic glasses, the volume change in the activated state (at the saddle point) may however be determinant in the evaluation of the associated energy barrier E_y [Schuh

5. We have assumed that the isotropic pressure p, which is associated to volumetric changes, remains continuous across the boundary $\partial\mathcal{S}$. This assumption is debatable in cases where significant dilation is observed in plastic regions.

et al., 2007]. Nevertheless, since the physical origin of energy barriers, or, equivalently, yield stresses, need not be specified in elastoplastic models, one might argue that this local dilational effect is included implicitly in E_y.

On the other hand, free volume diffusion due to local dilations is clearly discarded in the model, although, in metallic glasses, it is believed be connected with strain localisation [Manning et al., 2007, Bokeloh et al., 2011].

For soft jammed materials at high density, *e.g.*, concentrated emulsions, these dilational effects are arguably secondary, insofar as the flow is not accompanied by any observable variation in the local volume fractions [Goyon et al., 2008, Chaudhuri et al., 2012].

7.4.3 *Counter-reaction of the elastic medium*

Equation 7.6 entails a deformation of the incluson $\mathcal{S}$. But, since the inclusion is embedded in an elastic medium, its deformation induces additional elastic strain and pressure fields, $\underline{\underline{\epsilon}}^{(1)}(\boldsymbol{r})$ and $p^{(1)}(\boldsymbol{r})$, in the surrounding medium. Because the problem under consideration is purely linear, for any $\boldsymbol{r} \notin \mathcal{S}$, there exists a fourth-rank tensor $\underline{\underline{\underline{\underline{\mathcal{G}}}}}(\boldsymbol{r})$ relating the strain increment (per unit time) to the deformation of the boundary $\partial\mathcal{S}$ (per unit time), *viz.*,

$$\dot{\underline{\underline{\epsilon}}}^{(1)}(\boldsymbol{r}) = \underline{\underline{\underline{\underline{\mathcal{G}}}}}(\boldsymbol{r}) \dot{\underline{\underline{\epsilon}}}_{\text{in}}. \tag{7.7}$$

Moving back to the vicinity of region $\mathcal{S}$, if the inclusion is small enough and can be considered circular, the strain field increment will be approximately uniform at its outer boundary $\partial\mathcal{S}$. Its value obeys

$$\dot{\underline{\underline{\epsilon}}}^{(1)}_{\partial\mathcal{S}} = -g_0 \dot{\underline{\underline{\epsilon}}}_{\text{in}}, \tag{7.8}$$

where g_0 is a scalar (and not a tensor) because of symmetry arguments. Moreover, since the induced strain is a *counter-reaction* to the elastic stress applied on the boundary $\partial\mathcal{S}$, it will be of opposite sign, hence $g_0 < 0$. This is most easily understood in a one-dimensional geometry, as sketched in Fig. 7.1. Combining Eq. 7.8 with Eq. 7.6 and noting that $\dot{\underline{\underline{\epsilon}}}^{(1)}_{\partial\mathcal{S}} = \dot{\underline{\underline{\epsilon}}}_{\partial\mathcal{S}}$ because $\underline{\underline{\epsilon}}^{(0)}$ is constant, one finally arrives at

$$\dot{\underline{\underline{\epsilon}}}_{\partial\mathcal{S}} = \frac{-g_0}{\tau} \underline{\underline{\epsilon}}_{\partial\mathcal{S}}. \tag{7.9}$$

Equation 7.9 expresses the fact that the force driving the rearrangement is the elastic stress imposed on $\mathcal{S}$ by the rest of the system, and that, in opposing this force, dissipation sets a *finite* timescale τ to the plastic transformation,[6] up to a geometric prefactor g_0. Remarkably, Cloitre et al. [2003] suggested that the duration of a rearrangement in soft colloidal pastes coincides with the shortest structural relaxation time τ_β, which also results from a "competition between

6. The *finite* duration of a plastic rearrangement, which is neglected in SGR, the Kinetic Elastoplastic model [Bocquet et al., 2009], as well as in the mesoscopic models of Refs. [Baret et al., 2002, Homer and Schuh, 2009], might be key to understanding the compressed exponential relaxation of different soft materials. For details, see Refs. [Bouchaud, 2008, Ferrero et al., 2014].

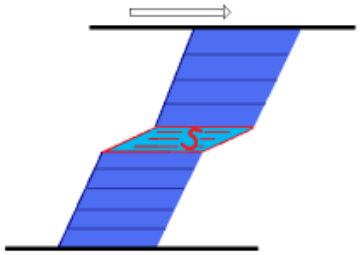

Figure 7.1: Sketch of a one-dimensional fluid inclusion $\mathcal{S}$ in an elastic medium. Since the inclusion deforms in reaction to the elastic stress to which it is subject, the effect of the deformation is to reduce the elastic stress in the vicinity of the inclusion, hence $g_0 < 0$ (see text).

elastic restoring forces and interparticle friction", and experimentally confirmed the proposed scaling $\frac{\eta_{\text{eff}}}{\mu}$ for the latter time. This scaling was also used to collapse flow curves onto a single master curve, which bolsters its relevance for the rheology of these materials. Moreover, Cohen-Addad et al. [1998] have introduced the same characteristic time $\tau = \frac{\eta_{\text{eff}}}{\mu}$ for the relaxation of weak inclusions in a coarsening liquid foam.

One is now left with the evaluation of the elastic propagator $\underline{\underline{\mathcal{G}}}(\boldsymbol{r})$ introduced in Eq. 7.7, which is one of the topics of the next chapter.

Key Points of the Chapter

- In athermal amorphous solids, the non constant flow curve results from an interplay between the external drive and (cascades of) localised rearrangements.
- During a rearrangement, the driving force, which is the elastic strain imposed at the boundary of the plastic inclusion, is opposed by dissipative forces (in the overdamped regime).
- The deformation of the inclusion lowers the driving force at the boundary; and a timescale set by dissipative forces is made apparent in the overdamped regime.

A

7.5 APPENDICES

7.5.1 *Is granular matter athermal?*

Are thermal fluctuations truly negligible in (sheared) granular media?

The mechanical properties of densely packed granular matter mostly originate in the contacts between grains.

But contacts between surfaces (and hence the friction coefficient) are known to mature with time, through a slow (logarithmic) increase of the contact area [Persson, 1999]. This increase results from the thermally activated nucleation of "joints" [Bureau et al., 2002]. For granular matter, these joints may be moisture-induced water bridges between grains [Bocquet et al., 1998]. As a complementary, or alternative, explanation, nonlinear acoustic measurements suggest that macroscopic contacts may age *via* the thermal rearrangement of the nanoscale contacts that form them (the failure of these nanocontacts is even claimed to be a precursor of macroscopic failure) [Zaitsev et al., 2008, 2014].

Additionally, granular media are sensitive to environmental fluctuations, such as mechanical vibrations or (repeated) variations of the temperature [Divoux et al., 2008], and we expect this sensitivity to be heightened when the (pre-sheared) material is on the brink of failure.

These different effects have the potential to explain the following paradox: granular contacts involve energies far larger than the thermal energy $k_B T$, so one would expect them to either fail immediately or resist forever upon the application of a force. Contrary to this intuition, pre-sheared granular media relax over surprisingly long timescales, with some rearrangements that were reported to occur hours after shear cessation [Hartley and Behringer, 2003].

On a more general note, it is important to realise that macroscopic failure can be greatly facilitated if it is mediated by cascading (asymmetric) microscopic processes, whether it be the formation of capillary bridges or the failure of nanocontacts. Thermal fibre bundle models (see Appendix 7.5.2) exemplify this effect, in the limit of fully irreversible microscopic failures.

Nevertheless, even if thermal fluctuations may indeed have a visible macroscopic effect on granular matter in some situations, it is dubious that temperature might significantly impact their rheology.

As an incidental remark, the foregoing discussion has underscored how interwoven tribology and the rheology of amorphous solids are [Bureau et al., 2002]; in particular, mean-field theories in the two fields bear striking resemblance. To convince himself or herself, the reader may simply compare the equations of the Hébraud-Lequeux model or SGR with Persson's[7] theory of friction [Persson, 1995, 1999]. The resemblance is even more striking in the case of SGR's transposition to granular media through the substitution of the stress ensemble for

7. The similarity was pointed out to me by Prof. Lydéric Bocquet.

the energy ensemble [Behringer et al., 2008, Bi and Chakraborty, 2009], and it is then hardly a surprise that both theories yield identical predictions, namely, $\Sigma - \Sigma_0 \sim \ln(\dot{\gamma})$, where $\dot{\gamma}$ is either the shear rate or the sliding velocity.

7.5.2 *Thermal fibre bundle models (or: why do firs break long after they have been covered with snow?)*

If the failure of a macroscopic contact is mediated by essentially irreversible microscopic processes, such as the failure of nanocontacts, then thermal fluctuations may play a decisive role. We purport to illustrate this with a simple fibre bundle model in which fibres may (irreversibly) break under the load they bear.

We should however emphasise that, insofar as the explanation is of quite general scope, similar models have already been proposed, and studied both more rigorously and in greater detail in the literature. In particular, disorder in the yield stresses of individual fibres was shown to lower the effective yield stress, or, equivalently, increase the effective activation temperature [Roux, 2000, Politi et al., 2002].

Let us consider a bond of yield energy $E_y \gg kT$, bearing a total load/energy E. Now, suppose that the bond is actually a bundle made of n microscopic bonds, of yield energy E_y/n each, and each bearing an energy E/n.

The yield rate of a microscopic bond is initially: $f = \exp\left(\beta \frac{E-E_y}{n}\right)$, where $\beta \equiv (kT)^{-1}$.

If $f \ll 1$, the first microscopic bond will break after time

$$\tau_1 = \frac{1}{n} \exp\left(\beta \frac{E_y - E}{n}\right),$$

and the load it used to bear will then be distributed among the surviving bonds, so that the second rupture will occur after a time

$$\tau_2 = \frac{1}{n-1} \exp\left(\beta \left(\frac{E_y}{n} - \frac{E}{n-1}\right)\right).$$

It immediately follows that total failure will occur at time

$$T = \sum \tau_i = \sum_{i=0}^{n-1} \frac{1}{n-i} \exp\left(\beta \left(\frac{E_y}{n} - \frac{E}{n-i}\right)\right).$$

Approximating the sum with an integral gives

$$\begin{aligned} T - \tau_{n-1} &\sim \int_{x=1/2}^{n-1/2} \frac{1}{n-x} \exp\left(\beta\left(\frac{E_y}{n} - \frac{E}{n-x}\right)\right) dx. \\ &\sim \exp\left(\beta\frac{E_y}{n}\right) \int_{y=1/2}^{n-1/2} \frac{\exp\left(-\beta\frac{E}{y}\right)}{y} dy \\ &\sim \exp\left(\beta\frac{E_y}{n}\right) \int_{z=\frac{1}{n-0.5}}^{2} \frac{\exp\left(-\beta E z\right)}{z} dz. \end{aligned}$$

Finally,

$$\begin{aligned} T &\sim \exp\left(\beta\frac{E_y}{n}\right) \int_{\frac{\beta E}{n-0.5}}^{\beta E} \frac{\exp\left(-\zeta\right)}{\zeta} d\zeta. \\ &\ll \exp\left[\beta\left(E_y - E\right)\right] \text{ for large } n. \end{aligned}$$

In conclusion, failure can be enormously accelerated if it is mediated by *irreversible* "microscopic" processes.

8

METHODS

In the previous chapter, we have highlighted key processes in the flow of glassy or jammed materials. These key processes should be the building blocks of any realistic mesoscopic model. Among them, the non-local phenomenon of stress redistribution is at the origin of avalanches of plastic events and correlations. In this chapter, the elastic propagator $\underline{\underline{\mathcal{G}}}(\boldsymbol{r})$ introduced in Eq. 7.7 and governing stress redistribution in a uniform elastic medium is derived, following (and extending) the calculations of Ref. [Picard et al., 2004]. In addition, technical details pertaining to the implementation of a lattice-based elastoplastic model are provided.

8.1 GENERAL ALGORITHM

First, we summarise the general algorithm.

The material is discretised into a regular square lattice of $N = L \times L$ elastoplastic blocks, labelled (i, j), of the typical size of an elementary shear rearrangement. In a time step of duration dt, each block receives a stress increment comprising a contribution $\dot{\boldsymbol{\Sigma}}_{\text{app}} dt$ from the macroscopic drive and a contribution from plastic events, *viz.*,

$$\partial_t \boldsymbol{\sigma}(i,j;t) = \dot{\boldsymbol{\Sigma}}_{\text{app}} + 2\mu \sum_{i'=1}^{L} \sum_{j'=1}^{L} \boldsymbol{\mathcal{G}}\left(i-i', j-j'\right) \cdot \dot{\boldsymbol{\epsilon}}^{\mathbf{pl}}(i',j';t), \tag{8.1}$$

where $\dot{\boldsymbol{\Sigma}}_{\text{app}}$ is the contribution from the macroscopic drive (in simple shear, the only nonzero component of $\dot{\boldsymbol{\Sigma}}_{\text{app}}$ will be $\mu\dot{\gamma}$), and $\dot{\boldsymbol{\epsilon}}^{\mathbf{pl}}(i,j;t) = \boldsymbol{\sigma}(i,j;t)/2\mu\tau$ if block (i,j) is plastic, $\mathbf{0}$ otherwise. The second term on the rhs accounts for (both local and non-local) stress redistribution during plastic events. Regarding the local term, note that $\boldsymbol{\mathcal{G}}(0,0)$ will have negative eigenvalues, leading, as expected, to the relaxation of stress during plastic events; also note that, during these events, the local stress is of dissipative nature (see Eqs. 7.4 and 7.6).

The dynamical rules governing the alternation between the elastic regime and the plastic phase shall be specified later.

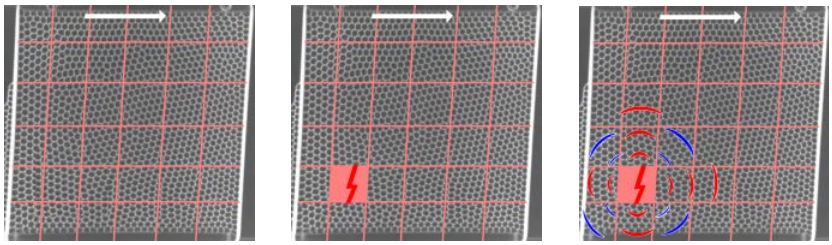

Figure 8.1: Modelling of a plastic event on a lattice.

8.2 DERIVATION OF THE ELASTIC PROPAGATOR IN A TWO-DIMENSIONAL UNIFORM ELASTIC MEDIUM

8.2.1 *Unbounded medium*

From Section 7.4.3, the elastic propagator $\underline{\underline{\underline{\underline{\mathcal{G}}}}}(\boldsymbol{r})$ is defined by the relation

$$\underline{\underline{\epsilon}}^{(1)}(\boldsymbol{r}) = \underline{\underline{\underline{\underline{\mathcal{G}}}}}(\boldsymbol{r}) \dot{\underline{\underline{\epsilon}}}_{\text{in}},$$

which solves the problem

$$\begin{cases} 2\eta_{\text{eff}} \nabla \cdot \dot{\underline{\underline{\epsilon}}}_{\text{in}} - \nabla p &= \mathbf{0} \text{ in region } \mathcal{S}, \\ 2\mu \nabla \cdot \underline{\underline{\epsilon}} - \nabla p &= \mathbf{0} \text{ outside } \mathcal{S} \\ 2\eta_{\text{eff}} \dot{\underline{\underline{\epsilon}}}_{\text{in}} &= 2\mu \underline{\underline{\epsilon}}_{\partial\mathcal{S}}, \end{cases} \tag{8.2}$$

where region $\mathcal{S}$ deforms with strain rate $\dot{\underline{\underline{\epsilon}}}_{\text{in}}$ and $\underline{\underline{\epsilon}}_{\partial\mathcal{S}} = \underline{\underline{\epsilon}}^{(0)}_{\partial\mathcal{S}} + \underline{\underline{\epsilon}}^{(1)}_{\partial\mathcal{S}}$. This decomposition highlights the fact that the "spontaneous" deformation of the boundary $\partial\mathcal{S}$ at a rate $\dot{\underline{\underline{\epsilon}}}^{\text{pl}} \equiv \underline{\underline{\epsilon}}^{(0)}_{\partial\mathcal{S}}/\tau$ is countered by the elastic reaction of the medium $\dot{\underline{\underline{\epsilon}}}^{(1)}$.

To a large extent, the problem formulated in Eqs. 8.2 is similar to Eshelby [1957]'s inclusion problem, except that the latter features an eigenstrain $\underline{\underline{\epsilon}}^{\star}$, *i.e.*, the spontaneous deformation that the inclusion would endure were it not constrained (hence, $\underline{\underline{\sigma}} = 2\mu(\underline{\underline{\epsilon}} - \underline{\underline{\epsilon}}^{\star})$), whereas the problem under consideration involves a plastic strain *rate* $\dot{\underline{\underline{\epsilon}}}^{\text{pl}}$.[1] To proceed, we resort once more to the linearity of the equations and the approximate circular symmetry of the inclusion to claim that, up to a hypothetical scalar factor that may anyway be absorbed in the timescale τ, the strain increments $\underline{\underline{\epsilon}}^{(1)} dt$ during time interval dt can be obtained

1. More rigorously, at any time, the strain field in the outer domain is the solution of an elastic problem with Neumann boundary conditions along $\partial\mathcal{S}$, namely, $2\mu \underline{\underline{\epsilon}}_{\partial\mathcal{S}} \cdot n = \underline{\underline{\sigma}} \cdot n$, where n is the normal vector to $\partial\mathcal{S}$ and $\underline{\underline{\sigma}}$ is the (uniform) stress in the inclusion. Therefore, it has a unique solution, regardless of the nature of the stress $\underline{\underline{\sigma}}$.

by replacing the plastic inclusion with an Eshelby-like inclusion of eigenstrain $\dot{\underline{\underline{\epsilon}}}^{\mathrm{pl}} dt$, *viz.*,

$$\begin{cases} 2\mu\nabla\cdot\left[\dot{\underline{\underline{\epsilon}}}^{(1)}(\boldsymbol{r}) - \dot{\underline{\underline{\epsilon}}}^{\mathrm{pl}}\Theta_{\mathcal{S}}(\boldsymbol{r})\right] - \nabla\dot{p}^{(1)}(\boldsymbol{r}) & = 0 \\ \nabla\cdot\dot{\boldsymbol{u}}^{(1)} = \mathrm{Tr}\left[\dot{\underline{\underline{\epsilon}}}^{(1)}\right] & = 0, \end{cases} \tag{8.3}$$

where the characteristic function $\Theta_{\mathcal{S}}$ takes the value of 1 inside the inclusion and 0 outside.

At this stage, let us remark that we can condense the notations for the stress and strain tensors as follows:

$$\underline{\underline{\epsilon}} \equiv \begin{pmatrix} \epsilon_{xx} & \epsilon_{xy} \\ \epsilon_{xy} & \epsilon_{yy} \end{pmatrix} \longrightarrow \boldsymbol{\epsilon} \equiv \begin{pmatrix} \frac{\epsilon_{xx}-\epsilon_{yy}}{2} \\ \epsilon_{xy} \end{pmatrix},$$

$$\underline{\underline{\sigma}} \equiv \begin{pmatrix} \sigma_{xx} & \sigma_{xy} \\ \sigma_{xy} & \sigma_{yy} \end{pmatrix} \longrightarrow \boldsymbol{\sigma} \equiv \begin{pmatrix} \frac{\sigma_{xx}-\sigma_{yy}}{2} \\ \sigma_{xy} \end{pmatrix} \text{ and } p \equiv -\frac{\sigma_{xx}+\sigma_{yy}}{2}.$$

Picard et al. [2004] solved the scalar version of Eqs. 8.3, thus obtaining the strain $\epsilon_{xy}^{(1)}$ induced by an eigenstrain $\dot{\boldsymbol{\epsilon}}^{\mathbf{pl}} = \begin{pmatrix} 0 \\ \epsilon_{xy}^{\mathrm{pl}} \end{pmatrix}$ aligned along the macrosopic shear direction, in the limit of a pointwise inclusion centred on the origin, *i.e.*, $\Theta_{\mathcal{S}}(\boldsymbol{r}) \to a^2\delta(\boldsymbol{r})$, in an incompressible medium. Here, we extend the derivation to tensorial strains and stresses.

Let us first drop the dots indicating time derivatives and the "(1)" superscripts denoting increments to the built-in elastic field, and recast Eqs. 8.3 as

$$\begin{cases} \mu\nabla^2\boldsymbol{u} - \nabla p & + \boldsymbol{f} = \boldsymbol{0} \\ \nabla\cdot\boldsymbol{u} & = 0, \end{cases} \tag{8.4}$$

where we have used the shorthand $\boldsymbol{f} \equiv -2\mu\nabla\cdot\left[\boldsymbol{\epsilon}^{\mathbf{pl}} a^2\delta(\boldsymbol{r})\right]$ and the equality $\nabla\cdot\left[\nabla\boldsymbol{u}^{\top}\right] = \partial_i\partial_j u_i = \partial_j\partial_i u_i = 0$ in the first line. Equations 8.4 define a well-known problem in hydrodynamics [Barthès-Biesel, 2010], whose solution is most conveniently expressed in Fourier space $\boldsymbol{q} = (q_x, q_y)$ with the help of the Oseen-Burgers tensor $\mathcal{O}(\boldsymbol{q}) = \frac{1}{\mu q^2}\left(\mathbb{I} - \frac{1}{q^2}\boldsymbol{q}\otimes\boldsymbol{q}\right)$, *viz.*,

$$\boldsymbol{u}(\boldsymbol{q}) = \mathcal{O}(\boldsymbol{q})\cdot\boldsymbol{f}(\boldsymbol{q}) = \frac{1}{2\mu q^2}\left(\mathbb{I} - \frac{1}{q^2}\boldsymbol{q}\otimes\boldsymbol{q}\right)\cdot\boldsymbol{f} \tag{8.5}$$

Finally, using $\boldsymbol{\sigma}(\boldsymbol{q}) = \mu i\,(\boldsymbol{q}\otimes\boldsymbol{u} + \boldsymbol{u}\otimes\boldsymbol{q}) - 2\mu\boldsymbol{\epsilon}^{\mathbf{pl}}$, we arrive at

$$\begin{pmatrix} \sigma_{xx} \\ \sigma_{xy} \end{pmatrix} = 2\mu\boldsymbol{\mathcal{G}}\cdot\begin{pmatrix} \epsilon_{xx}^{\mathrm{pl}} \\ \epsilon_{xy}^{\mathrm{pl}} \end{pmatrix} \tag{8.6}$$

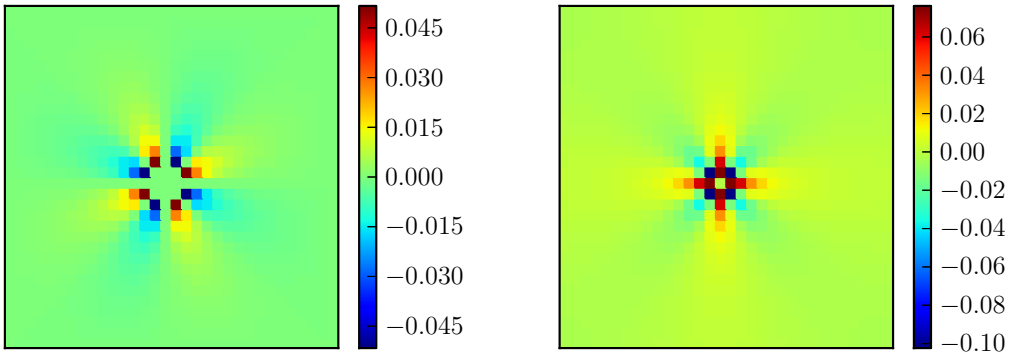

(a) σ_{xx} (b) σ_{xy}

Figure 8.2: Colour maps of the redistributed stress induced by a unit plastic strain along xy, localised at the origin. $N = 32 \times 32$. *(The central block is artificially coloured).*

where

$$\boldsymbol{\mathcal{G}} \equiv \frac{1}{q^4} \begin{bmatrix} -(q_x^2 - q_y^2)^2 & -2q_x q_y (q_x^2 - q_y^2) \\ -2q_x q_y (q_x^2 - q_y^2) & -4q_x^2 q_y^2 \end{bmatrix}. \tag{8.7}$$

The redistributed stress following a unit plastic event along xy, $\boldsymbol{\sigma} = 2\mu\boldsymbol{\mathcal{G}} \cdot (0\,1)^\top$, is shown in Fig. 8.2. As expected, the σ_{xy}-stress increment, $\mathcal{G}_{22}$, is identical to the *scalar* elastic propagator derived by *Picard et al. [2004]*. In real space, the elastic propagator coincides with the solution of Eshelby's inclusion problem in the limit of a pointwise inclusion, in an incompressible medium.

Incidentally, the assumption of isotropic elasticity could be questioned in the case of sheared granular media, which exhibit (anisotropic) force chains [Tordesillas et al., 2012] ; however, experimental observations support the existence of an Eshelby-like field [Le Bouil et al., 2014].

8.2.2 *Implementation*

At each time step, the redistributed strain $\underline{\underline{\epsilon}}^{(1)}$ given in Eq. 8.6 needs to be computed afresh.

To do so in a numerically efficient way, the (discretised) convolution in Eq. 8.1, *i.e.*, the second term on the rhs, is computed in Fourier space, with the expression of the elastic propagator $\boldsymbol{\mathcal{G}}$ given in Eq. 8.7. It is worth noting that, on a discrete lattice, only wavenumbers in the first Brillouin zone, *viz.*, $q_x, q_y \in]-\pi, \pi]$, will be relevant. In addition, periodicity will further restrict the nonzero Fourier modes to multiples of π/L.

For accuracy,[2] we resolve the stresses on a finer mesh, in which each elasto-plastic block is made of four subcells. This refinement of the grid somewhat

2. If the grid is not refined, the response field to $\epsilon_{xx}^{\mathrm{pl}}$ exhibits some numerical instability, with alternating blocks of "stronger" and "weaker" response, like a checkerboard.

affects stress redistribution in the near-field, also for the xy-component, but overall the effect on, *e.g.*, the flow curve (with the dynamical rules which will be introduced in Section 9.3) is relatively minor, albeit perceptible (*data not shown*). Also note that the computation of the elastic propagator in discrete space may slightly violate the equality of the streamline-averaged shear stresses imposed by static mechanical equilibrium. To recover strict mechanical equilibrium, we add a small *ad hoc* offset to each streamline at every time step. We checked that this procedure has only little impact on both the flow curve and the correlation functions.

The use of a Fast Fourier Transform routine leads to an algebraic speed up of the routine, insofar as each loop will only involve $\mathcal{O}\left(N \ln(N)\right)$ operations.

It should be pointed out that, because blocks have a finite size, the computation of the elastic response field based on Eq. 8.6 and the underlying assumption of pointwise plastic events actually miss some near field terms. We cannot exclude that this, in addition to the choice of a regular lattice, may induce numerical artifacts [Budrikis and Zapperi, 2013].

8.3 HOW TO ACCOUNT FOR CONVECTION

Although in reality shearing a material obviously leads to the displacement of material volumes, in our quest for minimalism we are tempted to discard these displacements and only consider the associated strains in each block. This crude simplification leads to a first class of models, called *static* here, in which elastoplastic blocks are pinned to a fixed position in space.

Convected models allow us to go beyond this simplification by accounting for the mechanically expected motion of the the blocks, albeit in a coarse manner, more precisely, only in the direction of the macroscopic flow. Because, to the best of my knowledge, we were the first to implement convection in an elastoplastic model, I will take the liberty to delve into the technical details of this aspect.

8.3.1 *Relative displacements of the streamlines*

In the continuum-mechanics based approach adopted here, notably in Section 8.2, the displacement (or velocity) field can be rigorously calculated at any position in space. However, in order to preserve the integrity of the lattice, blocks will not be displaced individually, but along with all other blocks on the same streamline, *i.e.*, at equal $y = y_0$. In other words, we shall incrementally shift streamlines in the flow direction x. Therefore, we can settle with the calculation

of the average (non-affine) displacement along x on streamline y_0 that is induced by plastic events, *viz.*,

$$\begin{aligned}\langle u_x \rangle_x (y_0) &\equiv L^{-1} \int u_x (x, y_0)\, dx \\ &= \sum_{q_y} u_x(q_x = 0, q_y) e^{i q_y y_0} \\ &= \sum_{q_y} \frac{-2i}{q_y} \epsilon_{xy}^{\mathrm{pl}} \left(q_x = 0, q_y\right) e^{i q_y y_0},\end{aligned}$$

where the sums run over all relevant wavenumbers $q_y = {}^{2\pi n}/_{L}$, $n \in \mathbb{Z}^\star$ and we have dropped the (1)-superscripts and the hats denoting Fourier transforms. To obtain the last equality, we have made use of Eq. 8.5. Finally, one arrives at,

$$\begin{aligned}\langle u_x \rangle_x (y_0) &= \sum_{q_y} \frac{-2i}{q_y} e^{i q_y y_0} \\ &\quad \times \left[L^{-1} \sum_{y_{ev}} \left\langle \epsilon_{xy}^{\mathrm{pl}}(x, y_{\mathrm{ev}}) \right\rangle_x e^{-i q_y y_{\mathrm{ev}}} \right] \\ &= \frac{-2i}{L} \sum_{y_{ev}} \left\langle \epsilon_{xy}^{\mathrm{pl}} \right\rangle_x (y_{\mathrm{ev}}) \sum_{q_y} \frac{e^{i q_y (y_0 - y_{\mathrm{ev}})}}{q_y} \\ &= \sum_{y_{ev}} \mathrm{sign}(y_0 - y_{ev}) \\ &\quad \times \left(1 - \frac{2\,|y_0 - y_{\mathrm{ev}}|}{L}\right) \left\langle \epsilon_{xy}^{\mathrm{pl}} \right\rangle_x (y_{\mathrm{ev}}),\end{aligned}$$

where the sum runs over all streamlines y_{ev} and, to get the last line, we have summed the second series over all $q_y = {}^{2\pi n}/_{L}$.

Whenever the cumulative displacement of a streamline in the flow direction reaches the size of a block, it is shifted. As a technical detail, note that we also regularly add a random displacement offset to *all* lines. Otherwise, lines with lower average *velocities* will be shifted less often than others and thus artificially pinned: they will tend to conserve their neighbours (in the velocity gradient direction) for a longer time - whereas the motion with respect to neighbouring lines should, in principle, be exclusively controlled by the local shear rate. It turns out that, in a simple shear situation, the system is quite sensitive to such a bias, which may lead 'pinned' lines to concentrate more plastic activity, and we have indeed observed this propensity of the plastic activity to localise on nearly immobile lines. The artifact vanishes when random displacement offsets are added to all lines, as explained above, and translational invariance is restored.

8.3.2 *Frame deformation*

There is an issue with the implementation of convection *via* incremental shifts of the streamlines, in the way that it has just been presented. Indeed, it creates a

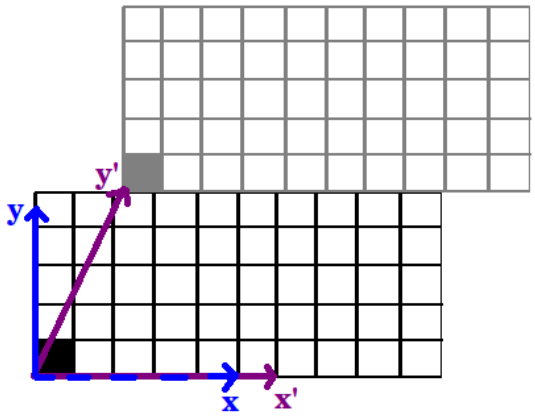

spurious discontinuity at the edge of the (periodic) simulation cell, because the "top" and "bottom" streamlines are shifted much more frequently with respect to one another than any other neighbouring streamlines. To remedy this, the whole simulation cell must to be deformed, in a fashion equivalent to Lees-Edwards boundary conditions in atomistic simulations: periodic replicas of the system in the velocity gradient-direction shall be displaced along the flow, while replicas in the flow direction remain unaffected. At a given time, the elastic propagator shall then be expressed in a deformed frame, with (contravariant) coordinates $(x', y') = (x - \gamma y, y)$, where γ is the average shear strain experienced by the cell. Here, unprimed quantities refer to the initial orthonormal frame. The corresponding transformation of the (covariant) Fourier wavenumbers reads $q' \equiv \left(q'_x, q'_y\right) = (q_x, q_y + \gamma q_x)$.

The metric tensor,

$$(g_{ij}) \equiv \frac{\partial s^k}{\partial s'^i}\frac{\partial s^l}{\partial s'^j}\delta_{kl} = \begin{pmatrix} 1 & \gamma \\ \gamma & 1+\gamma^2 \end{pmatrix}, \tag{8.8}$$

where $s = q$ or $s = (x, y)$, is a convenient tool to compute distances in the deformed frame; it relates covariant and contravariant quantities, $x'_j = g_{ij}x'^i$ as well as $q'_j = g_{ij}q'^i$, for $i, j \in \{x, y\}$. When $\gamma \neq 0$, the metric tensor g_{ij} differs from identity, so that $q'_i \neq q'^i$. Nevertheless, provided that this difference is accepted, Eq. 8.5 still holds, *viz.*

$$u'^i(q') = \frac{-2\mathrm{i}}{q'^4}\left[q'^2 q'_k \epsilon'^{\mathrm{pl}\,ki}(q') - q'^i q'_k q'_l \epsilon'^{\mathrm{pl}\,kl}(q')\right], \tag{8.9}$$

from which the strain tensor $\epsilon'^{ij} = \frac{q'^i u'^j + q'^j u'^i}{2}$ and the elastic (deviatoric) stress $\sigma'^{ij} = 2\mu\left(\epsilon'^{ij} - \epsilon^{\mathrm{pl}\,ij}\right)$ readily follow. Finally, the *components* of the stress tensor

(and not the *coordinates* of the points at which it is evaluated) are to be expressed in the original, orthogonal basis (x, y) , as follows:

$$\begin{aligned}\sigma^{ij}(q') &= \frac{\partial x^i}{\partial x'^r}\frac{\partial x^j}{\partial x'^s}\sigma'^{rs}(q') \\ &= \frac{2\mu}{q'^4}\Big[q'^2\left(\mathcal{A}_u\mathcal{P}^j\epsilon^{\mathrm{pl}\,ui}(q') + \mathcal{A}_u\mathcal{P}^i\epsilon^{\mathrm{pl}\,uj}(q')\right) \\ &- 2\mathcal{P}^i\mathcal{P}^j\mathcal{A}_u\mathcal{A}_v\epsilon^{\mathrm{pl}\,uv}(q')\Big] - 2\mu\epsilon^{\mathrm{pl}\,ij}(q'). \end{aligned} \tag{8.10}$$

Note that we have used the shorthands $q'^2 = q'_k q'^k = q^2$, $\mathcal{P}^i \equiv \frac{\partial x^i}{\partial x'^r} q^r$, and $\mathcal{A}_u \equiv \frac{\partial x'^k}{\partial x^u} q_k = \left(q_x, q_y - \gamma q_x\right)$.

Explicit evaluation of Eq. 8.10 with the metric tensor (Eq. 8.8) leads to our final result:

$$\begin{pmatrix} \sigma^{xx} \\ \sigma^{xy} \end{pmatrix}(q') = 2\mu\boldsymbol{\mathcal{G}}^{\infty} \cdot \begin{pmatrix} \epsilon^{\mathrm{pl}\,xx} \\ \epsilon^{\mathrm{pl}\,xy} \end{pmatrix}(q'), \tag{8.11}$$

with

$$\mathcal{G}^{\infty} \equiv \frac{1}{q'^4}\begin{bmatrix} -(q'^2_x - q^{(\gamma)\,2}_y)^2 & -2q'_x q^{(\gamma)}_y (q'^2_x - q^{(\gamma)\,2}_y) \\ -2q'_x q^{(\gamma)}_y (q'^2_x - q^{(\gamma)\,2}_y) & -4q'^2_x q^{(\gamma)\,2}_y \end{bmatrix} \tag{8.12}$$

and $q^{(\gamma)}_y \equiv \left(q'_y - \gamma q'_x\right)$.

With biperiodic boundary conditions, this propagator results in periodic images of the plastic events that are not aligned along the velocity gradient direction, but tilted with an "angle" γ.

Besides the (long-range) effect of these periodic images, the shape of the elastic propagator in real space should in principle be insensitive to the frame in which it is computed. However, we would like to indicate that the discrete nature and the symmetries of the meshgrid that we use introduce some near-field dependence of $\mathcal{G}^{\infty}$ on γ, up to a distance of few meshes away from the origin of the plastic event. It is therefore important to keep γ within a relatively narrow range, here, $[-1/2, 1/2]$, which is achieved thanks to the periodicity of the system in the flow direction.

A

8.4 APPENDIX

8.4.1 *Elastic propagator in three dimensions*

All the numerical work presented in this manuscript has been performed in two dimensions. Some of the scalings that we have observed, for instance that of the four-point stress susceptibility introduced in Chapter 12, would deserve to be checked in three dimensions (3D). But this extension naturally requires the derivation of the elastic propagator in 3D.

Here, I simply present the formulae associated therewith. [3]

Applying Eq. 8.5 to a 3D orthonormal frame, equipped with Fourier coordinates $\boldsymbol{q} \equiv (q_x, q_y, q_z)$, one gets

$$\boldsymbol{u}(\boldsymbol{q}) = \frac{-2i}{q^2} \begin{pmatrix} q_x \epsilon^{\mathrm{pl}}_{xx} + q_y \epsilon^{\mathrm{pl}}_{xy} + q_z \epsilon^{\mathrm{pl}}_{xz} - \frac{q_x}{q^2}\mathcal{A} \\ q_x \epsilon^{\mathrm{pl}}_{xy} + q_y \epsilon^{\mathrm{pl}}_{yy} + q_z \epsilon^{\mathrm{pl}}_{yz} - \frac{q_y}{q^2}\mathcal{A} \\ q_x \epsilon^{\mathrm{pl}}_{xz} + q_y \epsilon^{\mathrm{pl}}_{yz} + q_z \epsilon^{\mathrm{pl}}_{zz} - \frac{q_z}{q^2}\mathcal{A} \end{pmatrix}$$

where

$$\mathcal{A} \equiv q_x^2 \epsilon^{\mathrm{pl}}_{xx} + q_y^2 \epsilon^{\mathrm{pl}}_{yy} + q_z^2 \epsilon^{\mathrm{pl}}_{zz} + 2q_x q_y \epsilon^{\mathrm{pl}}_{xy} + 2q_x q_z \epsilon^{\mathrm{pl}}_{xz} + 2q_y q_z \epsilon^{\mathrm{pl}}_{yz}.$$

Using $\boldsymbol{\sigma} = \mu i \left(\boldsymbol{q} \otimes \boldsymbol{u} + \boldsymbol{u} \otimes \boldsymbol{q}\right) - 2\mu \boldsymbol{\epsilon}^{\mathbf{pl}}$, we get, in condensed form,

$$\begin{pmatrix} \sigma_{xx} \\ \sigma_{yy} \\ \sigma_{zz} \\ \sigma_{xy} \\ \sigma_{xz} \\ \sigma_{yz} \end{pmatrix} = 2\mu \begin{bmatrix} \mathcal{G}_{1111} & \mathcal{G}_{1122} & \mathcal{G}_{1133} & \mathcal{G}_{1112} & \mathcal{G}_{1113} & \mathcal{G}_{1123} \\ \mathcal{G}_{2211} & & & & & \\ \vdots & & & & & \\ \mathcal{G}_{2311} & & \cdots & & & \mathcal{G}_{2323} \end{bmatrix} \begin{pmatrix} \epsilon^{\mathrm{pl}}_{xx} \\ \epsilon^{\mathrm{pl}}_{yy} \\ \epsilon^{\mathrm{pl}}_{zz} \\ \epsilon^{\mathrm{pl}}_{xy} \\ \epsilon^{\mathrm{pl}}_{xz} \\ \epsilon^{\mathrm{pl}}_{yz} \end{pmatrix},$$

3. *Massively parallel 3D simulations are currently being performed by other members of my research group, namely,* Chen Liu *and* Dr. Luca Marradi, *along with* Dr. Kirsten Martens.

where, for $i \neq j \neq k$,

$$\begin{aligned}
\mathcal{G}_{iiii} &= \frac{2q_i^2}{q^2}\left(1-\frac{q_i^2}{q^2}\right)-1 \\
\mathcal{G}_{iikk} &= \frac{-2q_i^2q_k^2}{q^4} \\
\mathcal{G}_{iijk} &= \frac{-4q_i^2q_jq_k}{q^4} \\
\mathcal{G}_{iiik} &= \frac{2q_iq_k}{q^2}-\frac{4q_i^3q_k}{q^4} \\
\mathcal{G}_{ikii} &= \frac{q_iq_k}{q^2}-\frac{2q_i^3q_k}{q^4} \\
\mathcal{G}_{ikik} &= \frac{-q^2+q_i^2+q_k^2}{q^2}-\frac{4q_i^2q_k^2}{q^4} \\
\mathcal{G}_{ikjj} &= \frac{-2q_iq_kq_j^2}{q^4}
\end{aligned}$$

Note that the $q_z = 0$-modes, *i.e.*, $\boldsymbol{\mathcal{G}}(q_x, q_y, 0)$, boil down to the two-dimensional propagator of Eq. 8.7.

With Einstein's summation conventions, the above formulae can be condensed into

$$\sigma_{ij}(\boldsymbol{q}) = 2\mu\left(\frac{q_jq^l\delta_i^k+q_iq^k\delta_j^l}{q^2}-\frac{2q_iq_jq^kq^l}{q^4}-\delta_i^k\delta_j^l\right)\epsilon_{kl}^{\mathrm{pl}}(\boldsymbol{q})$$

with $\hat{\sigma}_{ij}(\boldsymbol{q}=\boldsymbol{0}) = -2\mu\epsilon_{ij}^{\mathrm{pl}}(\boldsymbol{q}=\boldsymbol{0})$.

The effect of a localised shear transformation $\boldsymbol{\epsilon}^{\mathbf{pl}}(\boldsymbol{r}=\boldsymbol{0})$ is presented in Fig. 8.3. It appears that most of the redistributed stress is contained in the plane of the shear transformation, and, in this plane, the redistributed stress profile is similar to that observed in 2D.

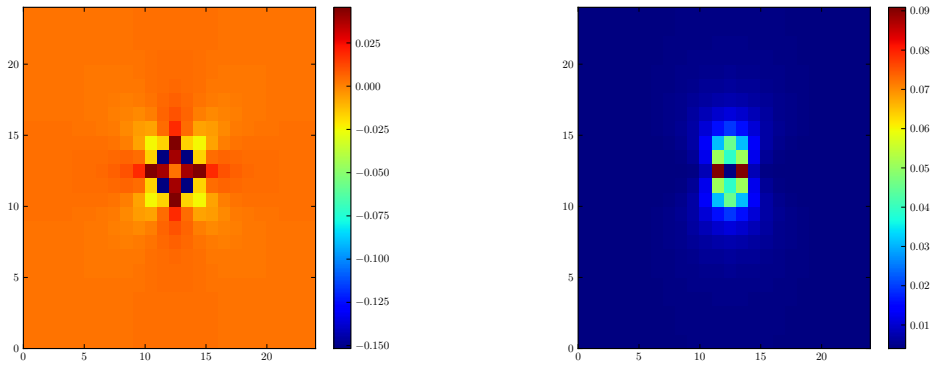

(a) In the xy-plane.

(b) In the xz-plane.

Figure 8.3: Colour maps of the redistributed stress σ_{xy}, in different cross sections, after a shear transformation localised at the origin and directed along xy. *(The central block is artificially coloured).*

Part III

NUMERICAL INVESTIGATION OF THE FLOW PROPERTIES USING AN ELASTOPLASTIC MODEL

Qu'importe que la conscience soit vivante,
si le bras est mort ?
Alfred de Musset, *Lorenzaccio*, act III, scene 3

Armed with the theoretical framework established in Chapter 7 and the numerical tools presented in Chapter 8, we are now in a position to assess the descriptive power of the model by investigating specific observables and different flow geometries.

In this endeavour, the paramount inquiry as to whether the model reproduces the physical behaviours observed in nature should be complemented with a question regarding the *minimal framework* required to reproduce such physical behaviour. In other words, to each considered observable must be assigned the model ingredients and the physical processes on which it hinges. For example, the importance of a tensorial description of the stress and of the inclusion of convection deserves to be assessed.

On the other hand, the pitfalls associated with such aspirations to simplicity and generality must be borne in mind. Danger lurks in the disconnection between the model and reality: indeed, models may be trimmed to such an extent that their building blocks can lose all connection with the deformation of real materials, despite some superficial similarity in the phenomenology. In order to avoid this snag, two chapters of this section are dedicated to direct quantitative comparisons with experiments and atomistic simulations.

To start with, in Chapter 9, we probe general flow properties, with the flow curve on the front line. Chapter 10 is concerned with effective temperatures and notably questions the idea of an effective activation temperature associated with mechanical noise. Closer attention is paid to the spatial organisation of the flow in Chapter 11, with an emphasis on the origin of strain localisation. This naturally leads to the study of correlations in the flow and correlation lengths, which is the topic of Chapter 12. Chapter 13 is centred on the effects of these correlations in a heterogeneous flow geometry, more precisely, in a microchannel flow, and offers a direct comparison with recent experimental results. Chapter 14 closes this part with a quantitative comparison with atomistic simulations at zero temperature, in which dynamical correlations between plastic events are exposed.

9

GENERAL FLOW PROPERTIES

In this chapter, we explore general flow properties such as the flow curve, yield angles, and stress overshoots, and we introduce new dynamical rules for the elastoplastic model, which, we claim, are more realistic than Picard's ones.

In addition, the impact of convection and stress tensoriality on these observables is to be discussed. Indeed, coarse-grained models are very generally *scalar*, insofar as they only retain one component of the stress tensor, σ_{xy}, if the macroscopic shear is directed along ϵ_{xy}, *e.g.*, if the material is confined between parallel plates at $y = 0$ and $y = L_y$ and one of these plates is moved in the x-direction. Besides the scalar approximation, lattice-based models usually neglect *convection, i.e.*, the fact that the mesoscopic blocks should be displaced as the material is sheared. On top of that, they are two-dimensional. It has been remarked that the vast technical simplifications involved in the models might jeopardise their validity [Barrat and Lemaître, 2011], insofar as the three aforementioned approximations are not bolstered by any rigorous justification. We choose to leave the third approximation, *i.e.*, the issue of spatial dimensionality, for future work, and only study the impact of the first two here, using the simple Picard model as a benchmark so as to facilitate the comparison,

9.1 FLOW CURVE WITHIN PICARD'S MODEL: ASSESSMENT OF THE IMPORTANCE OF STRESS TENSORIALITY AND CONVECTION

We start by investigating the flow curve in strain-controlled simulations, in line with what is frequently done experimentally.

9.1.1 *Picard's dynamical rules*

A trivial extension of Picard's dynamical rules to tensorial stresses is used, namely, a constant yield rate $l(\sigma)$ when the maximal local shear stress $\sigma = \|\boldsymbol{\sigma}\| \equiv \sqrt{\sigma_{xx}^2 + \sigma_{xy}^2}$ is larger than the yield stress $\sigma_y = 1$, and a constant rate of elastic recovery $e(\sigma) = \tau_{\text{res}}^{-1}$. These rules can be summarised as follows, with the Heaviside function Θ,

$$\text{elastic} \underset{\tau_{\text{res}}^{-1}}{\overset{\Theta(\sigma-1)\tau_{\text{liq}}^{-1}}{\rightleftharpoons}} \text{plastic},$$

and τ_{liq} is set to unity. At each time step, the probability of failure is $l(\sigma)dt$, while the probability of elastic recovery is $e(\sigma)dt$.

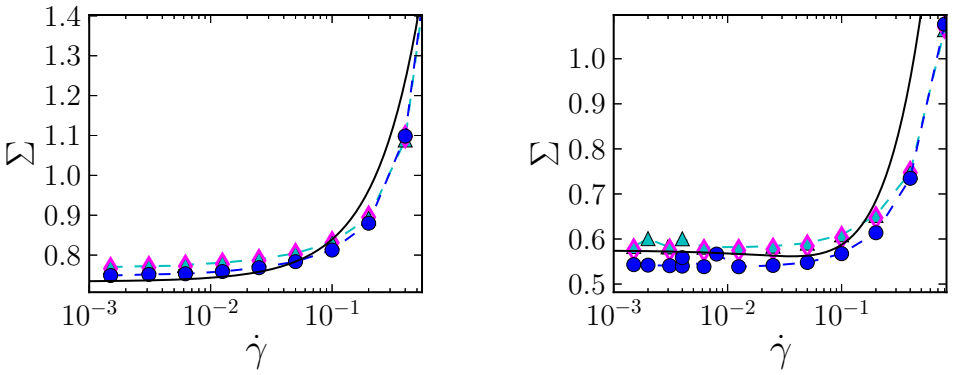

(a) $\tau_{\text{res}} = 1$ (b) $\tau_{\text{res}} = 5$

Figure 9.1: Dependence of the macroscopic shear stress Σ on the applied shear rate, for two distinct values of τ_{res}. (*Open diamonds*) Static scalar model; (*cyan triangles*) static tensorial model; (*blue dots*) convected tensorial model. $N = 64 \times 64$. (*Solid black line*) mean-field approximation of the model [Martens et al., 2012]. The dashed lines are guides for the eye.

9.1.2 *Numerical flow curves*

The model is simulated numerically by combining these stochastic rules with the elastoplastic master equation (Eq. 8.1), as explained in Chapter 8. The scalar model is straightforwardly obtained by focusing only on the xy-component of stresses and strains (in other words, $\sigma_{xx} = 0$ throughout the simulation). When needed, convection is implemented, with the protocol presented in Section 8.3.

The simulations generate the flow curves plotted on Fig. 9.1; the simulated system is large enough for finite-size effects to be negligible. Two observations are in order. First, the flow curve is hardly affected at all by the extension from a scalar stress to a tensorial one. Second, the inclusion of convection alters it perceptibly, but only to a very moderate extent.

The relative insensitivity of the flow curve to these technical refinements validates the use of a static scalar approach to describe the average flow in a simple geometry. In the light of this success of minimalism, an even more parsimonious approach can be envisioned: since Σ is a macroscopic, "one-point, one-time" observable, wouldn't a mean-field approximation of the problem be satisfactory?

In fact, this question was addressed by Martens et al. [2012]. In a typical mean-field spirit, these researchers averaged the local tress evolution equation (Eq. 8.1) over time and space and discarded fluctuations in the non-local stress redistributions; details of the calculations will be given in Section 11.1.1. The expression that they obtained is plotted in Fig. 9.1. Deviations from the numerical data are clearly visible but, overall, the agreement is reasonably good.

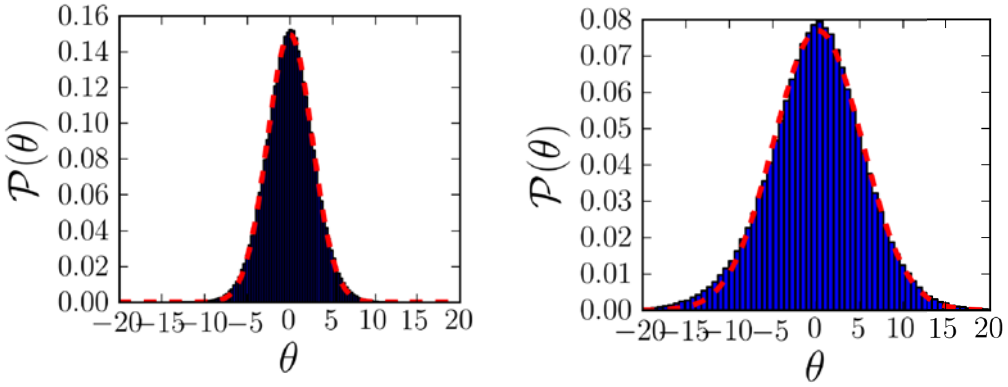

(a) Without convection

(b) With convection

Figure 9.2: Distribution of yield angles θ (in degrees) for $\tau_{\text{res}} = 1$ and $\dot{\gamma} = 6.2 \cdot 10^{-3}$ in the (a) static, (b) convected tensorial versions of the model. System size: $N = 64 \times 64$.

9.2 YIELD ANGLES

In the scalar description, plastic events occur exclusively along the macroscopic shear direction (xy). The tensorial model relaxes this constraint and features a distribution $\mathcal{P}(\theta)$ of angles of yield $\theta \in [-90°, 90°]$. This angle corresponds to the principal direction of plastic events, *i.e.*, $\cos(2\theta) = \frac{\sigma_{xy}}{\sigma}$, $\sin(2\theta) = \frac{-\sigma_{xx}}{\sigma}$; $\theta = 0°$ thus corresponds to a plastic event along (xy).

$\mathcal{P}(\theta)$ is shown in Fig. 9.2 for a restructuring time $\tau_{\text{res}} = 1$, in the static and convected versions of the model. In both cases, $\mathcal{P}(\theta)$ is well fit by a Gaussian distribution. To interpret the data, one should remark that, in the absence of cooperativity, plastic events would aligned along the macroscopic shear, hence $\mathcal{P}(\theta) = \delta(\theta)$. But cooperativity broadens the distribution $\mathcal{P}(\theta)$. Indeed, as τ_{res} increases from 1 to 10 time units, the standard deviation of the distribution, at a given shear rate, approximately doubles, which indicates enhanced cooperative effects. On the other hand, at a fixed restructuring time, say, $\tau_{\text{res}} = 1$, the breadth of $\mathcal{P}(\theta)$ does not vary much when the shear rate is changed, as long as the latter remains moderate ($\dot{\gamma} \leq 0.1$).

Switching on convection also leads to the doubling of the standard deviation of $\mathcal{P}(\theta)$. We ascribe this to the enhancement of fluctuations due to convection. At first sight, this feature could be an artifact rooted in our specific implementation of convection, insofar as the latter involves a deformation of the simulation cell, whose symmetries no longer coincide with those of the elastic propagator. However, we have observed a similar broadening of $\mathcal{P}(\theta)$ with a different implementation of convection, presented in Chapter 13, in which the simulation cell is not deformed. Moreover, the standard deviations measured with both implementations of convection are close, with a relative difference lower than 10% on the batch put under test. We are thus led to the conclusion that the enhancement of fluctuations, as reflected by the broadening distribution of yield angles, is a robust consequence of the inclusion of convection.

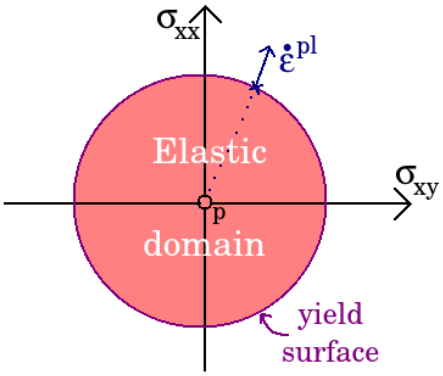

Figure 9.3: Elastic domain and yield surface of an elastoplastic block, with a von Mises yield criterion. The *in-plane* axes represent the deviatoric stress components σ_{xy} and σ_{xx}; the yield surface is invariant by translation along the out-of-plane axis (pressure).
Since $\dot{\epsilon}^{\mathrm{pl}} \propto \sigma$, the "normality rule", which states that $\dot{\epsilon}^{\mathrm{pl}}$ must be orthogonal to the yield surface, is clearly obeyed.

9.3 REALISTIC DYNAMICAL RULES IN THE ATHERMAL REGIME

So far, the discussion has been centred on the simple Picard model in order to assess the importance of technical aspects. However, we have already pointed out the weak points of such a model for the description of the rheology and the difficulty to root it in a PEL perspective. Accordingly, let us now propose more realistic dynamical rules.

The first step is to get rid the latency time τ_{liq}. From now on, the onset of a plastic event on a given block shall be determined by a von Mises yield criterion: *as soon as* the maximal shear stress $\|\boldsymbol{\sigma}(i,j)\| \equiv \sqrt{\sigma_{xx}^2(i,j) + \sigma_{xy}^2(i,j)}$ grows larger than the local yield stress, defined below, the block yields. The yield surface of a block is depicted in Fig. 9.3.

In addition, we introduce a distribution of yield stresses σ_y, or, equivalently, of energy barriers $E_y \equiv \sigma_y^2/4\mu$, and we modify the criterion for elastic recovery. To do so, we reason on the basis of a schematic vision of the PEL of a rearranging region. This landscape is composed of metabasins of exponentially distributed depths E_y, as suggested by some experimental results on colloidal glasses [Zargar et al., 2013] and as in the SGR model. For practical reasons, we neglect small jumps between PEL basins and focus on the larger jumps between metabasins, which correspond to the irreversible jumps at low enough temperature [Doliwa and Heuer, 2003, Heuer, 2008]; this is done by cutting off the energy barrier distribution at $E_y^{\min} = \mu\gamma_c^2/4$ with the help of a Heaviside function Θ, *viz.*,

$$P\left(E_y\right) = \Theta\left(E_y - E_y^{\min}\right) \lambda e^{\lambda\left(E_y^{\min} - E_y\right)}, \tag{9.1}$$

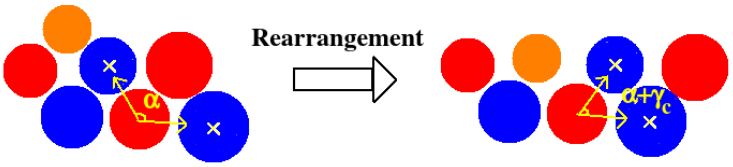

Figure 9.4: Schematic representation of the physical meaning of the typical "distance" γ_c between metabasins.

where λ is chosen so that the average yield strain $\langle \gamma_y \rangle$ takes a realistic value, say, 10% for concentrated emulsions [Hébraud et al., 1997]. In order to describe elastic recovery, we further assume that there is some typical distance (measured in terms of strain) between metabasin minima. This distance is related to the parameter γ_c used to define $E_y^{\min}$; for simplicity, we set it to γ_c exactly. The physical interpretation of this parameter is sketched in Fig. 9.4. A block will then remain plastic until the strain cumulated during plasticity reaches the value γ_c, that is, as long as

$$\gamma^{\mathrm{pl}} \equiv \int dt \, \|2\dot{\boldsymbol{\epsilon}}(i,j)\,(t)\| \quad < \quad \gamma_c, \tag{9.2}$$

where the local rate of deformation $\dot{\boldsymbol{\epsilon}}(i,j)$ is the sum of the plastic strain rate, $\dot{\boldsymbol{\epsilon}}^{\mathbf{pl}}(i,j)$, and an elastic component, $\partial_t \boldsymbol{\sigma}(i,j)/2\mu$, which includes the reaction of the medium and external loading (see Eq. 8.1). Finally, at the end of the plastic event, the local energy barrier is renewed.

The criterion for elastic recovery is somewhat arbitrary, but it provides a convenient way to implement the crucial disruption of plastic events by the drive, as discussed in Section 7.2.1. Moreover, it captures the observed decrease of the rearrangement (*T1* event) time at high enough strain rates in bubble clusters [Biance et al., 2009].

Incidentally, if the stress initally borne by a plastic block was large at the time of yield and the newly picked yield stress upon elastic recovery is relatively low, nothing prevents the block from yielding again immediately. In other words, several energy barriers may be crossed in a single plastic event, if the first elementary rearrangement does not dissipate (or transfer) enough energy. In a foam, this would simply correspond to a series of successive T1 events.

Apart from the *time and stress units*, τ and μ, the only parameter left free in the model is the ratio $\gamma_c/\langle \gamma_y \rangle$, which we set to 0.7.

Besides the dynamical rules, the backbone of the model is not altered: stress redistribution is still described by the elastic propagator $\boldsymbol{\mathcal{G}}$, and the evolution of the local stress tensor is still governed by Eq. 8.1.

In accordance with the discussion in Section 7.2.1, these new dynamical rules provide a more faithful reflection of the physical processes at work in a sheared amorphous solid. But do they yield a flow curve that better matches the widely observed Herschel-Bulkley behaviour, $\Sigma = \Sigma_0 + A\dot{\gamma}^n$, with $n \approx 0.5$ (see Section 5.4 and references therein).

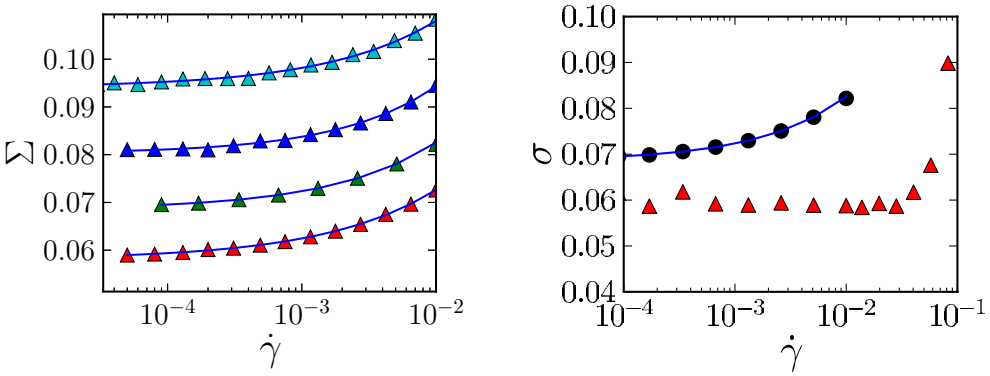

(a) $\gamma_c/\langle\gamma_y\rangle$ =(*cyan*) 0.4, (*blue*) 0.55, (*green*) 0.7, (*red*) 0.9. Solid lines are Herschel-Bulkley fits with exponents $n = 0.53$, 0.60, 0.57, 0.52, respectively. No structural ageing.

(b) Effect of short-term ageing: (*blue dots*) $k = \infty$, *i.e.*, no ageing, (*red triangles*) $k = 10^{-3}$.

Figure 9.5: Flow curves obtained with the new dynamical rules, in the tensorial convected version of the model. The system size is at least $N = 48 \times 48$ (negligible finite size effects).

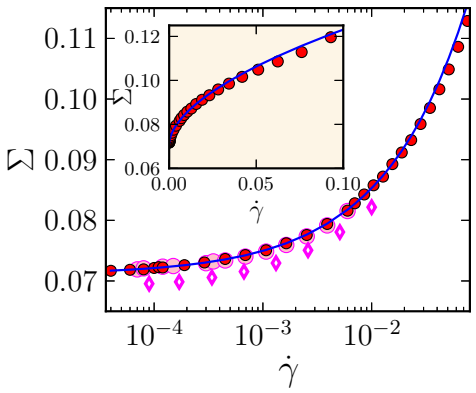

Figure 9.6: Flow curve for $\gamma_c = 0.7\langle\gamma_y\rangle$ in the (*dots*) static and (diamonds) convected versions of the tensorial model. (*Inset*) Same, plotted with linear-linear axes. $N =$ (*red dots*) 64×64, (*pink dots and fuchsia diamonds*) 128×128. The solid line is a fit to the Herschel-Bulkley equation $\Sigma = 0.07 + 0.19\dot{\gamma}^n$, with $n = 0.56$.

The flow curves are plotted in Fig. 9.5a for various model parameters $\gamma_c/\langle\gamma_y\rangle$. Quite interestingly, at reasonably low shear rates $\dot{\gamma} < 10^{-2}$, the curve is nicely fit by a Herschel-Bulkley equation with exponent $n \approx 0.5 - 0.6$. At higher shear rates, for $\dot{\gamma}\tau > \langle\gamma_y\rangle$, one enters a regime dominated by the dissipative stress during plastic events, which was assumed linear in the strain rate here.

Regarding the importance of convection, let us point out (although we might just be stating the obvious) that it should depend on the value of the average yield strain $\langle\gamma_y\rangle$, which sets the relative shift of neighbouring streamlines caused by a plastic event. Indeed, should this value decrease towards zero, then an increasingly large number of plastic events will have occurred by the time two neighbouring streamlines are shifted with respect to one another, thereby limiting the potential impact of convection. It is therefore a wise precaution to set $\langle\gamma_y\rangle$ to a realistic value for the materials under consideration. Here, we had materials akin to dense micrometric emulsions in mind [Mason et al., 1996, Hébraud et al., 1997]; had we instead focused on hard colloidal glasses, $\langle\gamma_y\rangle$ would have been reduced by approximately one order of magnitude and set to approximately one percent [Schall et al., 2007].

Summary of the Refined Athermal Model

Master equation (unaltered)

$$\partial_t \sigma(i,j;t) \quad = \quad \mu\dot{\gamma} + 2\mu \sum_{i'=1}^{L} \sum_{j'=1}^{L} \mathcal{G}\left(i-i', j-j'\right) \cdot \dot{\boldsymbol{\epsilon}}^{\mathrm{pl}}(i',j';t)$$

Dynamical rules

$$\text{elastic} \quad \underset{\gamma^{\mathrm{pl}} \geqslant \gamma_c}{\overset{\sigma \geqslant \sigma_y}{\rightleftharpoons}} \quad \text{plastic}$$

Distribution of yield stresses

Yield stress (σ_y) renewal after each plastic event, from the distribution

$$P\left(E_y\right) \quad = \quad \Theta\left(E_y - E_y^{\min}\right) \lambda e^{\lambda\left(E_y^{\min} - E_y\right)},$$

with $\sigma_y \equiv 2\sqrt{\mu E_y}$ and $E_y^{\min} = \mu\gamma_c^2/4$.

9.4 Extension to thermal materials; ageing

The refined athermal model does not describe ageing, *i.e.*, the exploration of deeper and deeper energy basins on average by the system at rest. However,

ageing and the associated phenomenon of shear rejuvenation [1] are prominent in a broad class of materials, encompassing glasses and gels, as well as (arguably and more surprisingly) granular matter.

Two types of ageing processes can be envisioned:

(i) ageing within a given metabasin ("short-term ageing"), and

(ii) ageing through hops between metabasins ("long-term ageing").

In practice, in our modelling framework, ageing of type (ii) will be mediated by plastic events, whereas short-term ageing will not require a significant rearrangement of the particles.

For sure, the frontier between the two types of ageing may be somewhat ill-defined. Nevertheless, we suggest some examples of physical processes that can be classified as type (i) or (ii), and we explore the consequences of each type within the model.

9.4.1 *Short-term ageing*

When a plastic event terminates, the mesoscopic region may not have reached its (locally) most stable configuration yet. In that case, the energy minimisation *within* the metabasin, which proceeds *via* hops between basins, is still ongoing at the end of the plastic event. Consequently, the inception of the elastic regime is accompanied by a phase of short-term ageing.

Hypothetical physical candidates for short-term ageing are the reorientation of particles in a Laponite suspension so as to maximise the electrostatic or van der Waals interactions or the ion exchanges with the solvents. For foams, it might be the time of recovery of the optimal angles between bubble walls at the Plateau borders, or, for high surface modulus foams, the relaxation of the surface tension of the liquid films upon a sudden variation of their area, which coincides with the chemical equilibration of the surfactants in the films [Denkov et al., 2009]. In granular matter, moisture-induced ageing has been reported at rest[Bocquet et al., 1998]. More generally, there is some nascent literature about ageing processes at granular nanocontacts, without the failure of the "macroscopic" contact; this is experimentally explored by means of nonlinear acoustic methods, for instance [Zaitsev et al., 2014]. It is noteworthy that this type of ageing does not require the *particles* to be significantly affected by thermal fluctuations.

In our approach, the diversity of these microscopic processes will be advantageously subsumed under a general recovery process, whereby, after a plastic event, the energy barrier $E_y(t)$ needs a finite time to reach its final value, *viz.*,

$$\dot{E}_y(t) = k\frac{E_y - E_y(t)}{E_y - E_y^{\min}}, \tag{9.3}$$

where k is a rate of recovery and stability is supposed to be minimal at the end of a plastic event, that is, $E_y(t_{\text{end}}) = E_y^{\min}$. Note that the shear-induced lowering

1. Shear rejuvenation corresponds to the shear-induced loss of the enhanced structural stability acquired through ageing: the sheared material lands in shallower energy basins [Rodney and Schuh, 2009, Rodney and Schrøder, 2011].

of the energy barriers has received at least numerical confirmation [Rodney and Schrøder, 2011].

Qualitatively, the rate of recovery k is analogous to the inverse of the restructuring time τ_{res} in Picard's model. When k is lowered, the macroscopic drive $\dot{\gamma}$ starts to compete with the recovery process, and a plateau develops in the flow curve (see Fig. 9.5b). A growing propensity to **shear localisation** is then observed. But this will be the topic of Chapter 11.

9.4.2 *Long-term ageing*

Long-term ageing is, presumably, of paramount importance for the comprehension of the solidity of a quiescent glass. Bouchaud's celebrated trap model notably runs along these lines [Bouchaud, 1992].

Here, we follow the trap model (or SGR) description of long-term ageing. To do so, we simply allow thermally activated plastic events by generalising the local yield rate to

$$l\left(\sigma\right) \quad = \quad \tau^{-1} \exp\left(\frac{E\left(\sigma\right) - E_y}{k_B T}\right), \tag{9.4}$$

where, as usual, σ is the maximal local shear stress, $E\left(\sigma\right) \equiv \sigma^2/4$, and $k_B T$ is the thermal energy. This generalised Arrhenius-like yield rate is adequate as long as the kinetic energy remains low, *i.e.*, at low temperatures and small shear rates. Beyond this limit, the local stress at yield (as determined by Eq. 9.4) will often significantly differ from σ_y, although both should theoretically coincide for the block to yield. A more rigorous way to account for thermal fluctuations in that case is presented in Appendix 9.5.1.

To highlight ageing effects, we let the quiescent system age and then investigate the transient rheological properties of the aged system.

Some technicalities, connected with the aforementioned discrepancy between the real local stress at yield and σ_y, force us to slightly modify the criterion for elastic recovery, in the quiescent system. Indeed, should we keep the previous criterion, some blocks would yield at very small stress because of thermal activation and the strain accumulation phase (ending only when $\gamma^{\text{pl}} = \gamma_c$) would take extremely long times. Consequently, we change it to a stress-based (rather than strain-based) criterion, *viz.*,

$$e(\sigma) = \tau^{-1} e^{\frac{-\|\sigma\|^2}{\alpha \langle \gamma_y \rangle^2}}.$$

On account of the sparsity of plastic events in the quiescent system, the value of α is expected to have but a minor role in the system at rest.

Structural ageing and shear-rejuvenation

We simulate a system at temperature $k_B T = 2.5 \cdot 10^{-3}$ in model units, with $\alpha = 0.3$. At rest, ageing transpires in the smooth rise of the average local yield

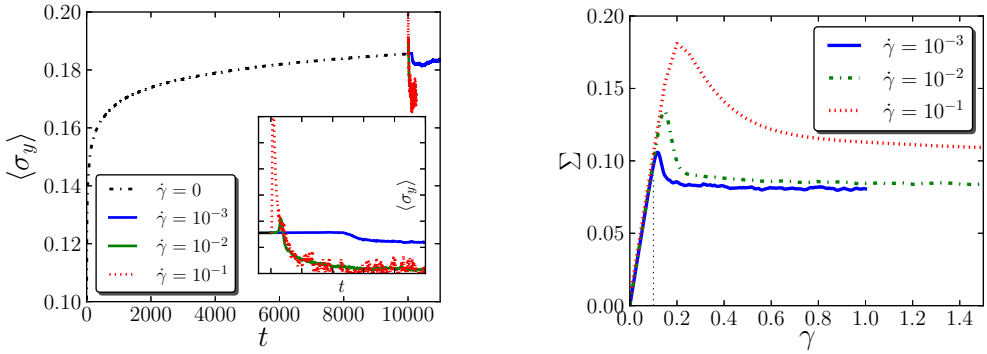

(a) Evolution of the average yield stress of the system as a function of time. Shear is applied from $t = 10000$ onwards, at the shear rates indicated in the legend. (*Inset*) Zoom on the sheared region.

(b) Stress *vs.* strain curves for various shear rates, corresponding to the same simulation as in Fig. 9.7a.

Figure 9.7: Structural ageing and stress overshoot.

stress $\langle \sigma_y \rangle$ (or, equivalently, $\langle E_y \rangle$), as shown in Fig. 9.7a for $t \leqslant 10,000$. From time $t = 10,000$ (corresponding to an energy barrier $\Delta E \simeq 9 k_B T$) onwards, shear is applied to the system. Shear rejuvenation is then clearly observed, in the form of a shear-rate-dependent decrease of $\langle \sigma_y \rangle$ (see inset of Fig. 9.7a).

Stress overshoot

Experimentally, the value of $\langle \sigma_y \rangle$ is not directly accessible. However, it is reflected in the magnitude of the stress overshoot σ_m of the sheared material, *i.e.*, the maximum in the stress *vs.* strain curve. Indeed, because up to the stress overshoot the deformation is in large part reversible, σ_m mirrors the stability of the aged structure of the material, prior to its rejuvenation by the flow.

Interestingly, *Divoux et al. [2011b]* reported that σ_m, defined as the maximum of the stress, follows a power-law scaling with the applied shear rate, $\sigma_m \sim \dot{\gamma}^{\beta}$, where β is a material-dependent exponent, of order 0.15. Our simulations also support a power-law dependence, rather than a logarithmic dependence (see Fig. 9.8). In addition, we find an exponent β quite similar to the aforementioned value: we get $\beta \sim 0.11$.

Although these results suggest that some kind of ageing is well accounted for in the model, a more exhaustive study would be required to get a more comprehensive view. In particular, the dependence on the waiting time reported by Divoux and co-workers,

$$\sigma_m \propto \begin{cases} \text{cst} & \text{for } t_w \dot{\gamma} \leq 2, \\ (t_w \dot{\gamma})^{\beta} & \text{otherwise,} \end{cases}$$

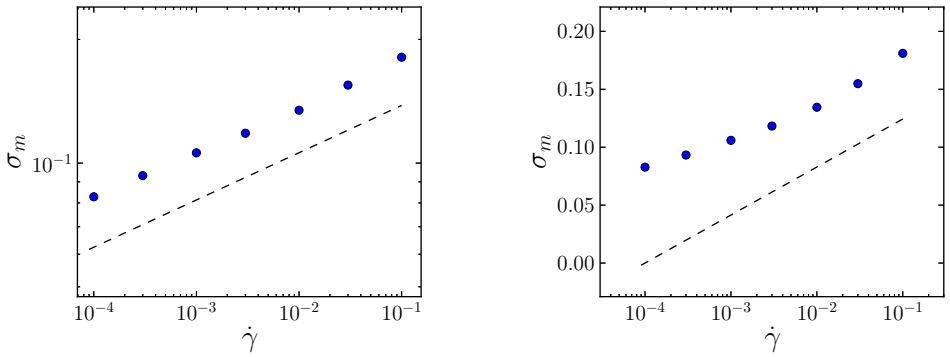

(a) Log-log scale

(b) Lin-log scale

Figure 9.8: Dependence of the stress overshoot σ_m on the applied shear rate. In subfigure (a), the dashed line represents $\sigma_m = 0.18\dot{\gamma}^{0.115}$.

would very much deserve further investigation. Also worth investigating are the hysteretic loops observed by Divoux et al. [2013] when sweeping the applied shear rate downards and upwards. The hysteretic loop is maximised for a given, finite sweep rate $\nu \equiv \frac{d\ln(\dot{\gamma})}{dt}$, which is interpreted as the inverse of a material time scale. On the contrary, in the model, hysteresis grows monotonically with ν (see Fig. 9.9), and the model counterpart of the time scale ν^{-1} remains mysterious to the present day.

We conclude these remarks about transient rheology by noting the expected inadequacies of the model when it comes to oscillatory rheology: experimentally, a fraction of the particles undergo reversible plastic rearrangements, with no net motion over one oscillation [Keim and Arratia, 2014]; this relies on the memory of the previous reference configuration or energy barrier, which is missing in the current version of the model.

Flow curves

Regarding steady-state rheology, the flow curves at low temperatures (*not shown*) feature large fluctuations that make them look erratic. This echoes Fielding et al. [2009]'s remark that, in an extended SGR model, "[n]umerical difficulties also impede detailed study of the limit $x \to 0$, which might be the realistic limit when true thermal noise is negligible".

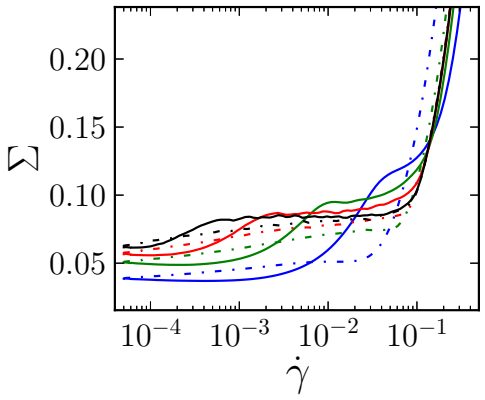

Figure 9.9: (*solid lines*) Downward and (*dashed lines*) upward strain rate sweeps. The system is prepared at a high shear rate $\dot{\gamma} \sim 1$. Then the applied shear rate is decreased incrementally (*solid lines*), with logarithmically spaced steps $\dot{\gamma}_{n+1} = 0.9\dot{\gamma}_{n+1}$. When reaching $\dot{\gamma} = 5 \cdot 10^{-5}$, it is increased (*dashed lines*) following the same protocol. The time spent at each point, i.e., shear rate is $\delta t =$ (*blue*) 0.2τ, (*green*) τ, (*red*) 8τ, (*black*) 16τ.

Key Points of the Chapter

- The flow curves are unaltered by the extension to a tensorial stress, and only moderately affected by the inclusion of convection.
- Convection enhances fluctuations in the angles of yield.
- Refined athermal dynamical rules yield the desired Herschel-Bulkley behaviour, with an exponent close to 0.5.
- Some (but not all) effects associated with structural ageing are reproduced by a thermal extension of the model.

A

9.5 APPENDIX

9.5.1 *A better account of kinetic energy?*

In Section 9.4, thermal fluctuations were included in the model by allowing activated plastic events below the yield stress σ_y, *via* an Arrhenius-like activation process. However, this might be problematic, insofar as the stress carried by a block at yield will then generally differ from σ_y, although in reality this should not be.

This inadequacy is benign at low temperatures, or, more rigourously, at low dressed Péclet numbers, when thermal activation takes much longer than shear-induced hops. However, it might undermine any attempt to bridge the gap between the low-temperature, solid regime and the liquid phase.

One could hope to remedy the defect by increasing the local stress to σ_y at the onset of plasticity, but this contrivance would require the regular input of energy into the system and create discontinuities in the evolution of local stresses.

Alternatively, one may wish to implement thermal fluctuations directly in the local stresses. But doing so while maintaining mechanical equilibrium has proved to result in considerable difficulties.

Further insight into the problem can be gained by more theoretical considerations. In the energy density of a mesoscopic region, we isolate a slowly evolving potential part $\bar{V}\left(\{\bar{\boldsymbol{r}}_i\}\right)$, where $\bar{\boldsymbol{r}}_i$ refers to the average position over a time window much longer than a molecular vibration but much shorter than the inverse shear rate $\dot{\gamma}^{-1}$. The complementary part is denoted by e_{rem} and includes (but is not limited to) the kinetic/vibrational contribution. Accordingly,

$$e = \bar{V}\left(\{\bar{\boldsymbol{r}}_i\}\right) + e_{\text{rem}}\left(\{\boldsymbol{r}_i, \boldsymbol{p}_i\}, \Lambda\right), \tag{9.5}$$

where $\boldsymbol{r}_i$ (resp., $\boldsymbol{p}_i$) is the instantaneous position (momentum) of particle i, , and Λ refers to a set of internal degrees of freedom. Note in particular that, for a system trapped in a metabasin, $\bar{V}\left(\{\boldsymbol{r}_i\}\right)$ cannot get larger than the local energy barriers E_y, whereas the total energy e can.

Considering e_{rem} first, we suppose that the potential energy $\bar{V}$ evolves on much longer timescales than e_{rem}, so that, on short timescales, we can write the following conservation equation,

$$\frac{\partial e_{\text{rem}}}{\partial t} + \nabla \cdot \boldsymbol{j}^e_{\text{rem}} = \mathcal{C}, \tag{9.6}$$

where $\boldsymbol{j}^e_{\text{rem}}$ is the energy current associated with e_{rem} and $\mathcal{C}$ is a volumic source term. Because energy is created and dissipated durings collisions and *via* the coupling to the bath, it is reasonable to assume that $\mathcal{C} \approx -\Gamma\left(e_{\text{rem}} - e^0_{\text{rem}}(T)\right)$,

where Γ is a coupling constant and $e^0_{\text{rem}}(T)$ is the complementary energy density in the quiescent system. Regarding the energy current j^e_{rem}, we tentatively approximate it to $j^e_{\text{rem}} \approx -D\nabla e_{\text{rem}}$, where the diffusivity D is positive, on the grounds that excitations in amorphous solids are notably more localised than their counterparts in crystals, namely, phonons.

Equations applying to the stress $\boldsymbol{\sigma}_{\text{rem}} \equiv {}^{\partial e_{\text{rem}}}/_{\partial \boldsymbol{\epsilon}}$ are obtained by deriving Eq. 9.6 with respect to the strain $\boldsymbol{\epsilon}$, *viz.*,

$$\frac{\partial \boldsymbol{\sigma}^{(d)}_{\text{rem}}}{\partial t} \approx \underbrace{D\nabla^2 \boldsymbol{\sigma}^{(d)}_{\text{rem}}}_{\text{diffusion}} - \underbrace{\Gamma \boldsymbol{\sigma}^{(d)}_{\text{rem}}}_{\text{dissipation}},$$

where $\boldsymbol{\sigma}^{(d)}_{\text{rem}}$ is the *deviatoric* component of the stress and we have used the fact that $\boldsymbol{\sigma}^0_{\text{rem}} \equiv {}^{\partial e^0_{\text{rem}}}/_{\partial \boldsymbol{\epsilon}}$ is purely isotropic, for symmetry reasons, and therefore has no deviatoric component.

As for the slowly evolving elastic part, we suppose that the system in configuration $\{\bar{\boldsymbol{r}}_i\}$ is in pseudo-static mechanical equilibrium at all times, *viz.*,

$$\nabla \cdot \boldsymbol{\sigma}_{\text{el}} \approx 0,$$

where $\boldsymbol{\sigma}_{\text{el}} \equiv {}^{\partial \bar{V}}/_{\partial \boldsymbol{\epsilon}}$. It follows that the elastic stress redistribution when a plastic event occurs can still be described by the instantaneous elastic propagator $\boldsymbol{\mathcal{G}}$.

To conclude, the dynamics of the two stress components are treated separately and the macroscopic drive is naturally borne by $\boldsymbol{\sigma}_{\text{el}}$ if the block is elastic, or $\boldsymbol{\sigma}_{\text{rem}}$ otherwise, *viz.*,

$$\begin{cases} \frac{\partial \boldsymbol{\sigma}_{\text{el}}}{\partial t} &= \mu\dot{\gamma}(1 - n^{\text{pl}}) + 2\mu \boldsymbol{\mathcal{G}} \star \dot{\boldsymbol{\epsilon}}^{\mathbf{pl}} \\ \frac{\partial \boldsymbol{\sigma}^{(d)}_{\text{rem}}}{\partial t} &= \mu\dot{\gamma} n^{\text{pl}} + D\nabla^2 \boldsymbol{\sigma}^{(d)}_{\text{rem}} - \Gamma \boldsymbol{\sigma}^{(d)}_{\text{rem}}, \end{cases} \tag{9.7}$$

where $n^{\text{pl}} = 0$ if the block is in the elastic regime, 1 otherwise, and $\dot{\boldsymbol{\epsilon}}^{\mathbf{pl}} = n^{\text{pl}} \boldsymbol{\sigma}_{\text{el}} / 2\mu\tau$. It should once again be recalled that $\boldsymbol{\mathcal{G}}(\mathbf{0})$ is negative, so that the local stress $\boldsymbol{\sigma}_{\text{el}}$ decays exponentially upon yield.

Equations 9.7 exhibit two salient features. First, they include a diffusive process, which, to some extent, is similar to the diffusion of the effective temperature χ in the STZ theory, for instance. Secondly, unlike the low temperature equations (Eq. 9.4), part of the stress is constantly damped, not only *via* the local component $\boldsymbol{\mathcal{G}}(\mathbf{0})$ in the first line but above all *via* the term $-\Gamma\boldsymbol{\sigma}^{(d)}_{\text{rem}}$ in the second line, which reflects the dissipative processes acting in a liquid. The fact that dissipation of the "complementary" energy e_{rem} occurs at all times, and not only during plastic events, stabilises a system that might otherwise turn unstable at high temperatures.

10

OF EFFECTIVE TEMPERATURES

The distinction made between thermal systems and athermal ones in Chapter 9 should not blur the fact that fluctuations are always present in the flow of these materials, even in the athermal case. In a system out of equilibrium, these fluctuations can be quantified by an *effective temperature*. This chapter aims to clarify this concept and its ramifications (effective fluctuation-dissipative temperature, effective activation temperature, etc.) with the help of elastoplastic models.

10.1 VARIOUS DEFINITIONS OF EFFECTIVE TEMPERATURES

It is relatively customary to introduce the theory of General Relativity by pointing out the accepted, but remarkable, coincidence between the inertial mass m_{inert} and the gravitational mass m_{grav}: the motion of an object freely falling in a gravity field $\boldsymbol{g}$, with acceleration $\boldsymbol{a}$, is suitably described by the equation $m_{\text{inert}}\boldsymbol{a} = m_{\text{grav}}\boldsymbol{g}$, with $m_{\text{inert}} = m_{\text{grav}}$. This provides a first clue that a gravity field is nothing but an acceleration field.

Similarly, a naive introduction to Statistical Physics could invite the reader to muse over the surprising coincidence between the various notions of temperature, say, the kinetic temperature, the fluctuation-dissipation temperature, and the activation temperature. To be concrete, consider an isolated colloidal particle of mass m in a solvent of viscosity η. Its velocity $\boldsymbol{v}$ obeys the Langevin equation of motion,

$$m\frac{d\boldsymbol{v}}{dt} = -\zeta m\boldsymbol{v} + \boldsymbol{f}^{\text{th}},$$

where $\left\langle f_\alpha^{\text{th}}(t) f_\beta^{\text{th}}(t') \right\rangle = 2m\zeta k_B T \delta_{\alpha\beta}\delta(t-t')$, $\alpha, \beta \in \{x, y, z\}$. For convenience, we set $k_B = 1$.

Temperature appears in at least three types of equalities:

① T is a measure of the ***kinetic energy*** of the particle,

$$\frac{1}{2}m\left\langle \boldsymbol{v}^2 \right\rangle = Td, \tag{10.1}$$

where d is the dimension of space. This is a microscopic quantity, but what can be measured macroscopically is the osmotic pressure Π, which scales with cT for a dilute dispersion of concentration c.

② T relates equilibrium ***fluctuations*** of the position of the particle, quantified by a diffusion coefficient D, to its ***response*** to a body force $\boldsymbol{F}^{\text{ext}}$, measured by its mobility μ, where $\boldsymbol{v} = \mu \boldsymbol{F}^{\text{ext}}$, *via* the Stokes-Einstein-Smoluchowksi relation

$$D = T\mu. \tag{10.2}$$

③ Now, suppose that the particle is trapped in a simple, *e.g.*, isotropic, energy basin $U(r)$, by means of optical tweezers, for instance. The escape time $\tau(E_a)$ needed to overcome a potential barrier of height E_a then follows an ***Arrhenius law***, *viz.*,

$$\frac{d\ln\tau}{dT} \sim \frac{-E_a}{T^2}. \tag{10.3}$$

10.1.1 *Convergence of the definitions at equilibrium*

Well established theories guarantee that these diverse temperatures match in a classical system at equilibrium, essentially because detailed balance is satisfied and the probability distribution in phase space depends only on a single parameter (the temperature T).

More precisely, Eq. 10.1 results from the equipartition theorem.

The Stokes-Einstein-Smoluchowksi (Eq. 10.2) is one of the many possible applications of the fluctuation-dissipation (FD) theorem, which relates the correlations of the fluctuations of observables A and B to the susceptibility $\chi_{AB}(\Delta t)$ of B to a perturbation imposed by the conjugate field of A, *viz.*,

$$\chi_{BA}(\Delta t) = \frac{-1}{T}\frac{d}{d\Delta t}\left\langle A(t)B(t+\Delta t)\right\rangle_t. \tag{10.4}$$

The theorem is most easily understood in the light of Onsager's fluctuation regression hypothesis: the average regression of thermal fluctuations at equilibrium is similar to the linear response of the system to a "macroscopic" perturbation of magnitude k_BT. In this perspective, the factor k_BT in Eq. 10.4 just sets the scale of equilibrium fluctuations.

Finally, the Arrhenius law (Eq. 10.3) has been theoretically bolstered by the works of Eyring, Christensen, and Kramers [Eyring, 1935, Kramers, 1940].

10.1.2 *Indeterminacy of the out-of-equilibrium case*

Contrary to the equilibrium situation, nothing guarantees the convergence of these definitions out of equilibrium. Worse still, there may not be a constant parameter T that sets the scale of fluctuations, *via* Eq. 10.4, at all time scales, and, even if there is, it may vary with the chosen observables A and B.

Successes of the notion of effective temperature

In the past two decades, the perspective of finding an *effective temperature* T_{eff} that could replace the bath ("room") temperature in Eqs. 10.1, 10.4, and 10.3 in ageing (or sheared) glasses has ignited intense research efforts.

Schematic mode-coupling approximations support the existence of an observable-independent effective temperature in FD relations (Eq. 10.4) at long lag times [Berthier et al., 2000]. At short times, on the other hand, the system is thermalised at room temperature, in accordance with the everyday expectation that a sheet of glass, or a mildly sheared emulsion, is not warmer by the touch than its environment [Cugliandolo et al., 1997].

This two-time-scale, two-temperature scenario was successfully tested by Barrat and Berthier [2000], Berthier and Barrat [2002b,a] on more realistic numerical models of supercooled and glassy materials. Along with others [Ono et al., 2002, Haxton and Liu, 2007], these researchers showed that a variety of observables yield the same long-time FD temperature, which grounds its use as a true thermodynamic (effective) temperature. In addition, the FD based effective temperature appeared to satisfy the equipartition theorem (Eq. 10.1) for tracer particles: the kinetic energy of light tracers, *i.e.*, particles with high vibrational frequency, is given by the bath temperature, or, equivalently, the short-time FD based temperature, whereas the kinetic energy of heavy particles, *i.e.*, low-vibrational-frequency tracers, reaches the long-time-scale effective temperature [Berthier and Barrat, 2002a].

Regarding Definition ③, numerical work indicates that an activation temperature such as that used in Eq. 10.3 does indeed exist; its value may be consistent with the other temperature definitions [Ilg and Barrat, 2007]. To reach this conclusion, Ilg and Barrat simulated the shear flow of a glassy material and seeded it with dimers connected with a double-well potential and maintained aligned in the neutral direction of the flow. The inversion rate of the dimer follow an Arrhenius law (Eq. 10.3) with a shear-rate-dependent effective temperature. Haxton and Liu [2007] then propounded the view that the macroscopic stress of glassy systems sheared at different temperatures is a function, not of T or $\dot{\gamma}$ alone, but of T_{eff}. To some extent, this lends support to mean-field models which offer a leading role to a (so far speculative) effective temperature: the mechanical noise temperature in the SGR model, or the effective temperature quantifying disorder fluctuations in the STZ model.

Issues

But, for all these successes, some contradictory results jeopardise the quest for the unification of effective temperatures. Indeed, not all observables yield the same FD temperature, and there is no clear reason to favour one definition over the others [O'Hern et al., 2004, Mizuno and Yamamoto, 2012]. Even in mean-field-like models for ageing glasses, and more specifically in the SGR model, the extraction of a FD temperature can be problematic, with parametric correlation-*versus*-reponse plots whose shape strongly depends on the observable [Fielding and Sollich, 2002].

Encouraged by the major role of simple spin-glass and/or mean-field models in the emergence and development of the concept of an effective temperature in sheared glasses, we hope that elastoplastic models can help clarify the situation and offer a new viewpoint.

10.2 EFFECTIVE TEMPERATURES BASED ON THE FLUCTUATION-DISSIPATION THEOREM

10.2.1 *Green-Kubo relation*

First, let us investigate effective temperatures based on the FD theorem. On account of the few degrees of freedom in elastoplastic models, the choice of observables is limited. We choose the stress and strain observables; the relevant FD relation is the (out-of-equilibrium extension of the) Green-Kubo equation:

$$G(\tau) = \frac{N}{T_{\text{eff}}} \langle \delta\Sigma(t)\, \delta\Sigma(t+\tau) \rangle , \tag{10.5}$$

where N is the number of blocks, the $\delta\Sigma$'s are the macroscopic stress fluctuations around the mean value Σ, *viz.*, $\delta\Sigma(t) \equiv \Sigma(t) - \Sigma$, and the dynamic shear modulus $G(\tau)$ is the susceptibility to strain: $\delta\Sigma(t) = \int_{-\infty}^{t} G(\tau)\, \delta\dot{\gamma}(t-\tau)\, d\tau$, with $\delta\dot{\gamma}(t) \equiv \dot{\gamma}(t) - \dot{\gamma}$. Because of ergodicity in the sheared system, the average can be performed over time t.

10.2.2 *Dynamic shear modulus*

$G(\tau)$ is obtained numerically by perturbing the sheared system with a small extra strain increment $\delta\gamma'$ at time $t = 0$ and measuring the response at $t > 0$,

$$\begin{cases} \dot{\gamma}'(t) & = \dot{\gamma} + \delta\gamma'\, \delta(t) \\ G(t) & = \delta\gamma'^{-1} \langle \Sigma'(t) - \Sigma \rangle_{\Gamma} \end{cases} \tag{10.6}$$

where the primes refer to the perturbed system and the average is performed over realisations Γ, *i.e.*, more pragmatically, over different values of the seed of the random number generator.

10.2.3 *Proposed generic scaling with the shear rate*

The path to an effective FD temperature is strewn with the following questions:

(i) Is there a linear response regime that allows the definition of G?

(ii) Is Onsager's fluctuation regression principle obeyed?

(iii) If it is, what sets the scale of stress fluctuations in the steady state?

In Appendix 10.4.1, we address these questions in a generic mean-field model, which slightly extends the frameworks proposed in Refs. [Hébraud and Lequeux, 1998, Bocquet et al., 2009]. Albeit approximate, the derivation suggests the following scaling for the magnitude of stress fluctuations, thus for the effective temperature (taking its existence for granted), in the shear-dominated regime:

$$T_{\text{eff}} \sim \sqrt{N_{\text{act}}} \sim \sqrt{\dot{\gamma}},$$

where N_{act} is the number of simultaneous plastic rearrangements per unit volume.

10.2.4 *Numerical study*

Let us now turn to a numerical study of these questions.

With the realistic athermal model introduced in Section 9.3, I was unfortunately unable to access the linear regime: [1] I never observed a response proportional to $\delta\gamma'$. This difficulty nips in the bud the quest for an effective temperature. As an alternative, I turned to a model featuring different dynamical rules, which will be presented in Chapter 13:

$$\begin{cases} l(\sigma) & = \tau^{-1}\Theta\left(\sigma - \sigma_{\mu y}\right) \exp\left(\frac{\sigma-\sigma_y}{x_{\text{loc}}}\right) \\ e(\sigma) & = \tau^{-1} \exp\left(\frac{\sigma_{\mu y}-\sigma}{x_{\text{res}}}\right), \end{cases}$$

where Θ is the Heaviside function. The parameters of the model, x_{loc}, x_{res}, and $\sigma_{\mu y}$, were fit to the experimental flow curve for a concentrated oil-in-water emulsion (see Chapter 13).

Within this model, the existence of a linear response regime is demonstrated by measuring the response to spikes of different magnitudes $\delta\gamma'$ in Eqs .10.6. In Fig. 10.1a, we see that the responses to distinct $\delta\gamma'$, averaged over many realisations [2], collapse onto a master curve, the dynamic shear modulus $G(t)$, when properly rescaled with $(\delta\gamma')^{-1}$.

To check the validity of the FD relation, we draw a parametric plot of $G(t)$ *versus* the stress correlation function $C_{\Sigma\Sigma}(t) \equiv N \langle \delta\Sigma(\cdot)\, \delta\Sigma(\cdot + t) \rangle$. Bearing in mind that G may not have been measured exactly in the linear regime, we find that the data agree reasonably well with a linear relation between the two quantities, thus pointing to a single effective temperature over all relevant time scales, according to Eq. 10.5. We choose to evaluate T_{eff} through the value of the instantaneous correlation $C_{\Sigma\Sigma}(t = 0)$, rather than the slope of the parametric plot, on account of the imperfections of the linear fit.

In the nonsaturated regime, in which plastic events do not invade the whole simulation box, the predicted scaling $T_{\text{eff}} \sim \sqrt{\dot{\gamma}}$ is consistent with the numerical

1. This problem might be connected with the *sharp* transition, at $\sigma = \sigma_y$, from the elastic regime to the plastic one, which is then violated if a spike $\delta\gamma'$ is applied.

2. On a technical note, computational costs impose a compromise between the signal-to-noise ratio and the use of $\delta\gamma'$ values that are small enough to be strictly within the linear regime.

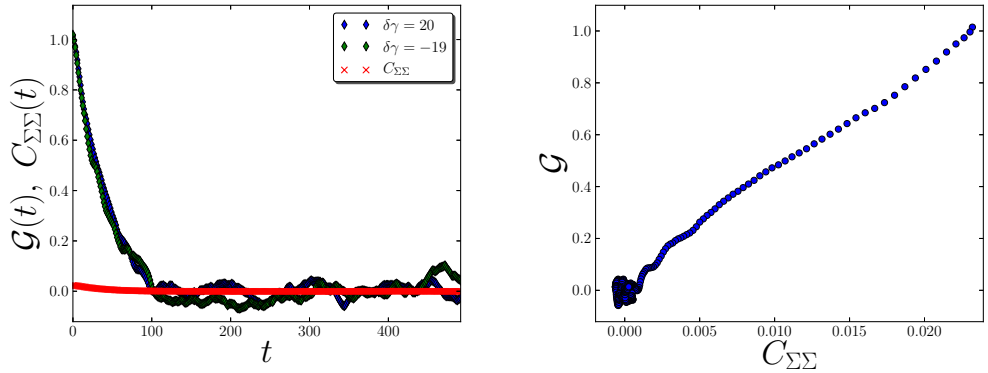

(a) $G(t)$ calculated with a perturbation $\delta\gamma'$, as indicated in the legend, and $C_{\Sigma\Sigma}(t)$.

(b) Parameteric plot of $G(t)$ as a function of $C_{\Sigma\Sigma}(t)$.

Figure 10.1: Dynamic shear modulus $G(t)$ and stress autocorrelation function $C_{\Sigma\Sigma}(t)$ for $\dot{\gamma} = 0.015$. $N = 128 \times 128$. ($G(t)$ is obtained by averaging over ~ 200 realisations.)

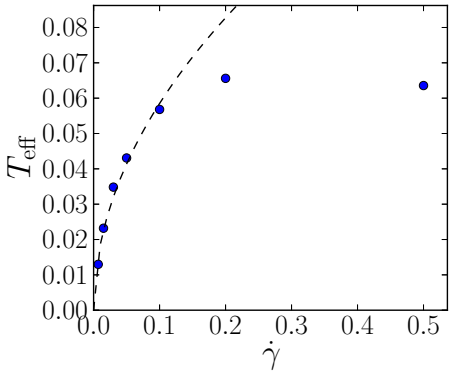

Figure 10.2: FD effective temperature T_{eff} as a function of the shear rate $\dot{\gamma}$. The dashed line is the curve $T_{\text{eff}} = 0.185\sqrt{\dot{\gamma}}$.

data. However, a more exhaustive study would be necessary to firmly establish this scaling.

10.3 AN EFFECTIVE ACTIVATION TEMPERATURE DUE TO MECHANICAL NOISE?

10.3.1 *A mechanical noise temperature?*

The foregoing study shows that the macroscopic drive generates stress fluctuations that can be captured by an effective FD temperature in the sense of Definition ② above. Do these fluctuations also lead to an effective activation temperature (Definition ③)?

More precisely, a mesoscopic region, considered as a subsystem, needs to overcome a potential barrier in order to undergo a rearrangement, whether it be a shear transformation in the sense of Argon and Kuo [1979] or the failure of a force chain in granular matter [Tordesillas et al., 2012]. Can the local mesoscopic fluctuations induced by the macroscopic drive, termed mechanical noise, *activate* such a rearrangement, in the same fashion as thermal fuctuations would?

Since mechanical noise can either stabilise or destabilise a region, the analogy with random thermal "kicks" is indeed tempting, and it lies at the heart of the SGR model (see Section 6.4) and of its extensions to granular matter [Pouliquen and Gutfraind, 1996, Pouliquen et al., 2001, Behringer et al., 2008, Bi and Chakraborty, 2009, Reddy et al., 2011]. One should recall that, in these models, energy barriers are deprimed to a lower energy $E(\gamma)$ by the homogeneous macroscopic shear, and mechanical noise then induces hops over the lowered barriers (particle rearrangements), which occur at an Arrhenius-like rate,

$$\omega = \omega_0 \exp\left(\frac{-E(\gamma)}{x}\right),$$

where x is a putative effective activation temperature associated with mechanical noise and ω_0 is an attempt frequency.

The present section runs counter to this idea and claims that the parallel between mechanical noise and thermal fluctuations is flawed at the theoretical level, because energy barriers couple to the former, whereas the latter operate in a fixed PEL, with fixed barriers.

10.3.2 *Numerical investigation*

Let us first address the question in the framework of the refined elastoplastic model presented in Section 9.3, before propounding more general arguments. We consider the static tensorial version, but we have gathered some evidence that both staticity and stress tensoriality are largely irrelevant when it comes to the picture presented here.

In the stress evolution equation, *i.e.*,

$$\partial_t \sigma(i,j) = \mu\dot{\gamma} + 2\mu \sum_{i',j'} \mathcal{G}_{i-i',j-j'} \dot{\epsilon}^{\mathbf{pl}}(i',j'), \tag{10.7}$$

the mechanical noise is unambiguously defined: it is the contribution from distant plastic events to the local stress, *i.e.*, the non-local part,

$$\partial_t \sigma_{\mathrm{nl}}(i,j) = \mu\dot{\gamma} + 2\mu \sum_{(i',j')\neq(i,j)} \mathcal{G}_{i-i',j-j'} \dot{\epsilon}^{\mathbf{pl}}(i',j'). \tag{10.8}$$

Incidentally, if we could only access information relative to a given block (i,j), we would not be able to distinguish between the two terms on the rhs of Eq. 10.8: both are transmitted by the surrounding medium through the boundaries of the region of interest and both have finite time-averages, the sum of which we shall write $\langle\dot{\sigma}\rangle \equiv \mu\dot{\gamma}_{\mathrm{eff}}$. This effective shear rate $\dot{\gamma}_{\mathrm{eff}}$ acts on σ as a drift term, and not

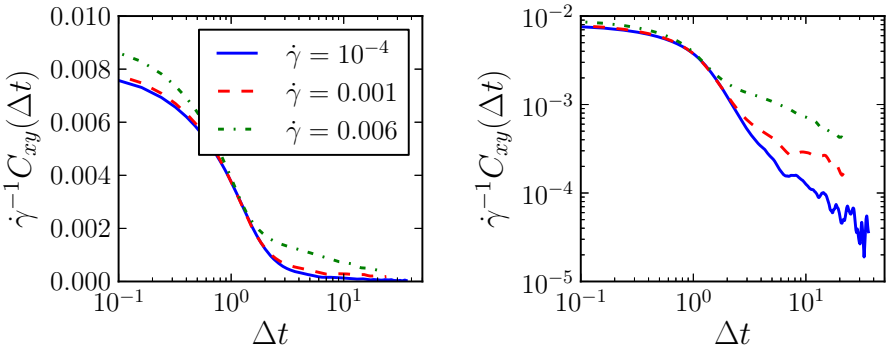

(a) $\dot{\gamma}^{-1}C_{xy}(\Delta t)$ *vs.* Δt.

(b) $\dot{\gamma}^{-1}C_{xy}(\Delta t)$ *vs.* Δt.

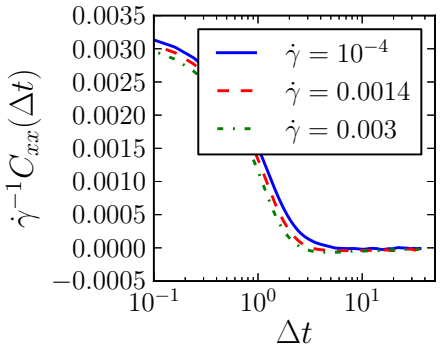

(c) $\dot{\gamma}^{-1}C_{xx}(\Delta t)$ *vs.* Δt.

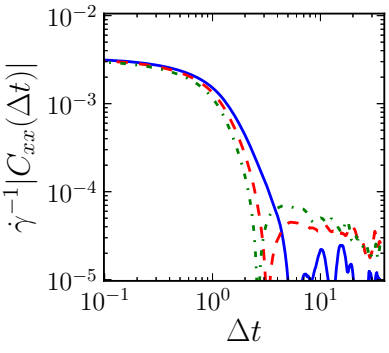

(d) $\dot{\gamma}^{-1}C_{xx}(\Delta t)$ *vs.* Δt.

Figure 10.3: Autoorrelations of the mechanical noise fluctuations (*top row*) $\delta\dot{\sigma}_{xy}$ and (*bottom row*) $\delta\dot{\sigma}_{xx}$, for various shear rates, as indicated in the legend. (*Left*) Semi-logarithmic plot, (*right*) logarithmic plot.

as "random kicks". Therefore, only the fluctuating part of the mechanical noise may be analogous to thermal *fluctuations*. Thus, for a randomly selected block, we keep track of the mechanical noise *fluctuations* that it experiences

$$\delta\dot{\sigma} \equiv \partial_t \sigma_{\mathrm{nl}} - \mu\dot{\gamma}_{\mathrm{eff}}.$$

The two-time autocorrelation function C_{xy} (resp., C_{xx}) of the steady-state fluctuations $\delta\dot{\sigma}_{xy}$ ($\delta\dot{\sigma}_{xx}$) of σ_{xy} (σ_{xx}) are plotted in Fig. 10.3. The magnitude of $\delta\dot{\sigma}$ naturally increases with the number of simultaneous plastic events, and therefore with $\dot{\gamma}$. Besides, its components display a fast initial decay, with a decay time similar to the plastic event lifetime. For $\delta\dot{\sigma}_{xy}$, a small fraction, however, remains correlated over much longer times, which we tentatively ascribe to long-lived correlations in the yield stresses of nearby blocks, and, thus, in the surrounding plastic activity, the yield stresses being renewed only every $\dot{\gamma}\dot{\gamma}_y^{-1}$. A clue in this direction is given by the fact that, when the distribution of yield stresses is replaced by a single yield stress, long-lived correlations are no longer observed.

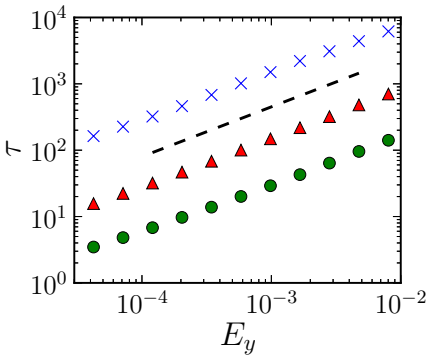

Figure 10.4: Yielding time $\tau(E_y)$ of a fictitious block with an energy barrier E_y, subject only to mechanical noise fluctuations.

Let us now study the yielding time $\tau(E_y)$ of a fictitious block subject only to such mechanical noise fluctuations, as a function of its energy barrier E_y, by measuring how long one has to wait before its elastic energy, $\frac{1}{4\mu}\left\|\int_0^t \delta\dot{\sigma}(t')dt'\right\|$, grows larger than E_y. The data plotted in Fig. 10.4 ***rule out the Arrhenius law characteristic of activated processes***, *i.e.*,

$$\tau\left(E_y\right) \quad \propto \quad e^{\frac{E_y}{x}}, \tag{10.9}$$

for any effective activation temperature x. Instead, they are in favour of a power law dependence, $\tau(E_y) \sim E_y^{n/2} \sim \sigma_y^n$, with $n \simeq 1.5$, which is associated with a hyperdiffusive process ($1 < n < 2$).

Before turning to more general arguments to support these findings, we would like to point out that the model used here boils down to a spatially resolved, athermal version of SGR if plastic events are made instantaneous and allow a complete relaxation of the local stress. In this limit, the evolution of the stress carried by a block as a function of time only consists of phases of elastic loading up to the local yield stress, followed by instantaneous resets of the local stress to zero. Thus, varying the applied shear rate $\dot{\gamma}$ is equivalent to rescaling time, $t \to \dot{\gamma}t$. The macroscopic stress is then clearly independent of $\dot{\gamma}$, contrary to the predictions of SGR at any finite temperature x; in other words, in the regime of negligible thermal fluctuations, the origin of the stress increase hypothesised in the mean-field SGR theory is inconsistent with a lattice-based implementation of the model. It must however be said that Sollich [1998] had explicitly identified the need for a time scale independent of the driving rate in SGR, and suggested that it might emerge from thermally induced hops.

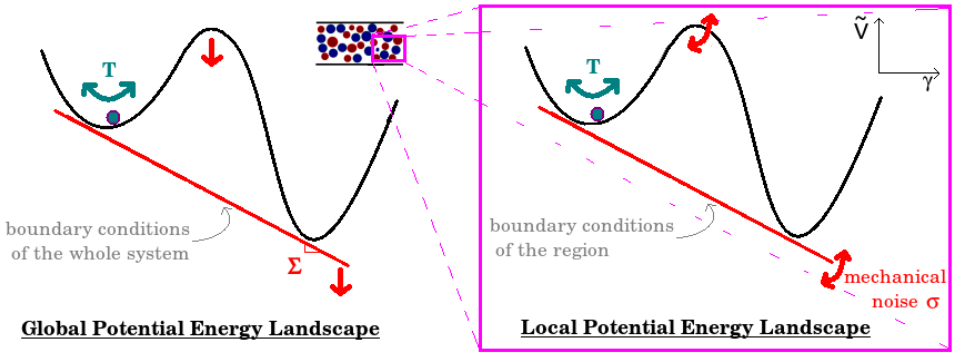

Figure 10.5: Schematic representation of the difference between thermal fluctuations and mechanical noise fluctuations. The sketch on the left depicts the PEL of the whole system being tilted by the application of a macroscopic stress. The rhs is the corresponding picture for a mesoscopic region.

10.3.3 *General arguments*

The results obtained with our model clearly conflict with the idea of a mechanical noise activation temperature. But what is the scope of these results? How general are they?

Let us recall that, in the theory of activated processes, a transition is completed when thermal fluctuations have pushed the system all the way up a potential barrier, in a *fixed* PEL $V(\Gamma)$ [Kramers, 1940]. Recall that $\Gamma \equiv (\boldsymbol{r}_1, \ldots, \boldsymbol{r}_N)$ is a high-dimensional vector containing the positions of all particles. The exponential dependence in the Arrhenius law (Eq. 10.3) hinges on the presence of recoil forces $-\nabla_\Gamma V$ that constantly oppose the uphill motion.

In contrast, consider a mesoscopic region $\mathcal{S}$. Mechanical noise fluctuations due to irreversible rearrangements cause persistent changes to its boundary conditions. These changing boundary conditions *durably* alter the effective PEL (see Section 1.5.1) of the mesoscopic region, along with its minima. (Of course, transient effects, such as temporary dilation, e.g., in metallic glasses [Spaepen, 1977, Bokeloh et al., 2011], or inertial vibrations [Salerno et al., 2012, Salerno and Robbins, 2013], may also occur during plastic events, but, being temporary, they will be subdominant, at least in the limiting case of large energy barriers.)

The disparity between thermal fluctuations and mechanical noise fluctuations is schematically illustrated in Fig. 10.5, in which Γ is substituted by a scalar reaction coordinate, the shear strain γ. In this picture, mechanical noise acts as a "random" external stress, which effectively tilts the PEL of the region of interest. Under its influence, energy barriers wax and wane.[3] Therefore, the flattening out of the barrier, which signals a plastic event, is similar to a first passage time problem in a simple diffusion process over a flat landscape, rather than to thermal activation.

3. ... unless they are located in a direction strictly orthogonal to the tilt, which is unrealistic

10.3.4 *Formalisation of the general arguments in a mesoscopic PEL*

More formally, consider the overdamped Langevin equation of a thermal system [4] (Eq. 2.2),

$$\mathbf{0} = -m\zeta \frac{d\boldsymbol{r_i}}{dt}(t) - \partial_{\boldsymbol{r}_i} V(\Gamma) + \boldsymbol{f_i^{th}}(t), \tag{10.10}$$

where ζ is a friction coefficient, $\langle \boldsymbol{f_i^{th}}(t) \rangle = \mathbf{0}$, and $\langle \boldsymbol{f_i^{th}}(t) \otimes \boldsymbol{f_j^{th}}(t') \rangle = 2m\zeta k_B T \delta(t - t') \delta_{ij} \mathbb{I}$ (where $\mathbb{I}$ is the 3D identity matrix). Following Section 1.5.1, mechanical noise effectively tilts the potential $V(\gamma)$ of the region, supposed of unit volume, into

$$\tilde{V}(\gamma, t) = V(\gamma) - \gamma\sigma(t), \tag{10.11}$$

where $\sigma(t) = \langle \dot{\sigma} \rangle t + f_{\text{mec}}(t)$ is the stress applied at the boundary of the region. Here, the shorthand $f_{\text{mec}}(t) \equiv \int_0^t \delta\dot{\sigma}(\tau) d\tau$ refers to the time integral of mechanical noise fluctuations. We examine the effect of $f_{\text{mec}}(t)$, *i.e.*, the fluctuations around the drift term $\langle \dot{\sigma} \rangle t$. Inserting Eq. 10.11 into the Langevin equation (Eq. 10.10), we get

$$0 = -m\zeta \frac{d\gamma}{dt}(t) - \frac{dV}{d\gamma}[\gamma(t)] + \langle \dot{\sigma} \rangle t + f_{\text{mec}}(t) + f_{\text{th}}(t).$$

Mechanical noise and thermal fluctuations differ in that $\langle f_{\text{th}}(t) f_{\text{th}}(t') \rangle \propto \delta(t - t')$, whereas $\langle f_{\text{mec}}(t) f_{\text{mec}}(t') \rangle = \int_0^t d\tau \int_0^{t'} d\tau' C(\tau - \tau')$. If the autocorrelation function $C(\Delta t) \equiv \langle \delta\dot{\sigma}(t) \delta\dot{\sigma}(t + \Delta t) \rangle$ decays to zero quickly, that is to say, displays neither a fat tail nor strongly negative portions, then $\langle f_{\text{mec}}(t) f_{\text{mec}}(t') \rangle \sim \min(t, t')$, and, in particular, $\langle f_{\text{mec}}(t)^2 \rangle \sim t$. It follows from Eq. 10.11 that an average time $\tau \sim (\max dV/d\gamma)^2 \equiv \sigma_y^2$ elapses before the energy barrier flattens out under the sole influence of f_{mec}, *i.e.*, $\max d\tilde{V}/d\gamma \to 0$.

This purely diffusive case is encountered in Picard's model (*data not shown*), in which the further assumption of linear elasticity implies $\tau \sim \sigma_y^2 \sim E_y$. For the model that we introduced previously, the process was in fact hyperdiffusive, owing to the presence of slowly decaying correlations of the noise. In any case, ***the escape occurs much faster than in an activated process***. In Appendix 10.4.2, we explain why this does not conflict with the numerical simulations of Ilg and Barrat [2007]

Although the reasoning is based on a one-dimensional PEL for convenience, in fact, it does not rely on dimensionality.

4. Note that, despite analogies in the considered mechanisms and the wording, the discussion presented here differs from the investigation of Bouchaud et al. [1995], performed in the context of Bouchaud's trap model, in that the latter considered the impact of *hops of caging particles* on the trajectory of a (caged) particle in the PEL, in terms of the *equilibrium distribution* (if it exists!) of the traps it explores, whereas we focus on the effect of non-local events on the *single barrier-crossing statistics* of a *mesoscopic region*. Nevertheless, formally, both processes can be described by a diffusive term (or assimilated).

10.3.5 *Hierarchy of processes in the limit of very large barriers*

It should be clear that the foregoing discussion focuses on mechanical noise fluctuations, *i.e.*, *corrections* to the effect of the drift term $\mu\dot{\gamma}_{\text{eff}}$. The SGR model is centred on the idea that the flow curve of soft glasses (*a priori*, without restriction) can be explained by these corrective terms. On the contrary, we claim that the flow curve of *athermal materials* results from the interplay between the drive and (cascades of) rearrangements, as explained in Section 7.2.1, and independently of the corrective terms.

To conclude, we can draw a more comprehensive picture of the hierarchy of processes involved in the escape from a (meta)basin in the mesoscopic PEL. The leading order term, $\mu\dot{\gamma}_{\text{eff}}$, is ballistic; the (hyper)diffusive corrective term due to persistent mechanical noise fluctuations comes next. Then, transient effets occurring during plastic events, for instance, dilation and inertial vibrations, along with true thermal fluctuations, yield exponentially weak corrections. This hierarchy of terms is presented in Table 10.1. Nevertheless, it is crucial to bear in mind that the hierarchy only holds in the asymptotic limit of large barriers or small fluctuations. It most surely breaks down for a high-temperature glass.

As a final word on the topic, we should note that there exists yet another effective temperature definition, used for instance in the Shear Transformation Zone (STZ) theory. The STZ temperature, usually denoted χ, does not control the local temporal fluctuations of an observable, but rather its variations in space, *i.e.*, the probability of finding, say, a given free volume at some position in space [Bouchbinder et al., 2007a,b], even though the distinction was originally misty (see Section III.A of Ref. [Falk and Langer, 1998]). In this respect, it is a measure of disorder in the system. It is therefore not incidental if it shares the same notation as the compactivity introduced by Edwards and Oakeshott [1989] for granular matter, and defined as the derivative of the volume V with respect to the entropy S, *viz.* $\chi \equiv \partial V/\partial S$.

Key Points of the Chapter[a]

- A fluctuation-dissipation based effective temperature quantifying the magnitude of stress fluctuations can be measured in one version of the elastoplastic model.
- Mechanical noise fluctuations lead to barrier-crossing statistics that differ in essence from those induced by thermal fluctuations (in the limit of large barriers), because the former are persistent whereas the latter induce recoil forces.

a. A paper presenting these findings has been submitted to *Europhysics Letters* [Nicolas et al., 2014a].

Material time scales	*Driving time scales*	*Nature of hops*	
Descent τ_{pl} Thermally activated hop τ_T	Macroscopic driving $\dot{\gamma}$	BALLISTIC	Uniform
	Average contribution from non-local plastic events $\dot{\gamma}^{\text{eff}} - \dot{\gamma}$		
	Persistent mechanical noise $\delta\dot{\gamma}$	"DIFFUSIVE"	Spatial
	Transient effects during plastic events (*e.g.*, inertial vibrations, dilation). Can be interpreted as zero-average mechanical noise.	ACTIVATED	

Table 10.1: Hierarchy of processes in the flow, sorted by the associated yield time $\tau(\sigma_y)$ of a block of yield stress σ_y. Ballistic hops refer to $\tau(\sigma_y) \sim \sigma_y$, "diffusive" hops refer to $\tau(\sigma_y) \sim \sigma_y^n$ with $n > 1$, and activated hops refer to $\tau(\sigma_y) \sim \exp(\sigma_y^n)$, $n > 0$. "Uniform" processes are those which are independent of the spatial position of the block.

A

10.4 APPENDICES

10.4.1 *Scale of stress fluctuations in a generic elastoplastic model*

We propose to consider a generic model in which the number $\mathcal{P}$ of sites having a local stress σ and the number $\mathcal{A}$ of *plastically active* sites with stress σ evolve as

$$\begin{cases} \frac{\partial P}{\partial t}(\sigma,t) &= \frac{\partial}{\partial \sigma}\left\{\mu\dot{\gamma}\mathcal{P} + j^{\text{pl}}\left[\mathcal{A}\right]\right\} \\ \frac{\partial \mathcal{A}}{\partial t}(\sigma,t) &= \underbrace{\frac{\partial}{\partial \sigma}\left\{\mu\dot{\gamma}\mathcal{A} + j^{\text{pl}}\left[\mathcal{A}\right]\right\}}_{\text{drift}} + \underbrace{\left[\mathcal{P}(\sigma,t) - \mathcal{A}(\sigma,t)\right] l(\sigma)}_{\text{yield}} - \underbrace{\mathcal{A}(\sigma,t)\, e(\sigma)}_{\text{el. recovery}}, \end{cases} \tag{10.12}$$

where $\mu\dot{\gamma}\mathcal{P}$ is the (constant) stress flux due to the macroscopic drive and the unspecified functional j^{pl} is the stress flux induced by plastic events. As usual, l and e are the rates of plastic yield and elastic recovery, respectively. Equations 10.12 can be derived from the master equation of our elastoplastic model (Eq. 8.1) by discarding all spatial information. To allow for a distribution of yield stresses, instead of a unique local yield stress, we replace σ with the distance to the local yield stress, $x \equiv \sigma_y - \sigma$ in Eqs. 10.12 , *viz.*,

$$\begin{cases} \frac{\partial \mathcal{P}}{\partial t}(x,t) &= -\frac{\partial}{\partial x}\left\{\mu\dot{\gamma}\mathcal{P} + j^{\mathrm{pl}}\left[\mathcal{A}\right]\right\} \\ \frac{\partial \mathcal{A}}{\partial t}(x,t) &= -\frac{\partial}{\partial x}\left\{\mu\dot{\gamma}\mathcal{A} + j^{\mathrm{pl}}\left[\mathcal{A}\right]\right\} + \left[\mathcal{P}(x,t) - \mathcal{A}(x,t)\right] l(x) - \mathcal{A}(x,t)\, e(x). \end{cases} \tag{10.13}$$

Regarding the validity of Onsager's hypothesis (Question (ii) of Section 10.2.3), it is clear that the response to a given perturbation $\delta\mathcal{P}\left(\sigma, t=0\right)$ is independent of the microscopic or macroscopic nature of this perturbation. On the other hand, the perturbation that is artificially created in order to measure G in Section 10.2.4, namely, a global shift of $\mathcal{P}$ at $t=0$, is most probably atypical in the unperturbed evolution of the system, so it is yet unclear whether the response to these atypical fluctuations will reflect the regression of steady-state fluctuations.

To assess the scale of the macroscopic stress fluctuations $\delta\Sigma\left(t\right) \equiv \int \sigma\delta\mathcal{P}(\sigma,t)d\sigma$ (Question (iii) of Section 10.2.3), let us first consider the fate of a spontaneous perturbation $\delta\mathcal{P}\left(x, t=0\right) = \alpha\delta\left(x - x_0\right)$. Following Eqs. 10.13, in the shear-dominated regime, the perturbation $\delta\mathcal{P}$ is first advected by the drift term $-\mu\dot{\gamma}\frac{\partial\mathcal{P}}{\partial x}$ to a region close to yield ($x=0$), where the yield rate $l(x)$ is large. Plastic yield creates a perturbation $\delta\mathcal{A}$, which obeys (see second line of Eqs. 10.13),

$$\frac{\partial\delta\mathcal{A}}{\partial t}\left(0, t \approx {}^{x_0}/_{\mu\dot{\gamma}}\right) \simeq \alpha\, l(0). \tag{10.14}$$

This excess/dearth of plastic activity helps relax $\delta\mathcal{P}$, thanks to the term $j^{\mathrm{pl}}\left[\mathcal{A}\right]$ in the first line of Eqs. 10.13.

Let us assume that the relaxation is essentially achieved after only *one* such cycle of yield. Considering that the fluctuations $\delta\mathcal{P}$ are more or less homogeneously distributed in x, Eq. 10.14 turns into

$$\frac{\partial\delta\mathcal{A}}{\partial t}\left(0, t \approx {}^{x_0}/_{\mu\dot{\gamma}}\right) \approx \|\delta\mathcal{P}\|\, l(0).$$

Since $\frac{\partial\delta\mathcal{A}}{\partial t}\left(0,t\right)$ scales with the fluctuations in $N_{\mathrm{act}}(t) \equiv \int \mathcal{A}(\sigma,t)d\sigma$, the total number of instantaneous plastic events, divided by the life time τ of a plastic event, we can assess the magnitude $\sqrt{\delta\mathcal{P}^2}$ of spontaneous perturbations by measuring the fluctuations in the plastic activity, that is,

$$\sqrt{\delta\mathcal{P}^2} \approx \frac{N_{\mathrm{act}}(t)}{\tau}\, l(0)^{-1}.$$

To conclude, the scale of macroscopic stress fluctuations is given by

$$\begin{aligned} \sqrt{\delta\Sigma^2} &= \sqrt{\int \sigma^2\delta\mathcal{P}(\sigma,t)d\sigma} \\ &\sim \sqrt{\delta\mathcal{P}^2}, \\ &\sim \sqrt{N_{\mathrm{act}}(t)}, \end{aligned}$$

with naturally very crude approximations. Nevertheless, recalling that in the shear-dominated regime $N_{\text{act}}(t) \propto \dot{\gamma}$, we reach the following conclusion: $\sqrt{\delta\Sigma^2}$ scales with $\sqrt{\dot{\gamma}}$, *ergo*, $T_{\text{eff}} \sim \sqrt{\dot{\gamma}}$.

Note that this result is relatively intuitive in the light of the central limit theorem.

Also note that the central role played here by the distribution of stresses close to the yield stress, *i.e.*, $\mathcal{P}(x \approx 0)$, echoes its importance in Refs. [Karmakar et al., 2010, Lin et al., 2014b,a].

In the former article, Karmakar et al. [2010] showed on the basis of atomistic simulations that the scaling[5] $\mathcal{P}(x) \sim x^{\theta}$ when $x \to 0$ differs qualitatively between the isotropic quenched state prior to shear, where $\theta > 0$ so that $\mathcal{P}(x) \to 0$, and the sheared steady state, where $\theta \lll 1$. In other words, the system needs to be destabilised by shear for a finite time before the distribution of x self-organises into a critical state capable of sustaining power-law avalanches [Bak et al., 1987], *i.e.*, in which enough regions have been brought on the brink of yielding ($x \approx 0$).

On their side, Lin et al. [2014b] studied the steady-state scaling exponent θ with a coarse-grained model similar to ours, and reported on its apparent independence with respect to the choice of dynamical rules. On the other hand, θ depends on the interaction range of the elastic propagator. In Ref. [Lin et al., 2014a], some of these authors insist that θ should be strictly positive for a propagator of non-constant sign, because, under the influence of the interactions, blocks then perform a random walk close to the "absorbing" boundary at $x = 0$, while a finite density of sites near $x = 0$, implying $\theta = 0$, is expected when the interaction is of constant sign, *i.e.*, always destabilising, as in the case of the depinning of a front line on a disordered substrate.

10.4.2 *Activation temperature measured with a two-state system*

We have shown that the hopping statistics do not obey the Arrhenius dependence characteristic of activated events, if the reaction coordinate that describes a hopping event is coupled to the mechanical noise. This is typically the case if the hop is a plastic event that is governed by the local stress or strain, presumably. On the other hand, an Arrhenius law is recovered when the equation of motion of the reaction coordinate (or equivalently the potential energy of the system as a function of the reaction coordinate) is not durably altered by mechanical noise fluctuations.

For instance, Ilg and Barrat [2007] performed molecular dynamics simulations of the shear flow of a glassy system and introduced bead-and-spring dumbbells in the flow. The dumbbells were maintained aligned in the neutral direction. The inversion rate of the dumbbells was measured, and it was observed to follow an Arrhenius law. To understand this point, one can argue that the frequent realignment of the dumbbells along the neutral direction erases the memory of

5. This scaling is inferred from the distribution of the minimal strain increments required to trigger a plastic event.

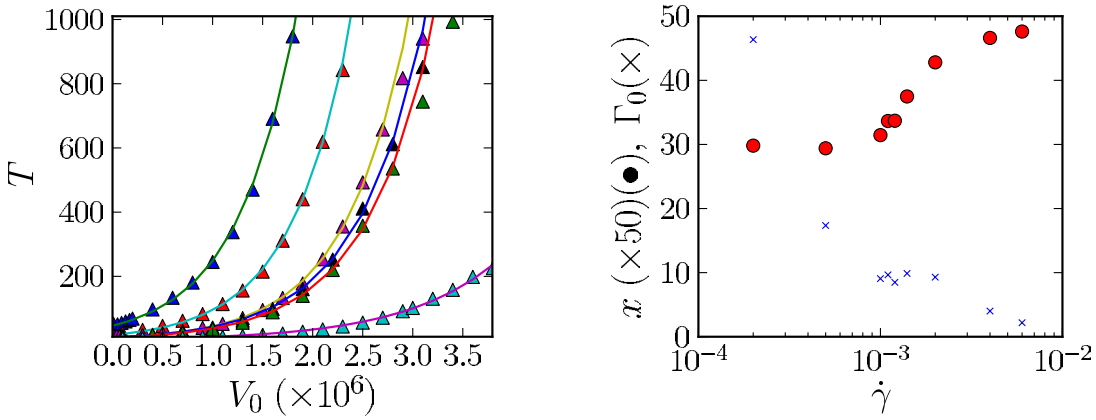

(a) Hopping time as a function of barrier height V_0 for $\dot{\gamma} = 2 \cdot 10^{-4}$, $5 \cdot 10^{-4}$, 10^{-3}, $4 \cdot 10^{-3}$, fitted with exponential functions $\omega_0 \exp\left(\frac{V_0}{x}\right)$.

(b) (*Red dots*) Effective activation temperature x and (*blue crosses*) attempt frequency $\Gamma_0 = \tau\omega_0$ as a function of the applied shear rate $\dot{\gamma}$.

Figure 10.6: Effective activation temperature of the dumbbell systems.

the effect of the mechanical noise on the reaction coordinate, namely, the distance between the beads, thereby turning it into a non-persistent fluctuation.

As a matter of fact, a similar attempt can be carried out in the framework of our coarse-grained model: In every elastoplastic block, we dispose a two-state dumbbell in the crosswise direction. The potential energy of the dumbbell only depends on the distance u between the beads and reads, $V(u) = V_0 \left(\frac{(u-u_0)^2-\epsilon^2}{\epsilon^2}\right)^2$, with $\epsilon \ll u_0$. Thus, the dumbbell has two ground states, at $u = u_0 - \epsilon$ (L) and $u = u_0 + \epsilon$ (R), separated by a barrier of height V_0. During the simulation, each of the beads is advected by the velocity field $v_y^{(\mathrm{ext})}(\boldsymbol{r}, t) = \int P(\boldsymbol{r} - \boldsymbol{r'}) \cdot \dot{\boldsymbol{\epsilon}}^{\mathbf{pl}}(\boldsymbol{r'}, t)\, d^2\boldsymbol{r'}$ created by plastic events, so that,

$$\zeta\left(\dot{u} - \nabla v_y^{(\mathrm{ext})}(t) \cdot u_0\right) \simeq \frac{dV}{du}(u),$$

where ζ is a friction coefficient. To measure the dumbbell L-R inversion rate, we define the exclusive attraction basins of the ground states L and R as $u - u_0 \in]-\infty, -\delta \cdot \epsilon]$ and $u - u_0 \in [\delta \cdot \epsilon, \infty[$, respectively with $0 < \delta \approx 0.5 < 1$ (the precise value of δ hardly affects the results).

In Fig. 10.6a, we show the resulting hopping times between the basins as a function of the potential V_0, measured in units of ζ, for a given ϵ. Note that the measured hopping times actually depend on ϵ, which controls the curvature of the potential. An Arrhenius law nicely fits their dependence on V_0, consistently with the findings of Ilg and Barrat. In Fig. 10.6b, the effective activation temperature associated with the Arrhenius law is plotted as a function of the applied shear rate $\dot{\gamma}$. Consistently with the expectations, it increases with the shear rate.

11

SHEAR LOCALISATION

The investigation of spatially averaged quantities in Chapters 9 and 10 has left aside the prominent question of spatial heterogeneities in the flow of disordered solids. To compensate, this chapter is concerned with the study of the spatial organisation of the flow on the macroscale; the specific aim is to determine the model ingredients (and the associated physical parameters) that give rise to the widely observed phenomenon of shear localisation.

11.1 ANALYTICAL APPROACH TO SHEAR LOCALISATION IN PICARD'S MODEL

In some parameter range, Picard's scalar model (exposed in Section 9.1.1) was reported to display shear localisation [Martens et al., 2012]. Accordingly, for a start, we carry on and deepen the analysis within this model, and its tensorial and convected extensions.

11.1.1 *Mean-field analysis*

Martens et al. [2012] performed a mean-field analysis of Picard's model in a simple shear setup. The starting point is the (scalar) stress evolution equation (equivalent to Eq. 8.1):

$$\partial_t \sigma(i,j;t) = \dot{\gamma} + \sum_{i',j'=1}^{L} \mathcal{G}\left(i-i', j-j'\right) n(i',j';t)\sigma(i',j';t), \tag{11.1}$$

where we have set $\mu = 1$ and $\tau = 1$. and $n(i,j;t)$ is the plastic activity of block (i,j), *i.e.*, $n = 1$ if the block is plastic, o otherwise. First, Eq. 11.1 is averaged over time and space, *viz.*,

$$\begin{aligned} \langle \partial_t \sigma \rangle &= \left\langle \dot{\gamma}^{\text{eff}} \right\rangle + \mathcal{G}\,(0,0)\,\langle n\sigma \rangle \\ \text{where } \dot{\gamma}^{\text{eff}}(\boldsymbol{r};t) &\equiv \dot{\gamma} + \sum_{\boldsymbol{r}' \neq \boldsymbol{r}} \mathcal{G}\left(\boldsymbol{r}-\boldsymbol{r}'\right)(n\sigma)\left(\boldsymbol{r}';t\right). \end{aligned}$$

Here, $\boldsymbol{r}$ stands for (i,j) and we have separated the non-local interactions, included in $\dot{\gamma}^{\text{eff}}$, from the local ones. In the steady state, using the shorthand $g_0 \equiv -\mathcal{G}\,(0,0) > 0$, we obtain

$$0 = \left\langle \dot{\gamma}^{\text{eff}} \right\rangle - g_0 \langle n\sigma \rangle . \tag{11.2}$$

Finally, in a mean-field spirit, the fluctuations of $\dot{\gamma}^{\text{eff}}$ are neglected, *i.e.*, $\langle \dot{\gamma}^{\text{eff}} \rangle \to \dot{\gamma}^{\text{eff}}$. With the help of Picard's dynamical rules, this leads to the desired relation $\langle \sigma \rangle = f(\dot{\gamma}^{\text{eff}})$, where the function f depends on τ_{res}, τ_{liq}, and g_0. Interestingly, when the restructuring time is long, f becomes non-monotonic, with a decreasing part at low shear rates. For $\tau_{\text{liq}} = 1$ and $g_0 = 0.57$, this occurs when $\tau_{\text{res}} \geqslant \tau_{\text{res}}^c \simeq 3.3$.

Such non-monotonicity signals the occurrence of shear-banding. Indeed, ***decreasing parts in the constitutive curve*** f are unstable, in the sense that, in this range of shear rates, the system will lose its homogeneity and split into a region of low (here, zero) shear rate and a region subject to high shear rates, both having equal stresses. The qualitative effect of τ_{res} is in line with the scenario described by Coussot and Ovarlez [2010], whereby long rearrangements imply long periods of low stress and therefore, since the number of rearrangements increases with the shear rate, lead to drastic shear-thinning, climaxing in non-monotonicity of the constitutive curve.

11.1.2 *Linear stability analysis*

In order to determine the spatial profile of the instabilities that can alter the mean-field picture, we perform a linear stability analysis of the homogeneous mean-field solution $\left(\langle \sigma \rangle, \langle n \rangle, \langle \dot{\gamma}^{\text{eff}} \rangle\right)$ with respect to a space-dependent perturbation $\left[\delta\sigma(\boldsymbol{r};t),\, \delta n(\boldsymbol{r};t),\, \delta\dot{\gamma}^{\text{eff}}(\boldsymbol{r};t)\right]$. After a transformation to Fourier space and a linearisation of the equations, we find that the $\boldsymbol{q}$-Fourier mode of the perturbation grows at an initial rate

$$\alpha_{\boldsymbol{q}} = \frac{\langle n \rangle \, \mathcal{G}(\boldsymbol{q})}{1 - \nu \langle \sigma \rangle \, \mathcal{G}(\boldsymbol{q})},$$

where ν is a strictly positive scalar and $\mathcal{G}(\boldsymbol{q}) = \frac{-4q_x^2 q_y^2}{\left(q_x^2+q_y^2\right)^2} \leqslant 0$, with $\boldsymbol{q} = \left(q_x, q_y\right)$, is the Fourier-transform of the elastic propagator. Consequently, all perturbation modes decay, except ***bands***, *i.e.*, perturbations with either $q_x = 0$ or $q_y = 0$, which have a zero growth rate and, therefore, an undetermined fate. This is compatible with numerical observations, where, in unstable situations, shear localises in bands (see below).

11.1.3 *Fluctuations and interface width*

The mean-field constitutive curve, complemented with the stability analysis, predicts the destabilisation of the system into solid bands and liquid bands, for long enough restructuring times and low enough shear rates. However, this analysis does not specify the number of such bands. Indeed, interfaces between bands are not assigned any "cost" nor any width. On the other hand, in the steady state, numerical simulations of the model as well as experiments rarely contain more than one band, whose interface has a finite width.

This discrepancy is reminiscent of Radulescu and Olmsted's observation that interfaces are infinitely sharp in reaction models if the stress equations are not complemented with a diffusive term of the form $D\nabla^2\sigma$ [Olmsted, 2008]. After inclusion of this term, interfaces scale with $\sqrt{D\tau}$, where τ is the characteristic time for stress relaxation. However, Eq. 11.1 features no diffusive term, but only a convolution with $\mathcal{G}$, which merely produces a *uniform* stress contribution when bands coexist. [1] What sets the finite width of the interface, then?

There are serious reasons to believe that the answer lies with the fluctuations of plastic activity in the sheared band. These fluctuations are always present in the model because of the dynamical rules. Were the interface between bands infinitely sharp, the propagation of these fluctuations with $\mathcal{G}$ would trigger plastic events outside the shear band, thereby rendering the interface more diffuse.

Accordingly, in this scenario, stress fluctuations play a major role in smoothing discontinuities between shear bands. Interestingly, they are also central in the fluidisation process of carbopol gels, which occurs after a long-lived shear-localised state: in the transient regime, shear is confined to a thin lubrication layer close to the rotor (of a Taylor-Couette apparatus), and erosion drives the bulk of the material into a critical state, presumably *via* the creation of stress fluctuations, until the whole sample finally (more or less) suddenly fluidises [Divoux et al., 2011a].

11.2 NUMERICAL INVESTIGATION OF SHEAR-BANDING IN PICARD'S MODEL

Let us now move on to a numerical study of the model. We fix $\tau_{\text{liq}} = 1$.

11.2.1 *Qualitative picture*

We simulate Picard's model in the static scalar version, the static tensorial version, and the convected tensorial version (see Section 9.1 and Chapter 8 for details). The system is prepared by pre-shearing at $\dot{\gamma} = 1$.

Figure 11.1 shows the localisation of the plastic activity in a band for $\tau_{\text{res}} = 10$ and $\dot{\gamma} = 10^{-2}$. The band widens linearly with the applied shear rate until homogeneity is restored [Martens et al., 2012]. Even though full shear localisation is observed in the steady state, the band(s) may diffuse over long times, because they are not pinned by a heterogeneity in the drive, as they would be in an experimental Taylor-Couette geometry owing to the larger stress at the rotor. The diffusivity is reduced when the system size is increased, so that one may expect a pinning of the band in the limit of an infinite system.

These general observations hold for all versions of the model, whether static or convected, scalar of tensorial. However, a major difference between static versions and tensorial ones should be noted. In the former, bands are observed

1. This is due to the fact that $\mathcal{G}(\boldsymbol{q}) = 0$ for $q_x = 0$ or (exclusive or) $q_y = 0$.

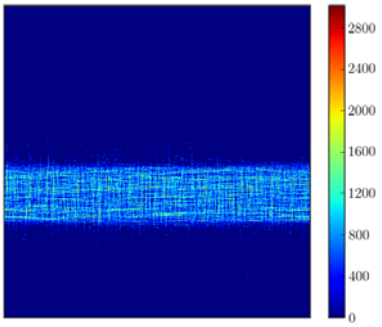

Figure 11.1: Cumulated plastic activity (*arbitrary units*) over a strain window $\Delta\gamma = 2$, close to the steady state, in the static tensorial model with $\tau_{res} = 10$, at $\dot{\gamma} = 10^{-2}$. System size: $N = 512 \times 512$.

both in the velocity direction and the velocity gradient direction, these directions being equivalent in the equations, because the deformation tensor is symmetric. Convection breaks this spurious equivalence through the displacement of the streamlines; as a result, shear bands are ***exclusively in the flow direction*** (and not perpendicular to it), in accordance with experimental observations.

Regarding the transient regime, as the shear rate is applied after pre-shear, we first observe the gradual emergence of thin "slip" bands throughout the system; longer-lived bands then appear. The final coalescence of these bands into a unique shear band occurs after a system-size-dependent shear strain $\Delta\gamma_{ss}$. For instance, for $\tau_{res} = 10$ and $\dot{\gamma} = 10^{-2}$, $\Delta\gamma_{ss} \simeq 6$ for a relatively small system of $N = 64 \times 64$ blocks, $\Delta\gamma_{ss} \simeq 36$ for $N = 256 \times 256$.

11.2.2 *The shear-banding observable*

To quantify to what extent shear localises, we introduce the shear-banding observable $\kappa(\Delta\gamma) \equiv (n_{max} - n_{min})/(n_{max} + n_{min})$, where n_{max} and n_{min} denote the maximum and minimum of the line-averaged cumulated plastic activities over strain windows $\Delta\gamma$, *i.e.*, the total time spent in the plastic state in that strain interal. To smooth out fluctuations, line averages are further averaged with the first neighbouring lines. With this definition, a vanishing value of κ signals homogeneous flow, whereas $\kappa = 1$ indicates full shear localisation. A finite value of the strain interval $\Delta\gamma$, in the range 10 to 30, is chosen, small enough to avoid significant shear band diffusion but long enough to wipe out the short-lived slip lines that are observed even in the absence of shear localisation. The picture is nevertheless robust to moderate variations of $\Delta\gamma$.

The shear-banding observable κ is shown in Fig. 11.2a for various τ_{res} and $\dot{\gamma}$ and confirms the enhanced propensity to shear-banding at low $\dot{\gamma}$ and large τ_{res}. The apparent decrease of κ at very low shear rates is most probably due to shear band diffusion, since the strain interval $\Delta\gamma$ corresponds to increasingly large time intervals as $\dot{\gamma}$ decreases.

A comparison between the different versions of the model for a strain window $\Delta\gamma = 30$ reveals that the tensorial, instead of scalar, description of stress in the static model has virtually no effect on the shear-banding diagram (Fig. 11.2a). On the other hand, convection curtails shear-localisation to some extent (Fig. 11.2b). We ascribe this to enhanced stress fluctuations outside the potential shear band in the convected model, which results in an increased band mobility. The static *vs.* convected discrepancy vanishes when the strain window is reduced, for instance, to $\Delta\gamma = 5$ (*data not shown*). For smaller system sizes ($N = 64 \times 64$), shear-banding profiles tend to be more diffuse, and shear bands are more mobile, owing to larger fluctuations, but the qualitative picture remains identical.

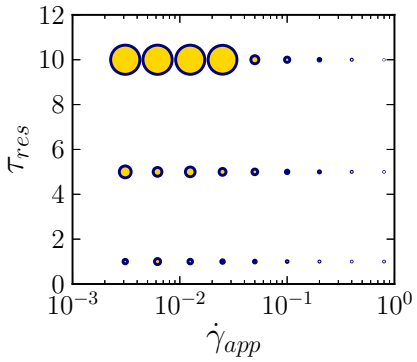

(a) (*Filled circles*) Static scalar model. (*Open circles*) Static tensorial model.

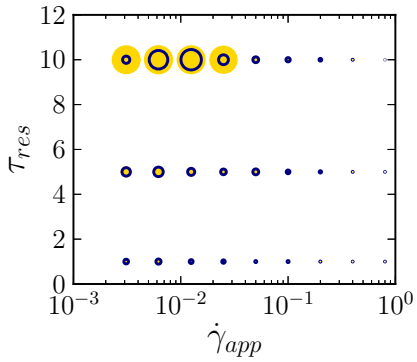

(b) (*Filled circles*) Static scalar model. (*Open circles*) Convected tensorial model..

Figure 11.2: Dependence of the shear-banding observable κ on the shear rate $\dot{\gamma}_{\text{app}}$ and τ_{res}, for a strain interval $\Delta\gamma = 30$, $N = 128 \times 128$. Circles are all the larger as κ is (proportionally) large.

11.3 SHEAR-LOCALISATION IN THE REFINED MODEL

Let us now consider the athermal model with the more realistic dynamical rules introduced in Sections 9.3-9.4.

In the absence of short-term ageing ("structural relaxation") after a plastic event, *i.e.*, for a rate of recovery $k = \infty$ of the maximal yield stress in Eq. 9.3, the model does not display shear localisation, as expected on account of the Herschel-Bulkley flow curve. As in Ref. [Jagla, 2007] (also see Section 6.3), structural ageing, obtained by taking a finite value of k, is therefore a prerequisite to shear localisation in this model.

Figure 11.3 presents the extent of shear localisation as a function of $\dot{\gamma}$ and k. Consistently with the observation of a plateau in the flow curve at low values of k in Fig. 9.5b, shear localisation is observed in these cases. Indeed, when k is too low, the driving rate $\dot{\gamma}$ competes with the recovery process: rupture in a region makes it durably weaker. Shear bands develop considerably faster than in Picard's model and tend to be very thin (acute shear localisation). When the shear

rate is reduced to extremely low values, $\dot{\gamma} \ll k$, one would expect to recover a homogeneous flow in the steady state, similar to that for $k = \infty$ [Chikkadi et al., 2011]; this still needs to be confirmed.

Qualitatively, the rate of recovery k is thus analogous to the inverse of the restructuring time τ_{res} in Picard's model. It is worth recalling that Vandembroucq and Roux [2011], too, have studied a spatially-resolved elastoplastic model with permanent strain weakening, which boils down to $k = 0$ with our notations. They also reported shear localisation in the shear weakening case (also see Section 6.2.3).

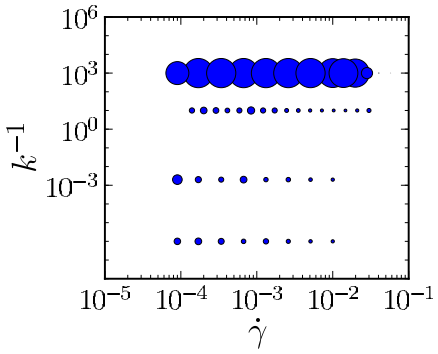

Figure 11.3: Dependence of the shear-banding parameter κ on the applied shear rate $\dot{\gamma}$ and the recovery time k^{-1}. The largest circle corresponds to $\kappa = 1$. The system consists of 128×128 blocks.

11.4 SPECULATIVE GENERAL CRITERION FOR SHEAR LOCALISATION

The related, but distinct, conditions for shear localisation in Picard's model and in the refined model elicit a more general criterion determining the onset of shear localisation.

We suggest to put the concept of ***healing time*** at the core of the criterion.

Indeed, there is now growing evidence that the longer the material needs to heal back to its pristine state after a plastic event, the more prone it is to shear localisation. The healing time following rupture-induced "damage" can take diverse forms in practice; it can be, for instance,

- the duration of the rearrangement itself as reported by Coussot and Ovarlez [2010], Martens et al. [2012],

- the thermally activated rebinding of failed contacts, *e.g.*, in fibre bundle models [Kun et al., 2008],

- the chemical relaxation time of the local mechanical (*e.g.*, surface tension in foams) properties towards their equilibrium values after a plastic event (which Denkov et al. [2009] argue results in a flatter flow curve for foams with high

surface modulus surfactants, as compared to their low surface modulus counterparts),

- the time to relax the local free-volume increase created by a rearrangement, in metallic glasses [Schuh et al., 2007], or

- the time to dissipate the induced heat [Shimizu et al., 2006].

Alternatively, in its initial state, the material may have been stabilised by ageing or a careful preparation protocol involving a slow cooling rate, the benefits of which are lost locally upon the occurrence of a plastic event [Shimizu et al., 2006].

In this vein, Kumar et al. [2013] recently reported that the lower the fictive temperature of a metallic glass, the more brittle it is.

Also, attractive interactions are often reported to enhance the heterogeneity of the flow, which may be connected to long timescales to form stable aggregates [Irani et al., 2014].

But the ***enhanced tendency to shear localisation upon increasing the healing time*** appears to transcend the variety of the mechanisms that are involved.

Key Points of the Chapter

- Shear localisation is observed in elastoplastic models for long restructuring times (Picard's model) or intense shear rejuvenation (refined model), regardless of the scalar or tensorial nature of the model.
- Convection aligns shear bands along the flow direction only (suppressing the situations of perpendicular alignment observed in static models).
- The overarching concept of long healing times accounts for the propensity to shear localise of very diverse materials.

12

CORRELATION LENGTHS

Even when the flow of amorphous solids is not permanently shear-banded on the macroscale, some of its average macroscopic properties cannot be described by the theory based on independent collisions or hopping events that is used for simple fluids. Before we address a situation which exemplifies this inadequacy in the next chapter, let us here examine the origin of this difference, namely, the existence of spatial correlations in the flow. These correlations should be particularly extended in a slow flow, while, at high shear rates, we expect them to be suppressed and a mean-field, simple-fluid-like picture to be restored.

How do the correlations quantitatively scale with the shear rate? In the limit of vanishing shear rates, is this scaling sensitive to the specific definition of the correlation length? Is it robust to changes in the dynamical rules of the elastoplastic model?

As in the previous chapter, we use Picard's model (see Section 9.1.1) as a benchmark and study different correlation lengths, before turning to the refined model. Throughout the chapter, we shall only consider macroscopically homogeneous flows, so that the observed correlations reflect the properties of the bulk flow and the 'hybridisation' effects that arise when shear bands co-exist in the system are avoided.

12.1 SCALINGS OF THE CORRELATION LENGTHS IN PICARD'S MODEL

12.1.1 *Picard's correlation length definition*

Picard et al. [2005] introduced a characteristic length ξ_P based on macroscopic stress drops. It stems from the observation that, below a $\dot{\gamma}$-dependent system size, macroscopic stress drops in the jerky stress *vs.* strain curve (normalised by the average stress) saturate due to finite-size effects. Since stress drops are caused by avalanches of plastic events, $\xi_P(\dot{\gamma})$ is defined as the linear system size below which saturation occurs. It was found to scale with $\dot{\gamma}^{-1/2}$.

After an examination of the values of ξ_P, it seems to us that saturation actually occurs when the applied shear rate is decreased to such an extent that there is at most one plastic event in the simulation cell at any time. In that case, the characteristic length is but a measure of the spacing between plastic events. In the athermal regime, the number of plastic events grows linearly with the shear rate, hence the scaling $\xi_P \sim \dot{\gamma}^{-1/2}$.

12.1.2 *Instantaneous cooperative disk*

Definition

Let us now propose an alternative protocol to define a correlation length, rooted in the interpretation of the onset of flow in an amorphous solid as a dynamic phase transition (see, *e.g.*, Ref. [Bocquet et al., 2009]). Setting the macroscopic shear stress σ_{xy} as a control parameter, we view the steady-state strain-rate tensor $\dot{\boldsymbol{\epsilon}}$ as an order parameter, which goes to zero below the yield stress and continuously increases above it.

One may then wonder whether a mean-field approach is applicable, or whether it breaks down because of (spatiotemporal) fluctuations. To answer this question, we assess how large the standard deviation of the fluctuations $\sqrt{\langle \|\delta\dot{\boldsymbol{\epsilon}}\|^2 \rangle}$ experienced at an arbitrary point M in the system is, compared to the mean value $\|\langle\dot{\boldsymbol{\epsilon}}\rangle\|$ of the order parameter. Except at very large shear rates, this ratio is always large, because plastic events occurring close to M cause very large fluctuations. But should we only consider the effect of *distant* plastic events, would the fluctuations then be negligible, and a mean-field treatment applicable to them?

Concretely, at arbitrary points, we compute the mechanical noise $\dot{\boldsymbol{\epsilon}}(\xi)$ due to plastic events taking place farther than some distance ξ from M. The use of a Ginzburg-Landau criterion $\sqrt{\langle \|\delta\dot{\boldsymbol{\epsilon}}\|^2 \rangle}/\|\langle\dot{\boldsymbol{\epsilon}}\rangle\|(\xi) < 1$ allows us to distinguish a cooperative disk of radius $\xi^\star$ around M, from an outer region which is amenable to a mean-field treatment, i.e., which satisfies the criterion. With regard to the *instantaneous* mechanical noise at M, the details of the individual plastic events occurring within the cooperative disk will matter, whereas outside the disk they will not.

In addition, the comparison between the cooperative length $\xi^\star$ and the size of a structural rearrangement (the unit size, here) will be a valuable hint as to whether our model gives credence to mean-field analyses [Dahmen et al., 2009], possibly complemented with a diffusion term to account for spatial fluctuations [Bocquet et al., 2009, Fielding et al., 2009, Kamrin and Koval, 2012].

Measurements

Figure 12.1 shows that the data collapse onto a master curve,

$$\frac{\sqrt{\langle \|\delta\dot{\boldsymbol{\epsilon}}\|^2 \rangle}}{\|\langle\dot{\boldsymbol{\epsilon}}\rangle\|}(\xi) \sim \frac{1}{\xi\sqrt{\bar{\gamma}}}. \tag{12.1}$$

We have checked that this scaling is not marred by finite-size effects. It immediately follows from Eq. 12.1 that $\xi^\star \sim \dot{\gamma}^{-1/2}$, which is confirmed by Fig. 12.2 for all versions of the model. The assumption [1] that plastic events should be only weakly interacting in a slow flow, at low temperature may therefore seriously be called into question.

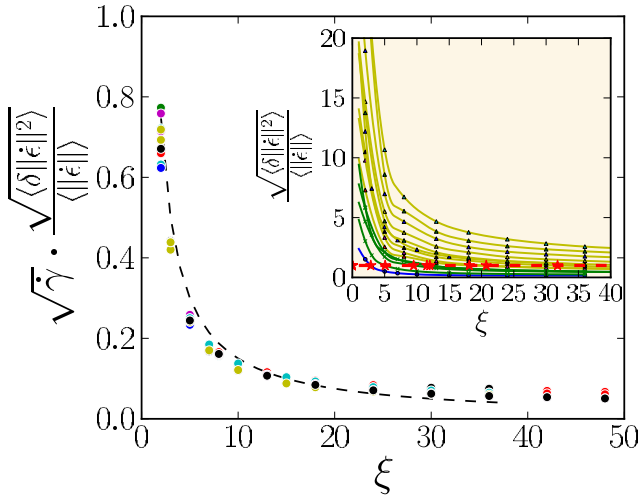

Figure 12.1: Ratio of fluctuations over mean value of the mechanical noise due to plastic events taking place farther than ξ, rescaled with $\sqrt{\dot{\gamma}}$, as a function of ξ, in the convected tensorial model. System size: $N = 256 \times 256$. Data include points at $\dot{\gamma} = 5.4 \cdot 10^{-4}$, $8.1 \cdot 10^{-4}$, $1.2 \cdot 10^{-3}$, $1.8 \cdot 10^{-3}$, $2.7 \cdot 10^{-3}$, $3.5 \cdot 10^{-3}$, $4.0 \cdot 10^{-3}$, $6.0 \cdot 10^{-3}$, $9.0 \cdot 10^{-3}$, $1.3 \cdot 10^{-2}$, $1.4 \cdot 10^{-2}$, $2.0 \cdot 10^{-2}$, $1.3 \cdot 10^{-2}$,$2.0 \cdot 10^{-2}$, $5.6 \cdot 10^{-2}$,$2.0 \cdot 10^{-2}$, 0.23. The dashed black line represents $y = {}^{1.5}/_{\xi}$. *Inset:* Same data, not rescaled with $\sqrt{\dot{\gamma}}$. The yellow ($\dot{\gamma} < 10^{-2}$), green ($10^{-1} < \dot{\gamma} < 10^{-2}$), and blue ($\dot{\gamma} > 10^{-1}$) lines are guides to the eye. The dashed red line marks the limit $\frac{\sqrt{\langle\|\delta\epsilon\|^2\rangle}}{\|\langle\epsilon\rangle\|} = 1$.

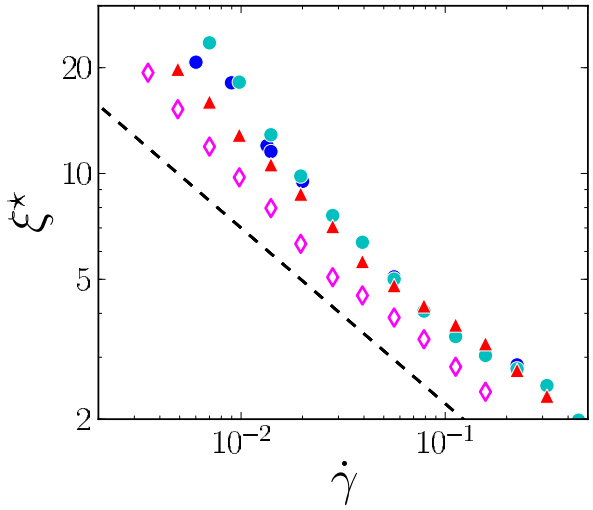

Figure 12.2: Dependence of the cooperative length $\xi^\star$ on $\dot{\gamma}$. The dashed line has slope $-1/2$. (*Open diamonds*) static scalar model; (*triangles*) static tensorial model; (*dots*) convected tensorial model. $N = 128 \times 128$, except for dark blue dots ($N = 256 \times 256$).

Rationalisation

Although the large values of $\xi^\star$ point to the sensitivity to the details of even rather distant plastic events , a simple calculation discarding static spatial correlations between these events already provides a satisfactory explanation of the scaling behaviour of $\xi^\star$ (Eq. 12.1). Indeed, under the assumption of randomly located plastic events, we recover the desired scaling law (Eq. 12.1), as detailed in Appendix 12.3.1. The derivation is based on the following: the typical mechanical noise $\|\dot{\boldsymbol{\epsilon}}\|$ created by a plastic event at a distance r amounts to $\frac{\dot{\epsilon}^{\mathrm{pl}}}{r^d}$ in d dimensions, whereas its mean value, for all possible relative positions, is only of order $\frac{\dot{\epsilon}^{\mathrm{pl}}}{L^d}$, where $L \equiv \sqrt{N}$ is the linear system size, because of the compensation between the positive and negative lobes of the elastic propagator; lastly, the average number of simultaneous plastic events is proportional to the shear rate.

We would like to emphasise that the scope of the derivation extends far beyond the present model; *in fine*, we simply find that the cooperative length scales with the spacing between homogeneously-distributed, simultaneous plastic events, although perhaps in a less crude way than Picard's definition. In other words, $\xi^\star$ is not sensitive to the presence of correlated "slip lines" in the flow and, more generally, other deviations from a homogeneous distribution of plastic events.

It is therefore not a surprise to find the same scaling of the correlation length as that used by Lemaître and Caroli [2009] to interpret the transverse diffusivity in their molecular dynamics simulations, namely a dependence on $\dot{\gamma}^{-1/d}$. Note that Lemaître and Caroli had rationalised it by secluding the non-overlapping near-field "flips" (plastic events) from an incoherent background of "flips". In many respects, our cooperative disk approach comes in the wake of theirs.

12.1.3 *Four-point stress correlator*

Definition

In glassy systems, instantaneous one-point observables hardly differ from their counterparts in the fluid state, and the search for an observable whose static correlations would distinguish the two states has not borne much fruit so far. On the other hand, time correlations of local observables have proven of great use as order parameters [Toninelli et al., 2005]. Here, we study the stress autocorrelation function $c\left(\boldsymbol{r}, \Delta t\right) \equiv \delta\sigma_{xy}\left(\boldsymbol{r}, 0\right) \delta\sigma_{xy}\left(\boldsymbol{r}, \Delta t\right)$, where $\delta\sigma_{xy} \equiv \sigma_{xy} - \bar{\sigma}_{xy}$. Spatial correlations are probed with the four-point correlator

$$\mathcal{G}_4\left(\Delta\boldsymbol{r}, \Delta t\right) \equiv \left\langle c\left(O, \Delta t\right) c\left(\Delta\boldsymbol{r}, \Delta t\right)\right\rangle - \left\langle c\left(O, \Delta t\right)\right\rangle^2, \tag{12.2}$$

where the brackets denote an average over time, or, equivalently, configurations (since the system is stationary). Note that the above definition is independent of the choice of origin O. If $\mathcal{G}_4\left(\Delta\boldsymbol{r}, \Delta t\right)$ for a given $\Delta\boldsymbol{r}$ is large, it means that regions separated by $\Delta\boldsymbol{r}$ are dynamically strongly correlated.

1. This assumption is explicit in Ref. [Langer, 2008] and implicit in all mean-field-like approaches.

The precise definition of $c\left(r, \Delta t\right)$ deserves a comment in the presence of convection, in which case blocks may move over Δt. In line with the definition of c as the stress autocorrelator, we adopt a Lagrangian description and compute c as $\left\langle \delta\sigma_{xy}\left(r, 0\right) \delta\sigma_{xy}\left(r', \Delta t\right)\right\rangle$, where r' is the convected position at Δt of the block that was initally at position r. Note that the same idea prevailed in Furukawa et al. [2009]'s definition of the four-point susceptibility of a system under shear.

Measurements

Figure 12.3 shows the spatial profile of $\mathcal{G}_4$ at $\dot{\gamma} = 10^{-3}$ for a time lag $\Delta t = 0.37$ of the order of the stress autocorrelation time. The profiles for the static versions of the model are indistinguishable with the naked eye, and remain identical if one substitutes $\sqrt{\sigma_{xx} + \sigma_{xy}}$ for σ_{xy} in the definition of the time correlator c. They display long branches in the velocity and velocity gradient directions, in accordance with the directions of the positive lobes of the xy-component of the elastic propagator $\mathcal{G}^{\infty}$. The large spatial extent of these branches is in part due to the periodicity of the system in the two directions.

Adding convection radically changes the picture. Most notably, the symmetry between the (Ox) (*i.e.*, flow) and (Oy) (*i.e.*, velocity gradient) directions is broken. The streamline going through the origin keeps a forward-backward ($x \to -x$) symmetry, but outside this line no such symmetry is preserved. In particular, the branch approximately along (Oy) direction is tilted, so that a block initially located at position $-x$ in this branch will be convected to position x after the lag strain $\Delta\gamma$, meanwhile passing through the (Oy)-lobe of the stress propagator. The distinction between the generic features of $\mathcal{G}_4$ and those specific to the present model shall be addressed in Section 12.2.2,

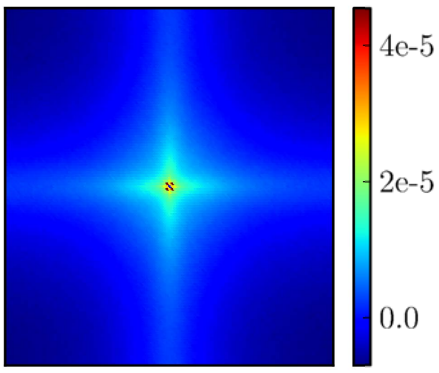

(a) Static tensorial model.

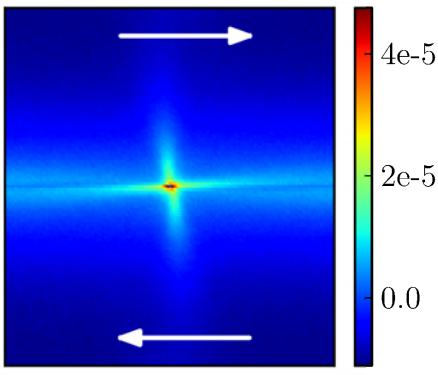

(b) Convected tensorial model. $\mathcal{G}_4$ is represented as a function of the *initial* positions of the convected blocks.

Figure 12.3: Spatial profile of the four-point correlator $\mathcal{G}_4$ at $\Delta\gamma = 0.37 \approx \Delta\gamma^{\star}$, $\dot{\gamma}_{app} = 10^{-3}$. System size: $N = 128 \times 128$. Because of the comparatively very large value of the stress autocorrelator $\mathcal{G}_4(0, \Delta t)$, the central cell has been artificially coloured.

12.1.4 *Four-point stress susceptibility*

Definition

The integral of $\mathcal{G}_4$ over space, at fixed Δt, yields the four-point susceptibility χ_4, that is, the variance of the two-time correlation function with time, $\chi_4(\Delta t) = V \cdot \mathrm{Var}(C(\Delta t))$, where V is the volume of the system, $C(\Delta t) \equiv V^{-1} \int c(\boldsymbol{r}, \Delta t)\, d\boldsymbol{r}$, and the variance operator Var has its usual definition, $\mathrm{Var}(\cdot) \equiv \langle \cdot^2 \rangle - \langle \cdot \rangle^2$. If the integral is normalised by the value at the origin [Toninelli et al., 2005], viz., $\tilde{\chi}_4(\Delta t) \equiv \chi_4(\Delta t)/\mathcal{G}_4(O, \Delta t)$, it then gives an estimate of the spatial volume in which the stress evolves in a correlated fashion with that at the origin. To illustrate this schematically, suppose that the system consists of V/V_{coop} entirely correlated, but mutually decorrelated, regions of volume V_{coop} each. A simple application of the central limit theorem yields

$$\begin{aligned} \tilde{\chi}_4(\Delta t) &= \frac{V \cdot \mathrm{Var}(C(\Delta t))}{\mathcal{G}_4(0, \Delta t)} \\ &\approx V_{\mathrm{coop}} \frac{\mathrm{Var}(c(O, \Delta t))}{\mathcal{G}_4(O, \Delta t)} \\ &\approx V_{\mathrm{coop}}. \end{aligned} \tag{12.3}$$

Measurements and scalings

The peak $\tilde{\chi}_4^\star$ of $\tilde{\chi}_4(\Delta t)$, which is reached at a time lag $\Delta t^\star$ close to the stress autocorrelation time, thus provides a measure of the maximal cooperativity in the flow. Here, $\Delta t^\star$ is such that $\dot{\gamma}\Delta t^\star \approx 0.3 - 0.5$ is of the order of the yield strain. The value of $\mathcal{G}_4(O, \Delta t^\star)$ depends even less on the shear rate.

We turn to a more detailed analysis of the variations of the cooperative volume $\tilde{\chi}_4^\star$ with the applied shear rate $\dot{\gamma}$, starting with the static models. At rather high shear rates, $\tilde{\chi}_4^\star$ is independent of the system size and exhibits the following shear rate dependence:

$$\tilde{\chi}_4^\star \sim \dot{\gamma}^{-\beta}, \tag{12.4}$$

with $\beta \approx 0.9$ for both the scalar and the tensorial models[2]. When the shear rate is decreased, the cooperative volume increases, and finally saturates at a value proportional to $L^{3/2}$ when the whole simulation cell becomes correlated. The transition takes place around a shear rate $\dot{\gamma}_c$ such that $\dot{\gamma}_c^{-\beta} \sim L^{3/2}$. Therefore, following Ref. [Martens et al., 2011], we propose the scaling

$$\tilde{\chi}_4^\star \sim L^{3/2} f\left(\dot{\gamma}^{-\beta} L^{-3/2}\right), \tag{12.5}$$

2. On a technical note, in order to get accurate measurements of χ_4, the variance of $C(\Delta t)$ must be calculated over long single-run simulations. It seems that averaging over many simulations of duration, say, $\Delta\gamma = 20$, sometimes leads to inaccuracies, perhaps because some unidentified structures take a long time (strain) to develop.

where $f(x) \sim x$ when $x \to 0$ and $f(x) \sim 1$ when $x \to \infty$. Figure 12.5 shows that a nice collapse can then be achieved.

Using the fractal dimension $3/2$ for the cooperative region, one can assess the four-point correlation length, $\xi_4 \sim \tilde{\chi}_4^{\star 2/3} \sim \dot{\gamma}^{2\beta/3}$. Interestingly, the exponent $2\beta/3 \approx 0.6$, for both scalar and tensorial models, is close to the exponent $1/2$ extracted in Ref. [Lemaître and Caroli, 2007] from the transverse diffusion coefficient in their 2D molecular dynamics simulations (although, admittedly, Lemaître and Caroli found linear avalanches in 2D, instead of our $3/2$ fractal exponent). On the other hand, it differs from the exponent $1/4$ predicted by the kinetic elastoplastic theory of Ref. [Bocquet et al., 2009]. More surprisingly, it also differs from the exponent reported in Ref. [Martens et al., 2011] for a slightly different rescaling of the observable, but with a model identical to the present one. We have checked that the scaling proposed in Ref. [Martens et al., 2011] provides a poorer fit to our more extensive data set (see Fig. 12.6).

The insertion of convection modifies the scaling thoroughly. Consistently with 2D atomistic simulations [Maloney and Lemaître, 2004, Lemaître and Caroli, 2009], linear correlations (referred to as "slip lines" in Ref. [Maloney and Lemaître, 2004], see Fig. 12.3) then dominate and $\tilde{\chi}_4^\star$ saturates at a value apparently almost proportional to the linear system size L (see Fig.12.7). The non-saturated regime in which the cooperative volume depends solely on $\dot{\gamma}$ is never truly reached in our simulations: finite-size effects are always dominant, which hampers our search for a scaling law.

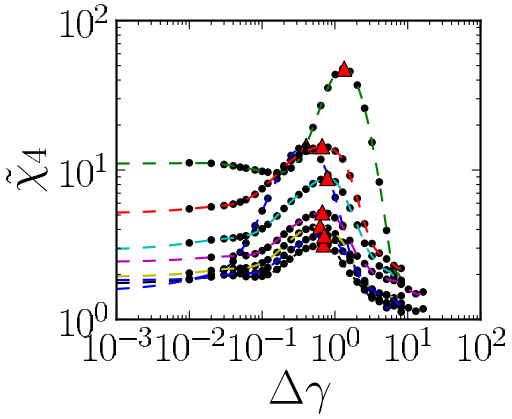

Figure 12.4: Four-point susceptibility as a function of strain delay $\Delta\gamma = \dot{\gamma}\Delta t$, for various shear rates (increasing $\dot{\gamma}$ from top to bottom), in the convected tensorial system. Red triangles indicate maximal values.

12.2 SCALINGS OF THE CORRELATION LENGTHS IN THE REFINED ATHERMAL MODEL

All correlation lengths that have been measured in Picard's model, in the previous section, are approximately proportional to the inverse square root of the

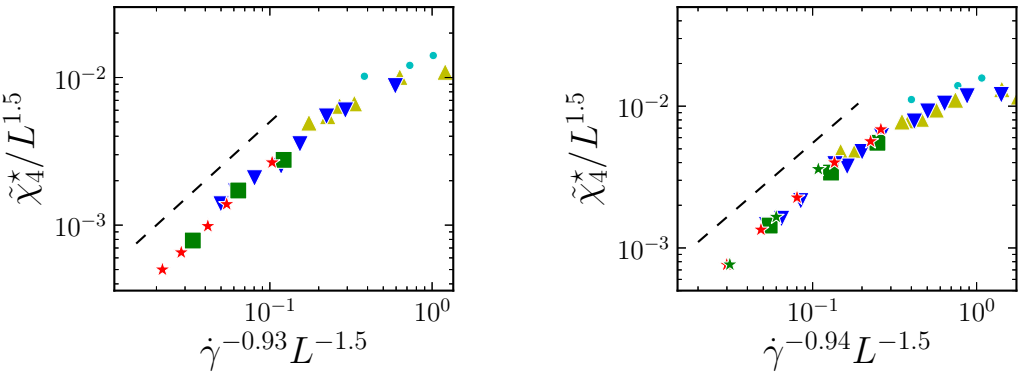

(a) Static scalar model.

(b) Static tensorial model.

Figure 12.5: Scaling of the maximal cooperative volume $\tilde{\chi}_4^\star$ as a function of $\dot{\gamma}$ in the static models. The vertical axis is $L^{-1.5}\chi_4^\star$, and the horizontal axis is the rescaled shear rate $\dot{\gamma}^{-\beta}L^{-1.5}$, with $\beta = 0.93$ for the scalar model and $\beta = 0.94$ for the tensorial model. Various linear sizes of the (square) system are studied: $L =$ (*cyan dots*) 32, (*yellow dots*) 64, (*blue triangles*) 128., (*green squares*) 192, (*red stars*) 256, (*green stars*) 384. As a guide to the eye, we have plotted a dashed line with slope 1.

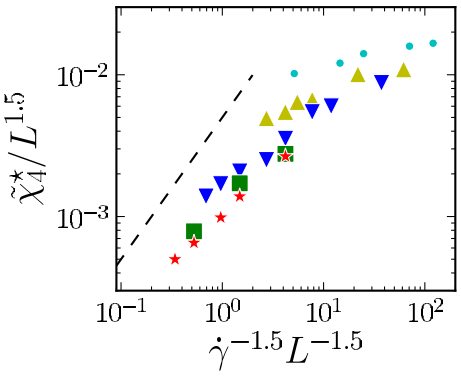

Figure 12.6: Test of the scaling of $\tilde{\chi}_4$ proposed in Ref. [Martens et al., 2011], *i.e.*, $\frac{\tilde{\chi}_4}{L^{3/2}} = f\left(\frac{\dot{\gamma}^{-3/2}}{L^{3/2}}\right)$, for the static scalar model. Various linear sizes of the system are studied: $L =$ (*cyan dots*) 32, (*yellow dots*) 64, (*blue triangles*) 128., (*green squares*) 192, (*red stars*) 256. As a guide to the eye, we have plotted a dashed line with slope 1. Data have been averaged over $\Delta\gamma \approx 300$.

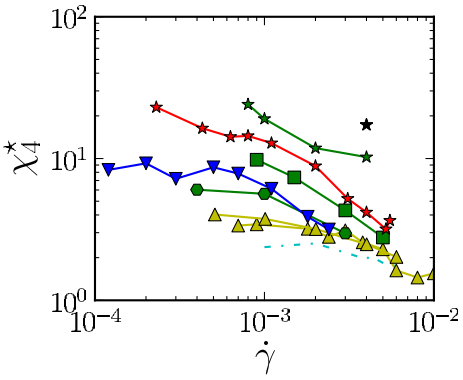

Figure 12.7: Maximal cooperative volume $\tilde{\chi}_4^\star$ in the convected tensorial model. Various linear sizes of the (square) system are studied: $L =$ (*cyan dash-dotted line*) 32, (*yellow triangles*) 64, (*green hexagons*) 96, (*blue triangles*) 128, (*green squares*) 192, (*red stars*) 256, (*green stars*) 384, (*black star*) 512.

shear rate, with the exception of the four-point correlation length in the convected system, whose scaling remains elusive for us. How universal is this $\dot{\gamma}^{-1/2}$-scaling (in 2D)? Spurred on by this question, we pursue the study in the model featuring more realistic dynamical rules introduced in Section 9.3. Here, we fix $k = \infty$, *i.e.*, short-term ageing is precluded; the flow is then macroscopically homogeneous; in addition, we choose the model parameter $\gamma_c = 0.7 \langle \gamma_y \rangle$.

12.2.1 *Cooperative disk*

As with the previous model, we determine, at an arbitrary point M in the system, the radius $\xi^\star$ of the cooperative disk outside which plastic events contribute to the instantaneous mechanical noise perceived at M essentially in a mean-field manner.

The inset of Fig. 12.8 shows that the scaling $\frac{\sqrt{\langle \|\delta\dot{\epsilon}\|^2 \rangle}}{\|\langle \dot{\epsilon} \rangle\|}(\xi) \sim \frac{1}{\xi\sqrt{\dot{\gamma}}}$ is also entirely satisfactory in this case. It follows that the scaling of the cooperative radius $\xi^\star$ with $\dot{\gamma}^{-1/2}$ is conserved, although a departure from this scaling is observed when $\xi^\star \gtrsim 20$, due to finite-size effects (see Fig. 12.8). This supports the idea that the arguments developed above to ground the scaling of the cooperative radius with the spacing between simultaneous plastic events are not model-specific. We hypothesise that they may also be relevant in the thermal regime.

12.2.2 *Four-point susceptibility*

The spatial profiles of the four-point stress correlator $\mathcal{G}_4(r, \Delta t^\star)$ (*not shown*) retain the symmetry described above, although in the convected version the crosswise lobe is now less skewed, owing to the lower yield strain. However, the integrals of $\mathcal{G}_4(r, \Delta t^\star)$ over growing disks centered at the origin scale differently with the disk radii R; here they scale with R^α for $1 \ll R \ll L$, with $\alpha \approx 0.6$ roughly in the static case.

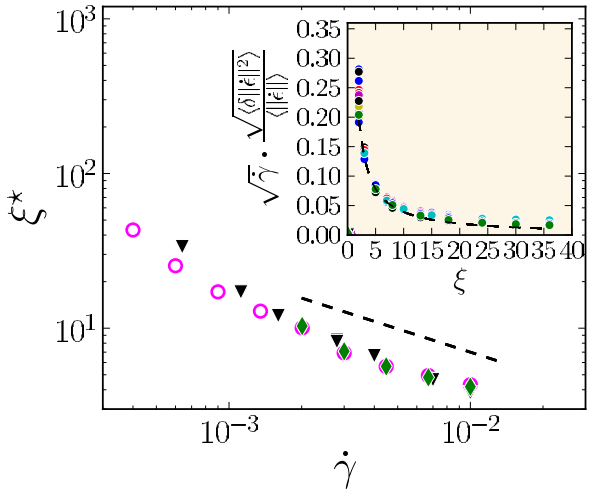

Figure 12.8: Cooperative radius $\xi^\star$ as a function of the applied shear rate $\dot\gamma$. Linear system size L =(*black triangles*) 128, (*pink circles*) 256, (*green diamonds*) 384. The dashed line has slope -0.5. (*Inset*) Rescaled fluctuation over mean value ratio $\sqrt{\dot\gamma}\frac{\sqrt{\langle\|\delta\dot\epsilon\|^2\rangle}}{\|\langle\dot\epsilon\rangle\|}$ as a function of ξ, for various $\dot\gamma$. The dashed line represents $0.39/\xi$.

To carry on with the quantitative study, we turn to the maximal cooperative volume $\tilde\chi_4^\star$. Since no obvious scaling was found in the convected case with the previous model, only the static tensorial model is studied here. For a given system size, say, $L = 128$, at relatively high shear rates, the exponent β in $\tilde\chi_4^\star \sim \dot\gamma^{-\beta}$ is of order 0.2-0.3, that is, significantly lower than its counterpart for the simplistic model. In spite of the scatter of the data, we clearly see that the scaling law used above is no longer valid for this model, as illustrated in Fig.12.9; universality in the variations of the cooperative volume with the system size and the shear rate is thus ruled out. In fact, the scaling form $\frac{\tilde\chi_4}{L^\alpha} = f\left(\frac{\dot\gamma^{-\beta}}{L^\alpha}\right)$ in general does not seem to provide any nice collapse of the data here.

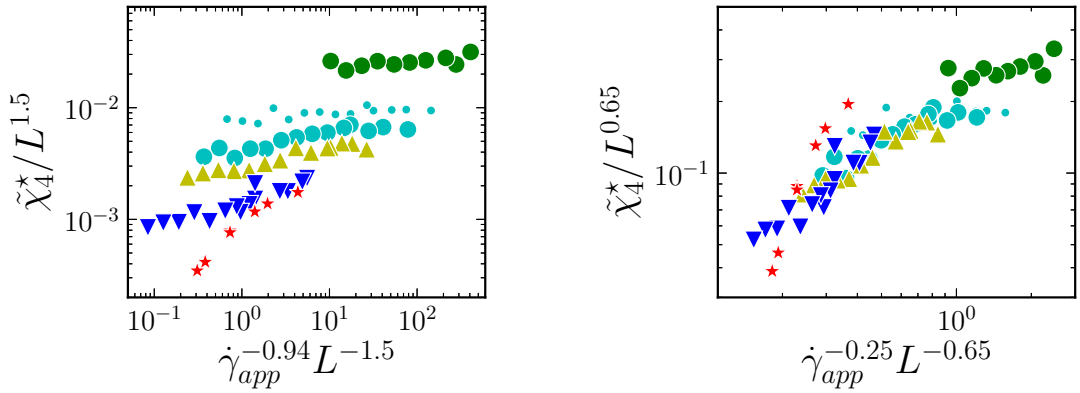

(a) $(\alpha = 1.5, \beta = 0.94)$ (b) $(\alpha = 0.65, \beta = 0.25)$

Figure 12.9: Maximal cooperative volume $\tilde{\chi}_4^\star$, rescaled according to $\frac{\tilde{\chi}_4}{L^\alpha} = f\left(\frac{\dot{\gamma}^{-\beta}}{L^\alpha}\right)$, for two distinct pairs (α, β): the exponents measured in the previous section, $(\alpha = 1.5, \beta = 0.94)$, and better suited exponents, $(\alpha = 0.65, \beta = 0.25)$. Various linear sizes of the (square) system are studied: $L =$ (*large green dots*)16, (*cyan dots*) 32, (*large cyan dots*) 48, (*yellow triangles*) 64, (*blue triangles*) 128, (*red stars*) 256. As a guide to the eye, we have plotted a dashed line with slope 1. Data have been averaged over $\Delta\gamma \approx 400 \left\langle \gamma_y \right\rangle$.

Key Points of the Chapter[a]

- A class of correlation lengths simply scale as the spacing between homogeneously distributed, simultaneous plastic events, *i.e.*, $\xi \sim \dot{\gamma}^{-1/d}$ in the shear-dominated regime. These correlation lengths are insensitive to avalanche shapes and are robust to changes in the elastoplastic model.
- On the other hand, the scaling of the cooperative volume assessed with the four-point stress susceptibility is model-dependent, thus ruling out universality in this respect.
- Scalar and tensorial models have identical scalings.
- Nevertheless, some aspects of structural disorder may be underestimated in the elastoplastic line of modelling, which would then overestimate cooperative lengths.

a. These results, along with those of Chapter 11, have been collected in a publication [Nicolas et al., 2014b]

A

12.3 APPENDIX

12.3.1 *Estimation of the cooperative length $\xi^\star$*

Simple arguments based on the crude assumption of randomly distributed plastic events explain the importance of the mechanical noise fluctuations measured at an arbitrary point, say the origin M, and the scaling law in $d = 2$ dimensions (Eq. 12.1), which is recalled here:

$$\frac{\sqrt{\langle \|\delta\dot{\boldsymbol{\epsilon}}\|^2 \rangle}}{\|\langle \dot{\boldsymbol{\epsilon}} \rangle\|}(\xi) \sim \frac{1}{\xi\sqrt{\bar{\gamma}}}. \tag{12.6}$$

Denoting by $p \in [0,1]$ the average surface fraction covered by plastic events at a given shear rate and calling $\dot{\epsilon}^{\mathrm{pl}} \sim \frac{\gamma_y}{\tau}$ the typical plastic strain rate, the mean value of the mechanical noise due to plastic events occurring farther than ξ is:

$$\begin{aligned} \|\langle \dot{\boldsymbol{\epsilon}} \rangle\| &\approx \int_{\xi}^{L}\int_{\mathcal{S}^d} \frac{p\dot{\epsilon}^{\mathrm{pl}}}{L^d} r^{d-1} dr d\theta \\ &\sim \frac{p\dot{\epsilon}^{\mathrm{pl}}\left(L^d - \xi^d\right)}{L^d}. \end{aligned}$$

Here, $\mathcal{S}^d$ denotes the unit sphere in d dimensions, and we have used that the spatially averaged contribution of a plastic event to the stress field is of order $\frac{\dot{\epsilon}^{\mathrm{pl}}}{L^d}$. Numerical prefactors are omitted.

Let us now turn to the fluctuations and start by computing $\delta\dot{\epsilon}(r)$, the contribution of plastic events taking place in a shell $[r, r+1]$ centred at M :

$$\begin{aligned} \delta\dot{\epsilon}(r)^2 &= \left(\int_r^{r+1} dr' \int_{\mathcal{S}^d} r'^{d-1} d\theta \mathcal{G}(r',\theta)\, n(r',\theta)\, \dot{\epsilon}^{\mathrm{pl}}\right)^2 \\ &\sim 0 + \int_r^{r+1} dr' \int_{\mathcal{S}^d} r'^{d-1} d\theta \left(\frac{\cos(4\theta)}{r^d} n(r,\theta)\, \dot{\epsilon}^{\mathrm{pl}}\right)^2 \\ &\sim \frac{p\cdot\left(\dot{\epsilon}^{\mathrm{pl}}\right)^2}{r^{d+1}}, \end{aligned}$$

where $n(r',\theta) = 0$ or 1 is the plastic activity at point (r',θ), and, crudely, we have assumed the absence of static spatial correlations between plastic events outside a fully correlated unit volume $r'^{d-1} dr' d\theta = 1$, *i.e.*, the volume of a single plastic event.

The sum $\delta\dot{\epsilon}$ of the contributions of the concentric shells of radius $r \geqslant \xi$ then reads:

$$\begin{aligned}
\delta\dot{\epsilon}^2 &\sim \left[\sum_{r=\xi}^{L} \delta\dot{\epsilon}\,(r)\right]^2 \\
&\sim \sum_{r=\xi}^{L} \delta\dot{\epsilon}\,(r)^2 \\
&\sim p \cdot \left(\dot{\epsilon}^{\mathrm{pl}}\right)^2 \left[\frac{L^d - \xi^d}{L^d \xi^d}\right].
\end{aligned}$$

Finally, the fluctuations-to-average ratio can be computed, in the limit $\xi \ll L$,

$$\frac{\sqrt{\delta\dot{\epsilon}^2}}{\|\langle\dot{\boldsymbol{\epsilon}}\rangle\|} \sim \frac{1}{\xi^{d/2}\sqrt{p}}. \tag{12.7}$$

To conclude, one just has to recall that, when thermal fluctuations are negligible, the density of plastic events is proportional to $\dot{\gamma}$, because the typical stress release per plastic event ϵ^{pl} shows no significant dependence on the applied shear rate.

13 FLOW IN A MICROCHANNEL

In the previous chapter, spatial correlations in the flow have been evidenced in a simple shear setup, which features a unique macroscopic shear rate $\dot{\gamma}$. But the effect of these correlations is magnified in intrinsically inhomogeneous flow geometries, displaying a continuum of shear rates. In this chapter, we investigate such a highly heterogeneous geometry, namely, flow in a microchannel. The interest of this geometry notably resides in its industrial relevance for the design of labs-on-a-chip or die extrusion of complex fluids. Moreover, recent experiments have revealed striking manifestations of cooperativity in this setup, as we shall see. Therefore, the study will afford a direct comparison between the model and experimental data, which is rare in the field.

13.1 SIMULATION OF A GENUINE 2D MICROCHANNEL

To our knowledge, the elastoplastic modelling of a channel flow is unprecedented. In fact, the simulation of a genuine microchannel in 2D requires two major changes with respect to simple shear flow. First, the shear stress applied on different streamlines will no longer be uniform, but linear in the crosswise coordinate. Second, channel walls need to be implemented.

13.1.1 *Implementation of the stress profile across the channel*

Let us recall the elastoplastic equation of evolution of the local stress (Eq. 8.1):

$$\partial_t \sigma(i,j;t) \quad = \quad \dot{\Sigma}_{\text{app}} + 2\mu \sum_{i'=1}^{L} \sum_{j'=1}^{L} \mathcal{G}\left(i-i', j-j'\right) \cdot \dot{\boldsymbol{\epsilon}}^{\mathbf{pl}}(i',j';t). \qquad (13.1)$$

Quite generally, the loading rate $\dot{\Sigma}_{\text{app}}$ corresponds to the response of a purely elastic solid, for which $\dot{\boldsymbol{\epsilon}}^{\mathbf{pl}} = \mathbf{0}$. For the specific case of a channel, the deformation of this purely elastic material is pressure driven and, on account of the symmetries, momentum conservation reads, in the steady state,

$$\sigma_{xy} \quad = \quad \nabla p \ \left(y - L_y/2\right),$$

where x and y are the streamwise and crosswise coordinates, respectively. It follows that $\dot{\Sigma}_{\text{app}} = 0$, and the initial state of the material should coincide with that of the purely elastic solid, *viz.*,

$$\sigma_{xy}(x,y;t=0) \quad = \quad \nabla p \ \left(y - L_y/2\right).$$

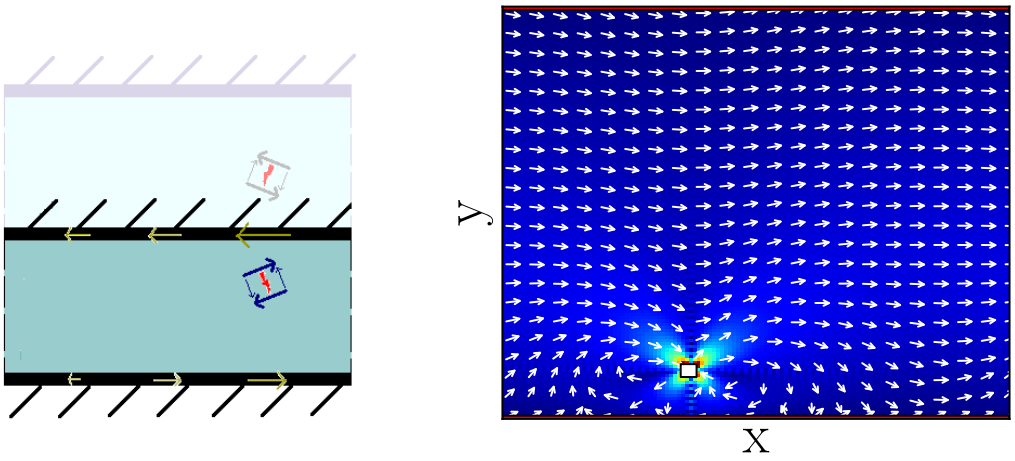

(a) Sketch of the duplicated system.

(b) Displacement field in the "real half" induced by a single plastic event, located in the white square.

Figure 13.1: Modelling a plastic event in a geometry confined by walls.
(b) The white arrows show the direction of the field, while the colour code represents the displacement amplitude (brighter colours indicate higher amplitude). Walls, drawn as red lines, are present at the top and at the bottom of the system.

The streamline-averaged stress conserves a linear profile throughout the simulation, because plastic events induce a homogeneous streamline-averaged stress, owing to mechanical equilibrium.

13.1.2 *Inclusion of confining walls*

In addition to changing the initial stress profile, the boundary conditions (BC) need to be adapted to account for the presence of two infinite parallel walls, directed along $\boldsymbol{e_x}$, bounding the flow, while keeping the periodicity along $\boldsymbol{e_x}$. The effect of the walls is modelled by imposing a no-slip BC at their locations, in line with what is commonly done in fluid mechanics.

To implement the no-slip BC, we extend the treatment of Ref. [Picard et al., 2004]: the system is duplicated in the direction perpendicular to the walls, so that the region $y \in [0, L_y]$ describes the real system, while the region $y \in [-L_y, 0]$ is fictitious. Now, the contrivance consists in adding appropriate "forces" outside the domain of interest to have the BC satisfied while still fulfilling the equations of elasticity in the real domain. With this objective in mind, for each plastic event (in the real system), a symmetric "image plastic event" is created in the fictitious half (see Fig. 13.1a). The y-component of the velocity field is thereby cancelled at the walls. To remove the x-component of the velocity, adequate forces directed along $\boldsymbol{e_x}$ are added at the walls. These (fictitious) forces add a corrective term $\boldsymbol{\epsilon}^{\text{corr}}$ to the deformation field $\boldsymbol{\epsilon}^{\infty}$ obtained for periodic BC (whose derivation can be found in Section 8.2.1):

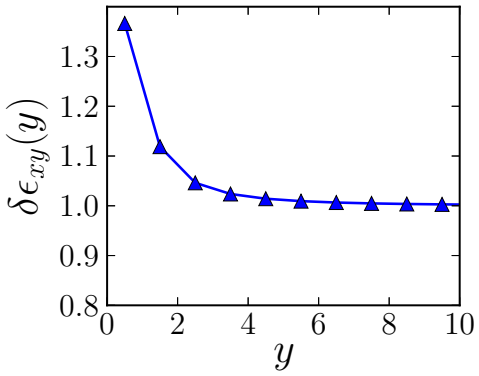

Figure 13.2: Decrease $\left|\epsilon_{xy}^{(1)}\right|$ of the *local* elastic strain induced by a given plastic strain $\epsilon_{xy}^{\mathrm{pl}}$ as a function of the distance y to the wall (expressed in block units, which is the only relevant length scale). Values have been normalised to the 'bulk' value, that is, the quantity measured infinitely far from the wall.

$$\boldsymbol{\epsilon}\left(\boldsymbol{q}\right) = \boldsymbol{\epsilon}^{\infty}\left(\boldsymbol{q}\right) + \boldsymbol{\epsilon}^{\mathrm{corr}}\left(\boldsymbol{q}\right).$$

The calculation of $\boldsymbol{\epsilon}^{\mathrm{corr}}\left(\boldsymbol{q}\right)$, which I defer to Appendix 13.5.1 because it is rather technical and lengthy, yields the following result:

$$\begin{pmatrix} \epsilon_{xx}^{\mathrm{corr}}\left(q_x,q_y\right) \\ \epsilon_{xy}^{\mathrm{corr}}\left(q_x,q_y\right) \end{pmatrix} = \begin{pmatrix} \frac{-2q_xq_y^2}{q^4}\left[i\sum_y \zeta_\delta\left(X\right)\ \mathcal{F}_x\epsilon_{xy}^{\mathrm{pl}}(q_x,y) + 2\sum_y \xi_\delta(X)\mathcal{F}_x\epsilon_{xx}^{\mathrm{pl}}(q_x,y)\right] \\ \frac{q_y\left(q_x^2-q_y^2\right)}{q^4}\left[i\sum_y \zeta_\delta\left(X\right)\ \mathcal{F}_x\epsilon_{xy}^{\mathrm{pl}}(q_x,y) + 2\sum_y \xi_\delta(X)\mathcal{F}_x\epsilon_{xx}^{\mathrm{pl}}(q_x,y)\right] \end{pmatrix}, \tag{13.2}$$

where $\sum_y$ denotes an integral over all streamlines $y = cst$ and $\mathcal{F}_x$ indicates a Fourier transformation along direction x. X is used as a shorthand for $\left(\frac{\pi y}{L_y}, \frac{q_x L_y}{\pi}\right)$ and the analytical expressions of the functions $\zeta_\delta\left(X\right)$ and $\xi_\delta\left(X\right)$ can be found in Appendix 13.5.1.

Note that the corrective term couples distinct Fourier modes so that the translational invariance of the propagator $\mathcal{G}$ is broken (in the y-direction). In particular, for a given plastic strain, the local strain response now depends upon the distance to the wall. The dependence on the distance for a plastic event $\left\{\epsilon_{xx}^{\mathrm{pl}} = 0, \epsilon_{xy}^{\mathrm{pl}} \neq 0\right\}$ is presented in Fig. 13.2, in the discrete system, with blocks of unit size. In particular, one can see that the local strain relaxation induced by a given plastic strain is around 35% higher in the direct vicinity of a wall than in the bulk case, owing to the vicinity of a solid boundary.

13.1.3 *Coarse-grained convection*

The implementation of (a coarse-grained version of) convection is considerably streamlined in comparison with the unbounded medium. Indeed, owing to

the confinement in the crosswise direction and the absence of interactions with periodic replicas in that direction, there is no need to deform the simulation cell. It is therefore sufficient to incrementally shift individual streamlines whenever their average displacement $\langle u_x \rangle_x (y_0)$ grows larger than a multiple of the block size, with

$$\begin{aligned} \langle u_x \rangle_x (y_0) &\equiv \frac{1}{L_x} \int_{-L_x/2}^{L_x/2} u_x (x, y_0)\, dx \\ &= \sum_{y_{ev}} \left[\text{sign}\,(y_0 - y_{ev}) \cdot \left(1 - \frac{|y_0 - y_{ev}|}{L_y} \right) + 1 - \frac{y_{ev}}{L_y} - \frac{y_0}{L_y} \right] \mathcal{F}_x \epsilon_{xy}^{pl} (m = 0, y_{ev}). \end{aligned}$$

Details of the algebra are provided in Appendix 13.5.2. As explained in Section 8.3.1, a homogeneous random displacement is also regularly added to all streamlines, in order to avoid the artificial "pinning" of lines with low average velocities.

13.2 SIMULATION OF THE FLOW

13.2.1 *Model*

For chronological reasons mainly, we resort to somewhat different dynamical rules in this chapter.

The rates $l(\sigma)$ and $e(\sigma)$ still govern the transition from the elastic to the plastic regime and the recovery of elastic behavior after initiation of the plastic event, respectively, *i.e.*,

$$\text{elastic regime} \underset{e(\sigma)}{\overset{l(\sigma)}{\rightleftharpoons}} \text{plastic event.}$$

But the distribution of yield stresses is reduced to a single value, σ_y, and, as in the Eyring model, the potential energy is supposed linear in the local stresses, instead of quadratic, *viz.*, $\tilde{V} = V - \sigma \langle \gamma \rangle$, where $\langle \gamma \rangle$ is a macroscopic strain and the activation volume has been set to unity. The yield rate then reads

$$l(\sigma) = \tau^{-1} \Theta (\sigma - \sigma_{\mu y}) \exp \left(\frac{\sigma - \sigma_y}{x_{\text{loc}}} \right),$$

where x_{loc} is a material-dependent activation temperature *of non-cooperative origin*: it accounts for local microscopic effects, but *not for the mechanical noise*. Note that the limit $x_{loc} \to 0$ coincides with the usual von Mises yield criterion. The Heaviside function, $\Theta (\sigma - \sigma_{\mu y})$ with a critical stress $\sigma_{\mu y} \ll \sigma_y$, is a convenient means to obtain a finite macroscopic yield stress in a thermal system without explicitly accounting for structural ageing (the issue associated with this was discussed in Section 7.3). Incidentally, Amon et al. [2012a], in a paper investigating the behaviour of granular matter on a tilted plane, recently called for a

model displaying two critical stresses, with a microfailure stress in addition to the macroscopic one, although with a distinct definition.

Regarding the duration of a plastic event, set by $e(\sigma)$, it was fixed on a *per T1 event* (or *per rearrangement*) basis in the previous refined model. The present choice of $e(\sigma)$ is premised on the idea that after the onset of a plastic event rearrangements will be taking place as long as the local stress σ remains large. Consequently, we define a threshold for the recovery of elastic stability, whose value is set to $\sigma_{\mu y}$ in order to limit the number of parameters. Introducing a new intensive parameter x_{res}, this allows us to write

$$e(\sigma) \quad = \quad \tau^{-1} \exp\left(\frac{\sigma_{\mu y} - \sigma}{x_{res}}\right).$$

The definition of the rates e and l completes the description of the model.

13.2.2 *Parameter fitting*

As usual, we use units of time and stress such that $\tau = 1$ and $\sigma_y = 1$. We set $\mu = \sigma_y$ (note that this only comes down to rescaling the shear rate if convection is omitted). Three parameters still need to be determined: $\sigma_{\mu y}$, x_{loc}, and x_{res}.

In the following, our numerical simulations are compared to experimental data for concentrated oil-in-water emulsions collected by two different groups, Goyon et al. [2010] and Jop et al. [2012]. The experimental systems are concentrated emulsions made of $6-7\mu m$ silicon oil droplets in a water-glycerol mixture. The oil volume fraction is $\phi \sim 0.75$, a value significantly larger than the jamming volume fraction. Both groups report a Herschel-Bulkley dependence of the shear stress on the shear rate, that is, $\sigma = \sigma_d \left[1 + (\tau_{HB}\dot{\gamma})^n_{\text{app}}\right]$, with an exponent $n \simeq 0.5$ in both cases.

This Herschel-Bulkley law allows us to fit the remaining model parameters. To do so, we simulate a simple shear flow ($\dot{\Sigma}_{\text{app}} = \mu\dot{\gamma}$ in Eq. 13.1). By varying the parameters, we find that the combination $\{\sigma_{\mu y} = 0.17,\ x_l = 0.249,\ x_e = 1.66\}$ provides quite a satisfactory fit to the flow curve, as shown in Fig. 13.3. Note that model units of time and stress have been appropriately rescaled in the figure, to allow for comparison with the experimental values. Of course, one may argue that the fitting to the flow curve only loosely constrains the parameters, implying that other combinations of parameters could yield the same result. Nevertheless, we would like to mention that, when starting with a moderately different set of parameters and fine-tuning it to better match the data, we have recovered parameters similar to those selected.

13.2.3 *General observations*

Having set the model, we now turn to the specific case of channel flow.

Conspicuous is, in the first place, the presence of a "plug" in the centre of the channel, *i.e.*, a solid-like region in which the material is convected, but not sheared. The plug is clearly seen in Fig. 13.4a, which demonstrates a nice agree-

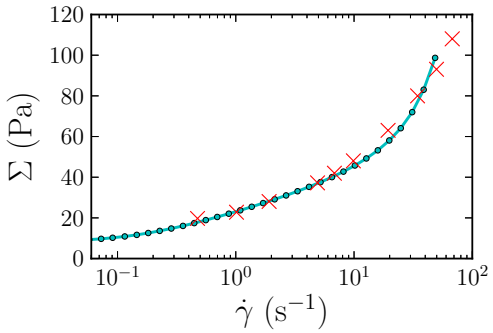

Figure 13.3: (×) Experimental and (•) simulated flow curve. The experimental were obtained by Goyon *et al.* for an emulsion of $\sim 6.5\,\mu$m silicon oil droplets in a water-glycerin mixture at volume fraction $\phi = 75\%$. The solid line is a guide to the eye.

ment between the numerical and the experimental (time averaged) velocity profiles across the channel. Note that showing the velocity differences with respect to the maximal velocity across the channel obviates the experimental issue of the determination of wall slip.

However, averaging over time masks the temporal fluctuations of the flow. If one heeds the variations of the maximal streamline velocity of the simulated flow with respect to time, flow intermittency becomes evident. [1] This phenomenon is more acute for narrow channels (*data not shown*), in agreement with results from numerical simulations regarding the effect of confinement [Chaudhuri et al., 2012]. Note that flow intermittency, or "stick-slip" behaviour, has often been reported experimentally, but it has been interpreted in various ways depending on the particular system under study: the creation and failure of force chains is put forward in the case of granular matter [Pouliquen and Gutfraind, 1996, Gutfraind and Pouliquen, 1996], while variations in the local concentrations of colloids and erosion by the solvent have been reported for concentrated colloidal suspensions [Isa et al., 2009].

The spatial distribution of plastic events is also of interest. Indeed, although the plug remains virtually still on average, sparse plastic events are clearly seen in that region (where $|\sigma(y)| \leqslant \sigma_y$) especially for narrow channels, and, consequently, below the bulk yield stress. Therefore, these plastic events essentially originate in cooperative effects, *via* stress redistribution. Being of cooperative nature, the principal direction of their stresses at the yielding point (the 'angle of yield' of the plastic event) is broadly dispersed, since it is not strongly biased by a fixed applied shear (see Fig. 13.4b).

13.2.4 *Cooperative effects in a microchannel flow*

Cooperativity is a general feature of the flow of amorphous solids, regardless of the flow geometry and the drive. Channel flow, however, is specific in that

1. However, these fluctuations would presumably vanish in our model if the channel were of infinite length.

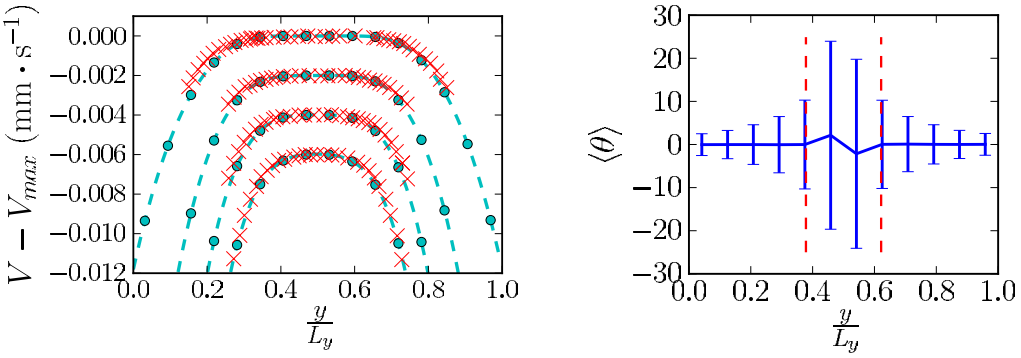

(a) Velocity profiles.

(b) Angles of yield.

Figure 13.4: (a) (×) Experimental and (•) simulated velocity profiles, for stresses at the wall σ_w = 141 Pa, 188 Pa, 235 Pa, 282 Pa, corresponding to σ_w=0.36, 0.48, 0.60, 0.72 in model units, from top to bottom. The experimental data are a courtesy of Jop *et al.* The model time and stress units have been rescaled to match the experimental data.
(b) Principal direction $\theta \in [-45°, 45°]$ of plastic events as a function of the position in the simulated channel. Channel width: 12. σ_w=0.6 in model units. The vertical dashed lines delimit the 'plug', *i.e.*, the region where $|\langle\sigma_{xy}\rangle| \leqslant \sigma_d$. The bars give the standard deviation, $\pm\langle\langle\theta^2\rangle - \langle\theta\rangle^2\rangle$.

(i) the non-locality of the stress redistribution couples streamlines subject to *different* shear stresses.

(ii) the presence of a wall, whether it be rough or smooth, may create a specific surface rheology, different from that in the bulk.

In practice, these effects are of primary importance for confined flows in microchannels, but they are not intrinsically caused by confinement.

In the following, we attempt to disentangle them in the experimental manifestations of cooperativity.

13.3 COOPERATIVITY IN THE BULK FLOW: A MANIFESTATION OF THE COUPLING BETWEEN HETEROGENEOUS REGIONS

13.3.1 *Origin and description of the non-locality in the flow*

Since streamlines subject to different stresses are coupled in the microchannel, one may then expect the behaviour of a given region to differ from that it would have in homogeneous flow. This is a serious issue, since it undermines the paradigm that there exists a constitutive equation relating the local shear rate to the local shear stress, as explained by Goyon and colleagues [Goyon et al., 2008, 2010].

To rationalise the deviations that they observed experimentally, Goyon *et al.* made use of a diffusion equation (Eq. 6.4) operating on the local fluidity $f(r) \equiv \frac{\dot{\gamma}(r)}{\sigma_{xy}(r)}$, which we recall here:

$$\xi^2 \Delta f - (f - f_{\text{bulk}}[\sigma(y)]) = 0, \tag{13.3}$$

where $f_{\text{bulk}}(\sigma)$ denotes the fluidity measured in a homogeneous flow at applied stress σ. The length scale ξ is a cooperative length, that scales with the particle diameter [Goyon et al., 2008, Kamrin and Koval, 2012].

Although the theoretical derivation of Eq. 13.3 by Bocquet et al. [2009] required strong approximations, namely, cutting off the propagator beyond the first neighbours and considering the limit of vanishing shear rate, the equation was found to provide a very satisfactory description of experimental and numerical data in several cases [Goyon et al., 2008, 2010, Jop et al., 2012, Chaudhuri et al., 2012, Geraud et al., 2013, Kamrin and Koval, 2012], provided that the parameters, that is, the cooperativity length ξ and the value f_{wall} of the fluidity at the wall, are carefully fitted.

Assuming that this equation offers a valid first-order approximation of the flow, we use it to assess the amplitude of the expected deviations from bulk behaviour.

To do so, we quantify the extent of the coupling by estimating the *relative* deviations $\delta f(y) \equiv f(y) - f_{\text{bulk}}$ of the fluidity. This defines a dimensionless number, the Babel number $\text{Ba} \equiv \frac{\delta f}{f}$. In Appendix 13.5.3, we show that, under the assumption of a Herschel-Bulkley constitutive equation, Ba is of order $\left(\xi \frac{\|\nabla \sigma\|}{\sigma - \sigma_d}\right)^2$, that is, $\left(\xi \frac{\|\nabla p\|}{\sigma - \sigma_d}\right)^2$ for a channel flow.

Noteworthy is the (quadratic) dependence of the Babel number on the stress gradient, *i.e.*, the pressure gradient in a Poiseuille flow. Indeed, it is generally several orders of magnitude larger in microchannels than in their larger counterparts, which explains why striking manifestations of cooperativity have been observed only in the former. The Babel number is also negligible in wide-gap Taylor-Couette geometry. For instance, a rough estimation yields $\text{Ba} \sim 10^{-9}$ at most in the wide-gap setup used in Ref. [Ovarlez et al., 2008], where no deviations from macroscopic rheology were reported.

The denominator of Ba, $(\sigma - \sigma_d)^2$, also deserves a comment: at high applied stresses, when the material is more fluid-like, relative deviations become less significant. We should however say that, to measure relative deviations, the absolute fluidity deviations are divided by the fluidity, which gets large as σ gets large.

13.3.2 *Non-local effects in the velocity profiles*

Following the above considerations, we expect deviations from macroscopic rheology to increase with confinement, at fixed wall stress.

Indeed, Goyon's experiments on emulsions confined in microchannels with *smooth* walls tend to indicate that the deviations of the velocity with respect to the bulk predictions follow such a trend. However, overall, these deviations were found to be rather small. The mentioned effect of confinement is also confirmed by Chaudhuri et al. [2012] with atomistic simulations of a Poiseuille flow with biperiodic BC with atomistic simulations.

Figure 13.5a shows a comparison between the actual velocity profile obtained with simulations of the mesoscopic model and the predictions from the (bulk) flow curve. As in experiments, small deviations can be observed. For the extent of these deviations to roughly match that in the experiments, the channel width must be of order 7-10 block units. From this we deduce a first estimate for the linear size a of a mesoscopic block in terms of particle diameters: $a \approx 2$, which is comparable to experimental values found in the literature [Schall et al., 2007].

Let us now investigate how compatible our simulation results are with the fluidity diffusion equation (Eq. 13.3). To solve Eq. 13.3, two BC are required: for symmetry reasons, we impose $f\left(y=0\right) = f\left(y=L_y\right)$, and we set the fluidity at a point close to the wall to the value measured in simulations. In addition, the shear-rate dependence of the cooperativity length ξ must be specified. Two possibilities are considered in Fig. 13.5b:

- either, following Ref. *[Goyon et al., 2008]*, ξ is supposed independent of the shear rate, *i.e.*, $\xi = \xi_0$,

- or a power-law dependence is assumed, $\xi\left(\dot{\gamma}\right) = \xi_0 \left(\dot{\gamma}\tau\right)^{-1/4}$, where $\dot{\gamma}$ is the product of the local shear stress and fluidity, as derived by Bocquet et al. [2009] in the limit $\dot{\gamma} \to 0$, and in reasonable agreement with the data of Jop et al. [2012].

In both cases, ξ_0 is adjusted by a least square minimization. Both cases give a reasonable fit, but neither matches our data accurately over the whole range of applied pressures. We ascribe this defect, among other details, to the approximation of long-range interactions by a diffusive term, and to the neglect of fluidity fluctuations.

In Figure 13.6, we assess the predictive capability of the theoretically derived Babel number for our channel flow simulations by plotting the $\frac{\delta f}{f}$ obtained in our simulations as a function of $\mathrm{Ba} = \left(\xi \frac{\|\nabla\sigma\|}{\sigma-\sigma_d}\right)^2$. It shows a global trend towards larger relative deviations from macroscopic rheology for larger Ba, but the correlations are poor. Nevertheless, one may expect Ba to still be a valid predictor in practice, when widely different situations are considered.

13.3.3 *Shear rate fluctuations in the plug*

Quite recently, Jop et al. [2012] showed experimentally that the seemingly quiescent plug in the centre of the microchannel actually sustains finite shear rate fluctuations. This observation is obviously consistent with the occurrence of sparse plastic events in the plug, in our simulations.

To go further than this qualitative agreement, we directly compare the local shear rate fluctuations $\delta\dot{\gamma}\left(x,y\right) = \sqrt{\left\langle \dot{\gamma}\left(x,y\right)^2 \right\rangle - \left\langle \dot{\gamma}\left(x,y\right)\right\rangle^2}$ to experimen-

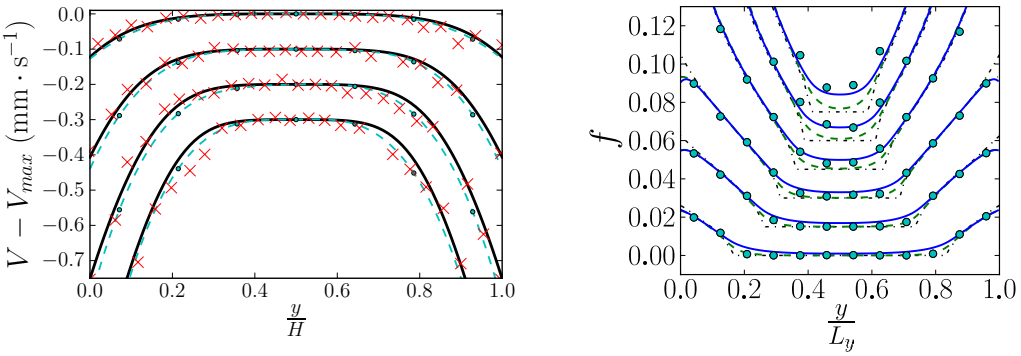

(a) Velocity profiles across the channel.

(b) Fluidity profiles.

Figure 13.5: (a) Velocity profiles for $\sigma_w = 45, 60, 75, 91$ Pa, i.e., $\sigma_w = 0.75, 1.0, 1.25, 1.52$ in model units, from top to bottom: (*dashed line*) simulation results, (*solid line*) predictions based on the numerical bulk flow curve. The crosses are experimental data obtained by Goyon *et al.*
(b) Fluidity profiles for $N_y = 12$, for $\sigma_w = 0.20, 0.28, 0.36, 0.48, 0.60, 0.72$ in model units. (*Filled circles*) numerical results, dashed green line: solution of Eq. 13.3 with $\xi(\dot{\gamma})/L_y = 0.03702$, *(solid blue line)* solution of Eq. 13.3 with $\xi(\dot{\gamma})/L_y = 0.01146\,\dot{\gamma}^{-0.25}$. The thin dash-dotted lines represent the bulk fluidity f_{bulk}.
Note that the curves in both subfigures have been shifted with respect to each other for clarity.

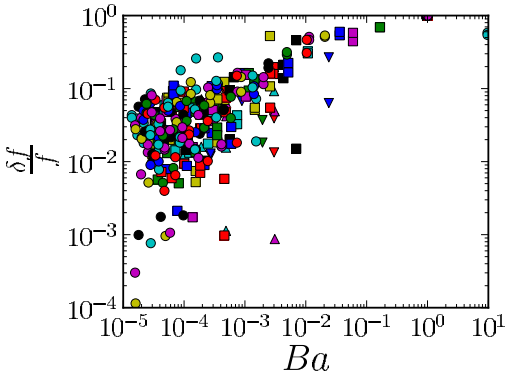

Figure 13.6: Relative deviations $\frac{\delta f}{f}$ of the local fluidity f from the bulk fluidity $f_{\text{bulk}}(\sigma)$ measured in simulations, where σ is the local shear stress, as a function of the estimated Babel number $\text{Ba} = \left(\xi_0 \frac{\nabla\sigma}{\sigma - \sigma_d}\right)^2$. We have set ξ_0 to 0.037 (see Fig. 13.5b). Data only include regions where $\sigma > \sigma_d$, but cover various applied pressures and channel widths: (▼) 6 blocks, (▲) 10 blocks, (■) 16 blocks, (●) 24 blocks.

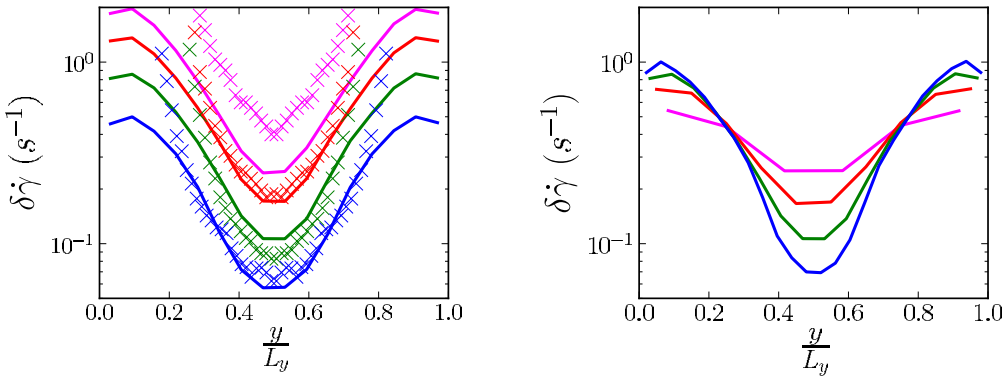

(a) Shear rate fluctuations $\delta\dot{\gamma}(y)$ (averaged along the x-direction), for $\sigma_w = 141\,\text{Pa}$, $188\,\text{Pa}$, $235\,\text{Pa}$, $282\,\text{Pa}$ (identical to Fig. 13.4a), from bottom to top. (×) Experimental data from Ref. Jop et al. [2012], (*solid lines*) numerical results for $L_y = 16$.

(b) Shear rate fluctuation profiles for a given stress at the wall, $\sigma_w = 0.48$ in model units, for different channel widths: (fuchsia) 6, (red) 10, (green) 16, and (blue) 24 blocks, in descending order of minimal values.

Figure 13.7: Shear rate fluctuations.

tal data [2], with the parameters used to fit the associated velocity profiles (see Fig.13.5a). Here, $\dot{\gamma}(x,y)$ is the local shear rate at point (x,y); it is given by $\dot{\gamma}(x,y) = 2\left(\dot{\epsilon}^{\text{pl}}_{xy}(x,y) + \dot{\epsilon}^{(1)}_{xy}(x,y)\right)$ in the model and is therefore obtained directly, that is, without deriving the velocity with respect to space. Figure 13.7a presents the experimental shear rate fluctuation profiles and their numerical counterparts for $L_y = 16$ blocks crosswise. Semi-quantitative agreement is observed in regions far from the walls - apart from the large discrepancy at the highest applied pressure. The discrepancies in the highly-sheared regions near the walls will be considered below. It is interesting to note that the fitted channel size provides another estimate for the size a of an elastoplastic block, which agrees with the first one, $a \approx 2$. Figure 13.7b shows the dependence of the shear rate fluctuations on the channel size for a given stress at the wall. As expected from the expression of the Babel number, fluctuations in the plug decay when the channel width is increased.

Let us note that the data collected by Jop and co-workers suggested a proportionality between the shear rate fluctuations and the local fluidity, implying that both are indicators of the intensity of the plastic activity. Figure 13.8 shows that the line-averaged plastic activity does indeed depend linearly on the local fluidity in our channel flow simulations, despite some discrepancies at low values of the fluidity, that is, probably in the plug. However, the relation between the shear rate fluctuations and the mean fluidity is much less clear (*data not shown*).

2. Note that we have discarded the two curves corresponding to the lowest applied pressures, which seem to plateau in the centre, because we were not entirely sure of the accuracy of these measurements.

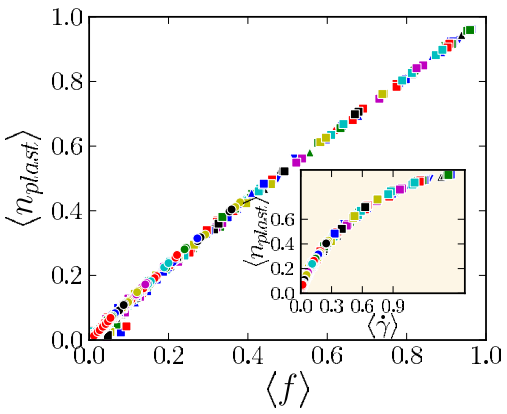

Figure 13.8: Time-averaged fraction of plastic blocks $\left\langle n_{\text{plast}} \right\rangle$ on a given streamline as a function of the mean fluidity $\langle f \rangle$ on that line, for diverse applied pressures and various channel widths: (▼) 6 blocks, (▲) 10 blocks, (■) 16 blocks, (●) 24 blocks. *Inset*: $\left\langle n_{\text{plast}} \right\rangle$ *vs.* the mean shear rate $\langle \dot{\gamma} \rangle$ on the line. (Same symbols).

13.4 A SPECIFIC RHEOLOGY NEAR THE WALLS?

In the previous section, we have dealt with the flow cooperativity associated with the coupling of heterogeneous streamlines, leaving aside another potentially significant difference with bulk homogeneous flow: the presence of walls bounding the flow, which is known to affect the flow of diverse complex fluids: wormlike micellar solutions [Masselon and Colin, 2010, Bécu et al., 2004], laponite [Gibaud et al., 2008], dense colloidal suspensions [Isa et al., 2007], etc. Indeed, Goyon et al. [2008] provided experimental evidence of the occurrence of ample changes when rough walls are substituted for smooth walls. Then, much larger deviations from bulk rheology are observed, especially at high applied pressures, and these deviations are maximal close to the walls, contrary to predictions based on the Babel number.

13.4.1 *Weak deviations due to no slip boundary condition*

Remember that walls are described by a no-slip boundary condition in our model. This condition results in a significantly larger dissipation during plastic events in their vicinity. Is this sufficient to capture the very large deviations observed experimentally?

Figure 13.9 shows the local flow curve for the simulations. To decouple to a certain extent the problem of wall rheology from the inhomogeneous drive, a relatively large channel is considered here. For each value of the wall stress, the points with the highest local shear rates in Fig. 13.9 are closest to the walls. We

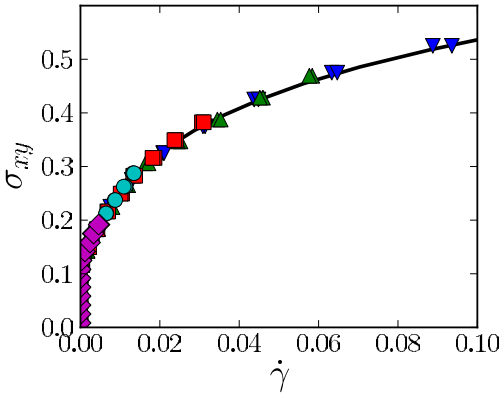

Figure 13.9: Local shear stress as a function of the local shear rate, for various applied pressures for a channel width of 24 blocks. The corresponding stresses at the walls are: (*purple rhombs*) $\sigma_w = 0.2$, (*cyan dots*) $\sigma_w = 0.2$, (*red squares*) $\sigma_w \simeq 0.4$, (*green upper triangles*) $\sigma_w \simeq 0.5$, (*blue lower triangles*) $\sigma_w = 0.6$.

do observe some slight deviations,[3] but they are clearly much weaker than in Goyon's observations (see Fig. 6 of Ref. [Goyon et al., 2010] for instance). In this respect, they much better describe the situation for smooth walls, which, at first, might seem surprising given the no-slip BC. Yet, in reality, the large slip observed at smooth walls should not give rise to significant changes: it only adds a simple global translation to the complex velocity field obtained with no-slip BC.

13.4.2 *Physical effect of rough walls*

As the deviations observed for rough walls are not captured by a simple no-slip BC, we discuss here some physical mechanisms that may be responsible for the observed behaviour.

First, the static structure near walls is known to differ from that in the bulk. For smooth, or not too rough, boundaries, stratification in layers is often reported over a distance of a few particle diameters [Ballesta et al., 2008, Mansard, 2012], though not systematically: the experiments of Ref. [Goyon et al., 2010], however, exhibited no such layering. Besides, the vicinity of a solid boundary hinders the mobility of Brownian particles [Pagac et al., 1996]. But these structural changes for the material at rest imply a decrease of the fluidity at the wall, as opposed to the enhancement that is experimentally observed by Goyon [Goyon et al., 2008] and Géraud [Geraud et al., 2013] at high enough stresses, *i.e.*, where the largest deviations occur. Alternatively, the specific behaviour at the wall is often rationalised by the existence of a depleted 'lubrication layer' close to the wall, as is often found in sheared dispersions [Yoshimura and Prud'homme, 1988, Barnes, 1995, Franco et al., 1998, Meeker et al., 2004a,b, Salmon et al., 2003, Bécu et al.,

3. Nevertheless, replacing the no-slip BC with a periodic BC will play a role if the Babel number is large enough. See Ref. Chaudhuri et al. [2012] for the effect of confinement on the observed yield stress in a biperiodic Poiseuille flow.

2005]. This phenomenon is more acute for deformable particles [Franco et al., 1998] undergoing high shear rates and/or high shear gradients; it generates an apparent wall slip. However, at the very high concentrations investigated here, owing to the large osmotic pressure, such a lubricating layer would have a thickness of order 100 nm or less [Salmon et al., 2003, Bécu et al., 2005, Goyon et al., 2010] (if the lubricating layer is composed of pure solvent). Effectively, Goyon directly measured the concentration profile across the channel and was not able to detect any significant variation. This finding is corroborated by the absence of radial droplet migration for a similar material in a Taylor-Couette cell, even at high shear rates, as reported in Ref. [Ovarlez et al., 2008]. Adding that soft particle suspensions have a much weaker viscosity dependence on concentration than their hard particle counterparts, effects of concentration variations could be ruled out as regards Goyon's experiments. Nevertheless, we attempted to simulate a less viscous layer close to the wall by decreasing the yield stress of the associated mesoscopic blocks, but this only had little effect on the rest of the system. Therefore, one is led to seek another explanation.

An aspect that has been overlooked so far is the reported observation of wall slip in Goyon's, Geraud's and Jop and Mansard's works, both with smooth and rough walls. In order to extract information that is relevant for the bulk flow, the authors measured the *local* velocities and shear rates in the channel by microscopic observation, so that the occurrence of slippage should not affect their results *a priori*. Indeed, in presence of smooth surfaces, where wall slip accounts for around 30% of the maximal velocity at the typical pressures applied by Goyon *et al.*, slip only results in a global translation of the system, that leaves the local flow curve strictly unaltered. For rough surfaces, let us first remark that the presence of wall slip is more surprising, since roughened surfaces[4] are often used to strongly suppress, or eliminate, slip for the very same type of materials, which is monitored by rheological measurements, and then used as benchmarks for a system without slip [Barnes, 1995, Sanchez et al., 2001, Mason et al., 1996, Meeker et al., 2004b, Meeten, 2004]. However, in several cases, measurements of local velocities in the flow, either with microvelocimetry with fluorescent tracers [Goyon et al., 2010, Goyon, 2008, Geraud et al., 2013] or through direct visualisation with confocal microscopy [Jop et al., 2012, Mansard, 2012], demonstrate that concentrated emulsions may slip along rough surfaces in microchannels. A seemingly quadratic [Goyon, 2008, Geraud et al., 2013], or linear [Mansard, 2012], dependence of the slip velocity on the shear stress at the wall in reported in these cases.

Now, when particles slide along a rough wall, they are expected to bump into, and be deformed by, the surface asperities. In the case of asperities that are large as compared to the "particle" size ($\sim$ 60 microns *vs.* from a few to 20 microns), this phenomenon is best exemplified by the spatiotemporal diagram acquired with ultrasonic velocimetry for a carbopol microgel, Fig. 6 of Ref. [Divoux et al., 2011a], where one can see a large deformation of the material that originates at

4. Diverse methods are available for roughening a surface, such as sandblasting, covering it with sandpaper, or coating it with particles.

the rotor and propagates almost instantaneously into the bulk; this signal was interpreted by the authors as the signature of a "bump" into a surface protuberance. Albeit less visible, the effect should also appear for smaller asperities: slip along rough walls should then create mechanical noise near the walls and cause deviations from bulk rheology. This tentative scenario has the potential to explain why deviations may, or may not, be observed in the vicinity of rough surfaces: for instance, Goyon *et al.* and Ovarlez *et al.*, as well as Seth et al. [2012], have reported that the local flow curves obtained in wide gap Taylor-Couette or plate-plate geometries with rough walls could be mapped onto the macroscopic flow curves; yet, they also indicated that, in those cases, no evidence of wall slip could be found. Very recently, Mansard endeavoured to investigate the impact of wall roughness by combining experiments and molecular dynamics simulations [Mansard, 2012, Mansard et al., 2014]. Non-monotonic variations of the wall fluidity as a function of the roughness were reported in the experiments, but the data did not allow for the extraction of the parameters responsible for the deviations from from macroscopic rheology. Nevertheless, he noted that "the particles must jump over the patterns [on the walls]. This effect induces the rearrangements and increases the wall fluidity".

Naturally, this prompts the following question: what determines the occurrence of slip along rough walls? This question lies far beyond the scope of the present study. Let us simply note that in Refs. [Goyon et al., 2008, 2010, Jop et al., 2012, Geraud et al., 2013] the size of surface asperities was a couple of microns at most, that is, significantly less than the typical "particle" size, which plausibly favours slip, as well as the high shear rates experienced at the microchannel walls. Nevertheless, recent theories of slip along smooth walls involved, in addition, parameters such as the deformability of the droplets [Meeker et al., 2004a,b] and the particle-wall interactions [Seth et al., 2008], not to mention the presumably significant impact of Brownian motion in cases where it is relevant [Besseling et al., 2009, Ballesta et al., 2012]. As far as we know, the somewhat daunting challenge to extend these theories to the case of rough walls still awaits a successful accomplisher. [5]

In the foregoing discussion, we have carefully eluded the question of the surface chemistry and its interactions with the particles. However, Seth and coworkers showed that they can play a signifiant role; in particular, for the yield stress fluid they studied, smooth attractive surfaces were observed to induced deviations from macroscopic rheology relatively far into the bulk, whereas smooth repulsive induced none at all.

Finally, we would like to mention another possible impact of the confinement of the material between walls. The channel may be so narrow that the layers where the specific wall rheology dominates start overlapping. This situation, which is described as strong confinement, is expected to occur when the channel width becomes of the order of, or smaller than, the cooperativity length ξ. For

5. A preliminary step in this direction has very recently been published by Mansard et al. [2014].

the data of Refs. [Goyon et al., 2008, 2010, Jop et al., 2012] discussed above, this mechanism is therefore not relevant.

13.4.3 *Artifical plastic events along the wall as mechanical noise sources*

As we have already noted, non-local effects leading to deviations from the macroscopic flow curve are often rationalised in terms of the fluidity diffusion equation (Eq. 13.3). In this approach, the fluidity at the wall is needed as an input parameter, whose precise value turns out to be determinant. Most likely, the suggested mechanical noise at the walls would be hidden in that value.

Our mesoscopic model is also oblivious to the microscopic details of the flow near a boundary and therefore cannot describe the effect of wall slip along a rough wall without further input. Nevertheless, since bumps generate mechanical noise in the system, one can attempt to account for their occurrence by adding artificial plastic events along the walls. Note that this *ad hoc* treatment is similar to imposing a wall fluidity larger than the bulk fluidity as a boundary condition when solving the fluidity diffusion equation (Eq. 13.3).

More precisely, we modify the implementation of the model slightly, so that a wall is now described as a line of plastically inert blocks: the bottom wall will, for instance, occupy the portion of space $0 \leqslant y \leqslant 1$, and the no-slip BC are imposed at its centre, *i.e.*, $y = 0.5$. On this line, a fraction of blocks is selected at random to act as sources of mechanical noise, that is, to mimic, e.g., bumps of particles into surface asperities. To do so, they shall release a constant plastic strain $\dot{\boldsymbol{\epsilon}}^{\mathbf{pl}}_{\mathrm{fict}}$ per unit time, along the direction of macroscopic shear (for simplicity). This does not violate mechanical equilibrium.

Figure 13.10a shows the local flow curves obtained with this protocol. The observed deviations are qualitatively similar to those reported by Goyon et al. [2010] (see Fig. 7 of that reference in particular). However, we must note that a rather intense mechanical noise is required to get such deviations $\left(\dot{\epsilon}^{pl}_{fict} \approx 5\right)$. (As the value of $\dot{\boldsymbol{\epsilon}}^{\mathbf{pl}}_{\mathrm{fict}}$ is arbitrary, we do not seek quantitative agreement with the experimental data here). In addition, these artificial plastic events also alter the shear rate fluctuation profile, as shown in Fig. 13.10b. Besides a global increase of the fluctuations, the profile no longer flattens in the vicinity of the walls, which renders it more consistent with the experimental results of Jop et al. [2012] (collected in a channel with rough walls).

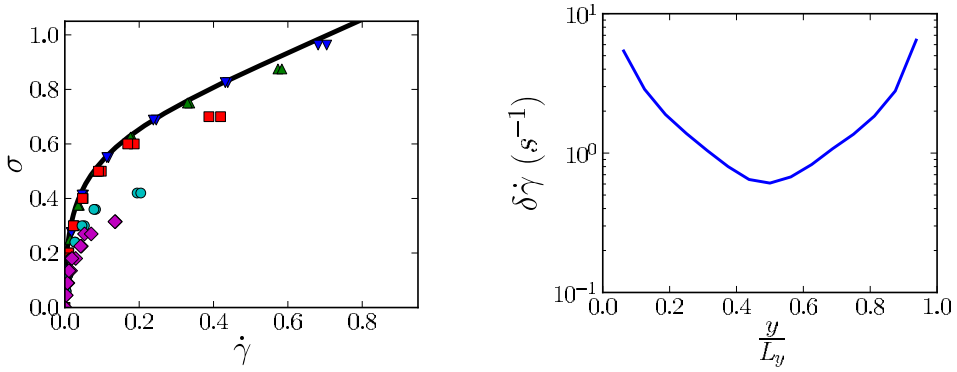

(a) Local shear rate $\sigma(y)$ *vs* local shear rate $\dot{\gamma}(y)$ (averaged on streamlines $y = \text{cst}$), for σ_w=(♦) 0.36, (●) 0.48, (■)0.8, (▲)1.0, (▼)1.1 in model units. (*Solid line*) macroscopic flow curve.

(b) Shear rate fluctuation profile.

Figure 13.10: Effect of artificial plastic events at the wall, designed to account for particle bumps. Artificial mechanical noise sources of intensity $\dot{\epsilon}^{\text{pl}}_{\text{fict}\,xy} = \pm 4.5$ are added on a fraction (1/3) of blocks on the wall lines.

Key Points of the Chapter [a]

- The elastoplastic model reproduces most features of experimental microchannel flows.
- In particular, spatial cooperativity associated with the coupling between streamlines subject to different stresses is well accounted for.
- The much larger deviations occurring in channels with rough walls can be assigned to a specific rheology near the walls.
- Pending experimental or theoretical confirmation, our hypothesis is that bumps of the particles against wall asperities cause these deviations.

a. These findings have found their way into two publications [Nicolas and Barrat, 2013a,b].

A

13.5 APPENDICES

13.5.1 *Derivation of the corrective terms to the propagator for a system bounded by walls*

The system covers the domain $(x, y) \in [0, L_x] \times [-L_y, L_y]$ and is periodically replicated throughout space. The region $y \in [0, L_y]$, bounded by walls at $y = 0$ and $y = L_y$ represents the *real* system, whereas the other half is a fictitious region introduced for the calculations.

For any plastic event $\boldsymbol{\epsilon}^{\mathbf{pl}} = \left(\epsilon^{\mathrm{pl}}_{xx}, \epsilon^{\mathrm{pl}}_{xy}\right)^{\top}$ occurring at position (x, y) in the real half, a symmetric plastic event $\boldsymbol{\epsilon}^{\mathbf{pl}\prime} = \left(\epsilon^{\mathrm{pl}}_{xx}, -\epsilon^{\mathrm{pl}}_{xy}\right)^{\top}$ is created at location $(x, -y)$ in the fictitious region. For symmetry reasons, the y-component of the velocity field is thereby cancelled on lines $y = 0$ and $y = L_y$ (bear in mind that the $2L_y$-wide system is periodically replicated).

Corrective forces to cancel u_x^{∞} at the walls

Let us now introduce forces ${\boldsymbol{f}_{\boldsymbol{x}}}^{(y=0)}$ and ${\boldsymbol{f}_{\boldsymbol{x}}}^{(y=L_y)}$ along $\boldsymbol{e_x}$ at the bottom $(y = 0)$ and top $(y = L_y)$ walls, respectively, to cancel the x-components. The Fourier transform of the force field reads:

$$\boldsymbol{f_x}(m, n) = {\boldsymbol{f}_{\boldsymbol{x}}}^{(y=0)}(m) + (-1)^n \, {\boldsymbol{f}_{\boldsymbol{x}}}^{(y=L_y)}(m)$$

Here, we have simplified notations by using the shorthand $g\,(m, n)$ for $g\,(\boldsymbol{q})$, for any function g, where $\boldsymbol{q} \equiv (p_m, q_n) \equiv \left(\frac{2\pi m}{L_x}, \frac{2\pi n}{2L_y}\right)$ is the Fourier wave vector. (Note the convenient change of notations: $q_x \to p_m$, $q_y \to q_n$.)

With these forces, the Fourier-transformed displacement field turns into:

$$\boldsymbol{u}^{(1)}\,(m, n) \;=\; \underbrace{\boldsymbol{\mathcal{G}}^{\infty}\,(m, n) \cdot \left(\boldsymbol{\epsilon}^{\mathbf{pl}}\,(m, n) + \boldsymbol{\epsilon}^{\mathbf{pl}\prime}\,(m, n)\right)}_{\equiv \boldsymbol{u}^{\star\infty}(m,n)} + \underbrace{\boldsymbol{\mathcal{O}}\,(m, n) \cdot \boldsymbol{f_x}\,(m, n)}_{\equiv \boldsymbol{u}^{\mathrm{corr}}(m,n)} \tag{13.4}$$

where $\boldsymbol{u}^{\mathrm{corr}}$ is the contribution from the wall forces and $\boldsymbol{\mathcal{O}}$ is the Oseen-Burgers tensor introduced in Section 8.2.1. The star in $\boldsymbol{u}^{\star\infty}$ only indicates that this symbol represents the velocity field induced by both the real plastic event and its symmetric counterpart.

Remarking that the condition of zero velocity at the bottom and top walls reads, in terms of Fourier components,

$$\forall m, \; \sum_n u_x^{(1)}(m, n) = 0$$

$$\text{and } \forall m,\ \sum_n (-1)^n u_x^{(1)}(m,n) = 0,$$

respectively, we obtain two equations on the f_x after substitution from Eq. 13.4. Adding and subtracting these equations yields, for any m:

$$\sum_{n\in O} u_x^{\star\infty}(m,n) + \mathcal{O}_{xx}(m,n)\cdot\left(\left(f_x^{(y=0)} - f_x^{\left(y=L_y\right)}\right)(m)\right) = \mathbf{0}$$

$$\sum_{n\in E} u_x^{\star\infty}(m,n) + \mathcal{O}_{xx}(m,n)\cdot\left(\left(f_x^{(y=0)} + f_x^{\left(y=L_y\right)}\right)(m)\right) = \mathbf{0}$$

where $O \equiv 2\mathbb{Z}+1$ is the set of odd integers, and $E \equiv 2\mathbb{Z}$ is the set of even integers.

Solution of the equations on the corrective forces

The solution of this linear system of equations is:

$$f_x(m\neq 0, n\in\delta) = \frac{-\mu}{e_\delta(m)}\sum_{n'\in\delta} u_x^{\star\infty}(m,n'), \tag{13.5}$$

where the symbol δ stands for either E (even n's) or O (odd n's) and μ is the shear modulus (it comes from the Oseen-Burgers tensor). The expressions for $m=0$ are written separately:

$$f_x(0, n\in 2\mathbb{Z}) = 0$$

$$f_x(0, n\in O) = \frac{-4\mu}{L_y^2}\sum_{n'\in O} u_x^{\star\infty}(m,n').$$

In Eq. 13.5, we have introduced auxiliary functions $e_E(m)$ and $e_O(m)$, which satisfy:[6]

$$e(m) \equiv \sum_{n\in\mathbb{Z}} \frac{q_n^2}{\left(p_m^2+q_n^2\right)^2} = \frac{L_y^2}{2\pi}\left[\frac{-\pi}{\sinh^2\left(\frac{2\pi L_y m}{L_x}\right)} + \frac{L_x}{2mL_y}\frac{1}{\tanh\left(\frac{2\pi L_y m}{L_x}\right)}\right]$$

$$e_E(m) \equiv \sum_{n\in E} \frac{q_n^2}{\left(p_m^2+q_n^2\right)^2} = {}^1\!/_4\, e(\frac{m}{2})$$

$$e_O(m) \equiv \sum_{n\in O} \frac{q_n^2}{\left(p_m^2+q_n^2\right)^2} = e(m) - {}^1\!/_4\, e(\frac{m}{2})$$

Now, the infinite summation in Eq. 13.5 needs to be calculated. For a single plastic event located at $(x_{\text{ev}}, y_{\text{ev}})$, that is, $\boldsymbol{\epsilon}^{\mathbf{pl}}(m,n) = e^{-ip_m x_{\text{ev}}} e^{-iq_n y_{\text{ev}}} \left(\epsilon_{xx}^{\text{pl}}, \epsilon_{xy}^{\text{pl}}\right)^\top$,

6. The analytical calculations leading to the second part of the equality involve the decomposition into simple elements and the use of well established summation results [Gradshteyn and Ryzhik, 1994].

expressing $u_x^{\star\infty}$ with the help of Eq. 8.5 and inserting the result into Eq. 13.5 leads to

$$\sum_{n'\in\delta} u_x^{\star\infty}(m,n') = 4e^{-ip_m x_{ev}}\left[\epsilon_{xy}^{\mathrm{pl}}\left(p_m^2\frac{L_y^3}{\pi^3}j_\delta(X) - \frac{L_y}{\pi}k_\delta(X)\right) - 2i\epsilon_{xx}^{\mathrm{pl}}p_m\frac{L_y^2}{\pi^2}s_\delta(X)\right], \tag{13.6}$$

where the δ-subscript stands for either E or O, and $X \equiv (x,\alpha) \equiv \left(\frac{\pi y_{ev}}{L_y}, \frac{p_m L_y}{\pi}\right)$.

Inserting Eq. 13.6 into Eq. 13.5, summing the plastic activity of all lines y, *i.e.*,[7] $y = 0.5,\ldots,L_y - 0.5$ $\left(L_y \in \mathbb{N}^\star\right)$ in the discretised version, and Fourier-transforming the results along direction x *via* the operator $\mathcal{F}_x$, defined by $\mathcal{F}_x\sigma = L_x^{-1}\int\sigma(x)e^{-ip_m x}dx$, one finally arrives at:

$$\boldsymbol{u}^{\mathrm{corr}}(m,n\in\delta) = \begin{pmatrix} \overbrace{\qquad\qquad}^{\equiv\zeta_\delta(X)} & \overbrace{\qquad\qquad}^{\equiv\xi_\delta(X)} \\ \frac{-4q_n^2}{4\mu q^4}\cdot\Big[\sum_y \overbrace{\left(\frac{p_m^2L_y^2\,j_\delta(X)}{e_\delta(m)\pi^3} - \frac{k_\delta(X)}{\pi}\right)}\mathcal{F}_x\sigma_{xy}^{\mathrm{pl}}(m,y) & -2i\sum_y \overbrace{\left(\frac{p_m L_y s_\delta(X)}{e_\delta(m)\pi^2}\right)}\mathcal{F}_x\sigma_{xx}^{\mathrm{pl}}(m,y)\Big] \\ \frac{4p_m q_n}{4\mu q^4}\Big[\sum_y\left(\frac{p_m^2L_y^2\,j_\delta(X)}{e_\delta(m)\pi^3} - \frac{k_\delta(X)}{\pi}\right)\mathcal{F}_x\sigma_{xy}^{\mathrm{pl}}(m,y) & -2i\sum_y\frac{p_m L_y s_\delta(X)}{e_\delta(m)\pi^2}\mathcal{F}_x\sigma_{xx}^{\mathrm{pl}}(m,y)\Big] \end{pmatrix}$$

where new summations appear and can be expressed analytically *via* a decomposition into simple elements and the use of known summation formulae [Gradshteyn and Ryzhik, 1994]:

$$\begin{aligned}
j(x,\alpha) &\equiv \sum_{k=-\infty}^{+\infty}\frac{k\sin(kx)}{(k^2+\alpha^2)^2} = \frac{\pi}{2\alpha^2}\frac{\sinh(\alpha(\pi-x))}{\sinh(\alpha\pi)} - \frac{1}{2\alpha^2}\mathcal{H}(x,\alpha)\\
j_E(x,\alpha) &= {}^1\!/_8\, j({}^x\!/_2, {}^\alpha\!/_2)\\
\mathcal{H}(x\neq 0,\alpha) &\equiv \sum_{k=-\infty}^{+\infty}\frac{k\sin(kx)}{(k-i\alpha)^2} = \frac{h(x,\alpha)+h(x,-\alpha)}{2}\\
h(x\neq 0,\alpha) &\equiv -i\sum_{k=-\infty}^{+\infty}\frac{k\exp(ikx)}{(k-i\alpha)^2} = \frac{\pi\exp(-x\alpha)}{1-\cosh(2\pi\alpha)}\left[x\alpha\left(e^{2\pi\alpha}-1\right)+2\pi\alpha-\left(e^{2\pi\alpha}-1\right)\right]\\
k(x,\alpha) &\equiv \sum_{k=-\infty}^{+\infty}\frac{k^3\sin(kx)}{(k^2+\alpha^2)^2} = \frac{\pi}{2}\frac{\sinh(\alpha(\pi-x))}{\sinh(\alpha\pi)} + \frac{\mathcal{H}(x,\alpha)}{2}\\
k_E(x,\alpha) &= {}^1\!/_2\, k({}^x\!/_2, {}^\alpha\!/_2)\\
s(x,\alpha) &\equiv \sum_{k=-\infty}^{+\infty}\frac{k^2\exp(ikx)}{(k^2+\alpha^2)^2} = \frac{\pi}{2}\frac{\cosh(\alpha(\pi-x))}{\alpha\sinh(\alpha\pi)} + \frac{\pi}{4}u(x,\alpha)\\
s_E(x,\alpha) &= {}^1\!/_4 s({}^x\!/_2, {}^\alpha\!/_2)\\
u(x,\alpha) &\equiv \frac{2x\cosh(\alpha(x-2\pi)) + (2\pi-x)\cdot 2\cosh(\alpha x)}{(1-\cosh(2\pi\alpha))}
\end{aligned}$$

The function j_O is obtained by writing $j(x,\alpha) = j_O(x,\alpha) + j_E(x,\alpha)$; the same applies to the other functions with subscripts O.

7. The $+0.5$ term comes from the fact that the y-coordinate of a block (of unit size) is evaluated at its centre.

The coincidence of the infinite summations and their analytical expressions has been verified numerically for particular values of the parameters.

As a technical remark, we would like to mention that the preceding formulae are difficult to evaluate numerically for $|\alpha| \gg 1$, on account of the large arguments of the hyperbolic functions. Nevertheless, the following approximations provide very satisfactory results in the limit of large positive α:

$$\frac{\sinh\left[\alpha\left(\pi - x\right)\right]}{\sinh\left(\alpha\pi\right)} \approx \exp\left(-x\alpha\right) - \exp\left(\alpha\left(x - 2\pi\right)\right)$$

$$\frac{\cosh\left[\alpha\left(\pi - x\right)\right]}{\sinh\left(\alpha\pi\right)} \approx \exp\left(-x\alpha\right) + \exp\left(\alpha\left(x - 2\pi\right)\right)$$

$$h(x,\alpha) \approx -2\pi\,\exp\left(-x\alpha\right)\left[x\alpha - 1\right]$$

$$u\left(x,\alpha\right) \approx -2\left[x\,\exp\left[\alpha\left(x - 4\pi\right)\right] + x\,\exp\left(-\alpha x\right) + \left(2\pi - x\right)\cdot\exp\left[\alpha\left(x - 2\pi\right)\right]\right]$$

Our final result is:

$$\begin{pmatrix} \sigma_{xx}^{\mathrm{corr}}(m,n) \\ \sigma_{xy}^{\mathrm{corr}}(m,n) \end{pmatrix} = \begin{pmatrix} \frac{-2p_m q_n^2}{q^4}\left[i\sum_y \zeta_\delta(X)\mathcal{F}_x\sigma_{xy}^{\mathrm{pl}}(m,y) + 2\sum_y \xi_\delta(X)\mathcal{F}_x\sigma_{xx}^{\mathrm{pl}}(m,y)\right] \\ \frac{q_n\left(p_m^2 - q_n^2\right)}{q^4}\left[i\sum_y \zeta_\delta(X)\mathcal{F}_x\sigma_{xy}^{\mathrm{pl}}(m,y) + 2\sum_y \xi_\delta(X)\mathcal{F}_x\sigma_{xx}^{\mathrm{pl}}(m,y)\right] \end{pmatrix}, \tag{13.7}$$

where one should note that $\zeta(0, n \in O) = \frac{-2}{L_y^2}$.

As a computational detail, the y-coordinates are here integers shifted by half unity, *i.e.*, of the form $p + 1/2$, $p \in \mathbb{N}$, whereas computational routines for Fast Fourier Transform take as input an array with integer indices. It is therefore easier to suppose that the walls are at positions $y = -1/2$ and $y = L_y - 1/2$. This translation is readily achieved by multiplying the Fourier components of the corrective term, as given above, by prefactors $\exp\left(\frac{iq_n}{2}\right)$.

Computational cost

Assuming a complexity $\mathcal{O}\left(N\,\ln N\right)$ for the Fast Fourier Transform of an array of N cells, the number of operations performed at each time step of our algorithm is of order $\mathcal{O}\left(L_x L_y^2\,\ln L_x\right)$ for large integers L_y and L_x, as is evident from Eq. 13.7. The numerical routine is easily parallelised.

13.5.2 *Calculation of the line-averaged velocity*

The line-averaged velocity on streamline $y = y_0$ reads:

$$
\begin{aligned}
\langle u_x \rangle_x (y_0) &\equiv \frac{1}{L_x} \int_{-L_x/2}^{L_x/2} u_x (x, y_0)\, dx \\
&= \sum_{n=-\infty}^{+\infty} u_x(m=0,n) e^{iq_n y_0} \\
&= \sum_{\substack{n=-\infty \\ n\neq 0}}^{+\infty} u_x^{\star\infty}(0,n) e^{iq_n y_0} + u_x^{\star\infty}(0,0) - \left(1 - \frac{2\,|y_0|}{L_y}\right) \sum_O u_x^{\star\infty}(0,\cdot) + \sum_E \overbrace{u_x^{\mathrm{corr}}(0,\cdot)}^{0} e^{iq_n y_0} \\
&= \sum_{y_{ev}} \frac{a}{2\mu} \left[\mathrm{sign}\,(y_0 - y_{ev}) \cdot \left(1 - \frac{|y_0 - y_{ev}|}{L_y}\right) + 1 - \frac{y_{ev}}{L_y} - \frac{y_0}{L_y} \right] \mathcal{F}_x \sigma_{xy}^{\mathrm{pl}}(m=0, y_{ev}),
\end{aligned}
$$

where the last summation is performed over all streamlines $y_e v$, and $u_x^{\star\infty}$ is the bulk contribution in the duplicated system.

13.5.3 *Estimation of the deviations due to bulk cooperativity*

Assume the fluidity diffusion equation is a valid approximation,

$$\xi^2 \Delta f - (f - f_{\mathrm{bulk}}) = 0$$

where $f = \frac{\dot\gamma}{\sigma}$ is the local fluidity, and ξ is a cooperativity length that may vary with the shear rate.

Let $\delta f = f - f_{bulk}$ be the deviation from the expected fluidity profile owing to cooperative effects between regions subject to different driving forces.

One now assumes $\delta f \ll f_{\mathrm{bulk}}$ and $\Delta \delta f \ll \Delta f_{\mathrm{bulk}}$.

To leading order, the fluidity diffusion equation reads

$$\xi^2 \Delta f_{\mathrm{bulk}} = \delta f$$

The amplitude of the deviations due to cooperativity is given by the Babel number $\mathrm{Ba} \equiv \frac{\delta f}{f} \approx \xi^2 \frac{\Delta f_{\mathrm{bulk}}}{f_{\mathrm{bulk}}}$

If the flow curve follows a Herschel-Bulkley law: $\sigma(\dot\gamma) = \sigma_d + A\dot\gamma^n$,

$$
f''_{\mathrm{bulk}} = \frac{\sigma'^2}{A^{1/n}} \frac{\sigma^{n-1} (\sigma - \sigma_d)^{1/n-1}}{n} \left[(1/n - 1) \frac{\sigma^{-n}}{\sigma - \sigma_d} \left((1-n) + n\frac{\sigma_d}{\sigma} \right)^2 - n\sigma^{-n-1} \left(1 - n + (1+n)\frac{\sigma_d}{\sigma} \right) \right]
$$

Here, the primes denote derivatives with respect to the space coordinate. Then,

$$
\frac{f''_{\mathrm{bulk}}}{f_{\mathrm{bulk}}} = \frac{\sigma'^2}{n(\sigma - \sigma_d)} \left[\frac{(1/n - 1)}{\sigma - \sigma_d} \left((1-n) + n\frac{\sigma_d}{\sigma} \right)^2 - \frac{n}{\sigma} \left(1 - n + (1+n)\frac{\sigma_d}{\sigma} \right) \right]
$$

To leading order, one finally arrives at $\frac{\delta f}{f} \sim \xi^2 \frac{\sigma'^2}{(\sigma - \sigma_d)^2}$.

14

SPATIOTEMPORAL CORRELATIONS BETWEEN PLASTIC EVENTS

After a first direct comparison with experimental data in the case of a microchannel flow, we come back to the study of simple shear flow and propose a comparison with athermal molecular dynamics (MD) simulations. Beyond the general flow properties, correlations will, once again, be at the core of this chapter. But, in comparison with Chapter 12 and recent independent works [Chikkadi et al., 2012, Mandal et al., 2013, Varnik et al., 2014, Chattoraj and Lemaître, 2013, Benzi et al., 2014], here, we shall measure dynamical correlations between the plastic events themselves, resolved both in space and in time, and study the influence of the applied shear rate. The comparison between atomistic simulations and the coarse-grained model will notably help us ascertain the origin of the prominent features of the correlations.

The MD simulations have been performed by Prof. Joerg Rottler *(University of British Columbia).*

14.1 COMPARATIVE STUDY OF GENERAL FLOW PROPERTIES OBTAINED IN MOLECULAR DYNAMICS (MD) AND WITH THE ELASTOPLASTIC MODEL

Before delving into the study of plastic correlations, we need to make sure that the (properly fitted) elastoplastic model can reproduce the general flow properties observed in MD, *i.e.*, the macroscopic rheology and the statistics of individual plastic events.

14.1.1 *MD simulations at zero temperature: Method*

We simulate the shear flow of a binary mixture of A and B particles, with $N_A = 32500$ and $N_B = 17500$, of respective diameters$\sigma_{AA} = 1.0$ and $\sigma_{BB} = 0.88$, confined in a square box of dimensions 205×205, with periodic BC. The system is at reduced density 1.2. The particles, of mass $m = 1$, interact via a pairwise Lennard-Jones potential,

$$V_{\alpha\beta}(r) = 4\epsilon_{\alpha\beta}\left[\left(\frac{\sigma_{\alpha\beta}}{r}\right)^{12} - \left(\frac{\sigma_{\alpha\beta}}{r}\right)^{6}\right],$$

where $\alpha, \beta = A, B$, $\sigma_{AB} = 0.8$,$\epsilon_{AA} = 1.0$, $\epsilon_{AB} = 1.5$, and $\epsilon_{BB} = 0.5$. The potential is truncated at $r = 2.5\sigma_{AA}$ and shifted for continuity. Simple shear γ is imposed at rate $\dot{\gamma}$ by deforming the box dimensions and remapping the particle positions.

We conduct our study in the athermal limit, by thermostatting the system to a zero temperature, so that no fluctuating force appears in the equations of motion, *viz.*,

$$\begin{cases} m\frac{d\boldsymbol{r_i}}{dt} &= \boldsymbol{p_i} \\ \frac{d\boldsymbol{p_i}}{dt} &= -\sum_{i\neq j}\frac{\partial V(\boldsymbol{r}_{ij})}{\partial \boldsymbol{r}_{ij}} - \frac{\boldsymbol{p_i}}{\tau_d} \end{cases} \tag{14.1}$$

where $(\boldsymbol{p_i}, \boldsymbol{r_i})$ are the momentum and position of particle i in the deforming frame. Besides the interparticle forces, the motion of particle i is subject to a damping force $-\frac{\boldsymbol{p}_i}{\tau}$, that models friction against solvent molecules in a mean-field way. Here, $\tau_d = 1$ is the Langevin damping time. The relevance of this specific implementation of friction shall be discussed in Section 14.3.4. Equations 14.1 are integrated with the velocity Verlet algorithm with $\delta t = 0.005$. In the following, we shall use $\tau_{LJ} \equiv \sqrt{m\sigma_{AA}^2/\epsilon}$ as the unit of time and σ_{AA} as the unit of length.

To obtain the initial glassy states, we quenched the system at constant volume from the liquid state $T = 1$ down to zero temperature at a fast rate, $2 \cdot 10^{-3}\tau_{LJ}^{-1}$. Note that, before any data were collected, the system was always pre-sheared for $\gamma = 0.2$ to ensure that the steady state had been reached. We have checked that pre-shearing the material over a longer strain window, $\gamma = 1.2$, leads to identical results.

14.1.2 *Elastoplastic model and model parameters*

With regard to the elastoplastic model, we shall employ the refined athermal dynamical rules introduced in Section 9.3. As a short reminder, they involve an exponential distribution of energy barriers with a lower cut-off at $E_y \equiv \mu\gamma_c^2/4$, *viz.*,

$$P\left(E_y\right) \quad = \quad \Theta\left(E_y - E_y^{\min}\right)\lambda e^{\lambda\left(E_y^{\min} - E_y\right)}, \tag{14.2}$$

a von Mises yield criterion for every block, and a plastic event lasts until a strain γ_c has been cumulated in the plastic phase.

14.1.3 *Flow curve*

The dependence of the macroscopic shear stress Σ on $\dot{\gamma}$ in MD is shown in Fig. 14.1; it is well described by the Herschel-Bulkley law $\Sigma = 0.73 + 2.9\dot{\gamma}^{0.48}$.

Regarding the bulk mechanical properties of the system, plotting the stress as a function of strain at a given shear rate yields an MD shear modulus $\mu \simeq 17$ for the system (prior to deformation) and a macroscopic yield strain γ_y of order 5-10%.

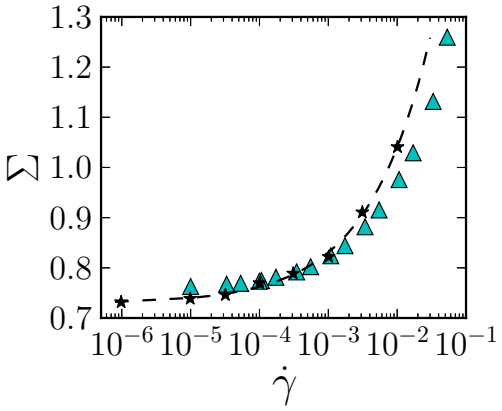

Figure 14.1: Dependence of the macroscopic shear stress Σ on the applied shear rate $\dot{\gamma}$. (*Black stars*) MD simulation; (*blue triangles*) coarse-grained model. The dashed black line is a fit to the Herschel-Bulkley equation, $\Sigma = 0.73 + 2.9\dot{\gamma}^{0.48}$.

Determination of the model parameters

Consequently, with respect to the parameters of the elastoplastic model, we adjust λ in the energy barrier distribution so that the ensemble average of the yield strain is $\langle \gamma_y \rangle = 0.1$.

To fit the flow curve, we choose $\gamma_c = 0.085 \langle \gamma_y \rangle$ and the units of time and stress are set to $\tau = 1.5\tau_{LJ}$ and $\mu = 12.5$, a value comparable to the shear modulus of the atomistic system prior to deformation ($\mu_{MD} = 17$). As can be seen in Fig. 14.1, this provides a satisfactory agreement between the elastoplastic and MD flow curves. In addition, their best fits by Herschel-Bulkley equations have very similar exponents n.

14.1.4 *Stress autocorrelation function*

Turning to a more local viewpoint, in Fig. 14.2a we plot the MD autocorrelation function

$$C_\sigma(\Delta\gamma) \equiv \frac{\langle \delta\sigma_{xy}(\gamma)\, \delta\sigma_{xy}(\gamma + \Delta\gamma) \rangle}{\langle \delta\sigma_{xy}^2 \rangle} \tag{14.3}$$

of the local shear stress fluctuations $\delta\sigma_{xy} \equiv \sigma_{xy} - \langle \sigma_{xy} \rangle$ experienced by each particle. The averages are performed over time t. We observe a nice collapse of the data for the different shear rates. This confirms that the applied strain $\Delta\gamma$, and not the absolute time t, causes the decorrelation in this driven athermal system, in line with the idea of periods of elastic accumulation of stress interspersed with shear-induced plastic events. The master curve is reasonably well fit by a stretched exponential $\exp\left[\left(\frac{-\Delta\gamma}{\Delta\gamma^\star}\right)^\beta\right]$, with an exponent $\beta = 0.68$ and a critical strain $\Delta\gamma^\star = 0.11$ close to the macroscopic yield strain.

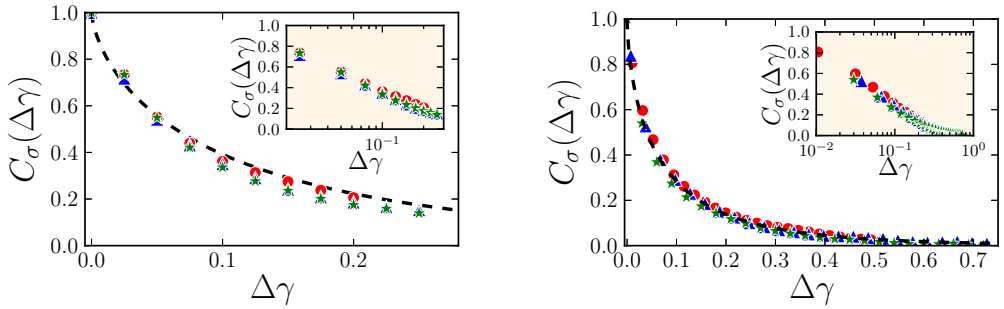

(a) MD simulations

(b) Elastoplastic model

Figure 14.2: Autocorrelation function $C_\sigma(\Delta\gamma)$ of the local shear stress fluctuations at applied shear rates (*red dots*) $\dot{\gamma} = 10^{-5}$, (*blue triangles*) $\dot{\gamma} = 10^{-4}$, and (*green stars*) $\dot{\gamma} = 10^{-3}$. The dashed lines represent a fitting to a stretched exponential $C_\sigma(\Delta\gamma) = \exp\left[\left(\frac{-\Delta\gamma}{\Delta\gamma^\star}\right)^\beta\right]$, with $(\beta = 0.68,\ \Delta\gamma^\star = 0.11)$ for the MD data and $(\beta = 0.65,\ \Delta\gamma^\star = 0.07)$ for the elastoplastic model. (*Inset*) Same data, plotted with a logarithmic horizontal axis.

The stress autocorrelations at different strain rates also collapse onto a master curve in the elastoplastic model, as shown in Fig. 14.2b. Interestingly, fitting this curve with a stretched exponential also yields $\beta = 0.65$, very close to the exponent used to fit the MD data, although the precise value of the critical strain obtained here, $\Delta\gamma^\star = 0.07$, differs by 50%.

14.1.5 *Indicator of plastic activity in the atomistic simulations*

Let us now focus on plastic events. In order to detect them in the atomistic simulations, we make use of the D^2_{min} quantity presented by Falk and Langer [1998], which evaluates deviations from an affine deformation on a local scale. This quantity has been used with noted success to characterise plasticity [Chikkadi et al., 2011, 2012, Chikkadi and Schall, 2012, Mandal et al., 2013, Varnik et al., 2014, Keim and Arratia, 2014]; in particular, it was shown to yield results consistent with other measures of non-affinity [Chikkadi and Schall, 2012]. D^2_{min} is defined locally, around a particle labelled i, as the minimum over all possible linear deformation tensors $\boldsymbol{\epsilon}$ of

$$D^2(i;t,\delta t) \quad = \quad \sum_j \left[r_{ij}(t+\delta t) - (\mathbb{I}+\boldsymbol{\epsilon})\cdot r_{ij}(t)\right]^2, \tag{14.4}$$

where the sum runs over all neighbours j of i, and $\mathbb{I}$ denotes the identity matrix. The value of the time lag δt ($\delta t = 4\tau_d$) was fine-tuned to provide a good signal over noise ratio while still being short enough to allow a temporal resolution of the plastic events. Figure 14.3 presents a snapshot of D^2_{min} values in the system: one clearly sees localised plastic regions embedded in an affinely-deforming medium.

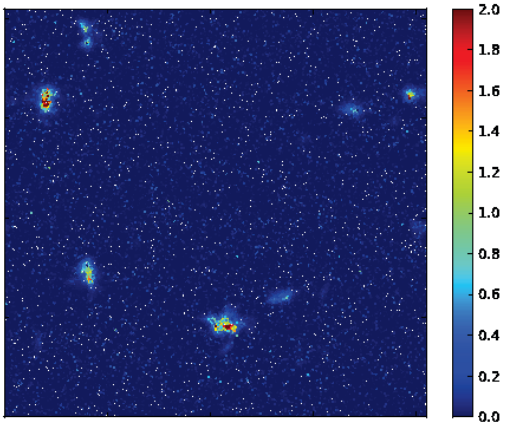

Figure 14.3: Snapshot of the D^2_{min} field at an applied shear rate $\dot{\gamma} = 10^{-4}$.

Interestingly, the regions with large D^2_{min} systematically coincide with the regions exhibiting large velocities relative to the average solvent flow. This coincidence between the non-locally-affine displacement field and the singular velocity confirms that a large local energy dissipation is the hallmark of a plastic event.

14.1.6 *Distribution of durations, magnitudes, and sizes of individual plastic events*

With a reliable tool to measure plastic activity in our hands, we can now study the properties of individual plastic events in detail.

First, by scrutinising a number of D^2_{min} snapshots such as that presented in Fig. 14.3, we observe that the size of plastic regions is typically a few particle diameters; this size does not depend dramatically on the shear rate. This point shall be confirmed in Section 14.3 by a detailed analysis of the spatial correlations of the D^2_{min} field.

Further insight is gained by computing the overall distribution of the measured D^2_{min} values, in Fig. 14.4a. All distributions exhibit an exponential tail, and they collapse upon rescaling with the inverse shear rate. Because of the cut-off introduced in the elastoplastic yield stresses (see Eq. 14.2), the distribution of plastic event magnitudes naturally differs between the two simulation methods, at least for small magnitudes. Nevertheless, the elastoplastic distribution is also roughly independent of the applied shear rate (*data not shown*).

Finally, the typical lifetime of a plastic event can be extracted from the temporal decay of the D^2_{min} autocorrelation function plotted in Fig. 14.4b. For the damping time used in this study, regardless of the shear rate, it is of the order of 3 time units. Turning to the elastoplastic model, the average life time of a single plastic event is of order a couple of τ's, too, (remember that we set τ to 1.5) at all shear rates. Paying a closer look at the distribution of life times, one may however notice a visible decrease of this quantity as the shear rate is increased, from 8.4 at $\dot{\gamma} = 10^{-5}$ to 4.2 at $\dot{\gamma} = 10^{-3}$. This is not unexpected, because the

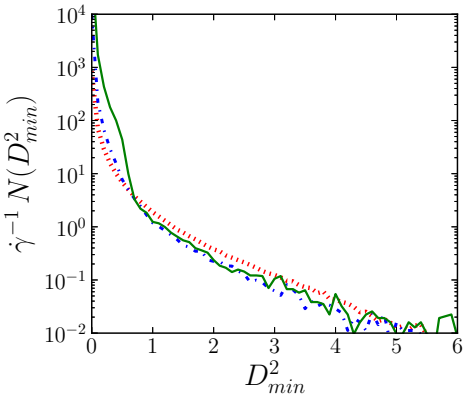

(a) Histograms of D^2_{min} values at shear rates (*dotted red line*)$\dot{\gamma} = 10^{-5}$, (*dashdotted blue line*)$\dot{\gamma} = 10^{-4}$, and (*solid green line*)$\dot{\gamma} = 10^{-3}$. The distributions have been renormalised with the inverse shear rate.

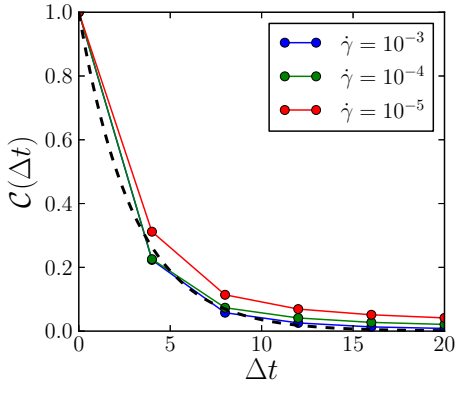

(b) D^2_{min} autocorrelation function $\mathcal{C}(\Delta t) \equiv \langle D^2_{\text{min}}(\boldsymbol{r}, t) D^2_{min}(\boldsymbol{r} + \boldsymbol{\epsilon}, t + \Delta t) \rangle \,/\, \left\langle \left(D^2_{\text{min}}(r, t) \right)^2 \right\rangle$ as a function of the time lag Δt, where $\|\boldsymbol{\epsilon}\| \simeq 0.005L$ has only been added to avoid numerical artifacts. The dashed black line represents $\exp\left(-\Delta t/3.0\right)$.

Figure 14.4: Properties of the plastic event indicator D^2_{min}.

criterion determining the duration of a plastic event (Eq. 9.2) involves the total local deformation rate.

14.1.7 *Surface coverage of plastic rearrangements*

To quantify the global plasticity of the system, we compute the instantaneous surface density of plastic events, *i.e.*, the fraction of blocks which are plastic at a given time. In the absence of thermally-activated plastic events, this quantity increases linearly with the shear rate, from 0.05% at $\dot{\gamma} = 10^{-5}$ to 0.36% at $\dot{\gamma} = 10^{-4}$ and 2.8% at $\dot{\gamma} = 10^{-3}$, in the elastoplastic model. These values are similar to those obtained from the atomistic simulations by integrating the tails of the D^2_{min} distributions, in Fig. 14.4a, down to a reasonable (but arbitrary) lower threshold: 0.07%, 0.3%, and 0.8%, respectively.

Thus, the elastoplastic model reproduces the MD macroscopic rheology and statistics of plastic events satisfactorily.

14.2 CONCEIVABLE PROTOCOLS FOR THE DETECTION OF PLASTIC EVENT AVALANCHES

Having verified the agreement of the coarse-grained model with the atomistic simulations with regard to the general flow properties, we can now move on to the study of the correlations in the flow. Ideally, we would like to compare the

avalanches of plastic events in both types of simulations. However, this requires to set up a protocol for the detection of avalanches.

14.2.1 *Fuzziness of the concept of avalanche at finite shear rates*

The definition of an avalanche in the quasi-static limit is self-evident: it is simply the succession of plastic events that follows an infinitesimal strain increment [Baret et al., 2002, Maloney and Lemaître, 2004, Maloney and Lemaître, 2006, Budrikis and Zapperi, 2013]. The stress *vs.* strain curve then displays long periods of stress accumulation interspersed by distinct unloading events corresponding to avalanches.

On the other hand, at any finite shear rate $\dot{\gamma} > 0$, the definition of an avalanche is more problematic. Indeed, avalanches are no longer incompatible with periods of macroscopic stress increase in the stress *vs.* strain curve, as they do not cover the whole system.. Moreover, the system may accommodate distinct avalanches occurring in parallel, which it is not straightforward to disentangle.

As a matter of fact, the very concept of avalanche becomes fuzzy $\dot{\gamma} > 0$. Suppose that n avalanches are occurring in parallel in a system. Consider a block that has just yielded. Over time, this block has received stress contributions from the macroscopic drive as well as from plastic events from the n avalanches. How should one then decide to which avalanche it should be assigned, or perhaps whether it is the source of a new avalanche?

14.2.2 *Salerno* et al.*'s protocol*

Salerno et al. made use of the following protocol to compute avalanche sizes in atomistic simulations, at vanishing shear rate, but with inertia [Salerno et al., 2012, Salerno and Robbins, 2013]: during the loading phases, the strain is increased at a finite (albeit small) strain rate, but, as soon as some plastic rearrangement is detected, the macroscopic drive is cut off and the avalanche is left free to develop.

A comparable approach could be undertaken in our simulations at finite shear rates: at a randomly chosen time t_0 in the simulation, $\dot{\gamma}$ can be switched to zero. It follows that all the blocks that yield thereafter are part of an avalanche that was active at t_0.

Nevertheless, disentangling the possibly many avalanches at t_0 would remain an issue.

14.2.3 *Plastic event removal*

Taking even greater advantage of the flexibility of numerical simulations, we suggest an alternative protocol. Suppose that a *fictitious* simulation (S_f) is run exactly identically to a reference simulation (S_r), *i.e.*, with the same parameters and the same set of random numbers, except that one randomly selected plastic event (P) in S_r is inhibited in S_f (and impose that plastic events may occur in S_f

only if they also occur in S_r). Then, the plastic events in S_r that have not taken place in S_f due to the non-occurrence of P belong to the avalanche triggered (or passed on) by P.

I have implemented this protocol, but it has encountered only little success: the avalanches thus detected were mostly limited to P only.

14.2.4 *Plastic correlator*

Jettisoning our hope to detect whole avalanches, we will in fact measure correlations between two plastic events. This is done with the following *plastic correlator*:

$$\mathcal{C}_2\left(\Delta\boldsymbol{r}, \Delta t\right) \equiv \alpha\left(\left\langle \overline{n\left(\boldsymbol{r}, t\right) n\left(\boldsymbol{r}+\Delta\boldsymbol{r}, t+\Delta t\right)}\right\rangle - \left\langle \overline{n\left(\boldsymbol{r}, t\right)} \cdot \overline{n\left(\boldsymbol{r}, t+\Delta t\right)}\right\rangle\right) \tag{14.5}$$

where the brackets denote an average over time t, the bars represent an average over spatial coordinate $\boldsymbol{r}$, and, as usual, $n(\boldsymbol{r}, t) = 1$ if the block at position $\boldsymbol{r} = (i, j)$ is plastic at time t, 0 otherwise. The prefactor $\alpha \equiv \left[\left\langle \overline{n(\boldsymbol{r}, t)^2}\right\rangle - \left\langle \overline{n(\boldsymbol{r}, t)}^2\right\rangle\right]^{-1}$ is chosen such that $\mathcal{C}_2\left(\Delta\boldsymbol{r} = \boldsymbol{0}, \Delta t = 0\right) = 1$.

An MD counterpart can straightforwardly be defined, *viz.*,

$$\mathcal{C}_2\left(\Delta\boldsymbol{r}, \Delta t\right) \equiv \alpha\left(\left\langle \overline{D^2_{\min}\left(\boldsymbol{r}, t\right) D^2_{\min}\left(\boldsymbol{r}+\Delta\boldsymbol{r}, t+\Delta t\right)}\right\rangle - \left\langle \overline{D^2_{\min}\left(\boldsymbol{r}, t\right)} \cdot \overline{D^2_{\min}\left(\boldsymbol{r}, t+\Delta t\right)}\right\rangle\right)$$

where $\alpha \equiv \left[\left\langle \overline{(D^2_{\min}(\boldsymbol{r}, t))^2}\right\rangle - \left\langle \overline{(D^2_{\min}(\boldsymbol{r}, t))}^2\right\rangle\right]^{-1}$.

Clearly, the two-point, two-time observable $\mathcal{C}_2$ measures the (enhanced or reduced) likelihood that a plastic event occurs at $\boldsymbol{r} + \Delta\boldsymbol{r}$ if a plastic event was active at position $\boldsymbol{r}$ some prescribed time Δt ago. Accordingly, it measures the extent to which the position of the next plastic event is influenced by that of its predecessors. We hold out hope that extensive information about the dynamical organisation of the flow will thus be revealed, even if we are unable to predict exactly where the next plastic event will occur in the material *without* detailed knowledge of the current, static configuration of the system [Widmer-Cooper et al., 2008, Tsamados et al., 2009].

14.3 CORRELATIONS BETWEEN PLASTIC EVENTS

14.3.1 *Correlated plastic events*

Before probing the simulated flows with the plastic correlator $\mathcal{C}_2$ that has just been introduced, let us briefly recall existing pieces of evidence pointing to correlations between plastic events.

In the athermal, quasi-static limit, Maloney and Lemaître showed numerically that they are essentially organised in strongly correlated avalanches [Maloney

and Lemaître, 2004]. By investigating the transverse particle diffusivity, Lemaître and colleagues then showed that these correlations persist at finite shear rates [Lemaître and Caroli, 2009] and at finite temperatures [Chattoraj et al., 2010, 2011]. The spatial structure of these correlations was revealed by Chikkadi, Mandal, Varnik, *et al.* [Chikkadi et al., 2012, Mandal et al., 2013]; these researchers provided convincing experimental and numerical evidence that the correlations between flow heterogeneities, quantified by D^2_{min}, are long-ranged and all the more anisotropic as shear prevails over thermal effects, i.e., at larger Peclet numbers. To do so, they monitored particle displacements in a driven "hard sphere" colloidal glass with confocal microscopy and were able to reproduce their experimental observations qualitatively with molecular dynamics simulations. Quantitatively, some discrepancies were found between simulations and experiments, the latter displaying longer correlations, with a power law decay in space.

Here, we purport to extend these studies and unveil the full dynamical picture.

14.3.2 *Decay of the intensity of the correlation with time*

Plastic correlations are expected to fade away with the time lag Δt, but one may wonder whether their decay is more appropriately described in terms of the absolute time t or the strain γ. Quite interestingly, in the atomistic simulations as well as in the coarse-grained model, absolute time turns out to be the adequate unit of measurement, as evidenced by comparing the evolution of the correlations at different shear rates.

It should be pointed out that this does not conflict with the decay of stress correlations as a function of the *strain*. The difference comes from the fact that plastic correlations are conditional probabilities, hinging on the occurrence of a first plastic event at $(\boldsymbol{r}, t)$. On the contrary, stress correlations involve all pairs of instants separated by a given Δt; therefore, one generally has to wait for the whole elastic regime to observe a decorrelation.

14.3.3 *Maps of plastic correlations at various shear rates*

The plastic correlations obtained in the atomistic simulations are shown in Figs. 14.6, 14.7, and 14.8 at different time lags for three distinct shear rates: $\dot{\gamma} = 10^{-5}$ (very low, quasi-static), $\dot{\gamma} = 10^{-4}$ (moderate) and $\dot{\gamma} = 10^{-3}$ (moderately high). The counterparts for the coarse-grained simulations are presented directly opposite to them so as to allow an easy comparison, but they will only be discussed later.

The presence of a spatial structure in the correlations is evident, which is strong evidence that plastic rearrangements are indeed interdependent, and not fully isolated events. The positive correlations in the streamwise and crosswise directions are strongly reminiscent of the positive lobes of the elastic propagator $\mathcal{G}$, which supports the idea of interactions via an elastic coupling. In diagonal directions, there tend to be anticorrelations. The (anti)correlations decay gradually, over approximately the same (absolute) time scale as the autocorrelation

function, i.e., their value at the origin. These features are common to the various shear rates studied here.

A closer investigation of the plots shows that the decay time tends to decrease with increasing shear rate, thereby reflecting the shear-induced decorrelation of the system. Moreover, while the streamwise and crosswise lobes are hardly distinguishable at high shear rates, at lower shear rates there is clearly an asymmetry between them. The propensity to shear localisation of the plastic activity is therefore enhanced at lower shear rates. This is more visible in Fig. 14.9a, where the correlations are integrated along the radial direction in different directions. An enhanced propensity to shear localisation, or, more generally, flow heterogeneities, with decreasing shear rates has already been reported in the literature [Picard et al., 2005, Martens et al., 2012, Divoux et al., 2011a], although, here, some artifact associated with the use of Lees-Edwards-like BC cannot be strictly excluded [Chattoraj and Lemaître, 2013].

An additional effect of the shear rate is that the anticorrelated lobes in the diagonal directions appear stronger at higher shear rates.

To assess the strength of the correlations, that is, to what extent they deviate from a random distribution of plastic events, we compare the probabilities that two plastic events, separated by a distance Δr and a time lag Δt, are aligned, on the one hand, along the velocity gradient direction $\boldsymbol{e}_\perp$ and, on the other hand, along the diagonal direction $\boldsymbol{e}_{\mathbf{diag}}$ with respect to the macroscopic shear. The anistropy ratio,

$$\alpha_\perp(\Delta r, \Delta t, \dot\gamma) \equiv \frac{\left\langle D^2_{\min}(\boldsymbol{r},t) D^2_{\min}(\boldsymbol{r}+\Delta r\, \boldsymbol{e}_\perp, t+\Delta t)\right\rangle}{\left\langle D^2_{\min}(\boldsymbol{r},t) D^2_{\min}(\boldsymbol{r}+\Delta r\, \boldsymbol{e}_{\mathbf{diag}}, t+\Delta t)\right\rangle}, \tag{14.6}$$

is plotted in Fig. 14.5a. We observe an enhancement of the probabilities of streamwise alignment (versus diagonal alignement) by, at most, 10 to 20%.

We now turn to the spatial extent of the correlations. In panel (a) of Fig. 14.10, we show how they decay along the flow direction, for distinct time lags. The decay, which is not purely exponential, depends only weakly on the shear rate, except at long time lags. Besides, it spreads over larger and larger distances as the time lag is increased; it should however be noted that the correlations have been rescaled so as to be equal to one close to the origin at all time lags, so that a slower spatial decay does not necessarily imply a larger *absolute* value far from the origin. This rescaling also entails that small fluctuations will be magnified when the correlations near the origin are small, e.g., for the long time lag $\Delta t = 20$, notably in the moderately high shear rate case.

At this stage, we should mention an extremely recent study by Varnik and coworkers, who reported that the spatial decay of the $D^2_{\min}$ correlations was highly contingent on the specific implementation of the friction force in the equations of motion [Varnik et al., 2014]. [1] More precisely, only a friction force based on

1. Note that, although these researchers have computed nominally "static" correlations, that is to say, at $\Delta t = 0$, the time δt which they used to compute D^2_{min} is very large, so that their data actually correspond to an integral of our dynamical correlations $C_2(\Delta r, \Delta t)$ over a wide range of time lags Δt.)

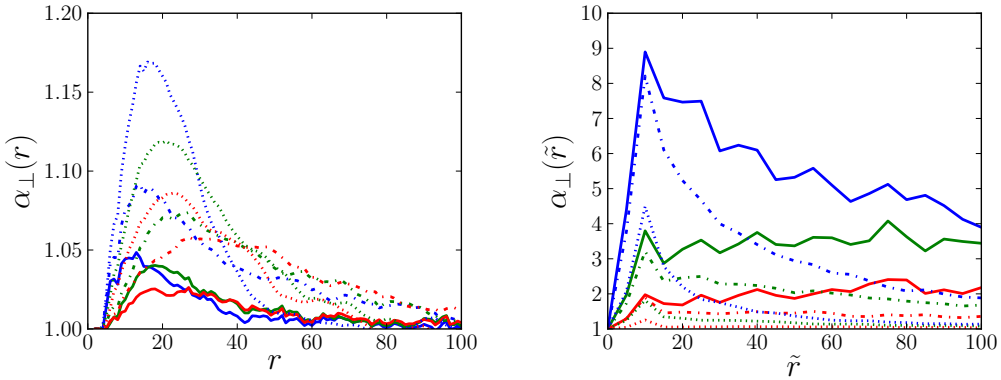

(a) MD simulations. (*Blue*) $\Delta t = 4$, (*green*) $\Delta t = 12$, (*red*) $\Delta t = 20$.

(b) Coarse-grained model. (*Blue*) $\Delta t = 1$, (*green*) $\Delta t = 8$, (*red*) $\Delta t = 16$.

Figure 14.5: Anisotropy ratio $\alpha_\perp(\Delta r, \Delta t, \dot{\gamma})$ for the different shear rates: (*solid line*) $\dot{\gamma} = 10^{-5}$, (*dash-dotted line*) $\dot{\gamma} = 10^{-4}$, and (*dotted line*) $\dot{\gamma} = 10^{-3}$. Various time lags Δt are considered (see subfigure captions).
To allow direct comparison, we have set the size of one coarse-grained block to $\tilde{r} = 5$.

the relative velocity of a particle with respect to its neighbours ("contact dynamics") could reproduce the power law decay observed in experiments on colloidal suspensions and immersed granular matter, whereas a mean-field dissipation scheme predicted a faster, exponential decay. Actually, the effect of the specific implementation of the frictional force has been the subject of a wider debate: Tighe *et al.*, for instance, reported that using a friction term based on relative particle displacements is key to finding suitable correlation functions in the vicinity of the jamming point [Tighe et al., 2010], while Vagberg *et al.* claimed that a critical behaviour is found with both schemes [Vågberg et al., 2013]. Here, we have used a mean-field friction force; accordingly, some quantitative discrepancies may be expected between the extent of the correlations that we have found and those measured in the experimental setups of Ref. [Chikkadi et al., 2012, Varnik et al., 2014]. However, our choice of friction force is, arguably, the more adequate one for confined two-dimensional geometries in which particles slide along a fixed plate, for instance, bubble rafts confined in between parallel glass plates [Debregeas et al., 2001].

14.3.4 *Successes and limitations of the coarse-grained model*

In the previous section, we have seen that the coarse-grained model gives a rather satisfactory description of the macroscopic properties, as well as the local ones. Here, we enquire how well it fares with respect to $\mathcal{C}_2$.

As shown in Figs.14.6 through 14.8, the correlation maps for the two models do bear some resemblance, but the agreement is at best very qualitative.

Among the satisfactory aspects, the coarse-grained model also indicates a decay of the correlations with absolute time and correlations display a four-fold

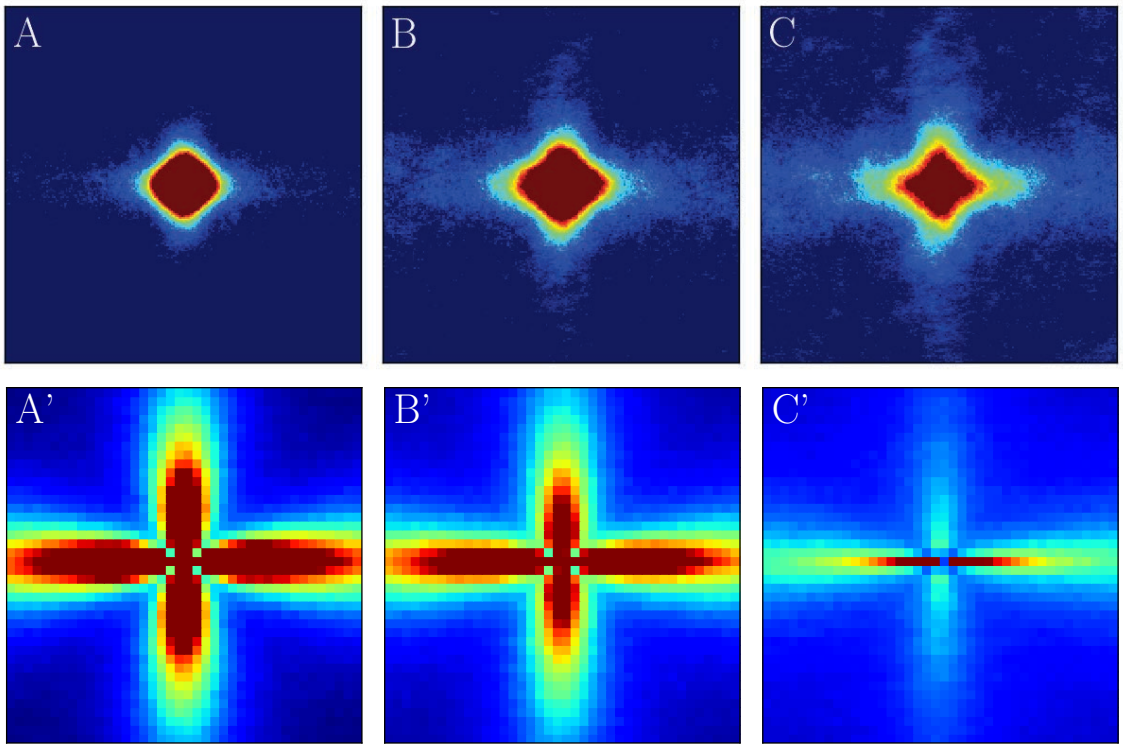

Figure 14.6: Colour maps of the plastic correlator $\mathcal{C}_2$ at very low shear rate $\dot{\gamma} = 10^{-5}$ for time lags (*A*) $\Delta t = 0$, (*A'*) $\Delta t = 1$, (*B and B'*) $\Delta t = 8$, (*C and C'*) $\Delta t = 20$. *Top row:* MD simulations. *Bottom row:* coarse-grained model. Note that for the coarse-grained model, we restrict the view to a region of the size (40x40 blocks) of the MD simulation cell. The colour code ranges from dark blue, for values below $-5 \cdot 10^{-4}$, to dark red, for all values $\geqslant 5 \cdot 10^{-3}$.

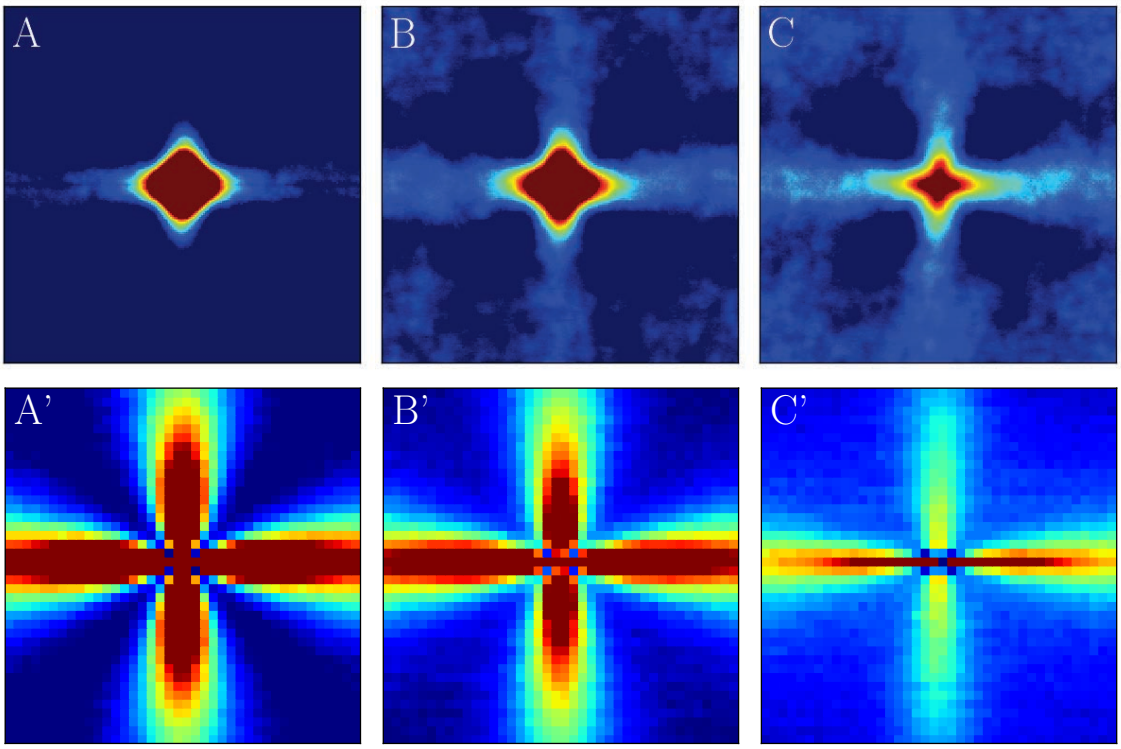

Figure 14.7: Colour maps of the plastic correlator $\mathcal{C}_2$ at the intermediate shear rate $\dot{\gamma} = 10^{-4}$. Refer to Fig. 14.6 for the rest of the caption.

angular symmetry. One should however admit that excessive correlations are predicted along the flow direction, especially in the near field. This is an artifact associated with the use of a regular lattice: as the frame is deformed, the positive lobe of the elastic propagator in the flow direction remains aligned with one axis of the lattice, while the alignment of the perpendicular lobe with the other axis is lost.

Moreover, the coarse-grained simulations are able to describe the anti-correlated lobes in the diagonal directions and their enhancement at higher shear rates.

On the downside, it is obvious that salient features of the plastic correlations are amiss. This discrepancy is interesting, because it is a hint that plastic correlations reveal some physical processes that may otherwise be left unnoticed, and that these processes have been omitted in the model.

First, the gradual growth with time of the correlations observed in MD is in stark contrast with the maximal extent of the correlations at vanishing time lag in the coarse-grained model. This indicates that the MD correlations do not grow because more and more shear stress is redistributed as the rearrangement proceeds, but because shear waves need a finite time to propagate (whereas instantaneous equilibration was assumed in the model). In other words, the acoustic delay for the propagation of strain-waves within an avalanche slows down the emergence of spatial correlations. Indeed, the initial growth of the correlations is consistent with the propagation of shear waves at the transverse sound velocity (of the undamped system), viz., $c_t = \sqrt{\mu/\rho} \simeq 4$. More details

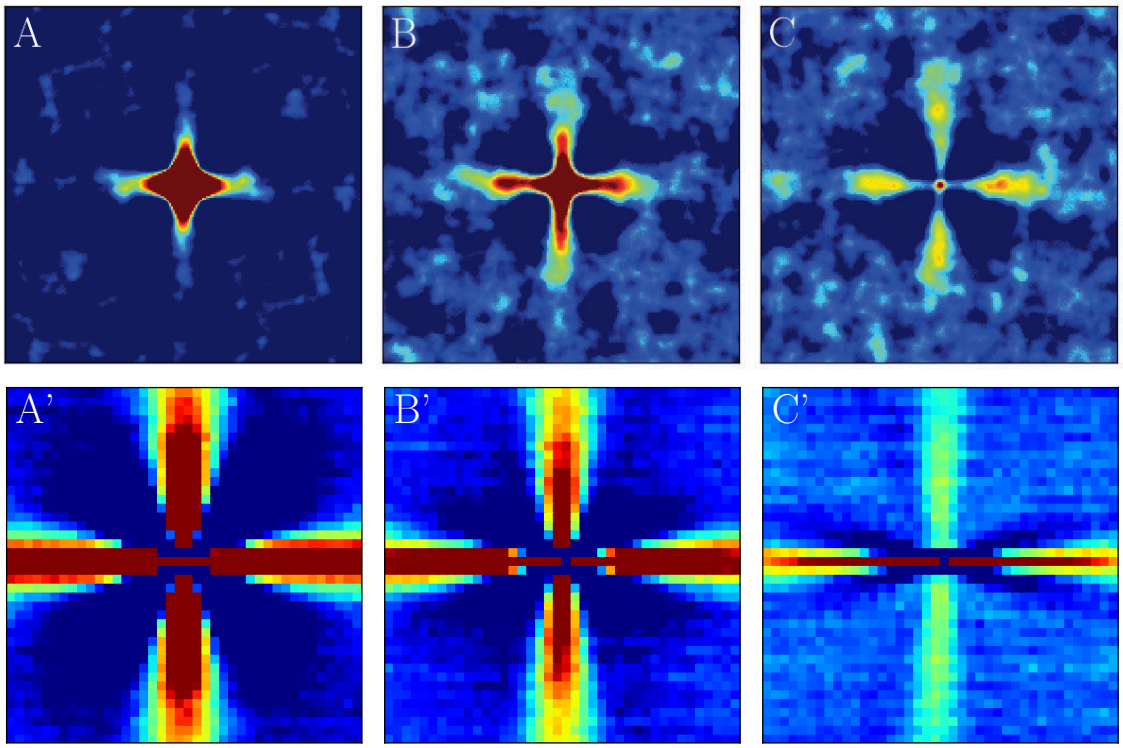

Figure 14.8: Colour maps of the plastic correlator $\mathcal{C}_2$ at the moderately high shear rate $\dot{\gamma} = 10^{-3}$. Refer to Fig. 14.6 for the rest of the caption. Note that, for the bottom row, we have used a sightly smaller lower bound for the colour code, $-1.5 \cdot 10^{-3}$ instead of $-5 \cdot 10^{-4}$ in the other cases.

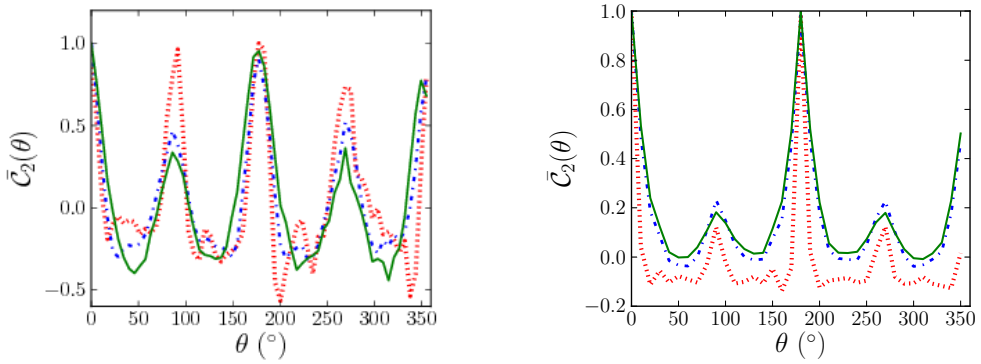

(a) MD simulations.

(b) Coarse-grained model.

Figure 14.9: Angular dependence of the correlations $\bar{\mathcal{C}}_2(\theta) \equiv \alpha \int_0^{L/2} \mathcal{C}_2(r, \theta; \Delta t)\, dr$, where L is the system size and $\Delta t = 20$ is the time lag, at shear rates (*solid green*)$\dot{\gamma} = 10^{-5}$, (*dashdotted blue line*)$\dot{\gamma} = 10^{-4}$, and (*dotted red line*)$\dot{\gamma} = 10^{-3}$. The prefactor α is chosen such that $\bar{\mathcal{C}}_2(\theta)$ has a maximum of 1.

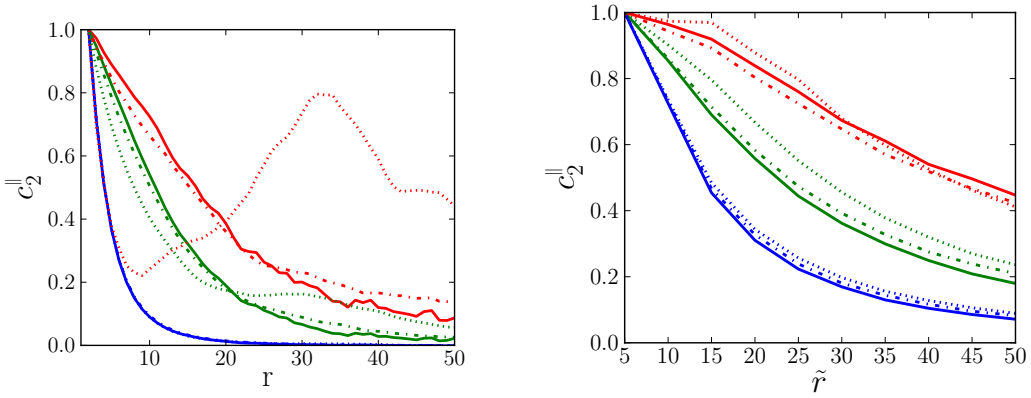

(a) MD simulations.

(b) Coarse-grained model.

Figure 14.10: Correlations along the stream direction, $c_2^{\parallel}(r, \Delta t) \equiv \mathcal{C}_2(r, \Delta t)/\mathcal{C}_2(\epsilon, \Delta t)$, where the postfactor rescales the correlations to unity close to the origin, $\epsilon = 2$ (5 for panel (b)). Data are shown for various time lags: (*blue*) $\Delta t = 0$ (1 for panel (b)), (*green*) $\Delta t = 8$, (*red*) $\Delta t = 16$, and for the different shear rates: (*solid line*) $\dot{\gamma} = 10^{-5}$, (*dash-dotted line*) $\dot{\gamma} = 10^{-4}$, and (*dotted line*) $\dot{\gamma} = 10^{-3}$. To allow direct comparison, we have set the size of one coarse-grained block to $\tilde{r} = 5$. To reduce the statistical noise, we have averaged the correlations over the three streamlines closest to the origin for the MD simulations.

abou the gradual expansion of the strain field created by a plastic event can be found in Refs. [Idema et al., 2013, Puosi et al., 2014, Chattoraj and Lemaître, 2013]. Note that, in this last reference, the authors also observed some advanced frontline moving at the longitudinal sound velocity $c_l > c_t$.

The second major difference lies in the spatial extent of the correlations, which is much larger in the coarse-grained approach. Of course, following Ref. [Varnik et al., 2014], the use of a frictional force based on relative velocities may have yielded larger correlations in MD: the mean-field damping scheme, which assumes the presence of a homogeneous solvent flow, tends to suppress correlations. However, the large deviation between the predictions of the atomistic and coarse-grained models does point to an additional source of discrepancy. We believe that the underestimation of structural disorder in the coarse-grained model is at the core of the divergence. Indeed, broadening the distribution of energy barriers in the model results in somewhat shorter correlations, at the expense of a poorer fitting of the macroscopic flow properties by our essentially one-parameter model. Of probably equal relevance is the questionable use of an 'ideal' elastic propagator. This propagator describes stress redistribution in a perfectly uniform elastic medium. Such a description is justified *on average*, but is inaccurate for a specific plastic event [Puosi et al., 2014], because elastic heterogeneities in the surrounding medium, i.e., the spatial variations of the local elastic constants, induce deviations from the ideal case. The insufficient account of structural disorder in the model is also reflected in the vastly overestimated

anisotropy of the correlations that it predicts, as measured by the directional probability enhancement (see Fig. 14.5b).

To our knowledge, neither of these points has ever been taken into account in a coarse-grained model. To what extent they may alter the organisation of the flow, in particular the potential onset of shear-localisation, is therefore undoubtedly an open question.

Key Points of the Chapter[a]

- The elastoplastic model and the MD simulations agree satisfactorily with respect to the general flow properties.
- The spatiotemporal correlations measured in both models bear some qualitative resemblance.
- But the elastoplastic model vastly overestimates these correlations and does not describe their emergence in time. This points to an underestimation of structural disorder and to the neglect of the finite velocity of shear waves.

a. These findings were gathered in an article [Nicolas et al., 2014c].

Key Points of this Part

- The extension to a tensorial stress has no effect on the flow curve, the correlation lengths, or the propensity to shear localise.
- Convection enhances fluctuations and breaks the spurious symmetry between the velocity and the velocity gradient directions.
- The generic concept of healing time overarches diverse physical processes leading to shear localisation.
- The model can describe the flow of an amorphous solid in a microchannel and the associated cooperative effects.
- In comparison to atomistic simulations, the model overestimates the correlations between plastic events and does not describe their emergence in time.

Part IV

ELASTOPLASTIC MODELLING BASED ON A SIMPLIFIED FINITE ELEMENT ROUTINE

Souvent l'art se transforme qu'ils [les grands édifices] pendent encore ; pendent opera interrupta *; ils se continuent paisiblement selon l'art transformé. L'art nouveau prend le monument où il le trouve, s'y incruste, se l'assimile, le développe à sa fantaisie et l'achève s'il peut.*

Victor Hugo, *Notre-Dame de Paris*, Book III, Chapter 1.

Although glasses are macroscopically isotropic and homogeneous, they display marked heterogeneities at the microscopic scale. In particular, the comparison between atomistic simulations and our elastoplastic model conducted in Chapter 14 suggests that the neglect of elastic heterogeneities may lead to an incorrect description of spatial correlations in the flow.

However, the elastoplastic model has so far been implemented with a (computationally very efficient) Fast Fourier Transform routine, relying on the ideal elastic propagator derived in Chapter 8. This method does not allow us to go beyond the assumption of uniform isotropic elasticity throughout the medium, nor does it provide a way to add inertial effects explicitly.

To overcome these deficiencies, I have chosen to turn to an implementation based on a much more flexible routine, namely, a (simplified version of) Finite Elements [2] (FE). The model ingredients, *i.e.*, the master equation and the dynamical rules, will mostly be similar to those used in the previous implementation, but the flexibility of the FE routine will afford a better account of structural disorder and inertial effects in the material. Accordingly, we expect a more accurate description of correlations and avalanche statistics within this new framework.

Our simplified FE routine is presented and tested in Chapter 15. To further validate the method, the time-dependent elastic response to a single shear transformation is investigated in Chapter 16 and compared to molecular dynamics simulations. Having ascertained the adequacy of the elastic part, we start probing the flow properties and the correlations between plastic events in Chapter 17. Finally, Chapter 18 discusses some specificities of granular media and reports on an early-stage endeavour to model the anisotropic force chains that have been observed in these materials.

2. In its present implementation, our simplified Finite Element routine is actually closer to a "Finite Volume" method [Rappaz et al., 2010].

15

FINITE ELEMENTS (FE): METHODS

The Finite Element (FE) approach emerged in the 1960s as an innovative and efficient way to solve complex problems, mostly in the fields of civil or aeronautical engineering. This technique can be regarded as an extension of the Finite Difference approach, in which spatial derivatives are discretised at the nodes of a regular lattice $\{(i,j)\}$, *viz.*, $\left.\frac{df}{dx}\right|_{i,j} \approx \frac{f_{i+1,j}-f_{i-1,j}}{x_{i+1}-x_{i-1}}$, with transparent notations. In FE, space is tiled into an arbitrary set of polygonal *elements*, *i.e.*, a *mesh*; in each element, a given number of *nodes* (shared with neighbouring elements) are used to interpolate the local displacement and stress fields. Since these fields should obey a given constitutive equation, the displacements and forces at the nodes of each element are constrained.

Extensive work has been dedicated to refining the technique, establishing criteria for its convergence, and implementing it in diverse configurations. In comparison with the finest developments of the art, our implementation is extremely crude. However, it is crucial to bear in mind the fundamental difference between customary uses of FE and its present status.

Traditionally, FE are used as a tool to solve a well-defined, often complex constitutive equation in a potentially complex geometry. The objective is then to develop a robust algorithm that yields an exact solution to the problem in the limit of an infinitely fine mesh.

On the other hand, we resort to (simplified) FE because, as far as we know, it is the *minimal framework* that can account for elastic heterogeneity and describe shear waves. Importantly, the elements are not pure mathematical constructs here, but they have a physical meaning, as elementary units of rearrangements. For the sake of clarity, let us anticipate the presentation of the dynamical rules in Chapter 17 and already mention that, in the FE-based approach, plastic events will be modelled by cancelling the elastic constants of plastic blocks, so that only their viscous (and inertial) forces can counter the elastic forces exerted by the surrounding medium on the region.

15.1 THE FINITE ELEMENT METHOD IN A GLANCE

Let us start with a concise and partial introduction to FE.

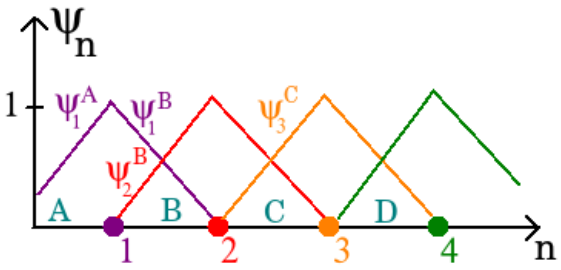

Figure 15.1: Linear interpolation function $\psi_n^{(e)}$ on a one-dimensional mesh, with nodes numbered from 1 to 4 and elements labelled from A to D.

15.1.1 *Interpolation functions*

Formally, it is convenient to view the discretisation of a continuous (*e.g.*, displacement, velocity, or pressure) field $g(\boldsymbol{r})$ onto a mesh as a projection onto a subspace of interpolation functions $\psi_n(\boldsymbol{r})$, *viz.*,

$$g(\boldsymbol{r}) \to \tilde{g}(\boldsymbol{r}) \quad = \quad \sum_n g_n \psi_n(\boldsymbol{r}),$$

where the g_n's are interpolation coefficients. In FE, all interpolation functions are local, *i.e.*, their support is limited to a single element, and associated with a node [Rappaz et al., 2010]. For instance, $\psi_n^{(e)}$ will be the interpolation function of element (e) associated with node n. It follows that

$$\tilde{g}(\boldsymbol{r}) \quad = \quad \sum_{\substack{\text{el'ts} \\ e}} \sum_{\substack{\text{nodes} \\ n \text{ of } e}} g_n \psi_n^{(e)}(\boldsymbol{r}),$$

where it should be recalled that the nodes (n), *ergo*, the coefficients g_n, are shared by neighbouring elements. As an example, a trivial set of interpolation functions on a one-dimensional mesh is illustrated in Fig. 15.1.

15.1.2 *A simple static example: linear elasticity*

To explain the principle of FE, let us consider a linear elastic problem over a 2D domain $\mathcal{U}$:

$$\begin{cases} \sigma(\boldsymbol{r}) & = \mathbf{C}\epsilon(\boldsymbol{r}) \text{ for } \boldsymbol{r} \in \mathcal{U} \\ \text{div}\,(\sigma) & = \mathbf{0} \\ \sigma(\boldsymbol{r}) \cdot \boldsymbol{n}(\boldsymbol{r}) & = \boldsymbol{T}(\boldsymbol{r}) \text{ for } \boldsymbol{r} \in \partial\mathcal{U}, \end{cases} \tag{15.1}$$

where $\boldsymbol{T}$ denotes the force (per unit area) applied on the boundary $\partial\mathcal{U}$ of the domain, of normal $\boldsymbol{n}(\boldsymbol{r})$ at $r \in \partial\mathcal{U}$, and $\mathbf{C}$ is the fourth-rank (stiffness) tensor relating strain ϵ and stress σ. Solving this elastic problem is equivalent to finding the displacement field $\boldsymbol{u}^\star$ that minimises the virtual work

$$W[\boldsymbol{u}] \equiv \int_{\mathcal{U}} \frac{1}{2} \left(\mathbf{C}\boldsymbol{\epsilon}[\boldsymbol{u}]\right) : \boldsymbol{\epsilon}[\boldsymbol{u}] \; d^2\boldsymbol{r} - \int_{\partial\mathcal{U}} \boldsymbol{T} \cdot \boldsymbol{u} \, d\boldsymbol{r},$$

where $\boldsymbol{\epsilon}[\boldsymbol{u}]$ is the strain field derived from $\boldsymbol{u}$. This directly leads to the saddle point equation:

$$\text{for all fictive displacement field } \boldsymbol{u}, \int_{\mathcal{U}} \frac{1}{2} \left(\mathbf{C}\boldsymbol{\epsilon}[\boldsymbol{u}^\star]\right) : \boldsymbol{\epsilon}[\boldsymbol{u}] \; d^2\boldsymbol{r} = \int_{\partial\mathcal{U}} \boldsymbol{T} \cdot \boldsymbol{u} \, d\boldsymbol{r}. \tag{15.2}$$

The FE approximation consists in enforcing this condition, not on all conceivable fields $\boldsymbol{u}$, but only on the interpolated fields

$$\tilde{u}_\alpha(\boldsymbol{r}) \quad = \quad \sum_{\substack{\text{el'ts} \\ e}} \sum_{\substack{\text{nodes} \\ n \text{ of } e}} u_{\alpha n} \psi_{\alpha n}^{(e)}(\boldsymbol{r}), \text{ where } \alpha \in \{x, y\} \text{ and } u_{\alpha n} \in \mathbb{R}. \tag{15.3}$$

Inserting Eq. 15.3 into the integral formulation (Eq. 15.2) and imposing that the coefficients in front of the $u_{\alpha n}$'s should vanish, one gets a set of coupled linear equations with the $u_i^\star$ coefficients as unknowns, which schematically reads

$$\mathbf{K} \begin{bmatrix} u_{xN}^\star \\ u_{yN}^\star \\ \vdots \\ u_{x1}^\star \\ u_{y1}^\star \end{bmatrix} = \begin{bmatrix} f_{xN} \\ f_{yN} \\ \vdots \\ f_{x1} \\ f_{y1} \end{bmatrix}, \tag{15.4}$$

where $\mathbf{K}$ is a mesh-dependent $N \times N$ matrix[1] and the external force field $\boldsymbol{T}$ at the boundary is included in the f_i's. Equation 15.4 is no more than the force balance equation at each node i.

15.1.3 *Brezzi-Babushka condition*

Unfortunately, the convergence of the nodal displacements $(\boldsymbol{u_1}^\star, \ldots, \boldsymbol{u_N}^\star)$ solving Eq. 15.4 to the continuous solution $\boldsymbol{u}(\boldsymbol{r})$ of the initial problem (Eq. 15.1), when the element size tends to zero, is not guaranteed for all meshes and interpolation functions. The convergence is controlled by a condition, established by Brezzi and Babushka [Fortin and Brezzi, 1991], which I will not present here.

1. Here, incompressibility may be enforced *via* the so called penalty method: if the bulk modulus included in $\mathbf{C}$ (Eq. 15.1), and therefore in $\mathbf{K}$, tends to infinity, then the u_i's will be constrained to satisfy incompressibility. An alternative method, generally used in Stokes' problem, is to introduce an explicit Lagrange multiplier to constrain the volume change, *i.e.*, $\mathrm{div}(\boldsymbol{u})$: this is the pressure p.

15.2 SPATIAL DISCRETISATION

In Section 15.1.2, the FE method was illustrated with a static linear elastic problem. However, the elastoplastic line of modelling requires to solve more complex problems.

15.2.1 *Continuum Mechanics formulation of the problem*

At all times, the effects of the macroscopic drive and of the current plastic events need to be computed. If inertial effects and dissipative forces (in particular, in rearranging regions) are taken into account, the momentum conservation equation in the bulk reads

$$\underbrace{\rho \frac{D\dot{\boldsymbol{u}}}{Dt}(\boldsymbol{r},t)}_{\text{inertial force}} = \underbrace{\nabla \cdot [\mathbf{C}(\boldsymbol{r},t)\boldsymbol{\epsilon}(\boldsymbol{r},t)]}_{\text{elasticity}} + \underbrace{\eta \nabla^2 \dot{\boldsymbol{u}}(\boldsymbol{r},t)}_{\text{viscosity}}, \tag{15.5}$$

where $\boldsymbol{u}$ and $\boldsymbol{\epsilon}$ are the displacement and strain fields, respectively, ${}^{D\bullet}/_{Dt} \equiv {}^{\partial\bullet}/_{\partial t} + \boldsymbol{v} \cdot (\nabla \bullet)$ denotes the convected derivative, ρ is the (area) density of the material, $\mathbf{C}$ denotes a local stiffness matrix, and η is the microscopic viscosity. Here, ρ and η will be assumed constant; accordingly, viscous forces will be operative in plastic blocks as well as in elastic blocks, even though they will be dominated by the elastic forces in the latter. On the other hand, the stiffness matrix $\mathbf{C}(\boldsymbol{r},t)$ is allowed to vary in time and in space, depending on the plastic activity of the blocks.

Below, we detail the steps and approximations that bridge the gap between the Continuum Mechanics formulation of Eq. 15.5 and the following FE problem,

$$\underbrace{\boldsymbol{\mathcal{M}} \begin{pmatrix} \ddot{u}_x^{(\mathbf{N-1})} \\ \ddot{u}_y^{(\mathbf{N-1})} \\ \vdots \\ \ddot{u}_x^{(\mathbf{0})} \\ \ddot{u}_y^{(\mathbf{0})} \end{pmatrix}}_{\text{inertial force}} = \underbrace{\boldsymbol{\mathcal{K}} \begin{pmatrix} u_x^{(\mathbf{N-1})} \\ u_y^{(\mathbf{N-1})} \\ \vdots \\ u_x^{(\mathbf{0})} \\ u_y^{(\mathbf{0})} \end{pmatrix}}_{\text{elasticity}} + \underbrace{\boldsymbol{\mathcal{H}} \begin{pmatrix} \dot{u}_x^{(\mathbf{N-1})} \\ \dot{u}_y^{(\mathbf{N-1})} \\ \vdots \\ \dot{u}_x^{(\mathbf{0})} \\ \dot{u}_y^{(\mathbf{0})} \end{pmatrix}}_{\text{viscosity}}, \tag{15.6}$$

where the $u_x^{(\mathbf{i})}$'s and $u_y^{(\mathbf{i})}$'s are the displacements at the nodes $i \in \{0, \ldots, N-1\}$ of a regular mesh. $\boldsymbol{\mathcal{M}}$, $\boldsymbol{\mathcal{K}}$, and $\boldsymbol{\mathcal{H}}$ are $2N \times 2N$ real matrices that are to be specified.

15.2.2 *Simple mesh and interpolation functions*

First, we need to select a convenient FE mesh.

Bearing in mind our pursuit of minimalism, but also practilities such as the finite duration of a PhD, I have chosen the simplest mesh possible, namely, the regular square grid sketched in Fig. 15.2, combined with bilinear interpolation

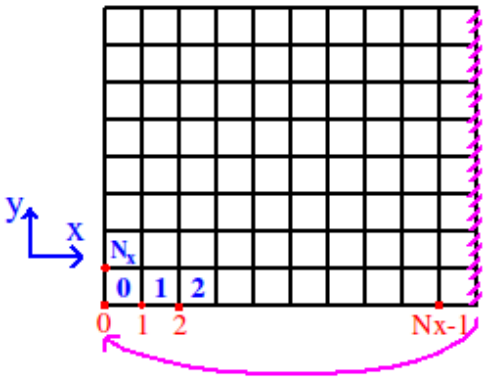

Figure 15.2: Sketch of the FE mesh. The system is periodic in the x-direction, so that column N_x coincides with column 0. There are $N = N_x \times N_y$ nodes, and $N_x \times (N_y - 1)$ elements.

functions for the displacements (u_x, u_y) and forces $\left(f_x^{\mathrm{el}}, f_y^{\mathrm{el}}\right)$. This mesh is simply the two-dimensional extension of the one-dimensional mesh whose interpolation functions are sketched in Fig. 15.1.

Let us number the nodes of each element from 0 to 3 counter-clockwise, starting from the bottom left corner, *viz.*, ${}^{3}_{0}\square^{2}_{1}$, and denote by $u_x^{(0)}$ the displacement along x at the (0) node, *etc.* In each element, the interpolated strain and stress fields are then given by

$$\begin{pmatrix} \epsilon_{xx} \\ \epsilon_{yy} \\ \sqrt{2}\epsilon_{xy} \end{pmatrix} = \mathbf{B}^\top \cdot \begin{pmatrix} u_x^{(0)} \\ u_y^{(0)} \\ \vdots \\ u_x^{(3)} \\ u_y^{(3)} \end{pmatrix} \text{ and } \begin{pmatrix} \sigma_{xx}^{\mathrm{el}} \\ \sigma_{yy}^{\mathrm{el}} \\ \sqrt{2}\sigma_{xy}^{\mathrm{el}} \end{pmatrix} = -\mathbf{B}^\top \cdot \begin{pmatrix} f_x^{\mathrm{el}\,(0)} \\ f_y^{\mathrm{el}\,(0)} \\ \vdots \\ f_x^{\mathrm{el}\,(3)} \\ f_y^{\mathrm{el}\,(3)} \end{pmatrix}, \quad (15.7)$$

where

$$\mathbf{B}^\top \equiv 1/2 \begin{bmatrix} -1 & & 1 & & 1 & & -1 & \\ & -1 & & -1 & & 1 & & 1 \\ -1/\sqrt{2} & -1/\sqrt{2} & -1/\sqrt{2} & 1/\sqrt{2} & 1/\sqrt{2} & 1/\sqrt{2} & 1/\sqrt{2} & -1/\sqrt{2} \end{bmatrix}.$$

Notice in particular that the strain and stress fields are uniform within each element; in other words, our simplified FE method is close to a Finite Volume method, in practice. The $\sqrt{2}$ prefactors have been introduced with foresight (see Section 15.2.3) and the "minus" sign preceding $\mathbf{B}^\top$ in Eq. 15.7 should not come as a surprise if one understands that $f^{\mathrm{el}\,(i)}$ is the force exerted *by* the element *on* node i.

A straightforward and symmetric (but on no account unique) way to invert Eq. 15.7 is

$$\begin{pmatrix} u_x^{(0)} \\ u_y^{(0)} \\ \vdots \\ u_x^{(3)} \\ u_y^{(3)} \end{pmatrix} = \mathbf{B} \cdot \begin{pmatrix} \epsilon_{xx}^{\mathrm{el}} \\ \epsilon_{yy}^{\mathrm{el}} \\ \sqrt{2}\epsilon_{xy}^{\mathrm{el}} \end{pmatrix} \text{ and } \begin{pmatrix} f_x^{\mathrm{el}\,(0)} \\ f_y^{\mathrm{el}\,(0)} \\ \vdots \\ f_x^{\mathrm{el}\,(3)} \\ f_y^{\mathrm{el}\,(3)} \end{pmatrix} = -\mathbf{B} \cdot \begin{pmatrix} \sigma_{xx}^{\mathrm{el}} \\ \sigma_{yy}^{\mathrm{el}} \\ \sqrt{2}\sigma_{xy}^{\mathrm{el}} \end{pmatrix}. \tag{15.8}$$

15.2.3 *Elastic force-displacement matrix*

To relate the nodal displacements and the nodal forces in each element, we make use of the constitutive equation of the material.

To start with, the elastic contribution is governed by Hooke's law. Its traditional expression with tensorial notations, *i.e.*, $\sigma_{ij}^{\mathrm{el}} = C_{ijkl}\epsilon_{kl}$, is conveniently replaced by the following condensed notations [Tsamados et al., 2009],

$$\begin{pmatrix} \sigma_{xx}^{\mathrm{el}} \\ \sigma_{yy}^{\mathrm{el}} \\ \sqrt{2}\sigma_{xy}^{\mathrm{el}} \end{pmatrix} = \mathbf{C} \begin{pmatrix} \epsilon_{xx} \\ \epsilon_{yy} \\ \sqrt{2}\epsilon_{xy} \end{pmatrix}, \tag{15.9}$$

where $\mathbf{C}$ is a 3×3 real matrix. Substituting from Eq. 15.7, one obtains the local relation between the forces exerted on the nodes by the material element under consideration and the displacements at the nodes, *viz.*,

$$\begin{pmatrix} f_x^{\mathrm{el}\,(0)} \\ f_y^{\mathrm{el}\,(0)} \\ \vdots \\ f_x^{\mathrm{el}\,(3)} \\ f_y^{\mathrm{el}\,(3)} \end{pmatrix} = -\mathbf{B}\mathbf{C}\mathbf{B}^{\top} \cdot \begin{pmatrix} u_x^{(0)} \\ u_y^{(0)} \\ \vdots \\ u_x^{(3)} \\ u_y^{(3)} \end{pmatrix}. \tag{15.10}$$

To proceed, the *local* elastic force-displacement matrices $\mathbf{K} \equiv -\mathbf{B}\mathbf{C}\mathbf{B}^{\top}$ are assembled into a global elastic force-displacement matrix $\mathcal{K}$, *viz.*,

$$\begin{pmatrix} f_x^{\mathrm{el}\,(\mathbf{N-1})} \\ f_y^{\mathrm{el}\,(\mathbf{N-1})} \\ \vdots \\ f_x^{\mathrm{el}\,(\mathbf{0})} \\ f_y^{\mathrm{el}\,(\mathbf{0})} \end{pmatrix} = \mathcal{K} \cdot \begin{pmatrix} u_x^{(\mathbf{N-1})} \\ u_y^{(\mathbf{N-1})} \\ \vdots \\ u_x^{(\mathbf{0})} \\ u_y^{(\mathbf{0})} \end{pmatrix},$$

where the bold superscripts refer to the global labels used in Fig. 15.2, by opposition with the elemental labels used in Eq. 15.10. Here, $\mathcal{K}$ is a sparse $2N \times 2N$ matrix.

15.2.4 *Viscous force-velocity matrix*

The foregoing derivation relies on the linear relation connecting local strains and elastic stresses. Thus, it can straightforwardly be extended to the viscous stresses, insofar as they are linearly related with the local strain rates, *viz.*,

$$\begin{pmatrix} \sigma_{xx}^{\mathrm{diss}} \\ \sigma_{yy}^{\mathrm{diss}} \\ \sqrt{2}\sigma_{xy}^{\mathrm{diss}} \end{pmatrix} = \mathbf{C}^{\mathbf{diss}} \begin{pmatrix} \dot{\epsilon}_{xx} \\ \dot{\epsilon}_{yy} \\ \sqrt{2}\dot{\epsilon}_{xy} \end{pmatrix}. \tag{15.11}$$

Globally, the viscous force-velocity relation reads

$$\begin{pmatrix} f_x^{\mathrm{diss}\,(\mathbf{N-1})} \\ f_y^{\mathrm{diss}\,(\mathbf{N-1})} \\ \vdots \\ f_x^{\mathrm{diss}\,(\mathbf{0})} \\ f_y^{\mathrm{diss}\,(\mathbf{0})} \end{pmatrix} = \boldsymbol{\mathcal{H}} \cdot \begin{pmatrix} \dot{u}_x^{(\mathbf{N-1})} \\ \dot{u}_y^{(\mathbf{N-1})} \\ \vdots \\ \dot{u}_x^{(\mathbf{0})} \\ \dot{u}_y^{(\mathbf{0})} \end{pmatrix},$$

where the $2N \times 2N$ matrix $\boldsymbol{\mathcal{H}}$ has been assembled from elemental matrices of the form $-\mathbf{B}\mathbf{C}^{\mathbf{diss}}\mathbf{B}^{\top}$.

15.2.5 *Inertial force-acceleration matrix*

Finally, we must express the inertial forces, that is to say, the matrix $\boldsymbol{\mathcal{M}}$ in Eq. 15.6. The convected part of the material derivative of the velocity, namely, $\boldsymbol{v} \cdot (\nabla \boldsymbol{v})$, which scales with v^2 for elements of unit size, is neglected.

One could consider calculating the inertial forces acting on a given *element* and then distributing them among its nodes. However, this leads to unphysical behaviour, as is easily understood for a plane shear wave: As soon as the wave front would hit one row of nodes, the inertial forces experienced by these nodes would be shared with the next row, so that the wave would propagate instantaneously over the size of an element.

To overcome this erratic behaviour, we compute the inertial forces directly at the nodes. In other words, each node is assigned a mass $m_0 \equiv \rho V_0$, where V_0 is the elemental volume (*i.e.*, area). Accordingly, the matrix $\boldsymbol{\mathcal{M}}$ connecting the accelerations at the nodes to the inertial forces at the nodes is a $2N \times 2N$ matrix with m_0 on the diagonal, *i.e.*,

$$\boldsymbol{\mathcal{M}} = \begin{pmatrix} m_0 & & \\ & \ddots & \\ & & m_0 \end{pmatrix}.$$

15.3 DISCRETISATION OF THE DYNAMICS

In the previous section, we have spatially discretised the Continuum Mechanics problem, Eq. 15.5, and we have arrived at a matricial equation whose structure is recalled here,

$$\boldsymbol{\mathcal{M}} \cdot \ddot{u} = \boldsymbol{\mathcal{K}} \cdot u + \boldsymbol{\mathcal{H}} \cdot \dot{u}, \tag{15.12}$$

where all variables depend on time and u is a shorthand for the nodal displacements $\left(\begin{array}{cccc} u_x^{(\mathbf{N-1})} & u_y^{(\mathbf{N-1})} & \dots & u_x^{(\mathbf{0})} \quad u_y^{(\mathbf{0})} \end{array} \right)^\top$.

Equation 15.12 is an ordinary differential equation with respect to time. To solve it numerically, the continuous time interval $[t_0, \infty[$ (with t_0 the initial time) is replaced by the discrete time interval $\{t_n \equiv t_0 + n\delta t,\ n \in \mathbb{N}\}$, with fixed time step δt; hence, Eq. 15.12 turns into

$$\forall n \in \mathbb{N},\ \boldsymbol{\mathcal{M}} \cdot \ddot{u}\left(t_n\right) = \boldsymbol{\mathcal{K}}\left(t_n\right) \cdot u\left(t_n\right) + \boldsymbol{\mathcal{H}} \cdot \dot{u}\left(t_n\right). \tag{15.13}$$

Here, we have highlighted the time-dependence of $\boldsymbol{\mathcal{K}}$, owing to changes in the elastic properties of the elements, to contrast it with the constancy of both $\boldsymbol{\mathcal{M}}$ and $\boldsymbol{\mathcal{H}}$.

Because keeping track of the cumulated displacements $u(t_n)$ is inconvenient (and all the more so as we intend to keep the grid fixed), we choose to compute only the *incremental* displacements $\delta u(t_n) \equiv u(t_n) - u(t_{n-1})$ at each time step. Comparing the evaluations of Eq. 15.13 at time steps t_{n-1} and t_n, one gets

$$\boldsymbol{\mathcal{M}} \cdot \delta\ddot{u}\left(t_n\right) = \boldsymbol{\mathcal{K}}\left(t_n\right) \cdot \delta u\left(t_n\right) - \delta f^{\mathrm{pl}}\left(t_n\right) + \boldsymbol{\mathcal{H}} \cdot \delta\dot{u}\left(t_n\right). \tag{15.14}$$

Here, we have used the shorthand $\delta f^{\mathrm{pl}}\left(t_n\right)$ for the elastic force $\left[\boldsymbol{\mathcal{K}}\left(t_{n-1}\right) - \boldsymbol{\mathcal{K}}\left(t_n\right)\right] \cdot \delta u\left(t_{n-1}\right)$ released due to plasticity (and the ensuing vanishment [2] of some elastic moduli in $\boldsymbol{\mathcal{K}}$).

To conclude, the time derivatives $\delta\dot{u}$ and $\delta\ddot{u}$ are discretised with the following central difference scheme,

$$\begin{aligned} \delta\dot{u}\left(t_n\right) &= \frac{\delta u\left(t_{n+1}\right) - \delta u\left(t_{n-1}\right)}{2\delta t} + \mathcal{O}(\delta t^2) \\ \delta\ddot{u}\left(t_n\right) &= \frac{\delta u\left(t_{n+1}\right) + \delta u\left(t_{n-1}\right) - 2\delta u\left(t_n\right)}{\delta t^2} + \mathcal{O}(\delta t). \end{aligned} \tag{15.15}$$

The central difference scheme conserves time reversibility and is more accurate than a forward difference method.

By inserting this numerical scheme into Eq. 15.14, one finally arrives at

2. As mentioned in the introduction, the shear moduli of plastic regions (contained in the local stiffness matrix $\mathbf{C}$) will vanish for the whole duration of the plastic events. The reader is referred to Section 17.2.2 for details.

$$\underbrace{\left(\boldsymbol{\mathcal{M}} - \frac{\delta t}{2}\boldsymbol{\mathcal{H}}\right)}_{\mathbb{M}} \cdot \frac{\delta u\left(t_{n+1}\right)}{\delta t} = \delta t\, \boldsymbol{\mathcal{K}}\left(t_n\right) \cdot \delta u\left(t_n\right) - \delta t\, \delta f^{\mathrm{pl}}\left(t_n\right) - \boldsymbol{\mathcal{H}} \cdot \frac{\delta u\left(t_{n-1}\right)}{2} + \boldsymbol{\mathcal{M}} \cdot \frac{2\delta u\left(t_n\right) - \delta u\left(t_{n-1}\right)}{\delta t}. \tag{15.16}$$

In practice, the problem is solved iteratively, *i.e.*, the displacement increments δu of the previous two time steps, t_{n-1} and t_n, are stored and $\delta u\left(t_{n+1}\right)$ is obtained from Eq. 15.16 through the inversion of the lhs matrix $\mathbb{M}$. The initial conditions for the problem are chosen as $\delta u\left(t_0\right) = \delta u\left(t_1\right) = 0$.

With regard to numerical efficiency, it should already be pointed out that $\mathbb{M}$ is constant and can therefore be inverted[3] once and for all at the beginning of the simulation.

15.4 BOUNDARY CONDITIONS

To conclude the presentation of our FE routine, let us specify the two types boundary conditions (BC) that will be used, alternatively.

15.4.1 *Semi-periodic system bounded by parallel walls*

The first BC involve periodicity along the flow direction x and infinite parallel walls bounding the crosswise direction y, at positions $y = 0$ and $y = L_y$.

Periodicity is readily implemented by welding the leftmost and rightmost columns of the system, that is to say, imposing that the left-hand neighbours of the first column be the nodes of the last column, and *vice versa*, as sketched in Fig. 15.2.

Walls are modelled with no-slip BC by controlling the displacements of the nodes along the wall ($\mathcal{W}$), *i.e.*, the first $2N_x$ and the last $2N_x$ nodes. This is achieved by replacing the associated rows in the lhs matrix $\mathbb{M}$ (in Eq. 15.16) with BC prescriptions, *viz.*,

$$\forall l \in \mathcal{W},\ \forall k \in \{0, \ldots, 2N_x - 1\},\ \mathbb{M}_{kl} \leftarrow \delta_{kl},$$

where δ_{kl} is the Kronecker symbol, and replacing the corresponding cells on the rhs vector (in Eq. 15.16) with the prescribed (x- or y-)displacements.

15.4.2 *Biperiodic system*

For the second type of BC, the system is periodic in both directions.

3. On a technical note, the inversion is computed with the Multifrontal Massively Parallel Solver (MUMPS) package (http://graal.ens-lyon.fr/MUMPS/), designed for sparse matrices.

The implementation of periodicity in the flow direction has already been discussed in the previous section (Section 15.4.1), but periodicity in the transverse direction y deserves closer attention, since periodic replicas in the y-direction must be shifted along the flow direction x with respect to each other, similarly to the Lees-Edwards BC used in atomistic simulations.

To simplify notations, we denote the displacements on a given row, *i.e.*, at $y = \text{cst}$, by

$$\begin{pmatrix} \text{Top row} \\ \text{Penult row} \\ \vdots \\ \text{Second row} \\ \text{Bottom row} \end{pmatrix}$$

Because of periodicity along the transverse direction y, the nodes of the top and bottom rows should be interconnected. Due to these interconnections, if the periodic replicas along y are unfolded, one gets

$$\begin{pmatrix} \text{Top row} \\ \text{Penult row} \\ \vdots \\ \text{Second row} \\ \text{Bottom row} \end{pmatrix} \longrightarrow \delta\tilde{u}_x = \begin{pmatrix} \vdots \\ \text{Bottom row} \\ \text{Top row} \\ \text{Penult row} \\ \vdots \\ \text{Second row} \\ \text{Bottom row} \\ \text{Top row} \\ \vdots \end{pmatrix}.$$

However, as mentioned earlier, we would like these replicas to be shifted at each time step because of the flow, by a distance $\dot{\gamma} L_y dt$ along $\boldsymbol{e}_x$, *viz.*,

$$\delta u_x = \begin{pmatrix} \vdots \\ \text{Bottom row} + \dot{\gamma} L_y t \Theta(t) \\ \text{Top row} \\ \text{Penult row} \\ \vdots \\ \text{Second row} \\ \text{Bottom row} + 0 \\ \text{Top row} - \dot{\gamma} L_y dt \Theta(t) \\ \vdots \end{pmatrix} = \delta\tilde{u}_x + \underbrace{\begin{pmatrix} \vdots \\ \dot{\gamma} L_y dt \Theta(t) \\ 0 \\ 0 \\ \vdots \\ 0 \\ 0 \\ -\dot{\gamma} L_y dt \Theta(t) \\ \vdots \end{pmatrix}}_{\delta u_x^{(\mathrm{BC})}(t)}.$$

While δu_x is the desired physical field, in practice only $\delta \tilde{u}_x$ is periodic and compatible with the interconnections between the nodes of the top and bottom rows. The problem is solved by substituting $\delta \tilde{u}_x + \delta u_x^{(\mathrm{BC})}$ for δu_x in Eq. 15.16, which leads to

$$\begin{aligned}
\mathbb{M} \cdot \frac{\delta \tilde{u}\,(t_{n+1})}{\delta t} + \mathbb{M} \cdot \frac{\delta u_x^{(\mathrm{BC})}\,(t_{n+1})}{\delta t} \;=\; & \delta t\, \boldsymbol{\mathcal{K}}\,(t_n) \cdot \delta \tilde{u}\,(t_n) - \delta t\, \delta f^{pl}\,(t_n) \\
& - \boldsymbol{\mathcal{H}} \cdot \frac{\delta \tilde{u}\,(t_{n-1})}{2} + \boldsymbol{\mathcal{M}} \cdot \frac{2\delta \tilde{u}\,(t_n) - \delta \tilde{u}\,(t_{n-1})}{\delta t} \\
& + \delta t\, \boldsymbol{\mathcal{K}}\,(t_n) \cdot \delta u_x^{(\mathrm{BC})}\,(t_n) - \boldsymbol{\mathcal{H}} \cdot \frac{\delta u_x^{(\mathrm{BC})}\,(t_{n-1})}{2} \\
& + \boldsymbol{\mathcal{M}} \cdot \frac{2\delta u_x^{(\mathrm{BC})}\,(t_n) - \delta u_x^{(\mathrm{BC})}\,(t_{n-1})}{\delta t}.
\end{aligned}$$

In the main system, the terms involving $\delta u_x^{(\mathrm{BC})}$ (in blue) build up a force $\delta f^{(\mathrm{BC})}$ that acts on the top and bottom rows.

In conclusion, the FE displacements $\delta \tilde{u}_x$ can be substituted for the physical field δu_x in Eq. 15.16, provided that auxiliary forces $\delta f^{(\mathrm{BC})}$ accounting for the shift between replicas are applied to the top and bottom rows, *viz.*, schematically,

$$\mathbb{M} \cdot \frac{\delta \tilde{u}\,(t_{n+1})}{\delta t} = \ldots + \delta f_x^{(\mathrm{BC})}.$$

15.5 SIMPLE TESTS AND APPRAISAL OF THE ALGORITHM

With our numerical FE routine in place, it is now time to test it and appraise its capabilities. In this section, as a simple test, we probe the response of uniform isotropic systems to shear.

15.5.1 *Stiffness and viscosity matrices of uniform isotropic media*

Let us first recall the expressions of the local stiffness and viscosity matrices, $\mathbf{C}$ and $\mathbf{C}^{\mathbf{diss}}$, introduced in Eqs. 15.9 and 15.11, in the case of uniform isotropic media:

$$\mathbf{C} = \begin{pmatrix} K+\mu & K-\mu & 0 \\ K-\mu & K+\mu & 0 \\ 0 & 0 & 2\mu \end{pmatrix} \text{ and } \mathbf{C}^{\mathrm{diss}} = \begin{pmatrix} \kappa+\eta & \kappa-\eta & 0 \\ \kappa-\eta & \kappa+\eta & 0 \\ 0 & 0 & 2\eta \end{pmatrix},$$

where K and μ are the elastic bulk modulus and shear modulus in two dimensions, and κ and μ are the bulk (or volume) viscosity and the shear viscosity, respectively. Note that, for an incompressible material, both the bulk modulus and the bulk viscosity diverge, *i.e.*, $K \to \infty$ and $\kappa \to \infty$.

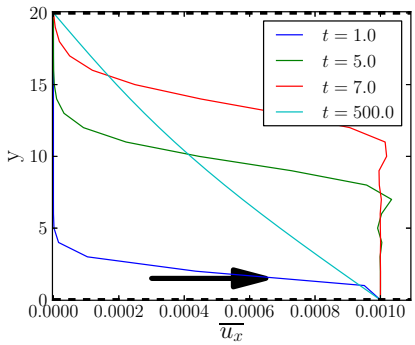

(a) Average displacement $\overline{u_x}$ along x on streamline y, at various times after shear initiation, for $u_x^0 = 10^{-3}$.

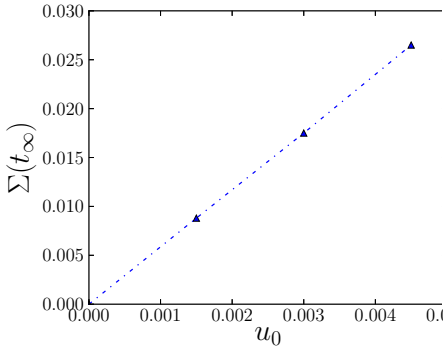

(b) Shear stress Σ in the steady state as a function of u_x^0.

Figure 15.3: Application of a shear strain step to a uniform incompressible, low-viscosity elastic medium, with $\mu = 12$, $\rho = 3$, $\eta = 1$, and $K = \kappa \approx 10^4$, in a system bounded by parallel walls ($N = 80 \times 20$). The bottom wall is displaced along the x-direction by u_x^0 at time $t = 0$, corresponding to a shear strain $\gamma = u_0/20$.

15.5.2 *Simple tests*

First, we consider a uniform, incompressible, almost inviscid, elastic medium, characterised by K, $\kappa \to \infty$, $\eta \to 0$, $\mu = \text{cst} = 12$, and $\rho = \text{cst} = 3$, with the notations used in the previous section. A shear strain step is applied to this material, and the results of the simulation are plotted in Fig. 15.3. These results are consistent with the theoretical value of transverse sound velocity (Fig. 15.3a), $c_t = \sqrt{\mu/\rho} = 2$, and, as expected, the average shear stress Σ is proportional to the applied strain γ, the proportionality coefficient being equal to μ (Fig. 15.3).

Secondly, we study the response of a purely viscous incompressible material, of viscosity $\eta = 10$, to a constant shear rate $\dot{\gamma}$, imposed by displacing the bottom wall. As shown in Fig. 15.4, the shear stress measured in the steady state obeys the expected relation $\Sigma = \eta\dot{\gamma}$.

Our sanity checks are thus satisfactory.

15.5.3 *Assets of our Finite Element algorithm*

Compared to the Fourier-Transform-based algorithms used in Parts II and III of this thesis, the (simplified) FE method provides considerably greater versatility, at the expense of somewhat heavier numerical costs. [4]

To begin with, more diverse flow geometries, *e.g.*, curved geometries, could be implemented with minimal efforts.

Furthermore, the FE routine better accounts for structural disorder, insofar as elastic heterogeneities can be handled, as well as the softening of regions under-

4. The use of a *fixed* FE mesh does however reduce the numerical cost of the algorithm.

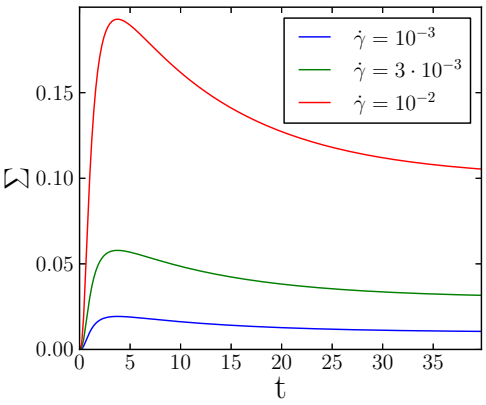

Figure 15.4: Shear stress of a purely viscous material, with $\eta = 10$ $\rho = 3$, $\mu = 0$, and $K = \kappa \approx 10^4$, in a system bounded by parallel walls ($N = 80 \times 20$), in response to a simple shear flow initiated at $t = 0$. The applied shear rates are indicated in the legend.

going a plastic event. In addition, it allows us to go beyond the assumption of pointwise rearrangements on which the ideal elastic propagator $\boldsymbol{\mathcal{G}}$ was based. The local anisotropy of the material can also be modelled, which may help describe the strongly anisotropic force chains in granular matter.

Finally, the FE framework paves the way for the study of the crossover between overdamped and underdamped (inertial) dynamics. In particular, the presence of inertia relaxes the former assumption of instantaneous mechanical equilibration.

15.5.4 *Limitations: marginal stability, staticity of the mesh*

Notwithstanding these assets, some serious limitations ought to be mentioned.

First and foremost, our routine is only marginally stable. Indeed, the regular square ("Q_1" in the FE literature) mesh that we use does not satisfy the Brezzi-Babushka stability criterion (see Section 15.1.3) and is known to yield erratic results when applied to Stokes problems.

In particular, a frequently encountered anomaly of major concern is the checkerboard issue, whereby high and low displacements/velocities alternate erratically in neighbouring cells, hence the image of a checkerboard. In the context of the (incompressible) Stokes problem, this is interpreted as a singularity of the matrix that must be inverted (the counterpart of $\mathbb{M}$ in Eq. 15.16).

In our routine, we do indeed encounter the checkerboard issue when $\rho = 0$, hence $\boldsymbol{\mathcal{M}} \to \mathbf{0}$. Somewhat counterintuitively, the code is stabilised by the inclusion of inertial forces, probably because the matrix $\mathbb{M} = \boldsymbol{\mathcal{M}} - \frac{\delta t}{2}\boldsymbol{\mathcal{H}}$ (where $\boldsymbol{\mathcal{M}}$ is a multiple of the identity matrix) is more readily invertible than $-\frac{\delta t}{2}\boldsymbol{\mathcal{H}}$.

A similar problem arises when one probes the elastic response of the medium to the imposed shear deformation of a *single* element. This elastic response is erratic, as can be seen Fig. 15.5a. The problem fades away if the shear deformation

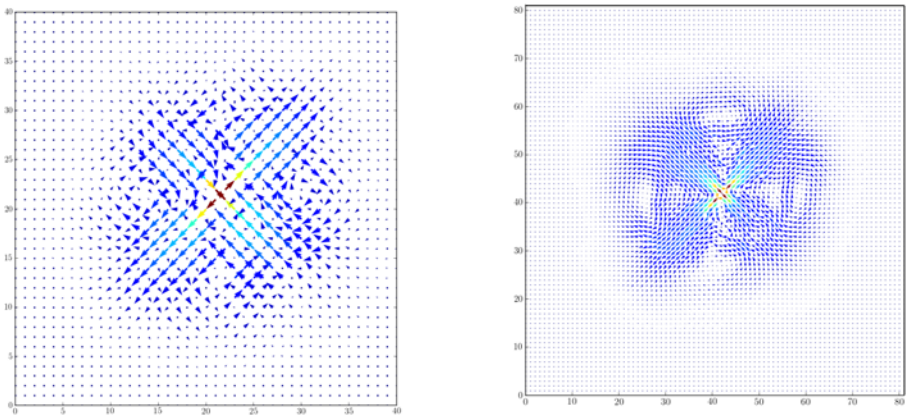

(a) Shear transformation is limited to one element.

(b) Shear transformation spans four elements.

Figure 15.5: Displacement field induced by applying a shear deformation to a region comprising either (a) one element or (b) four elements. The displacement arrows are coloured according to their norm.

covers four adjacent elements, *i.e.*, if the mesh is refined. The ensuing displacement field in the elastic medium is plotted in Fig. 15.5b but will be discussed at length in the next chapter. Consequently, in the simulations, each elastoplastic block will cover four elements.

One last issue should be mentioned: the implementation of convection is inconvenient in our fixed-mesh FE routine. Indeed, were it implemented along the same lines as in Chapter 13, *i.e.*, by incrementally shifting lines of elements, it would violate force balance, because elements would move along with the elastic stress they bear. Otherwise, if force balance were restored by imposing a stress redistribution whenever a line is convected, this would create spurious stress waves in the system.

However, the neglect of convection can also be supported (at least, partly) on a physical basis: we will mostly consider systems with low yield strains, say, $\gamma_y \leqslant 0.1$; it follows that more than 10 plastic events will have occurred by the time a block moves with respect to its first neighbours. In addition, unlike in the Fourier-Transform-based code, the streamwise and crosswise coordinates are never entirely symmetric here, because the FE routine computes displacements, and not only strains.

16

RESPONSE TO A SINGLE PLASTIC REARRANGEMENT

Very recently, Puosi et al. [2014] studied the time-dependent elastic response to an artificially triggered shear transformation with Molecular Dynamics (MD) simulations of a binary Lennard-Jones glass. With the objective of further validating the Finite Element (FE) routine presented in Chapter 15 and highlighting the impact of elastic heterogeneities on the propagation of stress waves, we undertake a similar study and compare the results to MD simulations.

16.1 MD SIMULATIONS WITH DISSIPATIVE PARTICLE DYNAMICS

Let us first present the MD system that will be used as a benchmark. It is the same athermal binary Lennard-Jones mixture as that presented in Section 14.1.1 and also used in Ref. [Puosi et al., 2014], except that a different damping scheme is employed. Indeed, instead of a mean-field dissipative force $\frac{-\boldsymbol{p}_i}{\tau_d}$, where $\boldsymbol{p}_i$ is the singular momentum of particle i with respect to an affine "solvent" flow and τ_d is the Langevin damping time, here we resort to Dissipative Particle Dynamics (DPD), whereby particles are damped on the basis of their relative velocities with respect to their neighbours. More precisely, the dissipative force experienced by particle i reads

$$\boldsymbol{f_i}^D = -\sum_{j\neq i} \zeta w^2\left(r_{ij}\right) \frac{\boldsymbol{v_{ij}}\cdot\boldsymbol{r_{ij}}}{r_{ij}^2}\boldsymbol{r_{ij}} \tag{16.1}$$

$$\text{where } w(r) \equiv \begin{cases} 1-\frac{r}{r_c} & \text{if } r < r_c, \\ 0 & \text{otherwise.} \end{cases}$$

Here, $\boldsymbol{v_{ij}} \equiv \boldsymbol{v_i} - \boldsymbol{v_j}$ denotes the relative velocity of particle i with respect to j, $\boldsymbol{r_{ij}} \equiv \boldsymbol{r_i} - \boldsymbol{r_j}$, the cut-off distance is set to $r_c = 3\sigma_{AA}$ (see Section 14.1.1 for the definition of σ_{AA}), and ζ controls the damping intensity. The projection of the force onto the radial vector $\boldsymbol{r_{ij}}$ is required in order to conserve angular momentum. In addition, on the basis of the work of Varnik et al. [2014], the use of *relative* particle velocities is expected to help overcome the deficiencies of the mean-field damping when it comes to reproducing experimentally measured correlations (the reader is referred to Section 14.3.3). Other virtues of DPD are exposed in Ref. [Soddemann et al., 2003].

The MD simulations have been performed by Dr. Francesco Puosi*, and the local elastic constants (see below) have been computed by Dr. Hideyuki* Mizuno.

16.2 FITTING OF THE MODEL PARAMETERS

Before comparing the elastic response to a shear transformation obtained in FE to that measured in MD, we need to fix the parameters of the FE system, *i.e.*, the density of the material, the size of an element, the local elastic constants and the viscosity. The first two parameters are readily adjusted: the size of an element is set to $2.5\sigma_{AA}$, *i.e.*, the approximate *radius* of a plastic rearrangement (recall, from Section 15.5.4, that shear transformations in the FE routine must be applied to macro-elements made of four adjacent sub-elements!), and the density is $\rho = 1.2/\sigma_{AA}^2 = 7.5$ in FE units. The last two parameters, on the other hand, deserve some more thoughts.

16.2.1 *Viscosity*

In MD, the damping magnitude is set by the coefficient ζ in the expression of the dissipative force ${f_i}^D$ (Eq. 16.1), whereas it is set by the viscosity η in FE. In order to match the damping in both simulations, we must connect the MD dissipative force ${f_i}^D$ to the viscous stress in FE, namely, $\boldsymbol{\sigma}^{\mathbf{diss}} = 2\eta\dot{\boldsymbol{\epsilon}}$ (see Eq. 15.5).

To this end, we consider a pure shear situation, in which particles are strictly advected by the flow

$$\begin{aligned} \boldsymbol{v}(\boldsymbol{r}) &= \dot{\boldsymbol{\epsilon}} \cdot \boldsymbol{r} \\ \text{with } \dot{\boldsymbol{\epsilon}} &\equiv \dot{\epsilon}_{xy} \left(\boldsymbol{e_y} \otimes \boldsymbol{e_x} + \boldsymbol{e_x} \otimes \boldsymbol{e_y} \right). \end{aligned}$$

On the one hand, in MD, the microscopic dissipative stress on particle i (of volume V_0) is obtained with the help of the Irving-Kirkwood formula, *viz.*,

$$\begin{aligned} \boldsymbol{\sigma}(\boldsymbol{r_i}) &= V_0^{-1} \sum_j \boldsymbol{r_{ij}} \otimes \boldsymbol{f_{ij}^D} \\ &= -\zeta V_0^{-1} \sum_j w^2\left(r_{ij}\right) \frac{\boldsymbol{v_{ij}} \cdot \boldsymbol{r_{ij}}}{r_{ij}^2} \boldsymbol{r_{ij}} \otimes \boldsymbol{r_{ij}}. \end{aligned}$$

Focusing on the xy-component of the stress and setting $\boldsymbol{r_i}$ as the origin of the frame, *i.e.*, $\boldsymbol{r_i} = \mathbf{0}$, for convenience, we get

$$\begin{aligned}
\sigma_{xy}(\boldsymbol{r_i} = \mathbf{0}) &= \zeta V_0^{-1} \sum_j w^2\left(r_j\right) \frac{\boldsymbol{v_j} \cdot \boldsymbol{r_j}}{r_j^2} x_j y_j \\
&= \zeta \dot{\epsilon}_{xy} V_0^{-1} \sum_j w^2\left(r_j\right) \frac{2 y_j x_j}{r_j^2} x_j y_j \\
&\simeq 2\zeta \dot{\epsilon}_{xy} V_0^{-1} \iint n g(r) w^2(r) \frac{x^2 y^2}{r^2} d^2 r \\
&= 2\zeta n \dot{\epsilon}_{xy} V_0^{-1} \int_0^{2\pi} \cos^2(\theta) \sin^2(\theta) d\theta \int_0^{\infty} g(r) w^2(r) r^3 dr \quad (16.2) \\
&= \frac{\pi}{2} \zeta n \dot{\epsilon}_{xy} V_0^{-1} \int_0^{\infty} g(r) w^2(r) r^3 dr.
\end{aligned}$$

Here, n is the average number density of the system and $g(r)$ is the (alledgedly isotropic) pair correlation function. Equation 16.2 expresses the stress in a volume of space occupied by a particle; elsewhere the stress is zero. Therefore, the average stress in the material reads

$$\begin{aligned}
\overline{\sigma_{xy}} &= (n V_0)\, \sigma_{xy}(\boldsymbol{r_i} = \mathbf{0}) \\
&= \frac{\pi}{2} \zeta \dot{\epsilon}_{xy} n^2 \int_0^{\infty} g(r) w^2(r) r^3 dr
\end{aligned}$$

On the other hand, in FE, the shear stress simply obeys $\overline{\sigma_{xy}} = 2\eta \dot{\epsilon}_{xy}$.
It immediately follows that

$$\boxed{\eta = \frac{\pi}{4} \zeta n^2 \int_0^{\infty} g(r) w^2(r) r^3 dr. \quad (16.3)}$$

If w^2 decreases fast (but smoothly) and the particles are hard and dense enough, so that $g(r)$ exhibits a sharp peak at $r = a_0$, the viscosity in Eq. 16.3 can be further approximated as

$$\begin{aligned}
\eta &\simeq \frac{1}{8} \zeta n (2\pi n) \int_{a_0-\epsilon}^{a_0+\epsilon} g(r) w^2(r) r^3 dr. \\
&\simeq \frac{\zeta n w^2(a_0)}{8} (2\pi n) \int_{a_0-\epsilon}^{a_0+\epsilon} g(r) r^3 dr \\
&\simeq \frac{1}{8} \zeta n w^2(a_0) a_0^2 z_c,
\end{aligned}$$

where z_c is the coordination number, *i.e.*, the number of first neighbours (at a distance $r \sim a_0$).

Equation 16.3 is valid for a one-component system, but the extension to binary mixtures, of components A and B, is straightforward; with transparent notations, the viscosity reads

$$\eta = \frac{\pi}{4}\zeta \int_0^\infty \left[n_A^2 g_{AA}(r) + 2 n_A n_B g_{AB}(r) + n_B^2 g_{BB}(r) \right] w^2(r)\, r^3 dr. \qquad (16.4)$$

In the considered Lennard-Jones system, this leads to $\eta = 0.726\,\zeta$.

16.2.2 *Local elastic constants*

Having determined the dissipative coefficient of the model, we turn our attention to the elastic properties of the system. Since Puosi et al. [2014] showed that structural disorder brings on large fluctuations of the elastic response of the material, we cannot settle with *global* elastic constants; instead, we must also probe the *local* elastic moduli.

The only relevant material lengthscale in the model being the typical size (a) of a rearrangement, we tile the system into subregions of size $a = 5\sigma_{AA}$ and compute the local stiffness tensors on this "mesoscopic" scale, with the local stress-affine strain method presented by Mizuno et al. [2013]. Details of this protocol and issues related to the rather unfamiliar local stiffness tensors are discussed in Appendix 16.8.1. With condensed notations, these tensors can be written as 3×3 real matrices in 2D, *viz.*,

$$\begin{pmatrix} \sigma_{xx} \\ \sigma_{yy} \\ \sqrt{2}\sigma_{xy} \end{pmatrix} = \underbrace{\begin{pmatrix} C_{xx,xx} & C_{xx,yy} & C_{xx,xy} \\ C_{yy,xx} & C_{yy,yy} & C_{yy,xy} \\ C_{xy,xx} & C_{xy,yy} & C_{xy,xy} \end{pmatrix}}_{\mathbf{C}} \begin{pmatrix} \epsilon_{xx} \\ \epsilon_{yy} \\ \sqrt{2}\epsilon_{xy} \end{pmatrix}, \qquad (16.5)$$

where σ_{xx}, σ_{yy}, and σ_{xy} are the linear elastic contributions to the local stress.

Contrary to their macroscopic counterpart, the local $\mathbf{C}$ matrices are not symmetric *a priori*, for very small regions [Tsamados et al., 2009]. However, the coarse grain $a = 5\sigma_{AA}$ is large enough here so that the assumption of symmetry can be a decent approximation. To limit the number of parameters, we further assume that isotropic contraction/dilation of the region only generates an isotropic stress, *i.e.*, that

$$\begin{pmatrix} \epsilon_{xx} & \epsilon_{yy} & \sqrt{2}\epsilon_{xy} \end{pmatrix}^\top = \sqrt{2}/2 \begin{pmatrix} 1 & 1 & 0 \end{pmatrix}^\top$$

is an eigenvector of $\mathbf{C}$ (these approximations are assessed in Appendix 16.8.1); by analogy with the macroscopic case, the eigenvalue c_3 associated with this pure contraction is (twice) the bulk modulus K, *viz.*, $c_3 = 2K$. The other two eigenvalues, c_1 and c_2, of the (symmetric) $\mathbf{C}$ matrix are then (twice) the shear moduli μ_1 and μ_2, *viz.*, $c_1 = 2\mu_1$ and $c_2 = 2\mu_2$ with $c_1 < c_2$, and are typically considerably smaller than c_3.

Denomination	*Symbol*	*Mean*	*Std dev.*
Shear modulus (weak direction)	μ_1	13.16	7.2
Shear modulus (strong direction)	μ_2	24.46	5.8
Average shear modulus	$\mu \equiv \frac{\mu_1+\mu_2}{2}$	18.81	5.3
Bulk modulus	K	99.9	8.4

Table 16.1: Statistical properties of the elastic constant distributions: mean values and standard deviations (std dev.).

These two assumptions, namely, tensorial symmetry and isotropy of the response to contraction, imply that the stiffness tensor should be of the form

$$\mathbf{C} = \begin{pmatrix} \alpha & \delta & \beta \\ \delta & \alpha & -\beta \\ \beta & -\beta & \upsilon \end{pmatrix}, \text{ where } \alpha, \delta, \beta, \upsilon \in \mathbb{R}. \tag{16.6}$$

Nevertheless, if we draw on the analogy with the macroscopic case, there exists a frame $(\boldsymbol{e}_x(\theta), \boldsymbol{e}_y(\theta))$, rotated by an angle θ with respect to the original frame, in which the stiffness tensor reads

$$\begin{pmatrix} K+\mu_2 & K-\mu_2 & 0 \\ K-\mu_2 & K+\mu_2 & 0 \\ 0 & 0 & 2\mu_1 \end{pmatrix}, \text{ with } \mu_1 \leqslant \mu_2.$$

Consequently, if the local stiffness tensor is approximated by its projection onto a matrix of the form given by Eq. 16.6, the following four local parameters suffice to determine it completely: θ, μ_1, μ_2, and K.

Table 16.1 summarises the characteristics of the distributions of μ_1, μ_2, and K measured in the Lennard-Jones glass under consideration; θ is uniformly distributed, in accordance with isotropy at the macroscale.

It is noteworthy that the local stiffness matrices exhibit significant anisotropy, as indicated by the discrepancy between the mean value of the shear modulus in the (locally) weaker direction, $\langle \mu_1 \rangle = 13.16$, and its strong counterpart, $\langle \mu_2 \rangle = 24.46$.

Some regions actually even display negative shear moduli μ_1. This is not unrealistic in the MD system, because these regions can be stabilised by the surrounding medium, but, in the following, they will be discarded, and arbitrarily set to zero, in the FE simulations, where they cause instabilities.

Lastly, the bulk modulus is much larger (by a factor of 5) than the shear moduli, in line with expectations. In addition, its distribution is by far narrower than the distributions of shear moduli, after rescaling by their respective mean values. Consequently, we will henceforth always neglect spatial fluctuations of the bulk modulus and set $K = 99.9$.

Summary of the three FE systems under investigation

Common properties
Uniform bulk modulus K, bulk viscosity κ, and shear viscosity

$$\begin{aligned} K &= \kappa = 99.9 \\ \eta &= 0.726\,\zeta \end{aligned}$$

① **Uniform system**

$$\mu_1 = \mu_2 = 18.8$$

② **Heterogeneous system with isotropic blocks ("het. iso.")**

$$\mu_1 = \mu_2 = \mu \text{ and } \mu = 18.8 \pm 5.3,$$

i.e., μ is normally distributed, with mean value 18.8 and standard deviation 5.3.
(Remember that each block is a macro-element made of four adjacent finite elements.)

③ **Heterogeneous system with anisotropic blocks ("het. aniso.")**

$$\mu_1 = 13.16 \pm 7.2 \text{ and } \mu_2 = 24.46 \pm 5.8$$

The angle θ defining the principal direction associated with μ_1 is picked at random from uniform distribution over $[0, 2\pi[$.

Figure 16.1: Characteristics of the FE systems.

16.2.3 *Finite Element Systems*

The foregoing study of the visco-elastic properties of the MD system leads us to choose a constant bulk modulus $K = 99.9$ and a constant viscosity $\eta = 0.726\,\zeta$ in the FE simulations. As for the distributions of shear moduli, three types of systems will be considered:

① a uniform system
② a heterogeneous system made of isotropic blocks ("het. iso.")
③ a heterogeneous system made of anisotropic blocks ("het. aniso.")

The characteristics of these systems are listed in Fig. 16.1.

The size of the FE system is adjusted to the MD simulation cell, and biperiodic boundary conditions are used in both cases.

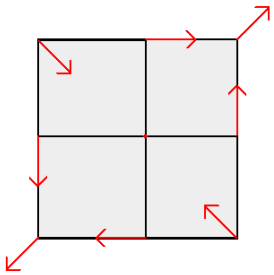

Figure 16.2: Sketch of the displacements applied to a macro-element to model a pure shear transformation.

16.2.4 *Verification*

By simulating an oscillatory plane shear wave, we have confirmed that the MD sound velocity is correctly matched by the FE simulations and that the order of magnitude [1] of the damping coefficient is correct (*data not shown*).

16.3 ARTIFICIALLY TRIGGERED SHEAR TRANSFORMATIONS

Following Ref. [Puosi et al., 2014], shear transformations are artificially created in the MD system by applying a pure shear strain ϵ_{xy} to a disk centred at (x_0, y_0) and of diameter $a = 5\sigma_{AA}$. To do so, particles whose initial position (x_i, y_i) belongs to this region are displaced to a new position (x_i', y_i') at $t = 0$, which satisfies

$$\begin{cases} x_i \to x_i' & = x_i + \epsilon_{xy}\,(y_i - y_0) \\ y_i \to y_i' & = y_i + \epsilon_{xy}\,(x_i - x_0)\,. \end{cases}$$

Their positions are then frozen for the whole simulation. In order to measure the elastic, *i.e.*, reversible, response of the medium, ϵ_{xy} never exceeds a few percent strain.

A similar shear transformation is applied in the FE simulations to a macro-element made of four adjacent elements (see Section 15.5.4), by controlling the positions of the nodes of these elements (*via* BC-like prescriptions), as sketched in Fig. 16.2.

16.4 DISORDER-AVERAGED PROPAGATION

Let us first study the propagation of the waves induced by the shear transformation, after averaging over disorder, *i.e.*, over many (50) locations (x_0, y_0) of the transformation in MD or over many (50) realisations of the elastic config-

1. These plane wave simulations have not allowed us to ascertain the accurate value of the damping.

uration of the system in FE. The average displacement at time t is denoted by $\boldsymbol{u}(\boldsymbol{r};t) \equiv \left\langle \boldsymbol{u}^{(d)}(\boldsymbol{r};t) \right\rangle_d$, where (d) refers to a particular disorder configuration..

Figures 16.3 and 16.4 show the cumulated displacement field at various time lags, for two distinct damping magnitudes: $\zeta = 1$ (relatively low damping), $\zeta = 100$ (overdamped regime). The visual agreement between the MD simulations and those obtained with the FE routine (het. iso.) is striking. In both cases, the propagation is radial, with (apparently two) circular wavefronts, not unlike the observations of Chattoraj and Lemaître [2013]. The maximal displacements are found in lobes oriented at $\frac{\pi}{4} \pm n\frac{\pi}{2}$, $n \in \mathbb{Z}$, with respect to the x or y direction, whereas vortices develop in the x and y directions, particularly conspicuously at intermediate times ($\Delta t = 10$) for $\zeta = 1$, and they clear the existing displacements in these directions.

Turning to a quantitative study, we make use of the average propagation radius $\Delta_r(t)$ introduced by Puosi et al. [2014] to measure the advance of the wave,

$$\Delta_r(t) \equiv \iint |u_r(\boldsymbol{r};t)| d^2\boldsymbol{r},$$

where $u_r(t)$ is the radial displacement at time t. If the final displacement, $u_r(\boldsymbol{r}; t = \infty) \sim r^{-1}$ in any given direction θ in the far field, is essentially achieved as soon as a region is reached by the wavefront, $\Delta_r(t)$ will grow as the linear size of the displaced region. The average propagation radius is plotted in Fig. 16.5 for diverse values of the damping ζ. The initial growth is ballistic in MD, with $\Delta_r(t) \sim t$, while, at long times, $\Delta_r(t)$ saturates at its steady-state value. Contrary to the findings reported in Ref. Puosi et al. [2014] for a mean-field dissipation scheme, here no clear diffusive regime $\Delta_r(t) \sim t^{1/2}$ is observed; in Appendix 16.8.2, we enquire into this difference. The evolution of $\Delta_r(t)$ before the steady state is reached strongly depends on ζ. With a low damping ($\zeta = 1$), the interaction with the waves generated by the periodic replicas of the shear transformation leads to particularly long-lived oscillations of $\Delta_r(t)$ (Fig. 16.5a), while stronger damping ($\zeta = 100$) completely suppresses these oscillations.

The FE simulations nicely capture this qualitative change, and the agreement both in the limit of low damping (Fig. 16.5a) and in the limit of strong damping (Fig. 16.5c) is excellent, at relatively long times. This is true for all three FE systems, including the uniform one, which supports the idea that the *average* propagation in elastically heterogeneous media is virtually identical to the propagation in a uniform medium.

For an intermediate value of the damping, namely, $\zeta = 10$ (Fig. 16.5b), the agreement is reasonable, but not quite as good, insofar as the oscillations observed in MD are damped perceptibly faster than their counterparts in FE, not only in the uniform system, but also in the heterogeneous one (het. iso.). This suggests that the FE viscosity is somewhat underestimated, or that, in MD, anharmonicities significantly contribute to the damping of the oscillations.

Finally, the short-time propagation is well described for low damping, but the agreement declines when ζ increases, in which case the FE method overestimates the propagation velocity over short distances.

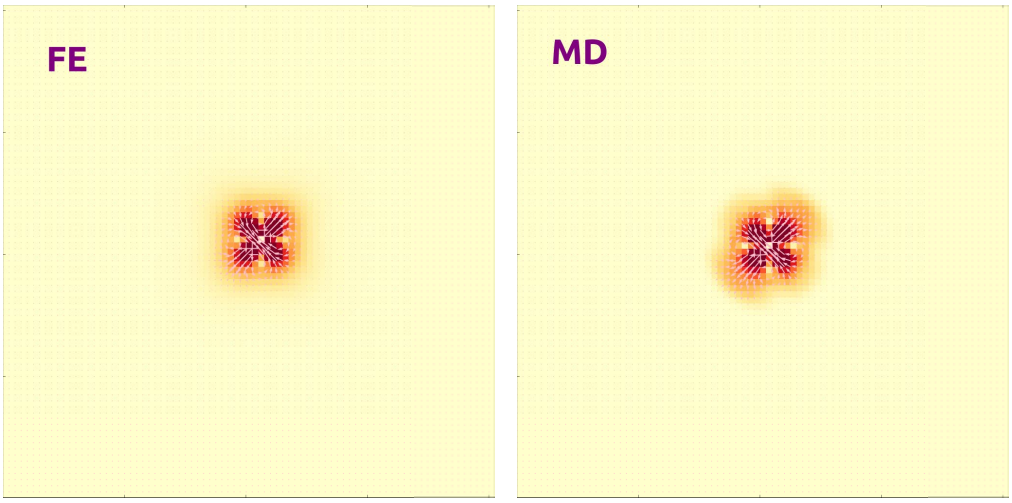

(a) $\Delta t = 2$

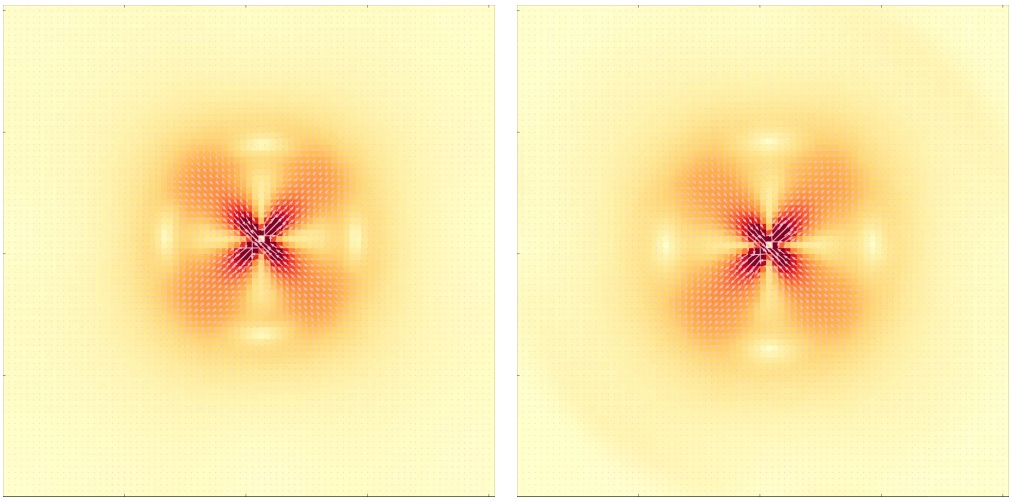

(b) $\Delta t = 10$

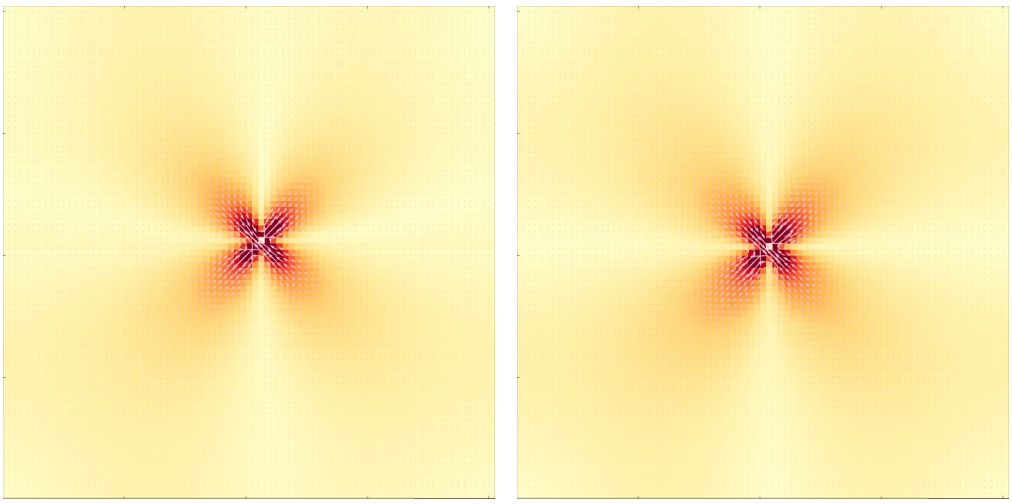

(c) $\Delta t = 1000$

Figure 16.3: Average displacement field induced by a shear transformation (at the centre of the cell), after a time lag Δt, for relatively low damping, $\zeta = 1$ (hence, $\eta = 0.726$). The pink arrows represent the displacement vectors and the background colour map is indicative of the norm of these vectors.
(*Left*) Finite Elements, het. iso.; (*right*) Molecular Dynamics.

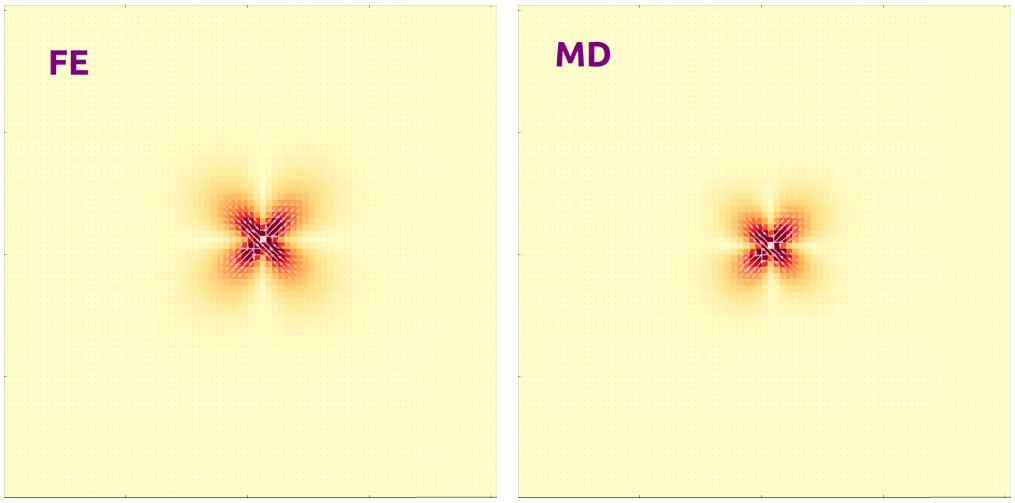

(a) $\Delta t = 2$

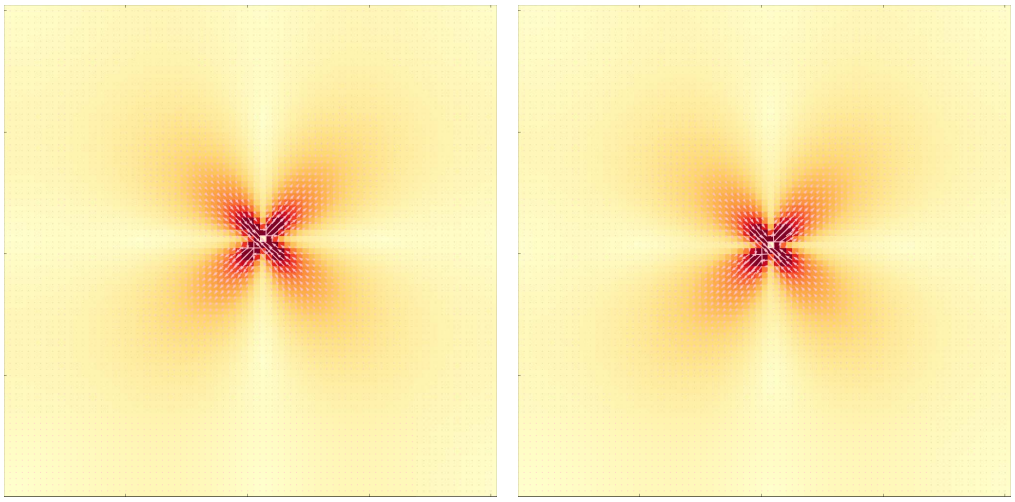

(b) $\Delta t = 10$

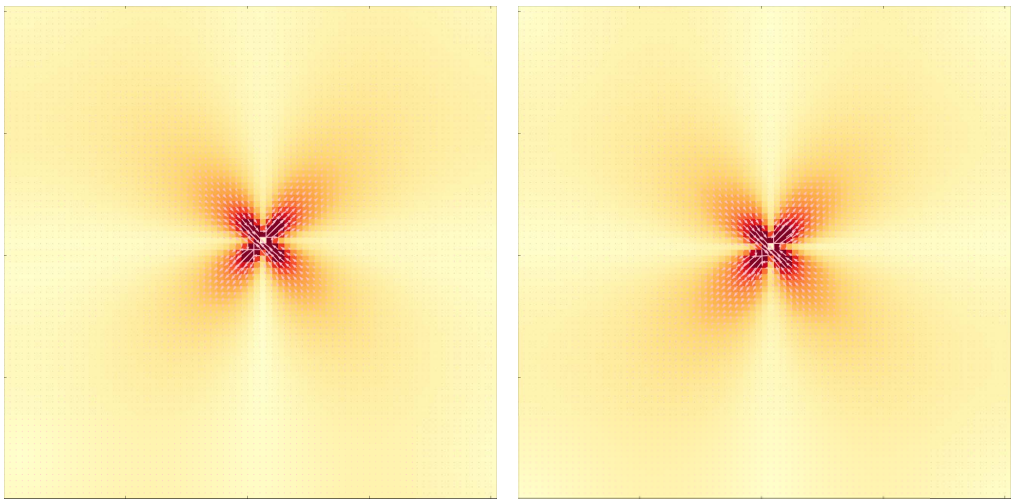

(c) $\Delta t = 1000$

Figure 16.4: Average displacement field induced by a shear transformation, after a time lag Δt, for strong damping, $\zeta = 100$ (hence, $\eta = 72.6$). Refer to Fig. 16.3 for the legend.

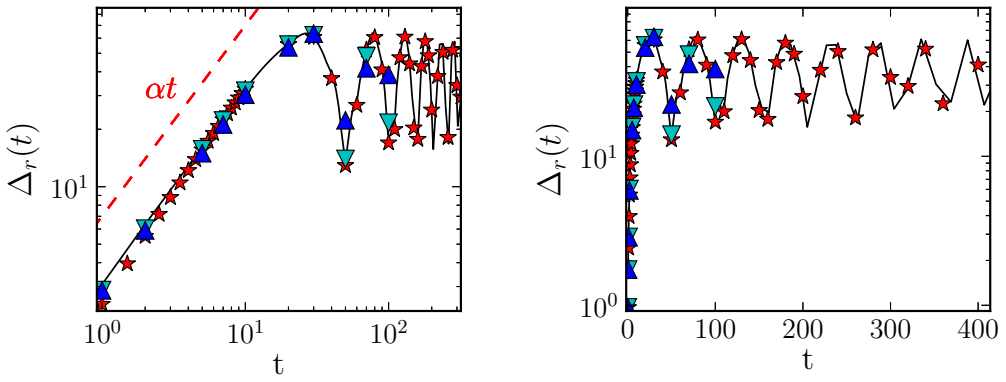

(a) $\zeta = 1$ ($\eta = 0.726$)

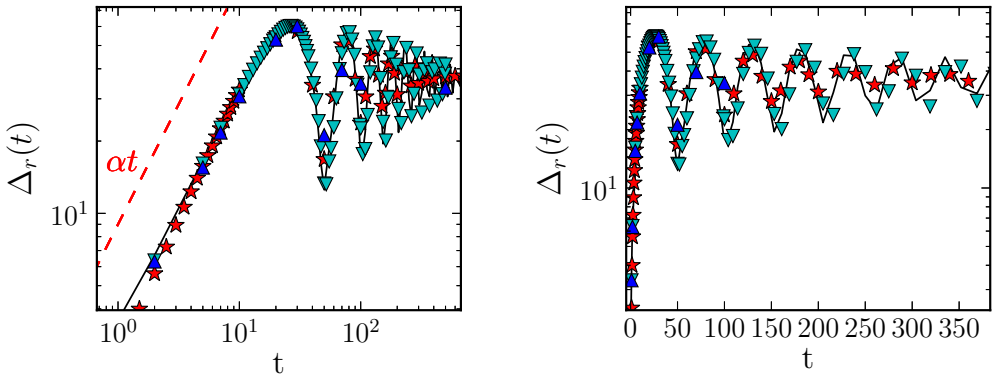

(b) $\zeta = 10$ ($\eta = 7.26$)

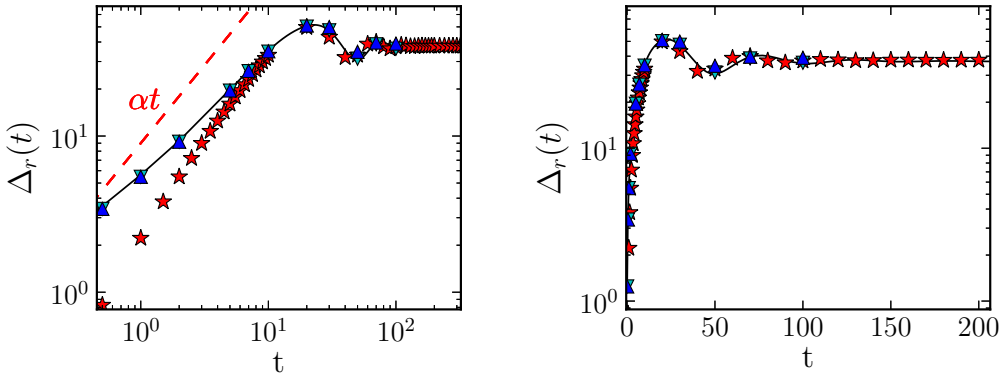

(c) $\zeta = 100$ ($\eta = 72.6$)

Figure 16.5: Average propagation radius Δ_r as a function of time, for different damping magnitudes.
(*Red stars*) MD data; (*inverted cyan triangles*) FE, het. iso.; (*blue triangles*) FE, het. aniso; (*solid black line*) FE, uniform system.
(*Left*) log-log plot, (*right*) same data, in semi-logarithmic plot.

16.5 EFFECT OF STRUCTURAL DISORDER

The disorder-induced fluctuations with respect to the average response are now examined.

The norm of the average displacement $\boldsymbol{u}(\boldsymbol{r};t)$ along a diagonal direction, at a long time lag $t = 1000$, is plotted in Fig. 16.6 for $\zeta = 1$ and $\zeta = 100$, together with the associated standard deviation δu, *i.e.*,

$$\delta u(\boldsymbol{r};t) = \sqrt{\left\langle \left[\boldsymbol{u}^{(d)}(\boldsymbol{r};t) - \boldsymbol{u}(\boldsymbol{r};t)\right]^2 \right\rangle_d}.$$

One may notice that, for $\zeta = 1$, the average displacements do not coincide satisfactorily between MD and FE, which is mostly due to the fact that the oscillations described in Section 16.4 have not died out yet at this time lag, and they are not perfectly in phase in the different systems. The agreement of the average values is much better for $\zeta = 100$.

Regarding the fluctuations, the paramount result is that their order of magnitude is well reproduced by the FE simulations, both with isotropic blocks (het. iso., $\mu_1 = \mu_2$) and with anisotropic blocks (het. aniso.), although, quite naturally, het. aniso. displays larger fluctuations than het. iso. Moreover, it is noteworthy that these corrections are roughly half as large as the mean reponse, *e.g.*, at a distance of $50\sigma_{AA}$. It should however be recalled here that the centre of mass of the MD simulation cell is kept fixed, to avoid the global translations of the system that we have sometimes observed otherwise (and which then dominate the fluctuations).

With regard to the distribution of δu in space, colour maps of the relative fluctuations $\delta u(\boldsymbol{r};t)/u(\boldsymbol{r};t)$ are presented in Fig. 16.7. In regions with non-negligible displacements, *i.e.*, $u(\boldsymbol{r};t) \geqslant 10^{-2}$, the relative fluctuations are approximately homogeneous and tend to increase slightly with time.

16.6 TIME-DEPENDENT RESPONSE TO A PARTICULAR PLASTIC EVENT

Even though the study of the propagation dynamics (Section 16.4) and of disorder-induced fluctuations (Section 16.5) is sufficient to validate the FE account of elastic propagation in a model, we would like to know whether the comparison can be pushed further. More precisely, can the FE routine describe the details of the elastic response in a *particular* configuration?

To address this question, within the third type of FE mode, namely, het. aniso., the local shear moduli μ_1 and μ_2 and the angle θ of each macro-element (*i.e.*, set of four adjacent elements) are directly extracted from the corresponding region in the MD system. Then, we compute the strain field [2] induced by shear trans-

2. In MD, local strains are computed after coarse-graining the displacement field on a grid similar to the FE one.

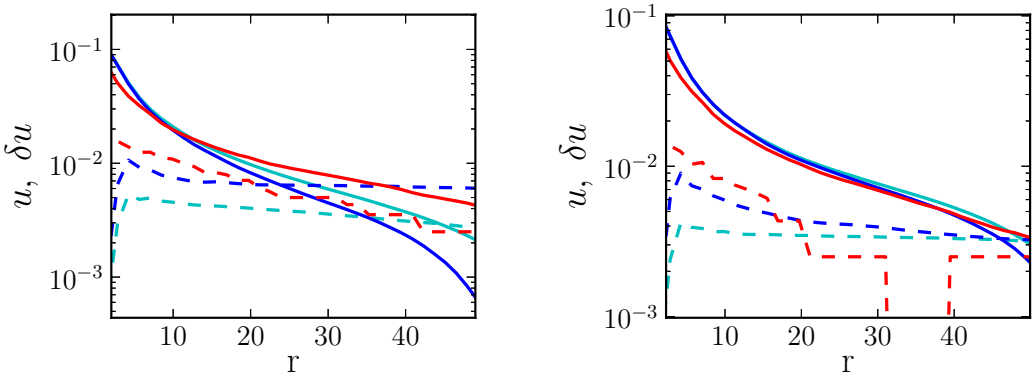

(a) $\zeta = 1.$ (b) $\zeta = 100.$

Figure 16.6: (*Solid lines*) mean value u and (*dashed lines*) standard deviation δu of the displacement norm along a diagonal axis $\boldsymbol{e}_{\text{diag}} = \frac{\sqrt{2}}{2}\left(\boldsymbol{e}_x + \boldsymbol{e}_y\right)$, after a time lag $\Delta t = 1000$, as a function of the distance (in FE units).
(*Red*) MD; (*cyan*) FE, het. iso.; (*blue*) FE, het. aniso.

formations occurring at given positions in the sample, an example of which is shown in Fig. 16.8.

Although the MD response and its FE counterpart look alike, we cannot assert that, beyond the average quadrupolar structure, the disorder-induced fluctuations are similar in MD and FE. The results are therefore inconclusive in this respect.

16.7 SHEAR REARRANGEMENT DYNAMICS

Throughout this chapter, shear transformations have been arbitrarily imposed, through an instantaneous displacement of particles (or FE nodes). However, in a *bona fide* simulation, the dynamics of shear transformations are determined by the system itself. Let me simply mention that at least two dynamical regimes can be envisioned:

If inertia is negligible, the competitition between elasticity and viscosity sets the timescale of the rearrangement, $\tau = \eta/\mu$, as discussed in Section 7.4.2.

If most of the rearrangement consists in the damping of the inertial force (initially generated by elasticity), then the duration of a rearrangement is set by the inverse damping coefficient ζ^{-1}.

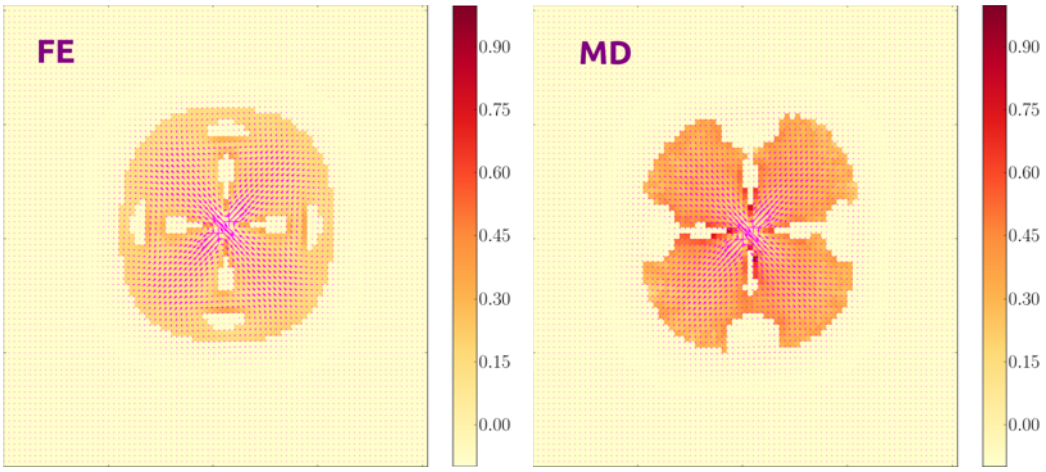

(a) $\Delta t = 10$

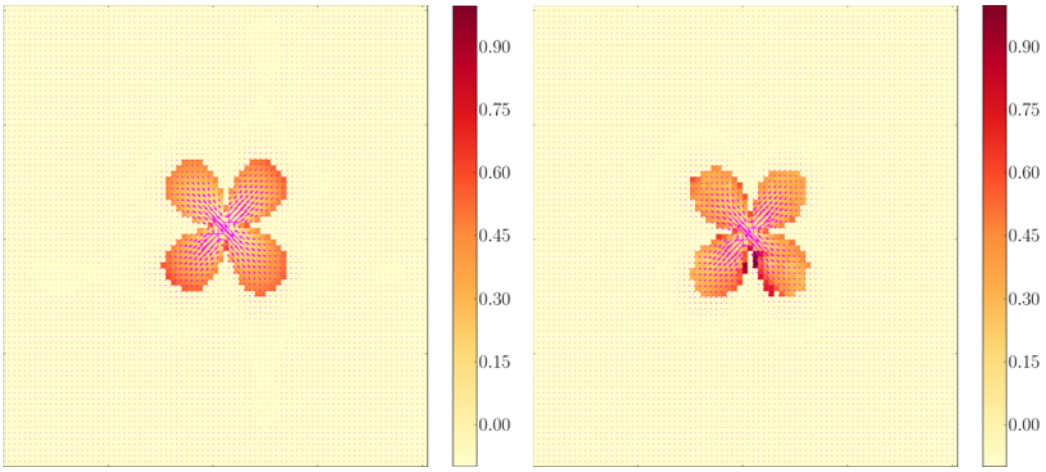

(b) $\Delta t = 100$

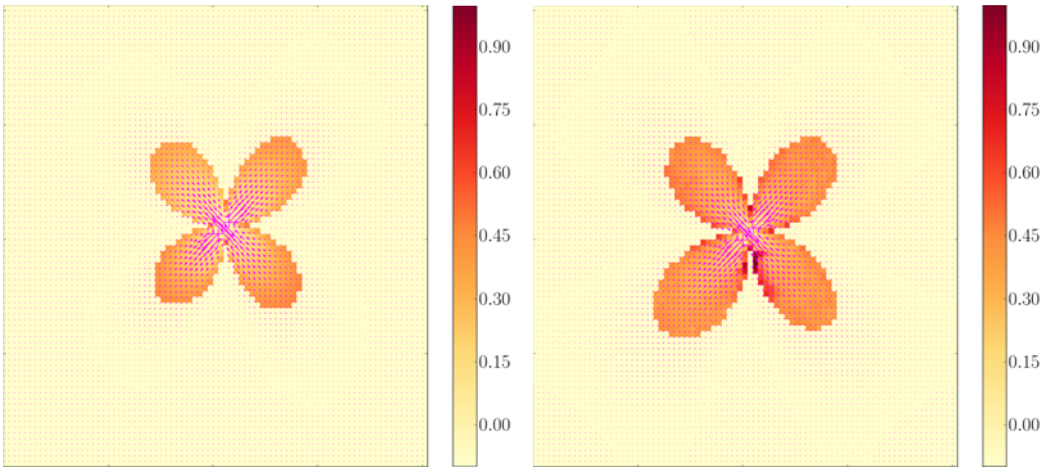

(c) $\Delta t = 1000$

Figure 16.7: Colour map of the relative displacement norm fluctuations $\delta u(\boldsymbol{r};t)/u(\boldsymbol{r};t)$ for $\zeta = 1$. The regions where $u(\boldsymbol{r};t) < 10^{-2}$ are overlaid in light yellow.

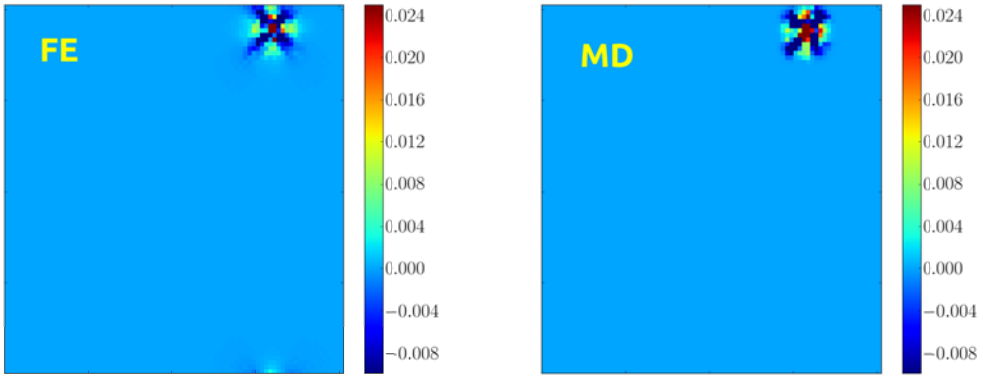

(a) $\Delta t = 1$

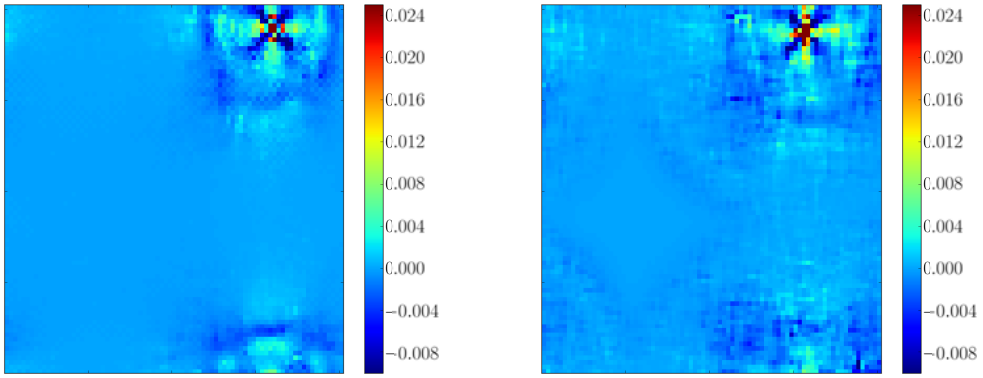

(b) $\Delta t = 10$

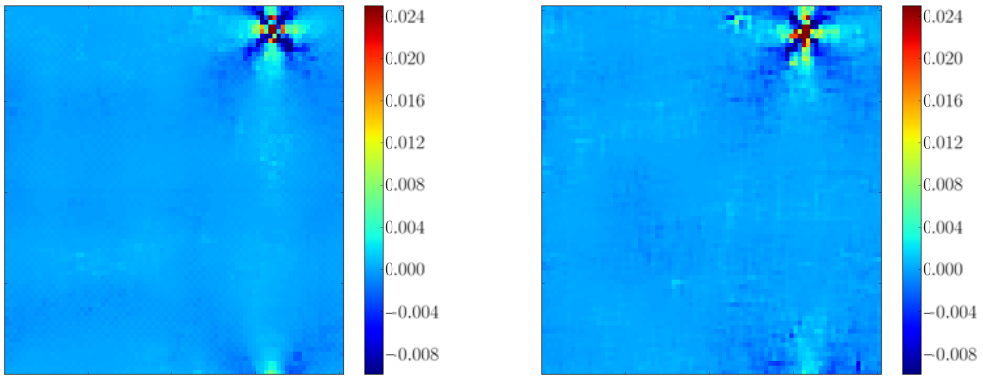

(c) $\Delta t = 100$

Figure 16.8: Local strain field induced by a particular shear transformation at different lag times, for $\zeta = 1$.
(*Left*) FE, with an elastic configuration modelled on the MD system; (*right*) MD.

Key Points of the Chapter

- Local shear moduli are more broadly distributed (on a relative basis) than local bulk moduli.
- The average time-dependent elastic response in a disordered medium is similar to the propagation in a uniform medium and it is well reproduced in the FE simulations.
- Fluctuations with respect to the average displacement field are considerable, with relative fluctuations of a few tens of percents.
- The order of magnitude of these fluctuations is captured by FE simulations on heterogeneous, but locally isotropic systems. The local anisotropy of the blocks does not play a major role in this respect.

A

16.8 APPENDIX

16.8.1 *Determination of the local stiffness tensors*

With our condensed notations for the stress and strain tensors (Eq. 16.5), the macroscopic stiffness tensor of an isotropic material of bulk modulus K and shear modulus μ reads (see Section 15.5.1)

$$\mathbf{C} = \begin{pmatrix} K+\mu & K-\mu & 0 \\ K-\mu & K+\mu & 0 \\ 0 & 0 & 2\mu \end{pmatrix}.$$

In comparison, local stiffness tensors display rather unusual properties. To grasp the meaning of their (lack of) symmetries, some brief general considerations about elasticity and deformation are in order.

Suppose that a small macroscopic strain $\bar{\boldsymbol{\epsilon}}$ is applied to a sample and focus on a mesoscopic region $\mathcal{S}$. The local linear strain tensor $\boldsymbol{\epsilon}$ is defined as the *symmetric* tensor that best matches the displacements of the particles in $\mathcal{S}$ due to the applied strain. Only if the deformation is strictly affine over the whole sample do the local strain tensors equate to $\bar{\boldsymbol{\epsilon}}$.

Because, for a given short-range interparticle potential, the local stress $\boldsymbol{\sigma}$ results from the local configuration of particles, it is reasonable (but not strictly necessary) to suppose the existence of a function f such that

$$\boldsymbol{\sigma} = f(\boldsymbol{\epsilon}).$$

Let us write the first-order Taylor expansion of f, provided that it exists,

$$\sigma_{\alpha\beta} - \sigma^{(0)}_{\alpha\beta} = C_{\alpha\beta\gamma\delta}\epsilon_{\gamma\delta} + \mathcal{O}\left(\|\boldsymbol{\epsilon}\|^2\right), \tag{16.7}$$

where $\alpha, \beta \in \{x, y\}$ and $\sigma^{(0)}_{\alpha\beta}$ is the quenched stress in the original configuration. With condensed notations, Eq. 16.7 turns into [3]

$$\begin{pmatrix} \sigma_{xx} \\ \sigma_{yy} \\ \sqrt{2}\sigma_{xy} \end{pmatrix} = \underbrace{\begin{pmatrix} C_{xx,xx} & C_{xx,yy} & C_{xx,xy} \\ C_{yy,xx} & C_{yy,yy} & C_{yy,xy} \\ C_{xy,xx} & C_{xy,yy} & C_{xy,xy} \end{pmatrix}}_{\mathbf{C}} \begin{pmatrix} \epsilon_{xx} \\ \epsilon_{yy} \\ \sqrt{2}\epsilon_{xy} \end{pmatrix} + \mathcal{O}\left(\|\boldsymbol{\epsilon}\|^2\right). \tag{16.8}$$

3. As a minor technical detail, note that, because the tensorial multiplication $C_{\alpha\beta\gamma\delta}\epsilon_{\gamma\delta}$ involves a summation on both ϵ_{xy} and ϵ_{yx}, components $C_{\alpha\beta,\gamma\delta}$ of the *second-rank* tensor $\mathbf{C}$ may not exactly equate to their counterparts in the *fourth-rank* tensor $C_{\alpha\beta\gamma\delta}$; for instance, $C_{xy,xy} = 2C_{xyxy}$.

The affine strain-local stress approximation consists in replacing the components of $\boldsymbol{\epsilon}$ on the rhs of Eq. 16.8 with those of the affine strain $\bar{\boldsymbol{\epsilon}}$, in order to determine $\mathbf{C}$ more easily. For subregions of size larger than $5\sigma_{AA}$, Mizuno et al. [2013] showed that this approximation is quite reasonable, although it slightly underestimates the spatial fluctuations of the elastic constants. On the other hand, should the local stress on the lhs be computed for a *local* deformation equal to $\bar{\boldsymbol{\epsilon}}$, *i.e.*, should the system not be allowed to relax to the energy minimum after the application of the affine strain $\bar{\boldsymbol{\epsilon}}$, then we would obtain the so-called Born term $\mathbf{C}^B$, which largely overestimates the stiffness of the disordered material [Mizuno et al., 2013].

For the time being, all components of the second-rank stiffness tensor $\mathbf{C}$ are independent. But, if the local stress derives from a (twice differentiable) local strain-energy density e, *i.e.*,

$$\sigma_{\alpha\beta} \equiv \frac{\partial e}{\partial \epsilon_{\alpha\beta}},$$

then

$$C_{\alpha\beta\gamma\delta} = \frac{\partial^2 e}{\partial \epsilon_{\alpha\beta} \partial \epsilon_{\gamma\delta}}.$$

It immediately follows that $C_{\alpha\beta\gamma\delta} = C_{\gamma\delta\alpha\beta}$; this symmetry property is transferred to the second-rank tensor $\mathbf{C}$ (thanks to the carefully chosen $\sqrt{2}$ prefactors in Eq. 16.8). Indeed, Tsamados et al. [2009] observed numerically that, for coarse-graining regions larger than 5 Lennard-Jones particles in diameter, assuming a symmetric stiffness matrix $\mathbf{C}$ creates an error of less than 1% on the local stress evaluations. In the MD system under consideration, we quantify the asymmetry of the mesoscopic stiffness matrices, computed over regions of size $a = 5\sigma_{AA}$, with the following measure:

$$\|\Delta\mathbf{C}\| \equiv \sqrt{\sum_{\substack{i,j \in \\ \{xx,yy,xy\}}} \Delta C_{i,j}^2} \text{ with } \Delta\mathbf{C} \equiv \mathbf{C} - \frac{\mathbf{C} + \mathbf{C}^\top}{2}.$$

What should $\|\Delta\mathbf{C}\|$ be compared with? At first sight, the answer would be $\|\mathbf{C}\|$, but the latter is dominated by large symmetric terms involving the bulk modulus $K \approx 100$. Thus, on second thoughts, it appears more informative to remove the terms involving K; $\|\Delta\mathbf{C}\|$ should then be compared to, *e.g.*, $\langle \mathrm{Tr}\,(\mathbf{C}) - 2K \rangle = 4\langle\mu\rangle$, with $\langle\mu\rangle = 18.8$. From the histogram of $\|\Delta\mathbf{C}\|$ values plotted in Fig. 16.9a, it transpires that deviations from symmetry in $\mathbf{C}$ are not strictly negligible, but symmetry may nevertheless be a decent *approximation*.

To further reduce the number of local parameters, the isotropic contraction/dilation vector $(\sqrt{2}/2\ \sqrt{2}/2\ 0)^\top$ is supposed to produce an isotropic compression and, thus, to be an eigenvector of $\mathbf{C}$, *ergo*

$$\begin{cases} C_{xy,xx} &= -C_{xy,yy} \\ C_{xx,xx} &= C_{yy,yy} \end{cases}$$

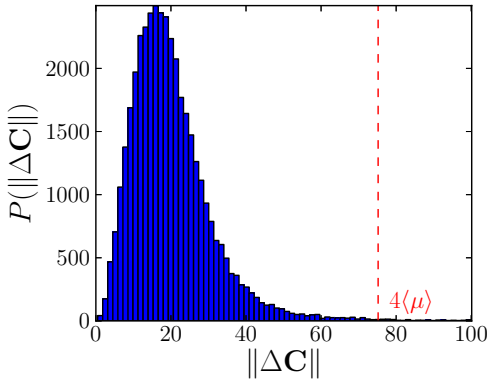

(a) Asymmetry.

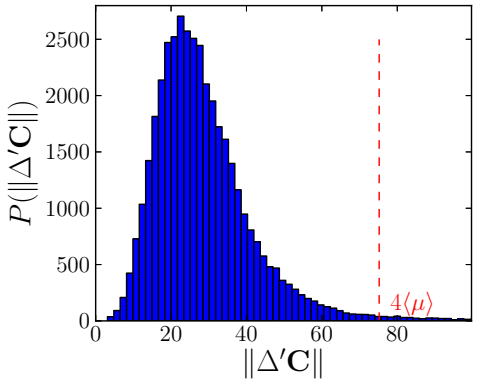

(b) Discrepancy with the matrix $\mathbf{C}'$ given in Eq. 16.9.

Figure 16.9: Histograms of the approximation errors made when supposing that the local stiffness tensors $\mathbf{C}$ are (a) symmetric, (b) of the form given in Eq. 16.9.

The assumptions of tensorial symmetry and isotropic response to contraction come down to projecting $\mathbf{C}$ onto a matrix of the form

$$\mathbf{C}' = \begin{pmatrix} \alpha & \delta & \beta \\ \delta & \alpha & -\beta \\ \beta & -\beta & \upsilon \end{pmatrix} \text{ with } \alpha, \delta, \beta, \upsilon \in \mathbb{R}, \tag{16.9}$$

where α and β will be the averages of the pairs $(C_{xx,xx}, C_{yy,yy})$ and $(C_{xy,xx}, -C_{xy,yy})$, respectively. The approximation error, quantified by $\|\Delta'\mathbf{C}\| \equiv \|\mathbf{C} - \mathbf{C}'\|$, is plotted in Fig. 16.9b. As expected, the deviations are somewhat larger than were $\mathbf{C}$ only symmetrised, but they remain under control.

For each matrix $\mathbf{C}'$, we compute the eigenvalues $c_1 \leqslant c_2 \leqslant c_3$ and define:
- the small local shear modulus $\mu_1 \equiv c_1/2$,
- the large local shear modulus $\mu_2 \equiv c_2/2$,
- and the bulk modulus is $K \equiv c_3/2$.

The distributions of these local elastic constants are presented in Fig. 16.10 and their mean values and standard deviations are summarised in Table 16.1. It should be noted that the average eigenvalues of the projected tensor $\mathbf{C}'$ differ by 10% or less from the eigenvalues of the full local stiffness tensors $\mathbf{C}$.

The components of $\mathbf{C}'$ can then be rewritten as follows

$$\begin{cases} \alpha & \equiv K + \mu_2 \cos^2 2\theta + \mu_1 \sin^2 2\theta \\ \delta & \equiv K - \mu_2 \cos^2 2\theta - \mu_1 \sin^2 2\theta \\ \beta & \equiv \frac{\sin 4\theta}{\sqrt{2}} (\mu_2 - \mu_1) \\ \upsilon & \equiv 2\mu_2 \sin^2 2\theta + 2\mu_1 \cos^2 2\theta \end{cases},$$

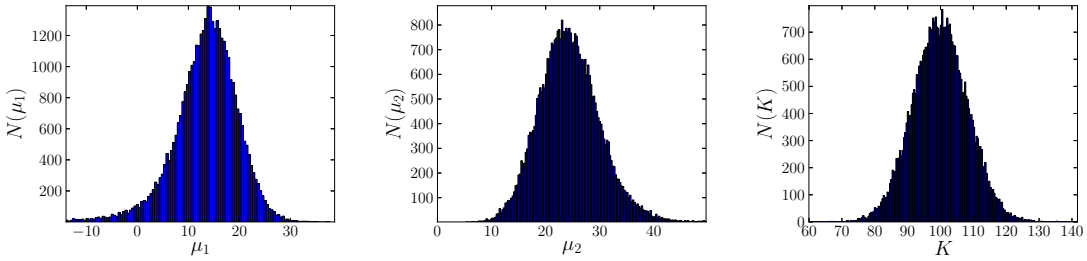

(a) μ_1 (b) μ_2 (c) K

Figure 16.10: Histograms (number of counts) of the measured values of the local elastic constants μ_1, μ_2, and K in subregions of size $5\sigma \times 5\sigma$ in the MD system.

where the angle θ has been defined in Section 16.2.2.

16.8.2 *Propagative regimes*

With a mean-field dissipative scheme, Puosi et al. [2014] observed a diffusive regime of growth of the average propagation radius $\Delta_r(t)$, *i.e.*, $\Delta_r(t) \sim t^{1/2}$, which is not apparent in the present DPD simulations. Can this difference be explained?

Mean-field dissipation

With a mean-field damping force $-p_i/\tau_d$, where $\boldsymbol{p_i}$ is the momentum in the deforming frame, in the overdamped regime, force balance on particle i can schematically be written as

$$\frac{\boldsymbol{p_i}(t)}{\tau_d} \approx k \sum_{\langle j|i \rangle} \left(\boldsymbol{u}_j(t) - \boldsymbol{u}_i(t) \right), \tag{16.10}$$

where the sum runs over the neighbours j of i, k is a typical stiffness, *i.e.*, the order of magnitude of the relevant Hessian components $\partial^2 V / \partial \boldsymbol{r_i} \partial \boldsymbol{r_j}$, and the $\boldsymbol{u}_j$'s are the displacements with respect to an equilibrium configuration. Let us now introduce a continuous, coarse-grained displacement field $\boldsymbol{u}(\boldsymbol{r}; t)$ and a typical interparticle distance a_0, and substitute the former into Eq. 16.10:

$$\frac{m}{\tau} \frac{\partial \boldsymbol{u}}{\partial t} \approx k a_0^2 \nabla^2 \boldsymbol{u}.$$

In this regime of negligible inertia, we thus obtain a diffusive equation for the particle displacements, consistently with the MD observations.

Very crudely, the DPD equation of motion is approximated by

$$\begin{aligned} m\ddot{\boldsymbol{u}} &\approx \tilde{\zeta} \sum_{\langle j|i \rangle} \left(\dot{\boldsymbol{u}}_j(t) - \dot{\boldsymbol{u}}_i(t) \right) + k \sum_{\langle j|i \rangle} \left(\boldsymbol{u}_j(t) - \boldsymbol{u}_i(t) \right) \\ m\ddot{\boldsymbol{u}} &\approx \tilde{\zeta} a_0^2 \nabla^2 \dot{\boldsymbol{u}} + k a_0^2 \nabla^2 \boldsymbol{u}, \end{aligned} \tag{16.11}$$

where $\tilde{\zeta} \equiv \zeta w^2 \left(a_0 \right)$.

Equation 16.11 is a diffusion equation (on $\dot{\boldsymbol{u}}$) *only if* the elastic force is negligible, which will not be the case in practice. This may explain why we have not observed a diffusive regime in the simulations. (More generally, Eq. 16.11 can be solved with a space-time Fourier transform, or a joint Laplace-Fourier transform).

17

CORRELATIONS BETWEEN PLASTIC EVENTS: A PRELIMINARY REVISITATION USING THE FE-BASED APPROACH

Chapter 16 has provided evidence that the Finite Element (FE) method satisfactorily describes the elastic response of a model glassy material and properly accounts for the heterogeneity-induced fluctuations with respect to the average response. It behoves us now to test the FE-based elastoplastic model in a situation of flow and to compare it to atomistic simulations. Will the spatiotemporal correlations that it predicts better match those measured in Molecular Dynamics (MD) than the Fourier Transform-based model?

This chapter is but a preliminary study of these important aspects. The comparison between FE and MD, in particular, is still inchoate.

17.1 MD SIMULATIONS WITH DISSIPATIVE PARTICLE DYNAMICS

The MD simulations were performed by Prof. Joerg Rottler.

Let us first present some results of MD simulations with a Dissipative Particle Dynamics (DPD) thermostat. The athermal Lennard-Jones glass under study has already been presented (see Section 14.1.1), and details of the DPD scheme and of its advantages can be found in Section 16.1. The damping coefficient ζ is set to 1 here.

17.1.1 *Flow curve*

The DPD flow curve (*not shown*) is very similar to that obtained with a mean-field dissipation scheme, with a Langevin damping time $\tau_d = 1$, except that the DPD yield stress is slightly lower.

17.1.2 *Plastic correlations*

As in Chapter 14, plastic rearrangements are detected with the $D^2_{\min}$ observable, with a time resolution (see Eq. 14.4) $\delta t = 4\tau_{LJ}$, where τ_{LJ} is the Lennard-Jones time unit.

Let us recall the expression of the plastic correlation function $\mathcal{C}_2(\Delta \boldsymbol{r}, \Delta t)$ from Section 14.2.4:

$$\mathcal{C}_2(\Delta \boldsymbol{r}, \Delta t) \equiv \alpha \left(\left\langle \overline{D^2_{\min}(\boldsymbol{r}, t)\, D^2_{\min}(\boldsymbol{r} + \Delta \boldsymbol{r}, t + \Delta t)} \right\rangle - \left\langle \overline{D^2_{\min}(\boldsymbol{r}, t)} \cdot \overline{D^2_{\min}(\boldsymbol{r}, t + \Delta t)} \right\rangle \right),$$

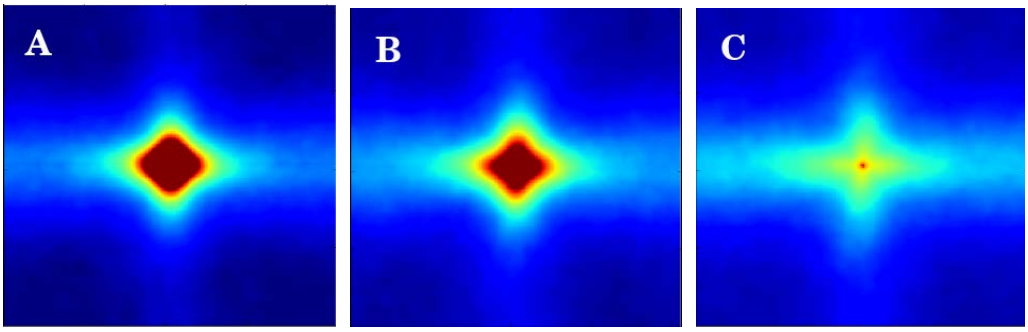

Figure 17.1: Colour maps of the plastic correlator $\mathcal{C}_2$ measured in DPD-MD simulations at $\dot{\gamma} = 10^{-4}$ and $\zeta = 1$ for time lags (*A*) $\Delta t = 0$, (*B*) $\Delta t = 8$, (*C*) $\Delta t = 20$. Dark blue regions are anticorrelated, while dark red ones are strongly correlated.

where $\alpha \equiv \left[\left\langle \overline{(D^2_{\min}(\boldsymbol{r},t))^2} \right\rangle - \left\langle \overline{(D^2_{\min}(\boldsymbol{r},t))}^2 \right\rangle \right]^{-1}$.

Colour maps of the plastic correlator are shown in Fig. 17.1 at three time lags, at an applied shear rate $\dot{\gamma} = 10^{-4}$. As expected from the findings of Varnik et al. [2014], spatial correlations appear to be more extended than with the mean-field damping scheme, judging by the comparison of Fig. 17.1 with Fig. 14.7. In addition, the "instantaneous" correlations at $\Delta t = 0$ are already spatially extended, and apparently more than the shear wave propagation during either δt or the duration of a rearrangement would allow. This suggests that $\mathcal{C}_2\,(\Delta \boldsymbol{r}, \Delta t = 0)$ does not merely reflect the causal links between two plastic events, but, above all, the spatial organisation of the flow. In other words, instead of being causally related, the plastic events that are correlated *via* $\mathcal{C}_2$ may have been triggered by the same (past) plastic event(s).

17.2 PRESENTATION OF THE ELASTOPLASTIC MODEL

We now turn to the elastoplastic model.

17.2.1 *Elastic properties*

As in Chapter 16, each elastoplastic block is a macro-element made of four adjacent finite elements which share the same elastic constants. Regarding these elastic properties, we study an elastically heterogeneous system with isotropic blocks: this is the "het. iso." model in the terminology of Fig. 16.1, except that we have chosen a slightly broader distribution of shear moduli (standard deviation of 7 instead of 5.3), because the fluctuations in the elastic response of het. iso. observed in Chapter 16 were slightly smaller than the MD fluctuations.

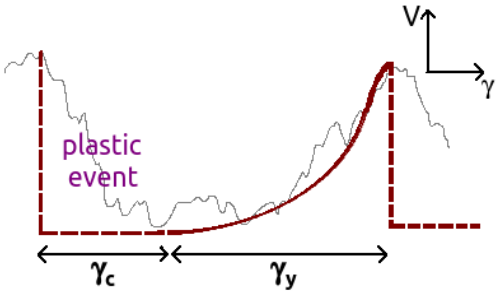

Figure 17.2: Mesoscopic PEL basis of the dynamical rules of the model. (*Thin black lines*) Sketch of a complex mesoscopic PEL, inspired from Fig. 1.2a. (*Thick brown lines*) Simplified PEL view used to establish the model rules. Dashed lines indicate plastic events, during which the *internal* elastic stress of the region is supposed to vanish; the event ends when the cumulated plastic strain reaches γ_c. Solid lines represent the elastic loading periods, associated with a yield strain γ_y.

17.2.2 *Dynamical rules*

The dynamical rules are closely connected to those of the refined athermal model presented in Section 9.3, but they are actually easier to explain within the present framework. The mesoscopic PEL perspective on which they are based is depicted in Fig. 17.2.

The loading phase is still described by linear elasticity, but the elastic blocks now also have a finite viscosity η and a finite density ρ [1] (see Eq. 15.5). A block (i,j) yields (becomes plastic) as soon as its maximal shear strain

$$\|2\dot{\boldsymbol{\epsilon}}\| \equiv \sqrt{\left[\epsilon_{xx}(i,j)-\epsilon_{yy}(i,j)\right]^2+\left[2\epsilon_{xy}(i,j)\right]^2}$$

exceeds the local yield strain γ_y. We choose an exponential distribution of yield strains, with no cut-off, *viz.*,

$$P(\gamma_y) \propto e^{-\gamma_y/\langle\gamma_y\rangle}. \tag{17.1}$$

To match the macroscopic value of the yield strain, of order 5-10%, $\langle\gamma_y\rangle$ is set to 0.05. The exponential distribution of *yield strains* of Eq. 17.1 differs from the exponential distribution of *energy barriers* in the refined model of Section 9.3; the change has only been prompted by our desire to use similar distributions for the yield strains and the plastic strains (see below) and it may be reconsidered in the future.

In the plastic regime, the internal elastic stress is dominated by the dissipative stress (which opposes the external stress deforming the region). Therefore, we neglect the former and set the shear modulus of the plastic block to zero, *i.e.*, $\mu_1 = \mu_2 = 0$ in plastic blocks, so that a plastic region is only subject to viscous (and inertial) forces. A plastic event ends when the total strain cumulated in the

1. Nevertheless, the viscous forces and the inertial forces are expected to be subdominant in the elastic regime.

plastic phase, $\int \|2\dot{\epsilon}(t')\|\, dt'$, reaches γ_c. Since Fig. 14.4a in Chapter 14 tentatively suggested an exponential distribution of plastic strains in the MD system, γ_c is assumed exponentially distributed, *viz.*,

$$P(\gamma_c) \quad \propto \quad e^{-\gamma_c/\langle\gamma_c\rangle}.$$

The (unique) freely adjustable parameter of the model, the average plastic strain $\langle\gamma_c\rangle$, is taken to be 0.015. Following Section 16.2, the viscosity is set to $\eta = 0.726\,\zeta$, with ζ the MD damping coefficient, and the density ρ is set to 7.5 (per finite element).

This completes the presentation of the FE-based elastoplastic model.

17.3 FLOW SIMULATIONS WITH THE ELASTOPLASTIC MODEL

17.3.1 *Flow curve*

We simulate the elastoplastic model presented in Section 17.2.2 for a large damping coefficient $\zeta = 100$ (*i.e.*, $\eta = 72.6$) and obtain a Herschel-Bulkley flow curve, shown in Fig. 17.3, with an exponent around 0.60 (whose precise value, however, depends on the fitted window of shear rates). The dynamical rules that have been implemented may therefore suitably describe the overdamped regime. But, for the time being, the flow curve has not been quantitatively adjusted to the DPD-MD measurements.

On the other hand, the flow curves obtained for a lower damping coefficient, *e.g.*, $\zeta = 1$, look erratic, insofar as they are either decreasing with the shear rate or non-monotonic, contrary to their MD counterparts. The dynamical rules will therefore need to be refined to also account for the inertial regime.

I would like to add that postulating instantaneous, fully relaxing plastic events has not allowed me to recover the desired Herschel-Bulkley flow curve. This suggests that the competition between the driving timescale $\dot{\gamma}^{-1}$ and the signal propagation time in plastic event avalanches, namely $l(\dot{\gamma})/c_t$ (where $l(\dot{\gamma})$ is the typical avalanche size and c_t, the transverse sound velocity), alone does not suffice to explain the flow curve.

17.3.2 *Plastic event correlator*

Coming back to the overdamped case $\zeta = 1$ and considering an applied shear rate $\dot{\gamma} = 7 \cdot 10^{-4}$, the plastic event autocorrelation function, plotted in Fig. 17.5a, is indicative of rearrangements of duration $\Delta t \approx 1$, in accordance with the direct measurement of the mean plastic event duration.

Shifting the focus to spatial correlations, in Fig. 17.4 we present colour maps of the plastic correlator $\mathcal{C}_2(\Delta\boldsymbol{r}, \Delta t)$, defined in Eq. 14.5, at different time lags. These plots display a distinct quadrupolar symmetry.

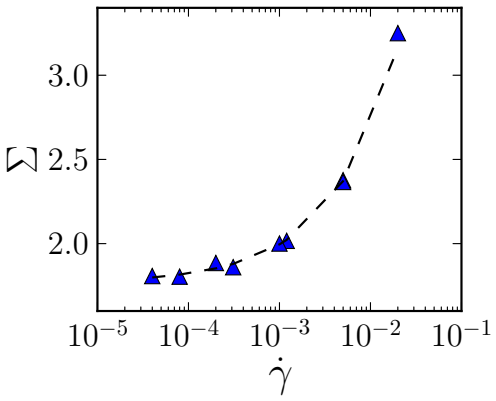

Figure 17.3: Flow curve measured with the FE-based model, for $\langle \gamma_y \rangle = 0.05$ and $\langle \gamma_c \rangle = 0.015$ (*blue triangles*). System size: 32×32 macro-elements. The dashed black line represents the Herschel-Bulkley equation $\Sigma = 1.8 + 14.7\dot{\gamma}^{0.60}$.

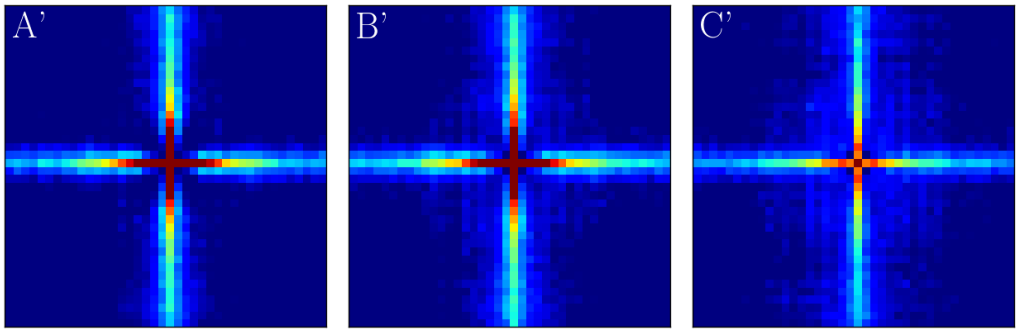

Figure 17.4: Colour maps of the plastic correlator $\mathcal{C}_2$ obtained with the FE-based model at $\dot{\gamma} = 7 \cdot 10^{-4}$ for $\langle \gamma_y \rangle = 0.05$ and $\langle \gamma_c \rangle = 0.015$. The time lags are ($A'$) $\Delta t = 0.5$, (B') $\Delta t = 20$, (C') $\Delta t = 60$. System size: 41×41 macro-elements. Dark blue regions are anticorrelated, while dark red ones are strongly correlated. Note that an upper threshold has been imposed; without it, short-range correlations, at the centre, completely outshine the rest of the picture.

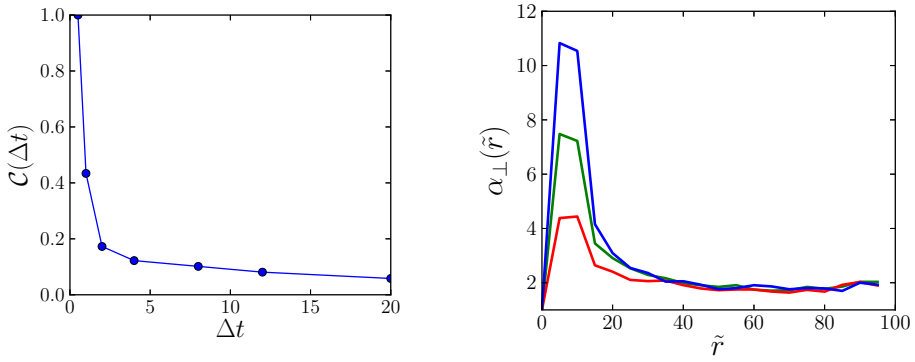

(a) Dependence of the plastic autocorrelation function $\mathcal{C}(\Delta t) \equiv \mathcal{C}_2(\mathbf{0}, \Delta t) / \mathcal{C}_2(\mathbf{0}, 0.5)$ on the time lag Δt.

(b) Directional probability enhancement factor $\alpha_\perp(\Delta r, \Delta t, \dot{\gamma})$ for time lags Δt =(*blue*) 1, (*green*) 8, (*red*) 16.

Figure 17.5: Plastic event correlations in the model for $\dot{\gamma} = 7 \cdot 10^{-4}$, $\langle \gamma_y \rangle = 0.05$ and $\langle \gamma_c \rangle = 0.015$.
(b) To facilitate the comparison with Fig. 14.5b, $\tilde{r}$ is expressed in units of σ_{AA} (as a reminder, the size of a finite element is $2.5\sigma_{AA}$).

Particularly strong correlations are observed on streamlines and perpendicularly to them, at short distances. This marked accumulation on thin lines is probably a spurious effect due to the symmetry of the mesh. It is reflected in the largely enhanced probability to have successive plastic events along streamlines or perpendicular lines, as compared to a diagonal alignment. The probability enhancement is quantified by the anisotropy ratio $\alpha_\perp$, defined in Eq. 14.6 and plotted in Fig. 17.5b. Apparently, the short-range plastic event correlations in the perpendicular direction are as overestimated in the FE implementation of the model as in the Fourier transform implementation. However, this similarity is somewhat misleading, because in the latter approach convection entailed the use of a "deformed" elastic propagator, which curtailed correlations in the perpendicular direction. Indeed, *along streamlines*, plastic correlations were even more overestimated,[2] whereas in the present approach plastic correlations are similar in both the streamwise and the crosswise directions ($\alpha_\parallel \approx \alpha_\perp$, *data not shown*).

Nevertheless, these short-range correlations are most likely still largely overestimated. This problem could be circumvented, without changing the underlying FE mesh, by introducing purely elastic defects in the grid, to break the symmetry of the *macro-element* lattice, as sketched in Fig. 17.6.

On the other hand, at larger distance, where $\alpha_\perp \approx 2$ (see Fig. 17.5b), the correlation results are not unrealistic, and a quantitative comparison between the FE-based model and DPD-MD simulations with regard to the intensity of the correlations will be very informative. This is ongoing work.

2. The parallel-*versus*-diagonal anisotropy ratio, $\alpha_\parallel$, was about six times as large as its perpendicular-*versus*-diagonal coutnerpart, $\alpha_\perp$, at short time lags and short distances.

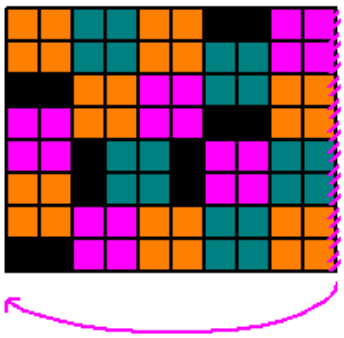

Figure 17.6: Introduction of purely elastic defects (in black) in the FE mesh in order to break the symmetry of the macro-element (represented as four adjacent element of the same colour) lattice. The defects would be purely elastic, with a shear modulus equal to $\langle \mu \rangle$.

Key Points of the Chapter

- In atomistic simulations, DPD generates longer correlations than the mean field dissipation scheme, in accordance with the findings of Ref. [Varnik et al., 2014].
- In the elastoplastic model, the dynamical rules controlling the alternation between the elastic loading phases and the viscous behaviour during plastic events yield a realistic flow curve in the overdamped regime. In the inertial regime, they need to be refined.
- The short-range plastic correlations are most likely still largely overestimated in the FE-based model, possibly because of the symmetry of the mesh.

18 FORCE CHAINS IN GRANULAR MEDIA

Throughout this thesis, the elastoplastic model has mostly been compared to concentrated emulsions and Lennard-Jones glass models, with some allusions to metallic glasses. Yet, in the introduction, we claimed that granular media also belong to the class of amorphous solids that can be handled in a common framework. Do elastoplastic models indeed describe the shear flow of (frictional) granular matter?

At first sight, we are forced to admit that these materials feature several unusual properties, compared to soft glassy materials. For instance, interparticular friction strongly impacts their rheology [Bi et al., 2011], and "force chains" (see below) are observed; moreover, the systems are prone to dilation under shear, an effect known as Reynolds' dilatancy [Reynolds, 1885].

This elliptic chapter is mainly aimed at opening up new perspectives with respect to the description of granular media by elastoplastic models. It suggests some novel ideas for the modelling of, *e.g.*, force chains and it highlights some unsettled questions. However, the detailed investigation that these matters certainly deserve is left for future work.

18.1 BASICS ABOUT SHEARED GRANULAR MEDIA

18.1.1 *Inertial and viscous numbers*

In Section 7.2.1, thanks to a discussion of the relevant timescales for the rheology, we clarified that, in the slow flow of athermal amorphous solids, the dependence of the stress on the shear rate $\dot{\gamma}$ originates in an interplay between the driving timescale $\dot{\gamma}^{-1}$ and (cascades of) localised rearrangements. In line with this idea, the authors of Refs. [da Cruz et al., 2005, Jop et al., 2006, Boyer et al., 2011] provided convincing experimental and numerical evidence that the ratio of the rearrangement time and the inverse shear rate is the correct adimensional number to describe the flow. In dry granular matter, this ratio is the inertial number

$$I \equiv \dot{\gamma} a_0 \sqrt{\frac{\rho}{p}},$$

where a_0 is the grain diameter, ρ is the density of the material, and p is the confining pressure, whereas in granular suspensions, it is called the viscous number and it reads

$$I_v \equiv \dot{\gamma} \frac{\eta_f}{p},$$

where η_f is the viscosity of the suspension fluid.

In both cases, the effective friction coefficients $\mu \equiv \Sigma/p$, where Σ is the shear stress and p is the pressure, collapse onto a master curve $\mu = f(I)$ (or $\mu = f(I_v)$) as a function of the inertial (or viscous) number, for diverse confining pressures and diverse restitution coefficients. This collapse notably indicates that experiments at constant applied pressure are easier to interpret than experiments performed at constant volume, the difference between the two being connected with Reynolds' dilatancy effect.

18.1.2 *Friction and force chains*

In order to dig underneath the macroscopic surface properties, Majmudar and Behringer [2005] used a two-dimensional (frictional) granular system made of photoelastic disks. They were thus able to image the spatial distribution of stresses in the material and observed linear filaments of grains connected by strong contacts (see Fig. 18.1), *i.e.*, contacts at which large forces are exerted, standing out of a background of weaker contacts. These so called force chains are isotropically oriented on average if the system is isotropically compressed. But, under shear, they are mainly aligned in the compressional direction and get visibly longer.

As had already been predicted theoretically by Cates et al. [1998], due to these oriented force chains, the material can resist shear in a particular direction. For the system to flow (in that direction), the chains must rupture. The buckling process at the origin of force chain failure was evidenced and analysed by Tordesillas et al. [2012].

Further evidence of the prominent role of force chains for the rheology comes from Azéma and Radjaï [2014]'s measurements of the local stress components in a three-dimensional Taylor-Couette flow. These researchers found that "contact anisotropy is the principal microstructural cause of the increase of effective friction" with the inertial number. In addition, Bi et al. [2011] showed that initially unjammed systems could jam through the application of shear. Jamming then coincides with the percolation of a network of force chains throughout the system.

18.1.3 *Gravity*

Gravity is another aspect that has been neglected so far in elastoplastic models. Its role is brought to the forefront in free-surface granular flows along inclined planes. Micro-gravity experiments are also particularly suitable to reveal the impact of granity; Murdoch et al. [2013] showed that secondary flows in dense sheared granular materials are suppressed in micro-gravity conditions, compared to high-gravity conditions.

To model gravity in the elastoplastic framework, body forces can be applied at the nodes of the FE mesh. Nevertheless, this will have very limited impact, *unless* we introduce some dependence of the shear moduli on the isotropic pressure $p \equiv \frac{\sigma_{xx}+\sigma_{yy}}{2}$, because these two elements are so far decoupled. For instance, imposing

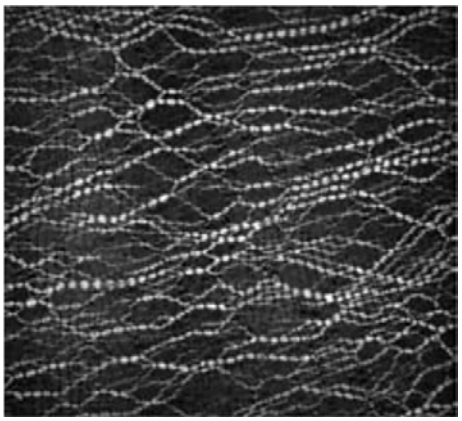

Figure 18.1: Observation of elongated force chains in sheared granular matter by means of photoelastic disks. Image taken from Ref. [Majmudar and Behringer, 2005].

that the shear modulus μ should grow linearly with p, *viz.*, $\mu \propto p$, while keeping the yield strain criterion for the onset of local plasticity, essentially results in the traditional Mohr-Coulomb criterion for cohensionless materials, whereby the sample fails when the ratio Σ/Σ_n (*i.e.*, the maximal shear stress divided by the normal stress Σ_n) exceeds a critical value $\tan(\phi)$, where ϕ is the Mohr-Coulomb angle.

18.2 How to model force chains in the elasto-plastic framework?

The main idea underlying the project emerged from a discussion with Prof. Mike Cates.

18.2.1 *"Shear polarisation"*

Can the particularly anisotropic force chains be described in the elastoplastic framework at minimal cost?

Our premise is that stress-carrying force chains are due to the anisotropic contacts, in excess in the compressional direction. Since these chains resist further compression in that direction, the local elastic properties must be coupled to the fabric, the latter being here amalgamated with the local deformation $\boldsymbol{\epsilon}$. Leaving aside isotropic contraction or dilation, we focus on the deviatoric part of $\boldsymbol{\epsilon}$ and call θ_ϵ the rotated frame in which $\boldsymbol{\epsilon}$ is diagonal, *i.e*, in which

$$\begin{pmatrix} \|\boldsymbol{\epsilon}\| & 0 \\ 0 & -\|\boldsymbol{\epsilon}\| \end{pmatrix}.$$

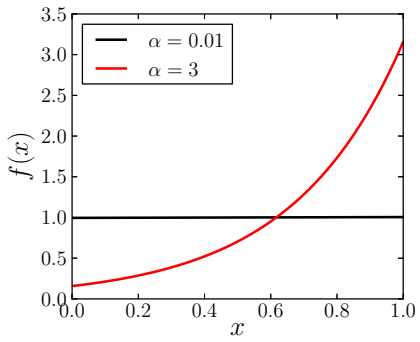

Figure 18.2: Anisotropy function $f(x) = \frac{\alpha}{e^\alpha - 1} e^{\alpha x}$ for two values of α, as indicated in the legend.

Recalling from Chapter 16 that the local stiffness tensor $\mathbf{C}$ is fully determined by a (constant, here) bulk modulus K, a weak shear modulus μ_1 and a strong shear modulus μ_2, in addition to the angle θ associated with μ_1, we postulate that the principal directions of the deformation tensor and of the stiffness tensor coincide, *i.e.*, $\theta_\epsilon = \theta$, and that

$$\begin{cases} \mu_1 &= \mu f\left(\frac{\|2\boldsymbol{\epsilon}\|}{\gamma_y}\right) \\ \mu_2 &= \mu f\left(0\right). \end{cases}$$

Here, μ is a material constant ($\mu = 18.81$) and f is an increasing function that controls how much stiffer a shear direction becomes if the region is strained in that direction. We posit

$$f\left(x\right) \equiv \frac{\alpha}{e^\alpha - 1} e^{\alpha x},$$

where α is the "shear polarisability" of the material. The prefactor $\alpha/(e^\alpha - 1)$ was chosen so that $\int_0^1 f(x)dx$ is independent of α.

We will study two different shear polarisabilities: $\alpha = 0.01$ and $\alpha = 3.0$. The dependence of the shear anisotropy function f on the rescaled deformation x is plotted in Fig. 18.2 for these two values. Clearly, for $\alpha = 0.01$, blocks are always quasi-isotropic, whereas marked anisotropy is observed for $\alpha = 3.0$ when the block is deformed ($x > 0$).

Note that linear elasticity imposes that infinitesimal deformations $\pm\delta\boldsymbol{\epsilon}$ produce the same stress increment, in magnitude, regardless of the sign (+ or -) of the deformation. Nevertheless, the effects of these opposite deformations do clearly differ: the one will reduce $\|\boldsymbol{\epsilon}\|$ and relax the block anisotropy μ_1/μ_2, while the other will further compress the block in one direction and further enhance the local anisotropy.

18.2.2 *Dynamical rules and model parameters*

We use dynamical rules that are similar to those described in Section 17.2.2, except that the distributions of plastic strains γ_c and yield strains γ_y are modified. (As a reminder, γ_c is the strain that needs to be cumulated during plasticity before elasticity is recovered.)

More precisely, the yield strain γ_y is normally distributed around $\langle \gamma_y \rangle = 0.1$, with standard deviation 0.05, while γ_c is set as a constant, *viz.*, $\gamma_c = \langle \gamma_y \rangle = 0.1$. In order to avoid numerical instabilities, a lower cut-off $\gamma_y^{\mathrm{cut-off}} = 0.01 \ll \langle \gamma_y \rangle$ is introduced in the distribution of γ_y.

For convenience, we still consider the overdamped regime, with viscosity $\eta = 72.6$, corresponding to a DPD damping coefficient $\zeta = 100$ (see Chapter 16). The density remains equal to 7.5 (in FE units).

18.3 PRELIMINARY RESULTS

18.3.1 *General observations*

A portion of the stress *versus* strain curve of a system with high shear polarisability, $\alpha = 3$, at very low shear rate $\dot{\gamma} = 10^{-4}$, is shown in Fig. 18.3a. At the strain positions indicated by the letters "a", "b", and "c" on the curve, we extract the instantaneous elastic configurations of the system and draw them in Fig. 18.4 by means of a colour map representing the local anisotropy ratio μ_1/μ_2 and short lines indicating the local compressional direction in each block. Similar colour maps are drawn at a somewhat higher shear rate, $\dot{\gamma} = 5 \cdot 10^{-3}$ in Fig. 18.5, whereas in Fig. 18.6 we show results for an almost isotropic system, characterised by $\alpha = 0.01$, at $\dot{\gamma} = 10^{-4}$. Biperiodic boundary conditions were used.

As expected, the density of plastic blocks increases with the shear rate, and anisotropy ratios are much higher in the highly polarisable material ($\alpha = 3$) than in its quasi-isotropic counterpart. Besides, in the vast majority of blocks, the *local* compressional direction is aligned with the compressional direction of the *macroscopic* shear, although this is perceptibly less true for the low-polarisability material.

These results are clearly very preliminary. They would deserve to be analysed in much greater detail, and it is still unclear whether the considered systems (or analogous ones with different parameters) exhibit linear groups of particularly strong blocks ($\mu_1 \gg \mu_2$) similar to force chains in granular media. A careful study of the influence of the shear polarisability α on the rheology would also be of great interest.

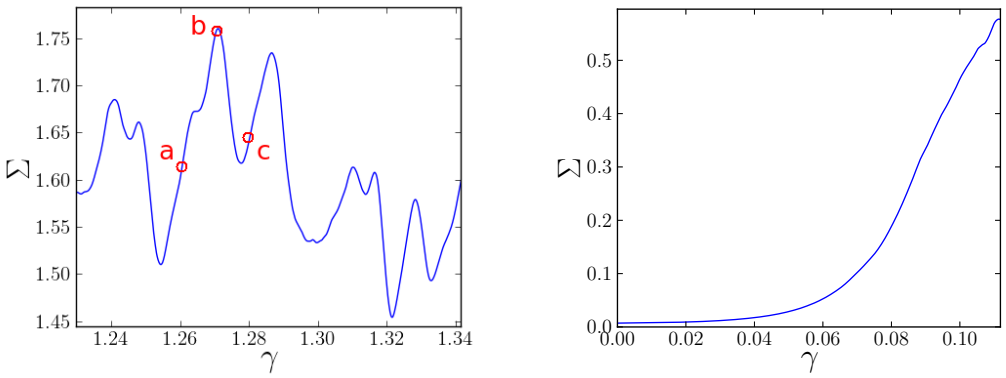

(a) $\alpha = 3$ (zoom). (b) $\alpha = 10$.

Figure 18.3: Stress *versus* strain curves for shear polarisable materials at an applied shear rate $\dot{\gamma} = 10^{-4}$. Indicated in Subfigure (a) are the strains (a, b, c) at which the snapshots of Fig. 18.4 were taken.
The systems consist of 24×24 macro-elements.

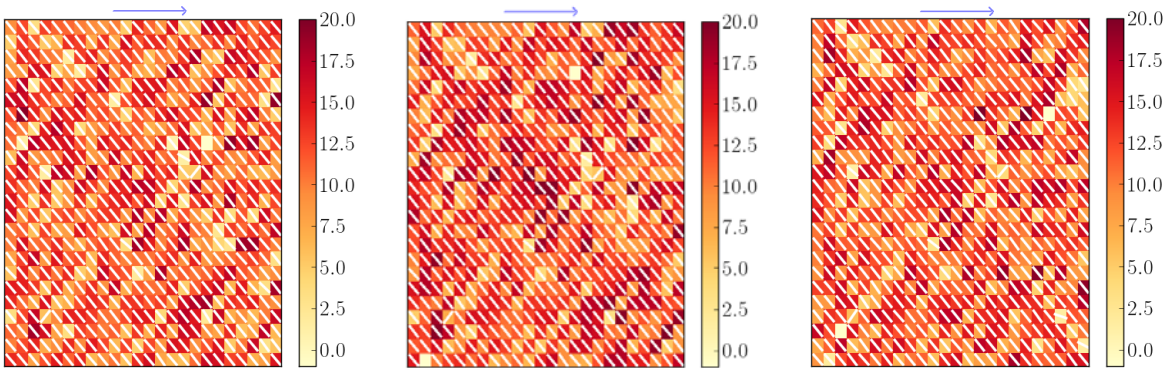

(a) $\gamma = 1.26$ (b) $\gamma = 1.27$ (c) $\gamma = 1.28$

Figure 18.4: Snapshots of the instantaneous configurations of the system at the strains indicated in Fig. 18.3a, for $\alpha = 3$ and $\dot{\gamma} = 10^{-4}$. The colours represent the local anisotropy ratio μ_1/μ_2, and the white line in each block indicates the compressional direction of the block, *i.e.*, the strong direction associated with μ_1. Blocks undergoing a plastic event are depicted in light yellow, without white line.

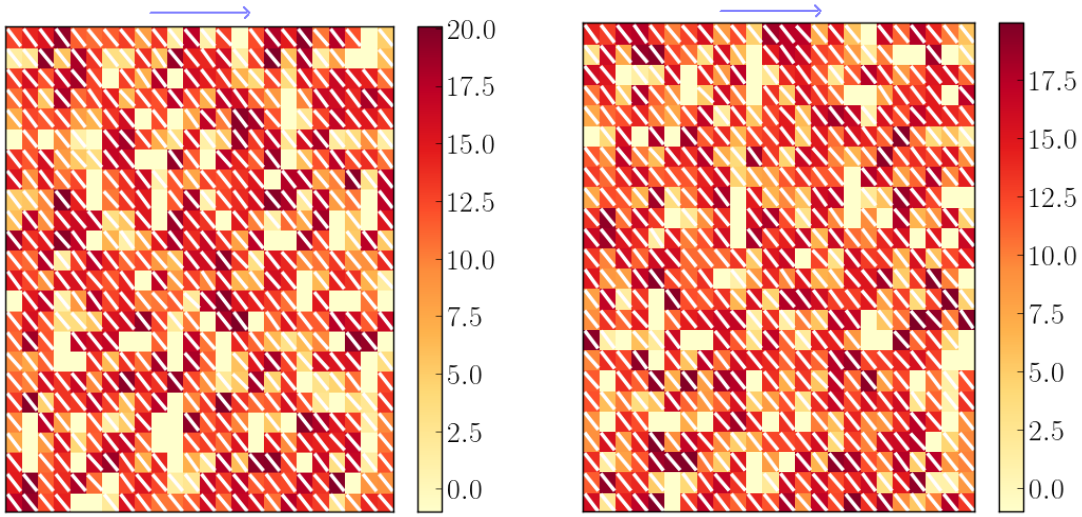

(a) $\gamma = 3.95$ (b) $\gamma = 3.4$

Figure 18.5: Snapshots of instantaneous configurations of the system, for $\alpha = 3$ and at an applied shear rate $\dot{\gamma} = 5 \cdot 10^{-3}$. Refer to Fig. 18.4 for the caption.

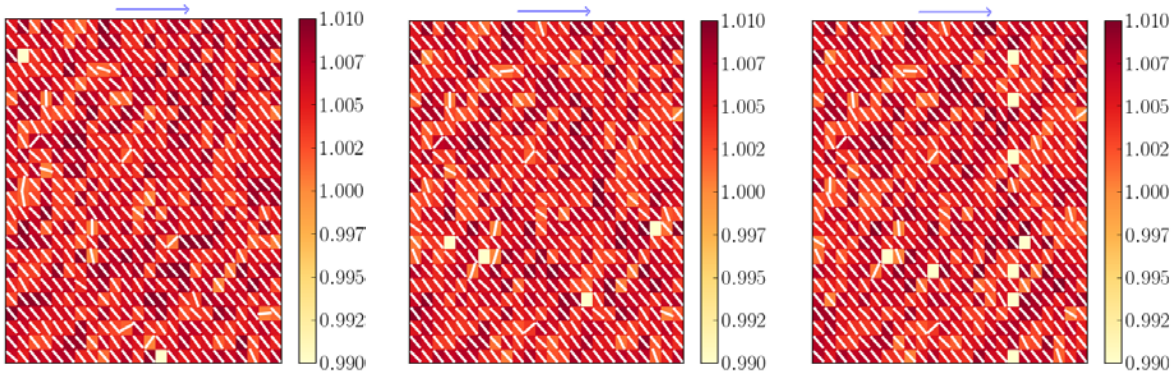

(a) $\gamma = 1.26$ (b) $\gamma = 1.27$ (c) $\gamma = 1.28$

Figure 18.6: Snapshots of instantaneous configurations of the system, for a tiny shear polarisability $\alpha = 0.01$, at $\dot{\gamma} = 10^{-4}$. Refer to Fig. 18.4 for the caption.

18.3.2 *Shear-jamming?*

Figure 18.3b presents the stress *versus* strain curve of a material with very high shear polarisability, $\alpha = 10$. It displays an effect akin to the shear-jamming phenomenon reported by Bi et al. [2011], insofar as the effective shear modulus of the material, which is almost zero initially, grows dramatically when shear is applied, so that the material apparently solidifies at $\gamma \approx 0.05$. Within the model, the solidification simply originates in the increase of the shear modulus μ_1 with increasing block compression in the macroscopic shear direction. The response of the material to shear in other directions is still pending.

18.4 SOME OPEN QUESTIONS

Open Questions

- Can the emergence and failure of individual force chains be observed in our model?
- Very recently, Le Bouil et al. [2014] reported on an experimental study of the homogeneous biaxial compression of a packing of glass beads, probed with dynamic light scattering. *Before* global failure of the material, *i.e.*, before the appearance of macroscopic shear bands, they observed a microstructure made of correlated plastic events, *i.e.*, in their terminology, transient micro-shear bands. Particularly puzzling is the fact that, while the transient micro-shear bands are oriented at an angle which is compatible with the directions of maximal redistributed stress in an Eshelby approach, the final macroscopic shear band is oriented at a *different* angle, close to the Mohr-Coulomb angle. This puzzle remains unsolved.

CLOSING WORDS

Contrary to the case of simple fluids, a finite stress is required to initiate the flow of amorphous solids, a broad class of materials ranging from bulk metallic glasses to foams and dense emulsions. Their solidity at rest, combined with the absence of ordered structure, and therefore of easily identifiable defects, has elicited the study of their rheology within a common framework.

In a first approach, the liquid regime is taken as a starting point. The mode-coupling theory describes the emergence of rigidity when the temperature declines or the density increases. Recently, the theory has been extended to situations of homogeneous flow. Since the flow becomes strongly inhomogeneous deeper in the solid phase, we have investigated to what extent heterogeneities can be accommodated within this framework. In particular, the physically expected advection term, which was absent in the homogeneous system, has been recovered in the equations, and we have derived a generic equation for the evolution of density fluctuations in the presence of heterogeneities. On the basis of a schematic constitutive equation, we have studied the linear stability of the flow of glassy materials in curved geometry and shown that, in this simple description, shear-thinning tends to suppress elastic instability.

At low temperatures, the flow consists of periods of elastic deformation interspersed with localised rearrangements of particles, called plastic events, that induce long-range elastic deformations and can thereby trigger new plastic events. This scenario is the cornerstone of another approach, rooted in the solid regime, namely, elastoplastic modelling.

A first aspect of my work has consisted in tightening the connection between the building blocks of elastoplastic models and the physical processes at play in reality. To this purpose, I have deepened the existing Continuum Mechanics description of plastic events, on the one hand, and endeavoured to root the dynamical rules of the model in a (very schematic) Potential Energy Landscape perspective, on the other hand.

Besides, various properties of the flow have been studied with the help of numerical simulations of these models.

With regard to the flow curve, general arguments indicate that it results from an interplay between the external drive and the (cascades of) localised rearrangements. By incorporating this interplay in the model, the desired Herschel-Bulkley relation between the shear stress and the strain rate, with an exponent close to 0.5, was recovered.

It is not rare, however, that the experimental flow curve deviates from the strictly monotonic Herschel-Bulkley behaviour at low shear rates. This is generally the hallmark of shear localisation. In different variants of the elastoplastic model, this phenomenon is observed. More precisely, this occurs whenever

blocks are durably weakened by plastic events. We have therefore proposed to subsume the diverse mechanisms leading to shear localisation under the overarching concept of long healing times.

Even when the flow is macroscopically homogeneous, strong correlations persist at low shear rates and low temperatures. We have shown that the scalings of these correlations are not universal in coarse-grained models, despite the existence of a broad class of correlation lengths that scale with the spacing between homogeneously-distributed simulataneous plastic events, *i.e.*, with $\dot{\gamma}^{-1/d}$ in the shear-dominated regime in d dimensions. In this respect as in many others, the extension from a scalar description of the stress to a tensorial one hardly makes any difference.

The aspiration to a direct comparison of model results with experimental data has led us to study flows through microchannels. Some striking manifestations of spatial cooperativity were recently observed in experiments on dense emulsions in this geometry, for instance deviations from bulk rheology and shear rate fluctuations in the seemingly quiescent plug in the centre of the channel. Part of these effects are rationalised by the existing coupling between streamlines subject to different shear stresses in that geometry, and captured by the model, at least semi-quantitatively. On the other hand, we pointed to another origin for the large deviations from bulk rheology that are observed in microchannels with rough walls. We hypothesised that they were caused by the mechanical noise generated by bumps of the emulsion droplets into wall asperities, in the (attested) presence of wall slip.

Further material for comparison came in the form of Molecular Dynamics simulations at zero temperature. While the agreement between these atomistic simulations and the elastoplastic description is good as far as the macroscopic rheology and the statistics of individual events are concerned, marked discrepancies are observed in the spatiotemporal correlations between plastic events, although their (quadrupolar) symmetry is well captured by the elastic propagator used in the model. The discrepancies are the magnitude of the correlations, which is vastly overestimated in the model, and the gradual growth of their spatial extent with the time lag, which goes amiss in the model.

To remedy these deficiencies, we have introduced a much more flexible implementation based on a simplified Finite Element routine. This notably allows us to better account for structural disorder in the material and to explictly include inertia in the model. We have gathered evidence, by comparison with Molecular Dynamics simulations, that the elastic response to a shear transformation is now faithfully described in our model, in terms of both mean response and fluctuations. The study of the spatiotemporal correlations between plastic events in this new framework is ongoing, as are the efforts to reproduce the force chains observed in granular media and, thus, adapt elastoplastic models to the description of these systems.

CONCLUSION

À la différence des liquides simples, les solides amorphes, une vaste catégorie de matériaux allant des verres métalliques aux mousses et aux émulsions concentrées, ne se mettent à s'écouler qu'au-delà d'une contrainte finie. Malgré leur diversité, la solidité au repos de ces matériaux, conjuguée à l'absence de structure ordonnée et donc de défauts aisément identifiables, permet d'étudier certains aspects de leur rhéologie dans un cadre commun.

En premier lieu, le régime liquide a servi de point de départ. La théorie du couplage de modes décrit alors l'émergence de la rigidité lorsque la température décroît ou lorsque la densité augmente. Cette théorie a récemment été étendue à la prise en compte d'écoulements *homogènes*. Étant donné que l'écoulement devient fortement hétérogène à basse température ou à très haute densité, comme cela a été établi expérimentalement, nous avons étudié dans quelle mesure ce cadre théorique se prête au traitement des inhomogénéités. En particulier, nous avons rétabli le terme d'advection dans les équations, lequel était appelé par des considérations physiques simples, mais jusqu'à présent absent du formalisme, et nous avons obtenu une équation générale pour l'évolution de fluctuations de densité en présence d'hétérogénéités. À l'aide d'une équation constitutive schématique, nous avons ensuite analysé la stabilité linéaire de l'écoulement de matériaux vitreux dans une géométrie courbée et montré que, dans le cadre de cette description, la rhéo-fluidification du matériau tend à étouffer le développement d'une instabilité élastique.

À basse température, l'écoulement se compose de phases de déformation élastique entrecoupées de réarrangements de particules, brusques et localisés, appelés événements plastiques et interagissant par le biais de la déformation élastique de longue portée qu'ils génèrent dans le milieu. Ce scénario sert de pierre angulaire à l'approche élasto-plastique, qui a donc pour point d'ancrage le régime solide.

En second lieu, nous avons cherché à renforcer le lien entre les éléments constitutifs de modèles élasto-plastiques et les processus physiques à l'œuvre dans la nature. À cette fin, nous avons, d'une part, approfondi la description des événements plastiques par une approche de type mécanique du milieu continu et, d'autre part, tenté d'ancrer les règles dynamiques du modèle dans un paysage d'énergie potentielle, quand bien même fort simplifié.

Diverses propriétés de l'écoulement ont ensuite été étudiées à l'aide de simulations numériques de tels modèles.

En ce qui concerne la courbe d'écoulement, sur la base d'arguments généraux, on peut montrer qu'elle provient d'une compétition entre le cisaillement macroscopique imposé et les (cascades de) réarrangements locaux. L'inclusion d'un

tel mécanisme de compétition dans la modélisation aboutit à une relation entre contrainte et taux de cisaillement de type Herschel-Bulkley, avec un exposant proche de 0.5, ce qui est conforme à des résultats expérimentaux et numériques sur des systèmes très variés.

Cependant, il n'est pas rare que la courbe d'écoulement expérimentale dévie de cette relation et perde sa stricte monotonie à faibles taux de cisaillement. Cela signale généralement la présence de cisaillement localisé. Dans plusieurs variantes de modèles élasto-plastiques, ce phénomène de localisation du cisaillement est observé. Plus précisément, il se produit dès lors que les blocs sont durablement endommagés par des événements plastiques. Nous avons donc proposé de résumer les différents mécanismes microscopiques conduisant à la localisation du cisaillement par le concept général de temps de guérison longs.

Même quand le cisaillement n'est pas macroscopiquement localisé, il existe de fortes corrélations dans l'écoulement à faibles taux de cisaillement et basses températures. Nous avons établi que les lois d'échelle que suivent ces corrélations ne sont pas universelles pour tous les modèles mésoscopiques, en dépit de l'existence d'une importante classe de longueurs de corrélation qui varient comme la distance entre des événements plastiques simultanés qu'on suppose distribués de manière à peu près homogène, c'est-à-dire comme $\dot{\gamma}^{-1/d}$ dans le régime dominé par le cisaillement, en d dimensions. Dans ce cas comme dans bien d'autres, le passage d'une description scalaire à une description tensorielle n'a quasiment aucun effet visible.

Afin de comparer directement les résultats du modèle à des expériences, nous nous sommes intéressé à l'écoulement en microcanal. D'impressionnantes manifestations de coopérativité spatiale ont récemment été relatées dans le cadre d'expériences sur des émulsions confinées dans cette géométrie, à l'instar des déviations observées entre rhéologie locale et rhéologie macroscopique du matériau, ou encore des fluctuations de taux de cisaillement mesurées dans le bouchon au centre du conduit, malgré l'apparente inactivité de ce dernier. Ces effets s'expliquent en partie par le couplage à l'œuvre dans un micro-conduit entre des lignes d'écoulement sujettes à des contraintes différentes, ce que permet de décrire notre modèle, au moins semi-quantitativement. D'autre part, les larges déviations par rapport à la rhéologie macroscopique, observées dans des canaux à parois rugueuses, échappent selon nous à cette explication, et nous avons émis l'hypothèse qu'elles seraient dues au bruit mécanique généré par les collisions des gouttelettes avec les aspérités des parois, en la présence (expérimentalement attestée) de glissement pariétal.

Des simulations de dynamique moléculaire à température nulle ont fourni matière à une autre comparaison directe. Tandis que la rhéologie macroscopique et les statistiques des événements plastiques individuels témoignent d'un bon accord entre ces simulations atomistiques et la description élasto-plastique, les corrélations spatio-temporelles entre événements plastiques font l'objet de divergences marquées, même si leur symétrie (quadrupolaire) est bien reproduite par le propagateur élastique utilisé dans le modèle. Les divergences concernent l'amplitude des corrélations, largement surévaluée dans le modèle, et leur extension progressive dans l'espace, extension qui est instantanée dans le modèle.

Pour parer à ces inconvénients, nous nous sommes tourné vers une implémentation bien plus flexible, à partir d'une routine simplifiée d'Éléments Finis. Celle-ci permet de bien mieux rendre compte du désordre structurel au sein du matériau et d'inclure explicitement les effets inertiels. Nous avons établi, par comparaison avec des simulations de dynamique moléculaire, que la réponse élastique à une transformation de cisaillement localisée est alors (statistiquement) décrite avec précision, aussi bien en termes de moyenne que de fluctuations. L'étude des corrélations spatio-temporelles entré événements plastiques dans l'écoulement, dans ce nouveau cadre, est en cours de réalisation, ainsi que l'est la tentative de modéliser les chaînes de force dans les matériaux granulaires, et donc d'adapter la modélisation élasto-plastique à ce type de systèmes.

BIBLIOGRAPHY

A.C.T. Aarts. *Analysis of the Flow Instabilities in the Extrusion of Polymeric Melts*. PhD thesis, Eindhoven University of Technology, 1997.

G. Adam and J.H. Gibbs. On the temperature dependence of cooperative relaxation properties in glass-forming liquids. *The Journal of Chemical Physics*, 43(1): 139–146, 1965.

C.P. Amann and M. Fuchs. Transient stress evolution in repulsion and attraction dominated glasses. *arXiv preprint arXiv:1406.1042*, 2014.

C.P. Amann, M. Siebenbürger, M. Krüger, F. Weysser, M. Ballauff, and M. Fuchs. Overshoots in stress-strain curves: Colloid experiments and schematic mode coupling theory. *Journal of Rheology*, 57(1):149, 2013.

A. Amon, R. Bertoni, and J. Crassous. Experimental Investigation of Plastic Deformations Before Granular Avalanche. 2012a.

A. Amon, A. Bruand, J. Crassous, E. Clément, et al. Hot spots in an athermal system. *Physical Review Letters*, 108(13):135502, 2012b.

P.W. Anderson. More is different. *Science*, 177(4047):393–396, 1972.

B. Andreotti, J.-L. Barrat, and C. Heussinger. Shear flow of non-brownian suspensions close to jamming. *Physical Review Letters*, 109(10):105901, 2012.

J. Antonaglia, W.J. Wright, X. Gu, R.R. Byer, T.C. Hufnagel, M. LeBlanc, J.T. Uhl, and K.A. Dahmen. Bulk metallic glasses deform via slip avalanches. *Physical Review Letters*, 112:155501, 2014.

A.S. Argon and H.Y. Kuo. Plastic flow in a disordered bubble raft (an analog of a metallic glass). *Materials Science and Engineering*, 39(1):101–109, 1979.

E. Azéma and F. Radjaï. Internal structure of inertial granular flows. *Physical review letters*, 112(7):078001, 2014.

N. Bailey, J. Schiøtz, A. Lemaître, and K. Jacobsen. Avalanche Size Scaling in Sheared Three-Dimensional Amorphous Solid. *Physical Review Letters*, 98(9), 2007.

P. Bak, C. Tang, and K. Wiesenfeld. Self-organized criticality: An explanation of the 1/f noise. *Physical Review Letters*, 59(4):381–384, 1987.

M. Ballauff, J. M. Brader, S. U. Egelhaaf, M. Fuchs, J. Horbach, N. Koumakis, M. Krüger, M. Laurati, K. J. Mutch, G. Petekidis, M. Siebenbürger, T. Voigtmann, and J. Zausch. Residual Stresses in Glasses. *Physical Review Letters*, 110 (21):215701, 2013.

P. Ballesta, R. Besseling, L. Isa, G. Petekidis, and W.C.K. Poon. Slip and Flow of Hard-Sphere Colloidal Glasses. *Physical Review Letters*, 101(25), 2008.

P. Ballesta, G. Petekidis, L. Isa, W.C.K. Poon, and R. Besseling. Wall slip and flow of concentrated hard-sphere colloidal suspensions. *Journal of Rheology*, 56(5): 1005, 2012.

J.-C. Baret, D. Vandembroucq, and S. Roux. Extremal model for amorphous media plasticity. *Physical Review Letters*, 89(19):195506, 2002.

H.A. Barnes. A review of the slip (wall depletion) of polymer solutions, emulsions and particle suspensions in viscometers: its cause, character, and cure. *Journal of Non-Newtonian Fluid Mechanics*, 56(3):221–251, 1995.

J.-L. Barrat and L. Berthier. Fluctuation-dissipation relation in a sheared fluid. *Physical Review E*, 63(1):012503, 2000.

J.-L. Barrat and A. Lemaître. Heterogeneities in amorphous systems under shear. In L. Berthier, G. Biroli, J.-P. Bouchaud, L. Cipelletti, and W. van Saarloos, editors, *Dynamical heterogeneities in glasses, colloids, and granular media*. Oxford University Press, Oxford, 2011.

D. Barthès-Biesel. *Microhydrodynamique et fluides complexes*. Les Editions de l'Ecole Polytechnique, 2010. ISBN 9782730215725.

A. Basu, Y. Xu, T. Still, P.E. Arratia, Z. Zhang, K.N. Nordstrom, J.M. Rieser, J.P. Gollub, D.J. Durian, and A.G. Yodh. Rheology of soft colloids across the onset of rigidity: scaling behavior, thermal, and non-thermal responses. *Soft matter*, 10(17):3027–3035, 2014.

L. Bécu, S. Manneville, and A. Colin. Spatiotemporal Dynamics of Wormlike Micelles under Shear. *Physical Review Letters*, 93(1), 2004.

L. Bécu, P. Grondin, A. Colin, and S. Manneville. How does a concentrated emulsion flow? *Colloids and Surfaces A: Physicochemical and Engineering Aspects*, 263(1-3):146–152, 2005.

L. Bécu, S. Manneville, and A. Colin. Yielding and Flow in Adhesive and Non-adhesive Concentrated Emulsions. *Physical Review Letters*, 96(13), 2006.

R.P. Behringer, D. Bi, B. Chakraborty, S. Henkes, and R.R. Hartley. Why Do Granular Materials Stiffen with Shear Rate? Test of Novel Stress-Based Statistics. *Physical Review Letters*, 101(26):268301, 2008.

U. Bengtzelius, W. Gotze, and A. Sjolander. Dynamics of supercooled liquids and the glass transition. *Journal of Physics C: Solid State Physics*, 17(33):5915–5934, 1984.

R. Benzi, M. Sbragaglia, P. Perlekar, M. Bernaschi, S. Succi, and F. Toschi. Direct evidence of plastic events and dynamic heterogeneities in soft-glasses. *Soft Matter*, pages –, 2014.

L. Berthier and J.-L. Barrat. Nonequilibrium dynamics and fluctuation-dissipation relation in a sheared fluid. *The Journal of Chemical Physics*, 116 (14):6228, 2002a.

L. Berthier and J.-L. Barrat. Shearing a Glassy Material: Numerical Tests of Nonequilibrium Mode-Coupling Approaches and Experimental Proposals. *Physical Review Letters*, 89(9), 2002b.

L. Berthier, J.-L. Barrat, and J. Kurchan. A two-time-scale, two-temperature scenario for nonlinear rheology. *Physical Review E*, 61(5):5464–5472, 2000.

R. Besseling, L. Isa, E.R. Weeks, and W.C.K. Poon. Quantitative imaging of colloidal flows. *Advances in colloid and interface science*, 146(1-2):1–17, 2009.

R. Besseling, L. Isa, P. Ballesta, G. Petekidis, M.E. Cates, and W.C.K. Poon. Shear banding and flow-concentration coupling in colloidal glasses. *Physical Review Letters*, 105(26):268301, 2010.

D. Bi and Bu. Chakraborty. Rheology of granular materials: dynamics in a stress landscape. *Philosophical Transactions of the Royal Society A: Mathematical, Physical and Engineering Sciences*, 367(1909):5073–5090, 2009.

D. Bi, J. Zhang, B. Chakraborty, and R.P. Behringer. Jamming by shear. *Nature*, 480(7377):355–358, 2011.

A.-L. Biance, S. Cohen-Addad, and R. Höhler. Topological transition dynamics in a strained bubble cluster. *Soft Matter*, 5(23):4672, 2009.

K. Binder and W. Kob. *Glassy materials and disordered solids: An introduction to their statistical mechanics*. World Scientific, 2011.

L. Bocquet, E. Charlaix, S. Ciliberto, and J. Crassous. Moisture-induced ageing in granular media and the kinetics of capillary condensation. *Nature*, 396(6713): 735–737, 1998.

L. Bocquet, A. Colin, and A. Ajdari. Kinetic theory of plastic flow in soft glassy materials. *Physical Review Letters*, 103(3):036001, 2009.

J. Bokeloh, S.V. Divinski, G. Reglitz, and G. Wilde. Tracer measurements of atomic diffusion inside shear bands of a bulk metallic glass. *Physical Review Letters*, 107(23):235503, 2011.

J.-P. Bouchaud. Weak ergodicity breaking and aging in disordered systems. *Journal de Physique I*, 2(9):1705–1713, 1992.

J.-P. Bouchaud. Anomalous relaxation in complex systems: from stretched to compressed exponentials. *Anomalous Transport*, 2008.

Jean-Philippe Bouchaud, Alain Comtet, and Cécile Monthus. On a dynamical model of glasses. *Journal de Physique I*, 5(12):1521–1526, 1995.

E. Bouchbinder, J.S. Langer, and I. Procaccia. Athermal shear-transformation-zone theory of amorphous plastic deformation. i. basic principles. *Physical Review E*, 75(3):036107, 2007a.

E. Bouchbinder, J.S. Langer, and I. Procaccia. Athermal shear-transformation-zone theory of amorphous plastic deformation. ii. analysis of simulated amorphous silicon. *Physical Review E*, 75(3):036108, 2007b.

F. Boyer, É. Guazzelli, and O. Pouliquen. Unifying Suspension and Granular Rheology. *Physical Review Letters*, 107(18):188301, 2011.

J.M Brader, T. Voigtmann, M. Fuchs, R.G Larson, and M.E Cates. Glass rheology: From mode-coupling theory to a dynamical yield criterion. *Proceedings of the National Academy of Sciences of the United States of America*, 106(36):15186–91, 2009.

J.M. Brader, M.E. Cates, and M. Fuchs. First-principles constitutive equation for suspension rheology. *Physical Review E*, 86(2):021403, 2012.

L. Bragg and J.F. Nye. A dynamical model of a crystal structure. *Proceedings of the Royal Society of London. Series A. Mathematical and Physical Sciences*, 190 (1023):474–481, 1947.

Z. Budrikis and S. Zapperi. Avalanche localization and crossover scaling in amorphous plasticity. *Physical Review E*, 88(6):062403, 2013.

V.V. Bulatov and A.S. Argon. A stochastic model for continuum elasto-plastic behavior. I. Numerical approach and strain localization. *Modelling and Simulation in Materials Science and Engineering*, 2(2):167–184, 1994a.

V.V. Bulatov and A.S. Argon. A stochastic model for continuum elasto-plastic behavior. II. A study of the glass transition and structural relaxation. *Modelling and Simulation in Materials Science and Engineering*, 2(2):185–202, 1994b.

V.V. Bulatov and A.S. Argon. A stochastic model for continuum elasto-plastic behavior. III. Plasticity in ordered versus disordered solids. *Modelling and Simulation in Materials Science and Engineering*, 2(2):203–222, 1994c.

L. Bureau, T. Baumberger, and C. Caroli. Rheological aging and rejuvenation in solid friction contacts. *The European Physical Journal E*, 8(3):331–337, 2002.

D.M.A. Buzza, C.-Y.D. Lu, and M.E. Cates. Linear shear rheology of incompressible foams. *Journal de Physique II*, 5(1):37–52, 1995.

M.E. Cates, J. Wittmer, J.-P. Bouchaud, and P. Claudin. Jamming, Force Chains, and Fragile Matter. *Physical Review Letters*, 81(9):1841–1844, 1998.

J. Chattoraj and A. Lemaître. Elastic signature of flow events in supercooled liquids under shear. *Physical Review Letters*, 111(6):066001, 2013.

J. Chattoraj, C. Caroli, and A. Lemaître. Universal additive effect of temperature on the rheology of amorphous solids. *Physical Review Letters*, 105(26):266001, 2010.

J. Chattoraj, C. Caroli, and A. Lemaître. Robustness of avalanche dynamics in sheared amorphous solids as probed by transverse diffusion. *Physical Review E*, 84(1):011501, 2011.

P. Chaudhuri and J. Horbach. Onset of flow in a confined colloidal glass under an imposed shear stress. *Physical Review E*, 88(4):040301, 2013.

P. Chaudhuri, V. Mansard, A. Colin, and L. Bocquet. Dynamical Flow Arrest in Confined Gravity Driven Flows of Soft Jammed Particles. *Physical Review Letters*, 109(3), 2012.

K. Chen, P. Bak, and S. Obukhov. Self-organized criticality in a crack-propagation model of earthquakes. *Physical Review A*, 43(2):625–630, 1991.

X. Cheng, J.H McCoy, J.N. Israelachvili, and I. Cohen. Imaging the microscopic structure of shear thinning and thickening colloidal suspensions. *Science (New York, N.Y.)*, 333(6047):1276–9, 2011.

V. Chikkadi and P. Schall. Nonaffine measures of particle displacements in sheared colloidal glasses. *Physical Review E*, 85(3):031402, 2012.

V. Chikkadi, G. Wegdam, D. Bonn, B. Nienhuis, and P. Schall. Long-range strain correlations in sheared colloidal glasses. *Physical Review Letters*, 107(19):198303, 2011.

V. Chikkadi, S. Mandal, B. Nienhuis, D. Raabe, F. Varnik, and P. Schall. Shear-induced anisotropic decay of correlations in hard-sphere colloidal glasses. *EPL (Europhysics Letters)*, 100(5):56001, 2012.

M. Cloitre, R. Borrega, F. Monti, and L. Leibler. Glassy Dynamics and Flow Properties of Soft Colloidal Pastes. *Physical Review Letters*, 90(6):068303, 2003.

S. Cohen-Addad, H. Hoballah, and R. Höhler. Viscoelastic response of a coarsening foam. *Physical Review E*, 57(6):6897, 1998.

P. Coussot and G. Ovarlez. Physical origin of shear-banding in jammed systems. *The European physical journal. E, Soft matter*, 33(3):183–8, 2010.

L.F. Cugliandolo, J. Kurchan, and L. Peliti. Energy flow, partial equilibration, and effective temperatures in systems with slow dynamics. *Physical Review E*, 55(4):3898–3914, 1997.

F. da Cruz, S. Emam, M. Prochnow, J.-N. Roux, and F. Chevoir. Rheophysics of dense granular materials: Discrete simulation of plane shear flows. *Physical Review E*, 72(2), 2005.

K.A. Dahmen, Y. Ben-Zion, and J.T. Uhl. Micromechanical model for deformation in solids with universal predictions for stress-strain curves and slip avalanches. *Physical Review Letters*, 102(17):175501, 2009.

G. Debregeas, H. Tabuteau, and J.-M. Di Meglio. Deformation and flow of a two-dimensional foam under continuous shear. *Physical Review Letters*, 87(17): 178305, 2001.

N.D. Denkov, S. Tcholakova, K. Golemanov, K.P. Ananthpadmanabhan, and A. Lips. The role of surfactant type and bubble surface mobility in foam rheology. *Soft Matter*, 5(18):3389–3408, 2009.

T. Divoux, H. Gayvallet, and J.-C. Géminard. Creep motion of a granular pile induced by thermal cycling. *Physical Review Letters*, 101(14):148303, 2008.

T. Divoux, C. Barentin, and S. Manneville. From stress-induced fluidization processes to Herschel-Bulkley behaviour in simple yield stress fluids. *Soft Matter*, 7(18):8409, 2011a.

T. Divoux, C. Barentin, and S. Manneville. Stress overshoot in a simple yield stress fluid: An extensive study combining rheology and velocimetry. *Soft Matter*, 7(19):9335, 2011b.

T. Divoux, V. Grenard, and S. Manneville. Rheological hysteresis in soft glassy materials. *Physical Review Letters*, 110(1):018304, 2013.

B. Doliwa and A. Heuer. Energy barriers and activated dynamics in a supercooled lennard-jones liquid. *Physical Review E*, 67(3):031506, 2003.

S.F. Edwards and R.B.S. Oakeshott. Theory of powders. *Physica A: Statistical Mechanics and its Applications*, 157(3):1080–1090, 1989.

J.D. Eshelby. The Determination of the Elastic Field of an Ellipsoidal Inclusion, and Related Problems. *Proceedings of the Royal Society A: Mathematical, Physical and Engineering Sciences*, 241(1226):376–396, 1957.

H. Eyring. The activated complex and the absolute rate of chemical reactions. *Chemical Reviews*, 17(1):65–77, 1935.

M. Falk and J. Langer. Dynamics of viscoplastic deformation in amorphous solids. *Physical Review E*, 57(6):7192–7205, 1998.

M.A. Fardin, T. Divoux, M.A. Guedeau-Boudeville, I. Buchet-Maulien, J. Browaeys, G.H. McKinley, S. Manneville, and S. Lerouge. Shear-banding in surfactant wormlike micelles: elastic instabilities and wall slip. *Soft Matter*, 8(8):2535, 2012a.

M.A. Fardin, T.J. Ober, V. Grenard, T. Divoux, S. Manneville, G.H. McKinley, and S. Lerouge. Interplay between elastic instabilities and shear-banding: three categories of Taylor-Couette flows and beyond. *Soft Matter*, 2012b.

E.E. Ferrero, K. Martens, and J.-L. Barrat. Consequences of elasticity on thermally activated dynamics in yield stress materials: a mesoscopic approach. *In preparation*, 2014.

S. Fielding and P. Sollich. Observable dependence of fluctuation-dissipation relations and effective temperatures. *Physical Review Letters*, 88(5):050603, 2002.

S.M. Fielding, M.E. Cates, and P. Sollich. Shear banding, aging and noise dynamics in soft glassy materials. *Soft Matter*, 5(12):2378, 2009.

Samuel Forest. *Milieux continus généralisés et matériaux hétérogènes*. Presses des MINES, 2006.

M. Fortin and F. Brezzi. *Mixed and hybrid finite element methods*. Springer, 1991.

F. Frahsa, A.K. Bhattacharjee, J. Horbach, M. Fuchs, and T. Voigtmann. On the bauschinger effect in supercooled melts under shear: Results from mode coupling theory and molecular dynamics simulations. *The Journal of chemical physics*, 138(12):12A513, 2013.

J.M. Franco, C. Gallegos, and H.A. Barnes. On slip effects in steady-state flow measurements of oil-in-water food emulsions. *Journal of Food Engineering*, 36 (1):89–102, 1998.

S. Fritschi, M. Fuchs, and T. Voigtmann. Mode-coupling analysis of residual stresses in colloidal glasses. *Soft Matter*, 2014.

M. Fuchs and M.E. Cates. Theory of Nonlinear Rheology and Yielding of Dense Colloidal Suspensions. *Physical Review Letters*, 89(24), 2002.

M. Fuchs and M.E. Cates. Schematic models for dynamic yielding of sheared colloidal glasses. *Faraday Discussions*, 123:267–286, 2003.

M. Fuchs and M.E. Cates. A mode coupling theory for Brownian particles in homogeneous steady shear flow. *Journal of Rheology*, 53(4):957, 2009.

A. Furukawa and H. Tanaka. Violation of the incompressibility of liquid by simple shear flow. *Nature*, 443(7110):434–8, 2006.

A. Furukawa, K. Kim, S. Saito, and H. Tanaka. Anisotropic cooperative structural rearrangements in sheared supercooled liquids. *Physical Review Letters*, 102(1): 016001, 2009.

C. Fusco, T. Albaret, and A. Tanguy. Rheological properties vs. local dynamics in model disordered materials at low temperature. *The European Physical Journal E*, 37(5):1–9, 2014.

G. Gagnon, J. Patton, and D.J. Lacks. Energy landscape view of fracture and avalanches in disordered materials. *Physical Review E*, 64(5):051508, 2001.

B. Geraud, L. Bocquet, and C. Barentin. Confined flows of a polymer microgel. *The European physical journal. E, Soft matter*, 36(3):9845, 2013.

T. Gibaud, C. Barentin, and S. Manneville. Influence of Boundary Conditions on Yielding in a Soft Glassy Material. *Physical Review Letters*, 101(25), 2008.

C. Goldenberg, A. Tanguy, and J.-L. Barrat. Particle displacements in the elastic deformation of amorphous materials: Local fluctuations vs. non-affine field. *EPL (Europhysics Letters)*, 80(1):16003, 2007.

M. Goldstein. Viscous liquids and the glass transition: a potential energy barrier picture. *The Journal of Chemical Physics*, 51(9):3728–3739, 1969.

W. Götze and T. Voigtmann. Statistische physik: Ideale glasübergänge: Die modenkopplungstheorie beschreibt die dynamik glasbildender systeme. *Physikalische Blätter*, 57(4):41–47, 2001.

J. Goyon. *Matériaux amorphes : des solides qui coulent de façon collective*. PhD thesis, Université Bordeaux I, 2008.

J. Goyon, A. Colin, G. Ovarlez, A. Ajdari, and L. Bocquet. Spatial cooperativity in soft glassy flows. *Nature*, 454(7200):84–7, 2008.

J. Goyon, A. Colin, and L. Bocquet. How does a soft glassy material flow: finite size effects, non local rheology, and flow cooperativity. *Soft Matter*, 6(12):2668, 2010.

I.S. Gradshteyn and I.M. Ryzhik. *Tables of Integrals, Series and Products, (edited by A. Jeffrey)*. Academic Press, Inc., San Diego, CA, 1994.

M. Gross, T. Krüger, and F. Varnik. Rheology of dense suspensions of elastic capsules: normal stresses, yield stress, jamming and confinement effects. *Soft matter*, 10(24):4360–4372, 2014.

R. Gutfraind and O. Pouliquen. Study of the origin of shear zones in quasi-static vertical chute flows by using discrete particle simulations. *Mechanics of Materials*, 24(4):273–285, 1996.

R.D.L. Hanes, C. Dalle-Ferrier, M. Schmiedeberg, M.C. Jenkins, and S.U. Egelhaaf. Colloids in one dimensional random energy landscapes. *Soft Matter*, 8 (9):2714–2723, 2012.

J.-P. Hansen and I.R. McDonald. *Theory of simple liquids*. Elsevier, 1990.

R.R. Hartley and R.P. Behringer. Logarithmic rate dependence of force networks in sheared granular materials. *Nature*, 421(6926):928–31, 2003.

T.K. Haxton and A.J. Liu. Activated Dynamics and Effective Temperature in a Steady State Sheared Glass. *Physical Review Letters*, 99(19):195701, 2007.

P. Hébraud and F. Lequeux. Mode-Coupling Theory for the Pasty Rheology of Soft Glassy Materials. *Physical Review Letters*, 81(14):2934–2937, 1998.

P. Hébraud, F. Lequeux, J.P. Munch, and D.J. Pine. Yielding and Rearrangements in Disordered Emulsions. *Physical Review Letters*, 78(24):4657–4660, 1997.

H.G.E. Hentschel, S. Karmakar, E. Lerner, and I. Procaccia. Size of Plastic Events in Strained Amorphous Solids at Finite Temperatures. *Physical Review Letters*, 104(2):025501, 2010.

A. Heuer. Exploring the potential energy landscape of glass-forming systems: from inherent structures via metabasins to macroscopic transport. *Journal of Physics: Condensed Matter*, 20(37):373101, 2008.

E.R. Homer and C.A. Schuh. Mesoscale modeling of amorphous metals by shear transformation zone dynamics. *Acta Materialia*, 57(9):2823–2833, 2009.

T. Idema, J.O. Dubuis, L. Kang, M.L. Manning, P.C. Nelson, T.C. Lubensky, and A.J. Liu. The syncytial Drosophila embryo as a mechanically excitable medium. *ArXiv e-prints*, 2013.

A. Ikeda, L. Berthier, and P. Sollich. Unified study of glass and jamming rheology in soft particle systems. *Physical Review Letters*, 109(1):018301, 2012.

A. Ikeda, L. Berthier, and P. Sollich. Disentangling glass and jamming physics in the rheology of soft materials. *Soft Matter*, 2013.

P. Ilg and J.-L. Barrat. Driven activation vs. thermal activation. *Europhysics Letters (EPL)*, 79(2):26001, 2007.

E. Irani, P. Chaudhuri, and C. Heussinger. Impact of attractive interactions on the rheology of dense athermal particles. *Physical Review Letters*, 112:188303, 2014.

L. Isa, R. Besseling, and W.C.K. Poon. Shear Zones and Wall Slip in the Capillary Flow of Concentrated Colloidal Suspensions. *Physical Review Letters*, 98(19), 2007.

L. Isa, R. Besseling, A. Morozov, and W. Poon. Velocity Oscillations in Microfluidic Flows of Concentrated Colloidal Suspensions. *Physical Review Letters*, 102 (5), 2009.

E.A. Jagla. Strain localization driven by structural relaxation in sheared amorphous solids. *Physical Review E*, 76(4):046119, 2007.

P. Jop, Y. Forterre, and O. Pouliquen. A constitutive law for dense granular flows. *Nature*, 441(7094):727–30, 2006.

P. Jop, V. Mansard, P. Chaudhuri, L. Bocquet, and A. Colin. Microscale rheology of a soft glassy material close to yielding. *Physical Review Letters*, 108(14): 148301, 2012.

K. Kamrin and G. Koval. Nonlocal constitutive relation for steady granular flow. *Physical Review Letters*, 108(17):178301, 2012.

S. Karmakar, E. Lerner, and I. Procaccia. Statistical physics of the yielding transition in amorphous solids. *Physical Review E*, 82:055103, 2010.

N.C Keim and P.E. Arratia. Mechanical and microscopic properties of the reversible plastic regime in a 2d jammed material. *Physical Review Letters*, 112(2): 028302, 2014.

A.S. Keys, L.O. Hedges, J.P. Garrahan, S.C. Glotzer, and D. Chandler. Excitations Are Localized and Relaxation Is Hierarchical in Glass-Forming Liquids. *Physical Review X*, 1(2):021013, 2011.

T.R. Kirkpatrick, D. Thirumalai, and P.G. Wolynes. Scaling concepts for the dynamics of viscous liquids near an ideal glassy state. *Physical Review A*, 40 (2):1045, 1989.

H.A. Kramers. Brownian motion in a field of force and the diffusion model of chemical reactions. *Physica*, 7(4):284–304, 1940.

G. Kumar, P. Neibecker, Y.H. Liu, and J. Schroers. Critical fictive temperature for plasticity in metallic glasses. *Nature communications*, 4:1536, 2013.

F. Kun, H.A. Carmona, J.S. Andrade Jr, and H.J. Herrmann. Universality behind basquin's law of fatigue. *Physical Review Letters*, 100(9):094301, 2008.

J.S. Langer. Dynamics of shear-transformation zones in amorphous plasticity: Formulation in terms of an effective disorder temperature. *Physical Review E*, 70(4):041502, 2004.

J.S. Langer. Shear-transformation-zone theory of plastic deformation near the glass transition. *Physical Review E*, 77(2):021502, 2008.

P. Langevin. Sur la théorie du mouvement brownien. *CR Acad. Sci. Paris*, 146 (530-533), 1908.

R.G. Larson, E.S.G. Shaqfeh, and S.J. Muller. A purely elastic instability in taylor–couette flow. *Journal of Fluid Mechanics*, 218:573–600, 1990.

A. Le Bouil, A. Amon, S. McNamara, and J. Crassous. Emergence of cooperativity in plasticity of soft glassy materials. *Physical Review Letters*, 112(24):246001, 2014.

M. Le Merrer, S. Cohen-Addad, and R. Höhler. Bubble Rearrangement Duration in Foams near the Jamming Point. *Physical Review Letters*, 108(18), 2012.

A. Lemaître and C. Caroli. Plastic response of a two-dimensional amorphous solid to quasistatic shear: Transverse particle diffusion and phenomenology of dissipative events. *Physical Review E*, 76(3):036104, 2007.

A. Lemaître and C. Caroli. Rate-dependent avalanche size in athermally sheared amorphous solids. *Physical Review Letters*, 103(6):065501–065501, 2009.

J. Lin, E. Lerner, A. Rosso, and M. Wyart. Scaling description of the yielding transition in soft amorphous solids at zero temperature. *arXiv preprint arXiv:1403.6735*, 2014a.

J. Lin, A. Saade, E. Lerner, A. Rosso, and M. Wyart. On the density of shear transformations in amorphous solids. *Europhysics Letters (EPL)*, 105(2):26003–26009, 2014b.

T.S. Majmudar and R.P. Behringer. Contact force measurements and stress-induced anisotropy in granular materials. *Nature*, 435(7045):1079–82, 2005.

C. Maloney and A. Lemaître. Subextensive Scaling in the Athermal, Quasistatic Limit of Amorphous Matter in Plastic Shear Flow. *Physical Review Letters*, 93 (1):016001, 2004.

C.E. Maloney and A. Lemaître. Amorphous systems in athermal, quasistatic shear. *Physical Review E*, 74(1):016118, 2006.

S. Mandal, V. Chikkadi, B. Nienhuis, D. Raabe, P. Schall, and F. Varnik. Single-particle fluctuations and directional correlations in driven hard-sphere glasses. *Physical Review E*, 88(2):022129, 2013.

M.L. Manning, J.S. Langer, and J.M. Carlson. Strain localization in a shear transformation zone model for amorphous solids. *Physical Review E*, 76(5):056106, 2007.

V. Mansard. *Non-local rheology of soft glassy materials*. PhD thesis, Université Bordeaux I, 2012.

V. Mansard, L. Bocquet, and A. Colin. Boundary conditions for soft glassy flows: slippage and surface fluidization. *Soft matter*, 2014.

R. Mari. *Transition vitreuse et transition de blocage : Les solides dÃ©sordonnÃ©s entre champ moyen et dimension finie*. PhD thesis, Université Pierre et Marie Curie, 2011.

R. Mari, F. Krzakala, and J. Kurchan. Jamming versus Glass Transitions. *Physical Review Letters*, 103(2), 2009.

K. Martens, L. Bocquet, and J.-L. Barrat. Connecting diffusion and dynamical heterogeneities in actively deformed amorphous systems. *Physical Review Letters*, 106(15):156001, 2011.

K. Martens, L. Bocquet, and J.-L. Barrat. Spontaneous formation of permanent shear bands in a mesoscopic model of flowing disordered matter. *Soft Matter*, 8(15):4197–4205, 2012.

T.G. Mason, J. Bibette, and D.A. Weitz. Yielding and flow of monodisperse emulsions. *Journal of Colloid and Interface Science*, 179(2):439–448, 1996.

C. Masselon and A. Colin. Influence of boundary conditions and confinement on nonlocal effects in flows of wormlike micellar systems. *Physical Review E*, 81(2), 2010.

S. Meeker, R. Bonnecaze, and M. Cloitre. Slip and Flow in Soft Particle Pastes. *Physical Review Letters*, 92(19), 2004a.

S.P. Meeker, R.T. Bonnecaze, and M. Cloitre. Slip and flow in pastes of soft particles: Direct observation and rheology. *Journal of Rheology (1978-present)*, 48(6):1295–1320, 2004b.

G.H. Meeten. Effects of plate roughness in squeeze-flow rheometry. *Journal of Non-Newtonian Fluid Mechanics*, 124(1-3):51–60, 2004.

K. Miyazaki, D.R. Reichman, and R. Yamamoto. Supercooled liquids under shear: Theory and simulation. *Physical Review E*, 70(1):011501, 2004.

H. Mizuno and R. Yamamoto. Mechanical responses and stress fluctuations of a supercooled liquid in a sheared non-equilibrium state. *The European Physical Journal E*, 35(4):1–14, 2012.

H. Mizuno, S. Mossa, and J.-L. Barrat. Measuring spatial distribution of the local elastic modulus in glasses. *Physical Review E*, 87(4):042306, 2013.

S.J. Muller, R.G. Larson, and E.S.G. Shaqfeh. A purely elastic transition in taylor-couette flow. *Rheologica Acta*, 28(6):499–503, 1989.

N. Murdoch, B. Rozitis, K. Nordstrom, S. Green, P. Michel, T.-L. de Lophem, and W. Losert. Granular Convection in Microgravity. *Physical Review Letters*, 110 (1):018307, 2013.

K. Nichol and M. van Hecke. Flow-induced agitations create a granular fluid: Effective viscosity and fluctuations. *Physical Review E*, 85(6), 2012.

K. Nichol, A. Zanin, R. Bastien, E. Wandersman, and M. van Hecke. Flow-Induced Agitations Create a Granular Fluid. *Physical Review Letters*, 104(7), 2010.

A. Nicolas and J.-L. Barrat. Spatial Cooperativity in Microchannel Flows of Soft Jammed Materials: A Mesoscopic Approach. *Physical Review Letters*, 110(13): 138304, 2013a.

A. Nicolas and J.-L. Barrat. Fd 167 a mesoscopic model for the rheology of soft amorphous solids, with application to microchannel flows. *Faraday Discuss.*, 167(1):567–600, 2013b.

A. Nicolas and M. Fuchs. *In preparation*, 2014.

A. Nicolas and A.N. Morozov. Nonaxisymmetric Instability of Shear-Banded Taylor-Couette Flow. *Physical Review Letters*, 108(8), 2012.

A. Nicolas, K. Martens, and J.-L. Barrat. Rheology of athermal amorphous solids: Revisiting simplified scenarios and the concept of mechanical noise temperature. *arXiv preprint arXiv:1401.6340*, 2014a.

A. Nicolas, K. Martens, L. Bocquet, and J.-L. Barrat. Universal and non-universal features in coarse-grained models of flow in disordered solids. *Soft Matter*, 10: 4648–4661, 2014b.

A. Nicolas, J. Rottler, and J.-L. Barrat. Spatiotemporal correlations between plastic events in the shear flow of athermal amorphous solids. *The European Physical Journal E*, 37(6):50, 2014c.

K.N. Nordstrom, E. Verneuil, P.E. Arratia, A. Basu, Z. Zhang, A.G. Yodh, J.P. Gollub, and D.J. Durian. Microfluidic rheology of soft colloids above and below jamming. *Physical Review Letters*, 105:175701, 2010.

P.R. Nott and J.F. Brady. Pressure-driven flow of suspensions: simulation and theory. *Journal of Fluid Mechanics*, 275(1):157–199, 1994.

C. O'Hern, A. Liu, and S. Nagel. Effective Temperatures in Driven Systems: Static Versus Time-Dependent Relations. *Physical Review Letters*, 93(16):165702, 2004.

J. Olivier. *Fluides vitreux, diffusion réactive, structures craniofaciales : quelques contributions Ã l'étude de ces systÃšmes multi-échelles ou singuliers*. PhD thesis, Université de Savoie, Chambéry, 2011.

P.D. Olmsted. Perspectives on shear banding in complex fluids. *Rheologica Acta*, 47(3):283–300, 2008.

P. Olsson and S. Teitel. Herschel-Bulkley Shearing Rheology Near the Athermal Jamming Transition. *Physical Review Letters*, 109(10):108001, 2012.

I. Ono, C. O'Hern, D. Durian, S. Langer, A. Liu, and S. Nagel. Effective Temperatures of a Driven System Near Jamming. *Physical Review Letters*, 89(9):095703, 2002.

G. Ovarlez, S. Rodts, A. Ragouilliaux, P. Coussot, J. Goyon, and A. Colin. Wide-gap Couette flows of dense emulsions: Local concentration measurements, and comparison between macroscopic and local constitutive law measurements through magnetic resonance imaging. *Physical Review E*, 78(3):036307, 2008.

E.S. Pagac, R.D. Tilton, and D.C. Prieve. Hindered mobility of a rigid sphere near a wall. *Chemical engineering communications*, 148(1):105–122, 1996.

P. Pakdel and G.H. McKinley. Elastic instability and curved streamlines. *Physical Review Letters*, 77(12):2459, 1996.

S. Papenkort and T. Voigtmann. Channel flow of a tensorial shear-thinning maxwell model: Lattice boltzmann simulations. *arXiv preprint arXiv:1310.7450*, 2013.

B. Persson. Theory of friction: Stress domains, relaxation, and creep. *Physical Review B*, 51(19):13568–13585, 1995.

B. Persson. Sliding friction. *Surface Science Reports*, 33(3):83–119, 1999.

G. Picard, A. Ajdari, F. Lequeux, and L. Bocquet. Elastic consequences of a single plastic event: a step towards the microscopic modeling of the flow of yield stress fluids. *The European physical journal. E, Soft matter*, 15(4):371–81, 2004.

G. Picard, A. Ajdari, F. Lequeux, and L. Bocquet. Slow flows of yield stress fluids: Complex spatiotemporal behavior within a simple elastoplastic model. *Physical Review E*, 71(1):010501, 2005.

A. Politi, S. Ciliberto, and R. Scorretti. Failure time in the fiber-bundle model with thermal noise and disorder. *arXiv preprint cond-mat/0206201*, 2002.

O. Pouliquen and R. Gutfraind. Stress fluctuations and shear zones in quasistatic granular chute flows. *Physical Review E*, 53(1):552, 1996.

O. Pouliquen, Y. Forterre, and S. Le Dizes. Slow dense granular flows as a self-induced process. *Advances in Complex Systems*, 04(04):441–450, 2001.

H.M. Princen. Rheology of foams and highly concentrated emulsions: I. elastic properties and yield stress of a cylindrical model system. *Journal of Colloid and interface science*, 91(1):160–175, 1983.

H.M. Princen. Rheology of foams and highly concentrated emulsions. II. experimental study of the yield stress and wall effects for concentrated oil-in-water emulsions. *Journal of Colloid and Interface Science*, 105(1):150–171, 1985.

H.M. Princen and A.D. Kiss. Rheology of foams and highly concentrated emulsions: Iv. an experimental study of the shear viscosity and yield stress of concentrated emulsions. *Journal of colloid and interface science*, 128(1):176–187, 1989.

F. Puosi, J. Rottler, and J-L. Barrat. Time-dependent elastic response to a local shear transformation in amorphous solids. *Physical Review E*, 89:042302, 2014.

M. Rappaz, M. Bellet, M. Deville, and R. Snyder. *Numerical modeling in materials science and engineering*, volume 32. Springer Science & Business, 2010.

K.A. Reddy, Y. Forterre, and O. Pouliquen. Evidence of Mechanically Activated Processes in Slow Granular Flows. *Physical Review Letters*, 106(10):108301, 2011.

C. Reichhardt and C.J.O. Reichhardt. Aspects of jamming in two-dimensional athermal frictionless systems. *Soft matter*, 10(17):2932–2944, 2014.

D.R. Reichman and P. Charbonneau. Mode-coupling theory. *Journal of Statistical Mechanics: Theory and Experiment*, 2005(05):P05013, 2005.

H.F. Reid. *The California Earthquake of April 18, 1906: The Mechanics of the Earthquake/By Harry Fielding Reid*. Carnegie Inst., 1910.

O. Reynolds. Lvii. on the dilatancy of media composed of rigid particles in contact. with experimental illustrations. *The London, Edinburgh, and Dublin Philosophical Magazine and Journal of Science*, 20(127):469–481, 1885.

H. Risken. *The Fokker-Planck Equation. Methods of Solution and Applications,*. 1989.

D. Rodney and T. Schrøder. On the potential energy landscape of supercooled liquids and glasses. *The European physical journal. E, Soft matter*, 34(9):1–7, 2011.

D. Rodney and C. Schuh. Yield stress in metallic glasses: The jamming-unjamming transition studied through Monte Carlo simulations based on the activation-relaxation technique. *Physical Review B*, 80(18), 2009.

J.-N. Roux. Geometric origin of mechanical properties of granular materials. *Physical Review E*, 61(6):6802–6836, 2000.

K Michael Salerno and Mark O Robbins. Effect of inertia on sheared disordered solids: Critical scaling of avalanches in two and three dimensions. *Physical Review E*, 88(6):062206, 2013.

K.M. Salerno, Craig E. Maloney, and Mark O. Robbins. Avalanches in Strained Amorphous Solids: Does Inertia Destroy Critical Behavior? *Physical Review Letters*, 109(10):105703, 2012.

J.-B. Salmon, A. Colin, and S. Manneville. Velocity Profiles in Shear-Banding Wormlike Micelles. *Physical Review Letters*, 90(22), 2003.

M.C. Sanchez, C. Valencia, J.M. Franco, and C. Gallegos. Wall slip phenomena in oil-in-water emulsions: effect of some structural parameters. *Journal of colloid and interface science*, 241(1):226–232, 2001.

P. Schall and M. van Hecke. Shear Bands in Matter with Granularity. *Annual Review of Fluid Mechanics*, 42(1):67–88, 2010.

P. Schall, D.A. Weitz, and F. Spaepen. Structural rearrangements that govern flow in colloidal glasses. *Science (New York, N.Y.)*, 318(5858):1895–9, 2007.

C.A. Schuh, T.C. Hufnagel, and U. Ramamurty. Mechanical behavior of amorphous alloys. *Acta Materialia*, 55(12):4067–4109, 2007.

J.R. Seth, M. Cloitre, and R.T. Bonnecaze. Influence of short-range forces on wall-slip in microgel pastes. *Journal of Rheology (1978-present)*, 52(5):1241–1268, 2008.

J.R. Seth, C. Locatelli-Champagne, F. Monti, R.T. Bonnecaze, and M. Cloitre. How do soft particle glasses yield and flow near solid surfaces? *Soft Matter*, 8(1): 140, 2012.

R. Seto, R. Mari, J.F. Morris, and M.M. Denn. Discontinuous shear thickening of frictional hard-sphere suspensions. *Physical Review Letters*, 111(21):218301, 2013.

E.S.G. Shaqfeh. Purely elastic instabilities in viscometric flows. *Annual Review of Fluid Mechanics*, 28(1):129–185, 1996.

E.S.G. Shaqfeh, S.J. Muller, and R.G. Larson. The effects of gap width and dilute solution properties on the viscoelastic Taylor-Couette instability. *Journal of Fluid Mechanics*, 235(-1):285–317, 1992.

F. Shimizu, S. Ogata, and J. Li. Yield point of metallic glass. *Acta materialia*, 54 (16):4293–4298, 2006.

M. Siebenbürger, M. Fuchs, and M. Ballauff. Core–shell microgels as model colloids for rheological studies. *Soft Matter*, 8(15):4014–4024, 2012.

L. Sjögren. Kinetic theory of current fluctuations in simple classical liquids. *Physical Review A*, 22:2866–2882, 1980.

T. Soddemann, B. Dünweg, and K. Kremer. Dissipative particle dynamics: A useful thermostat for equilibrium and nonequilibrium molecular dynamics simulations. *Physical Review E*, 68(4):046702, 2003.

P. Sollich. Rheological constitutive equation for a model of soft glassy materials. *Physical Review E*, 58(1):738, 1998.

P. Sollich, F. Lequeux, P. Hébraud, and M.E. Cates. Rheology of Soft Glassy Materials. *Physical Review Letters*, 78(10):2020–2023, 1997.

F. Spaepen. A microscopic mechanism for steady state inhomogeneous flow in metallic glasses. *Acta metallurgica*, 25(4):407–415, 1977.

F.H. Stillinger. A topographic view of supercooled liquids and glass formation. *Science*, 267(5206):1935–1939, 1995.

A. Tanguy, F. Leonforte, and J.-L. Barrat. Plastic response of a 2d lennard-jones amorphous solid: Detailed analysis of the local rearrangements at very slow strain rate. *The European Physical Journal E*, 20(3):355–364, 2006.

G.I. Taylor. Stability of a viscous liquid contained between two rotating cylinders. *Proceedings of the Royal Society of London. Series A*, 102(718):541–542, 1923.

B.P. Tighe. Relaxations and rheology near jamming. *Physical Review Letters*, 107 (15):158303, 2011.

B.P. Tighe, E. Woldhuis, J.J.C. Remmers, W. van Saarloos, and M. van Hecke. Model for the Scaling of Stresses and Fluctuations in Flows near Jamming. *Physical Review Letters*, 105(8):088303, 2010.

C. Toninelli, M. Wyart, L. Berthier, G. Biroli, and J.-P. Bouchaud. Dynamical susceptibility of glass formers: Contrasting the predictions of theoretical scenarios. *Physical Review E*, 71(4):041505, 2005.

A. Tordesillas, D. Walker, G. Froyland, J. Zhang, and R.P. Behringer. Transition dynamics and magic-number-like behavior of frictional granular clusters. *Physical Review E*, 86(1), 2012.

C.A. Truesdell and W. Noll. *Handbuch der Physik*. Springer, 1965.

M. Tsamados. Plasticity and dynamical heterogeneity in driven glassy materials. *The European Physical Journal E*, 32(2):165–181, 2010.

M. Tsamados, A. Tanguy, C. Goldenberg, and J.-L. Barrat. Local elasticity map and plasticity in a model Lennard-Jones glass. *Physical Review E*, 80(2), 2009.

D. Vågberg, P. Olsson, and S. Teitel. Universality of Jamming Criticality in Overdamped Shear-Driven Frictionless Disks. *ArXiv e-prints*, 2013.

D. Vandembroucq and S. Roux. Mechanical noise dependent aging and shear banding behavior of a mesoscopic model of amorphous plasticity. *Physical Review B*, 84(13):134210, 2011.

F. Varnik, S. Mandal, V. Chikkadi, D. Denisov, P. Olsson, D. Vågberg, D. Raabe, and P. Schall. Correlations of plasticity in sheared glasses. *arXiv preprint arXiv:1401.3986*, 2014.

J.L. White and A.B. Metzner. Development of constitutive equations for polymeric melts and solutions. *Journal of Applied Polymer Science*, 7(5):1867–1889, 1963.

A. Widmer-Cooper, H. Perry, P. Harrowell, and D.R. Reichman. Irreversible reorganization in a supercooled liquid originates from localized soft modes. *Nature Physics*, 4(9):711–715, 2008.

M. Wyart and M.E. Cates. Discontinuous shear thickening without inertia in dense non-brownian suspensions. *Physical Review Letters*, 112:098302, 2014.

A. Yoshimura and R.K. Prud'homme. Wall slip corrections for couette and parallel disk viscometers. *Journal of Rheology (1978-present)*, 32(1):53–67, 1988.

V.Y. Zaitsev, P. Richard, R. Delannay, V. Tournat, and V.E. Gusev. Pre-avalanche structural rearrangements in the bulk of granular medium: Experimental evidence. *EPL (Europhysics Letters)*, 83(6):64003, 2008.

V.Y. Zaitsev, V.E. Gusev, V. Tournat, and P. Richard. Slow relaxation and aging phenomena at the nanoscale in granular materials. *Physical Review Letters*, 112: 108302, 2014.

R. Zargar, B. Nienhuis, P. Schall, and D. Bonn. Direct Measurement of the Free Energy of Aging Hard Sphere Colloidal Glasses. *Physical Review Letters*, 110 (25):258301, 2013.